UNIVERSITÀ
DEGLI STUDI
FIRENZE

DOTTORATO DI RICERCA IN SCIENZE CHIMICHE

CICLO XXXIV

COORDINATORE PROF. PIERO BAGLIONI

PROBING THE NANOMECHANICAL PROPERTIES OF LAMELLAR AND NONLAMELLAR LIPID MEMBRANES

Settore Scientifico Disciplinare CHIM/02

Dottorando
Andrea Ridolfi

Tutore
Prof. Debora Berti

Co-tutore
Dr. Francesco Valle

Coordinatore
Prof. Piero Baglioni

ANNI 2018-2021

Abstract

One of the most significant consequences of lipid self-assembly is the formation of biological membranes. These lipid interfaces are ubiquitous in Nature, they can be found in viruses, bacteria, cells and cell-derived organelles, where they separate, define and protect these biological compartments from their outer environments. Lipid membranes also take part in numerous biological processes, such as endo/exocytosis, mitosis and signalling; in doing that, they undergo deformations and withstand stresses of different type and extent. Studying membrane nanomechanics, i.e. understanding the mechanical properties that regulate the response of these lipid interfaces to nanoscale deformations, represents a fundamental step for achieving a thorough comprehension of multiple biological phenomena. However, disentangling the different contributions that dictate the mechanical response of most lipid membranous assemblies still represents an intricate challenge; in addition to limiting the current knowledge about membrane-related processes, this problem is also hindering the development of numerous membrane-based biotechnological applications.

This work deals with the nanomechanics of both lamellar and nonlamellar lipid membranes; in particular, it describes how different membranous lipid assemblies respond to deformations and stresses occurring at the nanoscale level. Leveraging a wide range of techniques, spanning from Atomic Force Microscopy (AFM) to neutron/X-ray scattering, results shed new light on fundamental mechanisms pivoting around membrane nanomechanics. In particular, the effect of stiffness and membrane elasticity on the adsorption of unilamellar lipid nanovesicles to surfaces, and on the interaction of nanoparticles with their membranes are herein investigated. Moreover, an in-depth AFM-based Force Spectroscopy analysis elucidates how the mechanical response of a vesicle is made up by multiple cooperating parameters. With regards to nonlamellar membranes, our findings provide the first

nanomechanical analysis of cubic lipid architectures and show that these assemblies are characterized by a higher structural stability than lamellar ones, against the disruption induced by interacting nanoparticles.
The herein presented set of results enriches the current understanding on the nanomechanics of both lamellar and nonlamellar lipid membranes and offers valuable information for promising future developments in the field.

Contents

List of Publications

Contributions included in this thesis

- **Stiffness of Fluid and Gel Phase Lipid Nanovesicles: Weighting the Contributions of Membrane Bending Modulus and Luminal Pressurization**
  A. Ridolfi, L. Caselli, M. Baldoni, C. Montis, F. Mercuri, D. Berti, F. Valle and M. Brucale, *Langmuir* 2021, 37, 41, 12027-12037.
  (Paper 1)

- **AFM-based High-Throughput Nanomechanical Screening of Extracellular Vesicles**
  A. Ridolfi, M. Brucale, C. Montis, L. Caselli, L. Paolini, A. Borup, A. Toftegaard Boysen, F. Loria, M. J. van Herwijnen, M. Kleinjan, P.Nejsum, N. Zarovni, M. Wauben, D. Berti, P. Bergese and F. Valle, *Analytical Chemistry* 2020, 92 (15), 10274-10282.
  (Paper 2)

- **A Plasmon-Based Nanoruler to Probe the Mechanical Properties of Synthetic and Biogenic Nanosized Lipid Vesicles**
  L. Caselli, A. Ridolfi, J. Cardellini, L. Sharpnack, L. Paolini, M. Brucale, F. Valle, C. Montis, P. Bergese and D. Berti, *Nanoscale Horizon*, 2021, 6, 543-550.
  (Paper 3)

- **Gold nanoparticles interacting with synthetic lipid rafts: an AFM investigation**
  A. Ridolfi, L. Caselli, C. Montis, G. Mangiapia, D. Berti, M. Brucale and F. Valle, *Journal of Microscopy* 2020, 00, 1–10.
  (Paper 4)

- **Nanoscale structural and mechanical characterization of thin bicon-**

tinuous cubic phase lipid films
A. Ridolfi, B. Humphreys, L. Caselli, C. Montis, D. Berti, T. Nylander, F. Valle and M. Brucale, *Colloids and Surfaces B: Biointerfaces* (Under review).
(Paper 5)

- **Interaction of nanoparticles with lipid films: the role of symmetry and shape anisotropy**
  Lucrezia Caselli, Andrea Ridolfi, Gaetano Mangiapia, Pierfrancesco Maltoni, Jean-Francois Moulin, Debora Berti, Nina-Juliane Steinke, Emil Gustafsson, Tommy Nylander, Costanza Montis, *Physical Chemistry Chemical Physics* 2021, DOI: 10.1039/D1CP03201A.
  (Paper 6)

Other contributions

- **Malignant ascites-derived small extracellular vesicles in advanced ovarian cancer patients: insights into the dynamics of extracellular matrix**
  Barbara Bortot, Maura Apollonio, Enrico Rampazzo, Francesco Valle, Marco Brucale, Andrea Ridolfi, Blendi Ura, Riccardo Addobbati, Giovanni Di Lorenzo, Federico Romano, Francesca Buonomo, Chiara Ripepi, Giuseppe Ricci, Stefania Biffi, *Molecular Oncology* 2021.

- **Two Dimensional-Difference in Gel Electrophoresis (2D-DIGE) Proteomic Approach for the Identification of Biomarkers in Endometrial Cancer Serum**
  Blendi Ura, Stefania Biffi, Lorenzo Monasta, Giorgio Arrigoni, Ilaria Battisti, Giovanni Di Lorenzo, Federico Romano, Michelangelo Aloisio, Fulvio Celsi, Riccardo Addobbati, Francesco Valle, Enrico Rampazzo, Marco Brucale, Andrea Ridolfi, Danilo Licastro, Giuseppe Ricci, *Cancers* 2021, 13.14: 3639.

- **Nanoanalytical analysis of bisphosphonate-driven alterations of microcalcifications using a 3D hydrogel system and in vivo mouse model**
  J. L. Ruiz, J. D. Hutcheson, L. Cardoso, T. Pham, F. Buffolo, S. Busatto, S. Federici, A. Ridolfi, M. Aikawa, P. Bergese, S. Weinbaum and E. Aikawa, *Proceedings of the National Academy of Sciences (PNAS)* 2021, 118.4.

- **Extracellular Vesicles Analysis in the COVID-19 Era: Insights on Serum Inactivation Protocols Towards Downstream Isolation and**

Analysis
R. Frigerio, A. Musicò, M. Brucale, A. Ridolfi, S. Galbiati, R. Vago, G. Bergamaschi, A. M. Ferretti, M. Chiari, F. Valle, A. Gori, M. Cretich, *Cells* 2021, 10.3: 544.

- **Augmented COlorimetric NANoplasmonic (CONAN) method for grading purity and determine concentration of EV microliter volume solutions**
  Andrea Zendrini, Lucia Paolini, Sara Busatto, Annalisa Radeghieri, Miriam Romano, Marca HM Wauben, Martijn JC Van Herwijnen, Peter Nejsum, Anne Borup, Andrea Ridolfi, Costanza Montis, Paolo Bergese, *Frontiers in bioengineering and biotechnology* 2020, 7: 452.

- **Exploitation of a novel biosensor based on the full-length human F508del-CFTR with computational studies, biochemical and biological assays for the characterization of a new Lumacaftor/Tezacaftor analogue**
  Pasqualina D'Ursi, Matteo Uggeri, Chiara Urbinati, Enrico Millo, Giulia Paiardi, Luciano Milanesi, Robert C Ford, Jack Clews, Xin Meng, Paolo Bergese, Andrea Ridolfi, Nicoletta Pedemonte, Paola Fossa, Alessandro Orro, Marco Rusnati, *Sensors and Actuators B: Chemical* 2019, 301: 127131.

- **Interaction of extracellular vesicles with Si surface studied by nanomechanical microcantilever sensors**
  Stefania Federici, Andrea Ridolfi, Andrea Zendrini, Annalisa Radeghieri, Elza Bontempi, Laura E Depero, Paolo Bergese, *Applied Sciences* 2018, 8.3: 404.

List of Abbreviations

ACF	Autocorrelation function
AFM	Atomic Force Microscopy
AFM-FS	Atomic Force Microscopy-based Force Spectroscopy
AuNPs	Gold nanoparticles
AuNSs	Gold nano spheres
AuNRods	Gold nano rods
CLSM	Confocal Laser Scanning Microscopy
CTAB	Cetyltrimethyl ammonium bromide
DOPC	1,2-dioleoyl-sn-glycero-3-phosphocholine
DPPC	1,2-dipalmitoyl-sn-glycero-3-phosphocholine
DSPC	1,2-distearoyl-sn-glycero-3-phosphocholine
ER	Endoplasmic Reticulum
EVs	Extracellular vesicles
FS	Force Spectroscopy
GISANS	Grazing Incidence Small Angle Neutron Scattering
GISAS	Grazing Incidence Small Angle Scattering
GMO	Glycerol Monooleate
GUV	Giant Unilamellar Vesicles
IPMS	Inifinite Triply Periodic Minimal Surfaces
MVB	Multivesicular bodies
NPs	nanoparticles
NR	Neutron Reflectivity
POPC	1-Palmitoyl-2- oleoyl-sn-phosphocholine
$\mathbf{Q}_{II}$	Inverse Bicontinuous Cubic
$\mathbf{Q}_{II}^{D}$	Inverse Bicontinuous Cubic Double Diamond
SANS	Small Angle Neutron Scattering
SAS	Small Angle Scattering
SAXS	Small Angle X-ray Scattering
SLB	Supported Lipid Bilayer

SLD	Scattering Length Density
TMA	N,N,N-trimethyl(11-mercaptoundecyl)-ammonium bromide
TST	Thin Shell Theory
XR	X-ray Reflectivity

Thesis outline

This work reports on the nanomechanics of lamellar and nonlamellar lipid membranes; more precisely on how natural and synthetic membranous self-assemblies, respond to nanoscale deformations. Understanding and characterizing the mechanical properties of lipid membranes is of fundamental importance and could help to better rationalize various biological processes that involve interactions with membranes and/or membrane delimited compartments.

The first part of the thesis presents those fundamental concepts that are needed for a complete understanding of the subsequently reported findings, together with a brief description of the main systems and techniques that were adopted.

Chapter 1 introduces lipid membranes and the process of self-assembly, showing that lipid interfaces are ubiquitous in Nature and describing the main parameters used to unambiguously identify different mesophases. It then provides examples of lamellar and nonlamellar membranes, found in both natural and synthetic systems. The final part stresses the importance of understanding the nanomechanics of lipid membranes, it presents the main types of deformations to which a membrane is subjected and explains the theoretical models commonly used in studies dealing with membrane mechanics.

Chapter 2 describes the instrumentation, techniques and systems employed in all the manuscripts included in this work. Most of the times, in order to characterize lipid self-assemblies under controlled conditions and to avoid complications connected with the intrinsic complexity of most natural systems, synthetic lipid models are used. When possible, findings are then transposed to natural systems, which in this case are represented by Extracellular vesicles (EVs).

The second half of the thesis presents the obtained results and it is organized in two main parts, addressing the nanomechanical analysis of lamellar and nonlamellar membranes, respectively. The mechanics of lamellar lipid membranes is covered in chapters 3 and 4.

Chapter 3 reports on the findings of Paper 1, in which, by probing the mechanical properties of both SLBs and liposomes by means of AFM, we shed light on how

membrane elasticity and internal pressurization contribute to the overall mechanical response of both gel and fluid phase lipid vesicles to nanoscale deformations.
Chapter 4 reports on the findings of three different manuscripts and is subdivided into three main sections. The first section reports on Paper 2 and shows how the stiffness of lipid vesicles influences their adsorption on rigid substrates; the second section describes findings from Paper 3, demonstrating that even the interaction of gold nano particles (AuNPs) on the vesicle membrane is predominantly regulated by this mechanical property. Findings from both the studies were also applied to natural analogs, i.e. EVs, and used for developing two independent high-throughput mechanical characterizations of lipid vesicles presenting unknown stiffness. The last section presents findings from Paper 4, where the adsorption and internalization of AuNPs is investigated using model membranes presenting lateral heterogeneities in the form of lipid rafts. The obtained results show that also membrane heterogeneity can influence interactions with nanomaterials
The second part of the results deals with the mechanical and structural characterizations of nonlamellar lipid membranes, in particular inverse bicontinuous cubic phase membranes.
Chapter 5 deals with the nanomechanics of bicontinuous cubic phase architectures; by presenting findings from Paper 5, it describes an AFM-based mechanical and structural characterization of cubic membranes. Such analysis shows for the first time that the response of these nonlamellar mesophases to nansocale deformations is deeply related to their topology.
The last chapter deals with the structural stability of cubic membranes following the interaction with external nanomaterials, such as AuNPs of different shape; all the results are included in Paper 6. In this work, by combining multiple scattering techniques, we show that cubic membranes seem to be more stable than lamellar ones against the disruptive action of AuNPs.
The full text and supporting information of the six above-mentioned manuscripts are attached in the Appendix.
Taken together, the herein presented findings shed light on how lipid membranes of different architecture respond to nanoscale deformations; moreover, given the pivotal role of membrane mechanics in numerous biological processes, our results could lead to a better understanding of multiple fundamental yet not fully understood interactions.

Part I

Fundamentals

Chapter 1

Introduction

Surfactants and more specifically lipids, represent amphiphilic molecules that, once brought in contact with a solvent, can self-assemble into a plethora of different mesophases. Among the fundamental phenomena deriving from lipid self-assembly, the formation of membranes retains a top position and had a crucial importance for the development of life [1]. As displayed in Figure 1.1, lipid membranes can be found in viruses, bacteria, cells and cell-derived organelles; they define and hence separate the above-mentioned compartments from the outer environments and also take part in almost every biological process.

Depending on the shape and packing degree of their molecular constituents, lipid

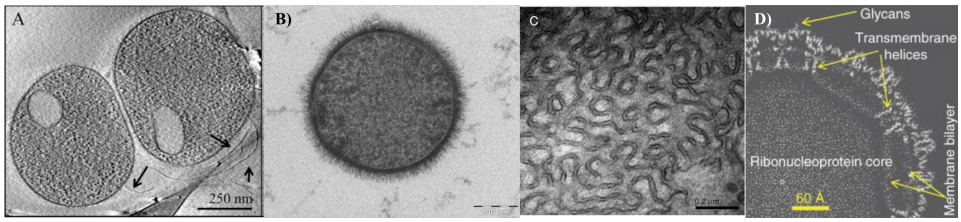

Figure 1.1: Cryo-electron microscopy images of biological compartments delimited by lipid membranes. a) AMD plasma cells with putative pili (arrows) [2]. b) The Bacterium Bacillus subtilis taken with a Tecnai T-12 TEM. Taken by Allon Weiner, The Weizmann Institute of Science, Rehovot, Israel. 2006. c) Nonlamellar cubic membranes in UT-1 cells [3]. d) Mature dengue virus [4].

membranes can display either lamellar or nonlamellar architectures; each structure presents characteristic features in terms of curvature and topology.

Lipids are the most abundant constituents of natural membranes, due to their amphiphilic nature, these molecules usually arrange themselves into bilayers; structures that allow sequestering the hydrophobic portion of these molecules from the

hydrophilic environment. The shape and packing degree of the lipid molecules not only dictate the type of membrane that will be formed, they are also responsible for its physico-chemical properties, e.g. its surface charge, stability and mechanics. Probing these properties is of fundamental importance for understanding multiple membrane-related biological processes and for the development of promising membrane-based biomedical applications.

1.1 Different lipid molecules generate different membrane types

This section will briefly describe how the structure of most lipid self-assemblies is highly dependent on the shape and packing degree of their lipid constituents. Based on this, parameters that are commonly used for the characterization of lipid mesophases will be introduced, together with some examples of membranes and/or membranous structures presenting either lamellar or nonlamellar geometries.

Lipid packing and membrane curvature

Lipids are amphiphilic molecules characterized by an hydrophilic (water soluble) head and one or multiple hydrophobic (water insoluble) tails. Within a liquid environment, lipid molecules try to shield their hydrophobic tails from the aqueous solvent by self-assembling into larger aggregates, in order to minimize their free energy. It is hence possible to predict the size and shape of the aggregate by relating molecular parameters such as hydrophobic volume v, tail/chain length l_0 and head group area a_0 with intensive variables like temperature and ionic strength [5]. This is because the free energy of the self-assembly is made up of three main terms:

- an hydrophobic contribution from the hydrocarbons tails, which tries to avoid any contact with the solvent;
- a surface term, coming from the repulsive and attractive interactions between the head groups;
- a packing term, coming from the exclusion of both solvents and head groups from the hydrocarbon region.

The combination of these three parameters can be summarized in the so-called *Packing parameter* P, which, according to Israelachvili et al. [6], is related to the

above-mentioned molecular parameters by Equation 1.1.

$$P = v/l_0 a_0 \tag{1.1}$$

Following 1.1, multiple self-assemblies can be generated; some of them are presented in Figure 1.2.

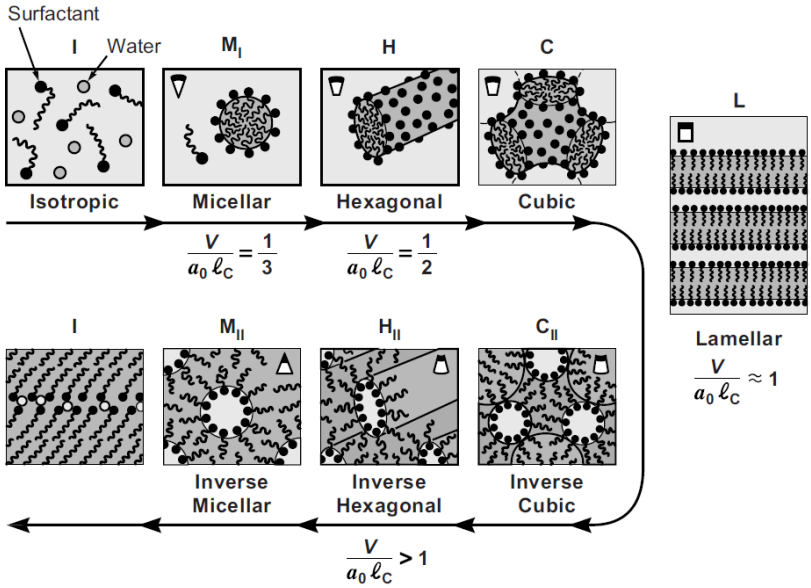

Figure 1.2: Different types of structures and mesophases formed by amphiphiles in aqueous solutions depending on their packing parameter $v/l_0 a_0$. Figure adapted from [7].

Double chain surfactants (like some phospholipids) tend to form structures like vesicles and liquid crystals; whose membranes possess interfacial curvatures that can be either lamellar or nonlamellar. These different structures can be characterized by employing an alternative approach, which instead of focusing on the packing parameter of single molecular constituents, analyses the curvature of the aggregate's interface [5]. In particular, given k_1 and k_2 the principle curvatures at a specific point on a membrane, we can define the mean curvature H, using Equation 1.2:

$$H = 1/2(k_1 + k_2) \tag{1.2}$$

It is possible to calculate H in various regions of the membrane; a common choice is to use the lipid/water interface (i.e. the surface originated by the region that separates the lipid headgroups from the aqueous solvent) [8]. Conventionally, positive mean interfacial curvatures describe situations in which the membrane bends towards the hydrocarbon chain region, while negative mean interfacial curvatures

identify the opposite scenario. From the application of Equation 1.2, a vesicle (a sphere) will be characterized by $k_1 = k_2 = 1/R$ and so $H = 1/R$, where R is the radius of the vesicle itself, while a planar bilayer will have $k_1 = k_2 = 0$ and so $H = 0$. Another parameter that helps to unequivocally identify a specific mesophase is the Gaussian curvature. The Gaussian curvature (K), is defined by Equation 1.3

$$K = k_1 k_2 \tag{1.3}$$

Taken together, the values of H and K allow differentiating between all the possible lipid mesophases.

Lamellar membranes

Lamellar membranes are the most commonly encountered mesophases as they can be formed by a wide variety of double- and/or higher- chained amphiphiles. In these mesophases, the packing parameter of the lipid constituents is typically ≈ 1, which means a nearly cylindrical molecular shape. They consists of one or multiple stacked planar amphiphilic bilayers, forming sheets with 1D periodicity [9]. Each sheet has an extremely tiny aspect ratio, with the lateral dimensions being orders of magnitude larger than the thickness, which is usually ≈ 5 nm. In order to avoid edge effects, lamellar lipid bilayers usually bend and form closed unilamellar lipid envelopes such as cells, vesicles and other organelles (Figure 1.3). In order

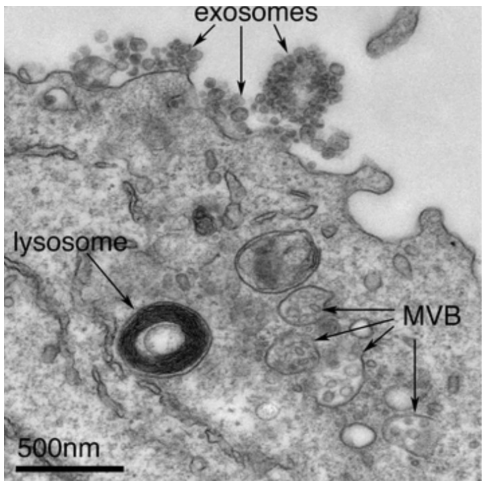

Figure 1.3: Cells, vesicles and organelles are mostly characterized by lamellar membranes. A transmission electron micrograph of an Epstein–Barr virus-transformed B cell with exosomes budding from the plasma membrane. Multivesicular bodies (MVB) can be seen which can deliver content to lysosomes for degradation or can fuse with the cell surface to release intraluminal vesicles as exosomes. Figure adapted from [10].

to study the above-mentioned natural compartments and their membranes under controlled and simplified conditions, synthetic lipid-based models are commonly employed; they feature Giant Unilamellar Vesicles (GUV) (i.e. micrometer sized lipid vesicles) [11] and Liposomes (i.e. nanometer sized lipid vesicles) [12] as mimics of cells, EVs (more on them in the next section) and their membranes. It is also possible to realize synthetic planar lipid membranes (or stacks of bilayers) either supported by a substrate (called Supported Lipid Bilayers, SLBs) or free to fluctuate (called floating bilayers) [13]; these planar membrane models allow performing various interface and structural studies avoiding the problems related to the three dimensional complexity of the previously-mentioned lipid compartments. Figure 1.4 displays some examples of synthetic models used to study the structure of lamellar membranes.

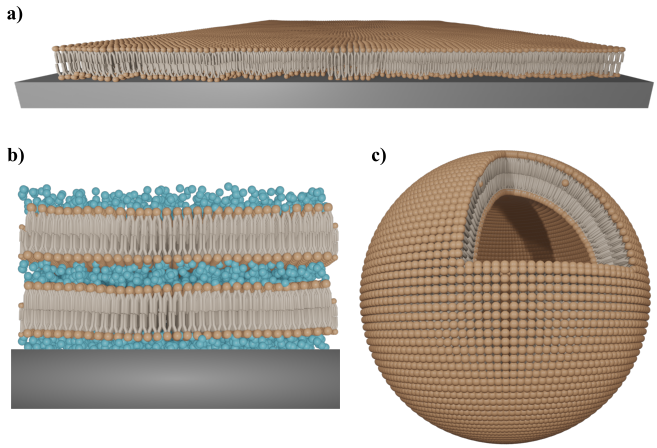

Figure 1.4: Examples of most commonly used synthetic models for studying lamellar membranes under controlled conditions. a) a Supported Lipid Bilayer (SLB), formed by a lipid bilayer deposited on a rigid substrate; b) multilamellar floating bilayers, constituted of a stack of lipid bilayers separated by water interlayers; c) a unilamellar lipid vesicle whose membrane is made of a curved lipid bilayer; depending on its size it is classifies as GUV or liposome.

Extracellular vesicles

Extracellular vesicles (EVs) are an heterogeneous group of biogenic lipid vesicles, presenting sizes that range from tenths to hundreds of nanometres [14]. They are produced by cells according to different biogenic pathways; some of them originate from the Multivesicular Bodies (MVBs) in the intraluminal region of cells while others directly shed from the plasma membrane; depending on their origin, they can be differentiated in multiple subpopulations, such as exosomes and microvesicles.

As displayed in Figure 1.5, EVs are characterized by a lamellar lipid membrane in which various types of proteins and glycans are embedded; their cargo mostly consists of nucleic acids (like mRNA/miRNA, DNA and other non-coding RNAs), carbohydrates, proteins and lipids. Serving as cargoes for biological material, EVs

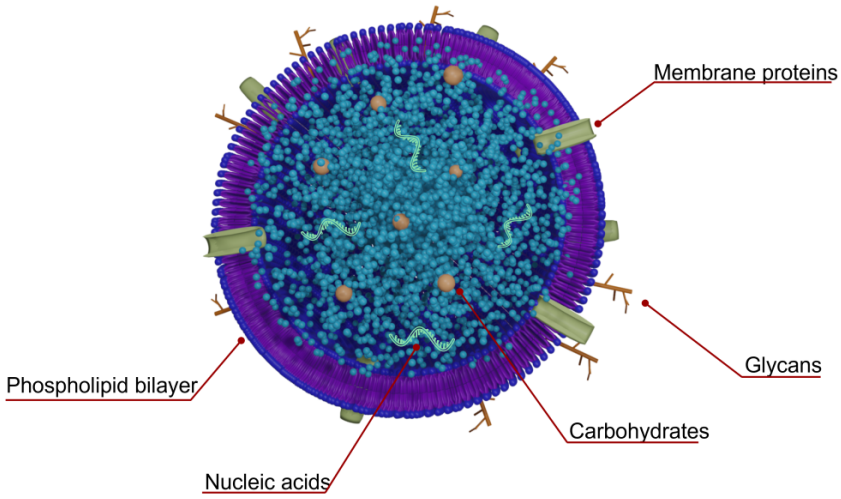

Figure 1.5: Schematic representation of an Extracellular vesicle (EV) with all its major components.

play a crucial role in intercellular communication and are actively involved in various physiological processes, such as coagulation and immune system activation [15]. Due to their properties and functions, they represent promising candidates for multiple diagnostic applications; indeed, it has been found that pathological events like the initiation of pre-metastatic niche and the colonization of healthy organs by malignant tumours are both mediated by EVs [16]. In addition to the field of diagnostics, EVs could provide huge contributions also to drug delivery applications; compared to even the most advanced synthetic nanoparticles, they possess improved targeting, and circulation performance combined with increased bioavailability, personalization and sustainability [15].
Due to their intrinsic heterogeneity, the taxonomy of EVs still represents a widely open issue [17]; several criteria, such as biogenesis, morphometry, composition etc... have to be taken into account for obtaining a thorough characterization of a single EV population.
The mechanical properties of EVs represent another fundamental criteria for dis-

criminating among different EV populations; moreover, several studies reported on alterations in the mechanical characteristics of EVs, induced by the presence of a pathological condition [18–21].
In the following chapters, most of the knowledge derived from the study of synthetic lamellar membrane models will be translated to EV samples collected from very different natural sources, in the attempt to provide useful methods for their characterization and for shedding light on relevant, as yet unsolved issues, such as their mechanical properties.

Nonlamellar membranes

Although the membranes of cells and most cell-derived organelles consist of flat sheets, multiple studies revealed that lipid membranes may fold into "unusual", highly organized structures, presenting 2D or 3D periodicity [3]. These structures are ubiquitous in Nature and have been spotted in all kingdoms of life, both under physiological or pathological conditions, such as in mitochondria or in virally infected cells. Nonlamellar membranes also occur in the endoplasmic reticulum (ER) of every human cell. Figure 1.6 displays few examples of nonlamellar membranes occurring in Nature. These architectures can be characterized based on

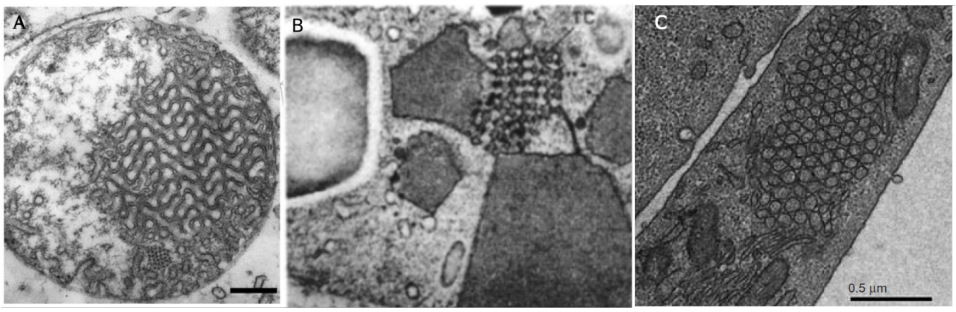

Figure 1.6: Nonlamellar membranes occurring in natural systems. A) A mitochondrion of 10 days starved amoeba Chaos cells (scale bar: 250 nm); B) hexagonal membrane organizations observed in UT-1 cells, 48–72 hours after compactin (40 μM) treatment; C) A cubic membrane in leucoplasts of root tip cells, where they are actively involved in "protein storage". Images adapted from [3].

their lipid/water interface [8]. While amphiphiles with a packing parameter ≈ 1 self-assemble into lamellar structures, i.e. with zero mean interfacial curvature, cone-shaped and wedge-shaped amphiphiles favour the formation of mesophases with positive and negative interfacial H, respectively.
Among the various nonlamellar membranes, bicontinuous cubic phase membranes are of particular interest, especially due to their peculiar 3D architecture, characterized by a continuous lipid bilayer that subdivides the three-dimensional space into

two interwoven systems of water channels [22]. More precisely, in these mesophases, lipid molecules self-assemble in a curved bilayer, whose middle plane topology can be described by one of the three Schwarz's Infinite Triply Periodic Minimal Surfaces (IPMS) [23, 24], i.e. the primitive (P), double diamond (D) and gyroid (G); all of them are displayed in Figure 1.7.

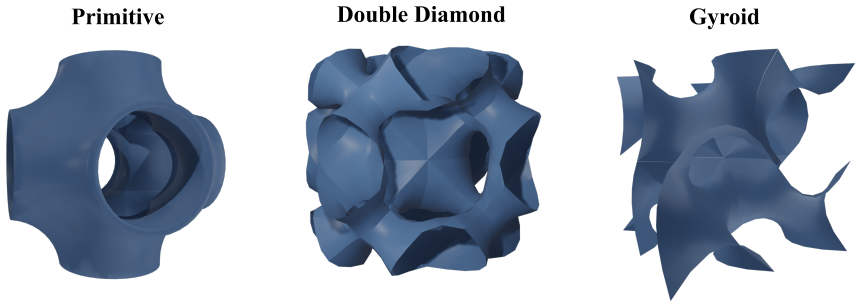

Figure 1.7: The three Schwarz's Infinite Triply Periodic Minimal Surfaces (IPMS). The IPMS describe the midplane of the curved lipid bilayer forming the bicontinuous cubic phase membranes.

1.2 The mechanical properties of lipid membranes

As anticipated in the previous section, lipid membranes participate in multiple biological processes and in doing that, they are subjected to stresses and deformations of various type and extent. In exo/endo-cytosis, the plasma membrane bends and locally adopts highly curved configurations, in order to internalize and/or release material; the same happens when lipid vesicles fuse or bud from cells or when they interact with other interfaces (e.g. when adsorbing on a rigid surface), they experience nanometric deformations. Another slightly different example is offered by cell division, where the plasma membrane has to stretch; even in that case, the mechanical properties of the lipid bilayer represent fundamental regulators of the process. Moreover, the mechanical properties of cells and cell-derived nanovesicles, such as Extracellular vesicles (EVs), have been reported to vary in the presence of pathological conditions [18, 19, 25, 26] and thus represent important indicators of an organism's health condition.
From all these examples it is clear that elucidating the mechanics of lipid membranes would represent a fundamental achievement for multiple research fields; it would shed light on numerous open issues in different biological processes and provide relevant information regarding how these natural interfaces modulate the interaction of our organism with external materials, such as nanoparticles and biomolecules.

The following sections briefly describe the most important contributors to the mechanics of a lipid membrane, providing the basic knowledge on the concepts exploited in the next chapters for elaborating the experimental data and deriving the presented results.

Membrane physical state

It is impossible to think about the mechanical and structural properties of a lipid membrane, without taking into account the physical state of the membrane itself, which depends on both temperature and degree of unsaturation of the lipids hydrocarbon chains. For what concerns the mechanical properties of lipid bilayers, an important distinction has to be made between fluid and gel phase bilayers; in the so-called fluid phase, lipid molecules are able to diffuse freely in the lateral directions, while they move in the perpendicular one only on very long time scales. In the so-called gel phase, lipid molecules are more tightly packed, thus generating a more rigid bilayer in which, even the lateral motion of the molecules implies an energetic cost. A schematic representation of fluid and gel phase bilayer membranes is given in Figure 1.8. Variations in the rigidity of the bilayer also affect the amp-

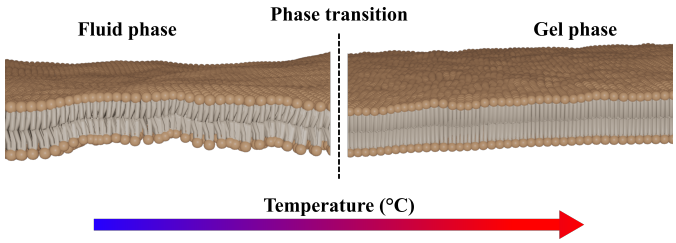

Figure 1.8: Representation of fluid and gel phase bilayers. Fluid bilayers are softer than gel ones and display larger fluctuations; moreover, their lipid molecules are less tightly packed and more free to diffuse laterally. The same bilayer may undergo a phase transition as a consequence of temperature variations; the temperature at which the phase changes is called melting temperature T_m.

litude of its thermal fluctuations, which in the case of multiple bilayer stacks means different water interlayer thickness values. Based on this, lipids presenting one or more unsaturations along their hydrocarbon chains will be more stable in the fluid phase and will generate softer membranes, compared to lipids that present long and fully saturated hydrocarbon chains. Lipid bilayers may undergo phase transitions when the temperature of the system is varied; higher temperatures imply an increased thermal agitation of the molecules and hence a transition towards the fluid phase; on the contrary, lower temperatures favour the presence of gel phase. Each lipid molecule undergoes phase transition at a specific temperature, called *melting*

temperature, T_m (more details can be found in [27]). Therefore, when comparing the mechanical properties of different lipid membranes, it is important to take into account the phase state of their molecular constituents, since it can provide fundamental information for understanding the observed properties.

Membrane mechanics: deformations and free-energy

According to Phillips et al. [28] and as shown in Figure 1.9, it is possible to recapitulate the various kinds of deformation that usually characterize a lipid membrane into four main types:

- **stretching:** when the area of a patch of membrane is increased by an amount Δa, along the membrane plane;
- **bending:** when the local curvature of a membrane is varied from its spontaneous configuration;
- **compression:** when the thickness of a membrane is altered from its equilibrium value;
- **shearing:** when the two monolayers are not completely free to slide one upon the other, there will be some shearing deformations and stresses associated to their motion.

All the above-mentioned membrane deformations always come with an associated free-energy penalty; this is because it takes some energy to alter the equilibrium configuration of a membrane. Over the years, different models and techniques have been developed in order to probe the mechanical properties of lipid membranes, some of them rely on the use of supported planar membranes while others on the use of lipid vesicles. In order to compare results obtained on different systems (either vesicles or planar membranes), membrane elasticity has to be expressed employing intrinsic biophysical parameters. The bending modulus (κ), which describes the energy required to deform a membrane from its spontaneous curvature [29], is one of the most important and widely used indicators. This is because the deformation energy required for numerous biological processes to take place is mostly ascribable to bending deformations of the membrane. Other theories [30, 31] derive another descriptor of membrane elasticity, the so-called Young Modulus (E), which describes the tendency of a material to deform along the axis where the forces are applied. These two different membrane descriptors are related, according to the Theory of Elasticity [32], by Equation 1.4, where ν is the Poisson modulus and h the membrane thickness.

$$\kappa = \frac{Eh^3}{12(1-\nu)} \tag{1.4}$$

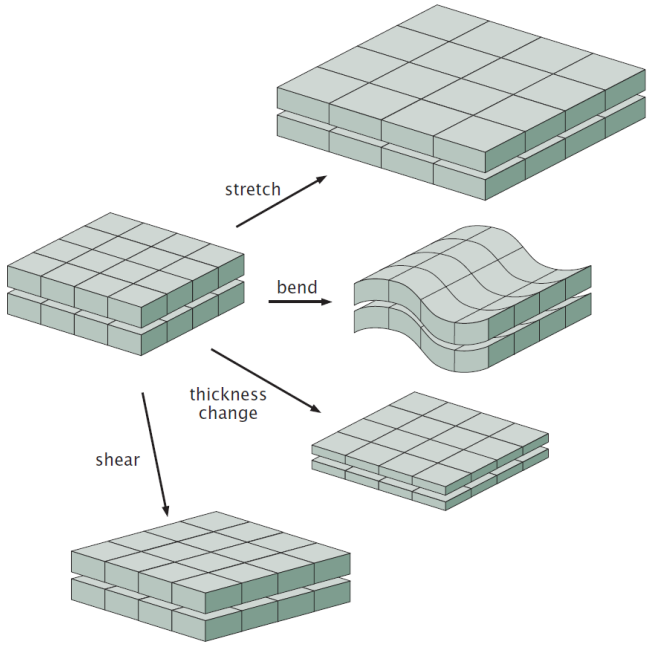

Figure 1.9: Different types of membrane deformations; from top to bottom: stretching, bending, compression and shearing. Picture adapted from [28]

.

As will be detailed in the next chapter, one of the most classical way to probe the mechanics of lipid membranes is to use a nano-indenter to impart a nanoscale deformation to the system (a vesicle or a supported planar membrane); in these experiments, a relation between force and deformation is obtained. In order to estimate biophysical parameters of membrane rigidity, such as κ, from this type of experiments, numerous theoretical models have been developed, among which, the ones that will be covered in the next chapters are:

- **Hertz theory** [33]: introduced by Heinrich Hertz to describe the stresses originating from the contact of two bodies, it relies on the assumptions that i) the surfaces are smooth and frictionless, ii) the contact area is small compared to the size of the bodies, iii) the bodies are isotropic and elastic. This model can be used for analysing the indentation of flat supported membranes (such as Supported Lipid Bilayers, SLBs); in the years that followed its publication, other refinements and/or variants have been derived by Boussinesq, Landau and Sneddon [30, 34, 35] also accounting for different indenter geometries. The most recent advancement was proposed by Dimitriadis et al. [36], who modified the Hertz theory in order to account for the effects originating from finite sample thickness. According to [36], Equation 1.5 summarizes the re-

lationship between force (F) and indentation depth (δ), and allows finding the Young modulus (E) of the probed material, knowing the indenter radius (R_{tip}), and $\chi = \sqrt{R_{tip}\delta/h}$, where h is the membrane thickness.

$$F = \frac{16}{9} E R_{tip}^{\frac{1}{2}} \delta^{\frac{3}{2}} \left[1 + 0.884\chi + 0.781\chi^2 + 0.386\chi^3 + 0.0048\chi^4\right] \tag{1.5}$$

- **Thin Shell Theory (TST)**: based on the Theory of Elasticity, by Landau [30], TST can be used to describe the indentation of spherical shells, such as viruses and lipid vesicles. In the latter case, the theory models the indented vesicle as being solely constituted by a homogeneous shell with thickness equal to the height of its lipid bilayer. Despite being extensively used, this theory does not account for the internal pressurization of lipid vesicles and attributes all the energetic cost of deformation to the shell, i.e. the vesicle membrane. More recently, Reissner [31], generalized the theory and proposed an analytical solution which takes into consideration the presence of transverse shear deformations (Equation 1.6) and allows calculating the Young modulus of the indented vesicle's membrane. Multiple works in literature employed TST-based models to derive the mechanical properties of lipid vesicles [37–39].

$$F = \left(\frac{4Eh^2}{R\sqrt[2]{3(1-\nu^2)}} \right) \delta \tag{1.6}$$

- **Canham-Helfrich Theory**: based on the works of Canham and Helfrich for describing the shape of red blood cells [40] and membranes with non-zero spontaneous curvature [41], respectively; it has been widely used for characterizing membranes in numerous studies (mostly on vesicles of different size) [42–45]. According to this theory, the two monolayers composing the lipid membrane are free to slide upon each other, thus experiencing negligible shear stresses; moreover, the effect of internal pressurization is now taken into account. Based on this, it is possible to express the free energy of the system (an indented vesicle) using Equation 1.7

$$E = \int \left(\frac{\kappa}{2}(2H - c_0)^2 + \sigma \right) dA - \Delta p(V - V_0) \tag{1.7}$$

where κ is the bending modulus of the membrane, H and c_0 the mean and spontaneous curvatures, σ the membrane tension and Δp the pressure gradient across the interior and exterior of the vesicle, generated by the volume variation $V - V_0$.

Despite the high accuracy with which these theories describe stresses and deforma-

tions, the compositional heterogeneity and intrinsic complexity of most natural membranous systems still hinder a precise characterization of their mechanics. Given the fundamental role played by lipid membranes in numerous biological processes, understanding their mechanical properties represents a hot and yet complicated research topic, with a dramatic impact on life science.

Mechanics of nonlamellar membranes

The mechanical response of nonlamellar membranes to stresses and deformations is largely unknown and the debate regarding their functions and properties is still open. Some studies hypothesized that cubic membranes might originate as a specific cellular response, induced by viral infections in order to create a protective environment to facilitate virus assembly and proliferation [46]; other works suggest that these membranes represent adaptive cellular strategies to withstand unhealthy conditions [47].

Multiple rheological characterizations of nonlamellar assemblies have been performed in order to obtain information about the biophysical descriptors of these architectures [48–50]. Results highlight that these nonlamellar lipid assemblies possess viscoelastic properties which are strongly frequency dependent; moreover, their rheological properties have been found to be affected by concentration, water fraction present within the architecture and ultimately topology of the interface. However, it has to be stressed that rheological characterizations are always performed on lipid bulk phases (which do not closely resemble natural nonlamellar membranes), hence they are not able to directly probe the mechanical response of a membrane to localized deformations, like the ones happening in most biological processes. In this framework, the nanomechanics that regulates the stability and the structure of these highly curved interfaces represents an almost completely unexplored field.

Chapter 2

Materials and Methods

In this chapter, the main systems and techniques used in all the reported manuscripts are briefly introduced. For the accurate descriptions of the experimental apparati employed in every experiment, please refer to the specific manuscripts in the Appendix.

2.1 Synthetic membrane models

Numerous membrane models have been developed throughout the years with the aim of studying natural systems using mimics that present only those specific features under investigation. The following sections, describe the main synthetic membrane models that have been exploited for performing the reported studies.

Liposomes

Liposomes are spherical soft-matter particles consisting of one or more bilayer membrane(s), usually composed of phospholipids [51]. One of the most commonly utilized phospholipid type is phosphatidylcholine, which presents a neutrally charged polar head group; however, either negatively or positively charged phopsholipid molecules are extensively used without further complications. Apart from charge, the nature of the hydrocarbon tails in each lipid molecule, particularly the number and position of double bonds along the chains, are responsible for fundamental bilayer properties such as phase behaviour and elasticity (more on this has been said in the previous chapter). Despite the nature of their membrane, liposomes are usually classified based on their size and degree of lamellarity, i.e. the number of bilayers present within the vesicle; Figure 2.1 reports different types of liposomes

that can be obtained following standard lab practices [52]. Apart from being ver-

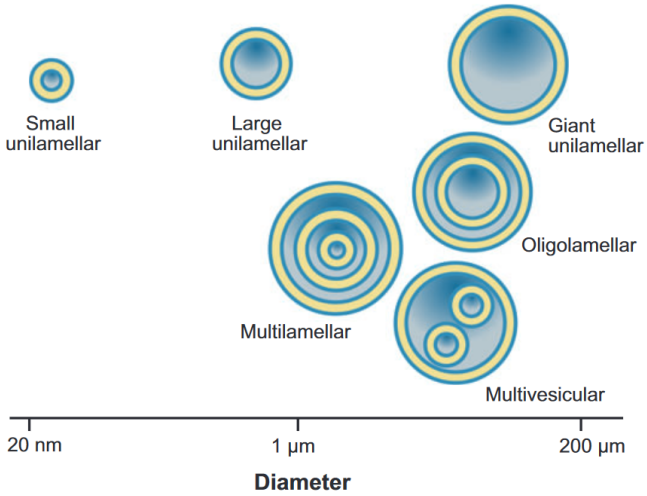

Figure 2.1: Schematic representation of the most commonly encountered liposome types. As can be seen, their size can vary from tenths of nm to hundreds of μm. Figure adapted from [51].

satile synthetic membrane models, liposomes have huge potential as drug delivery systems; indeed, hydrophilic drugs can be entrapped in their lumen while lipid soluble drugs can be incorporated into the hydrophobic core of the phospholipid bilayer [53, 54].
In the works presented in the following chapters, nanosized liposomes of multiple types, have been extensively used as models of EVs, allowing for the study of vesicle nanomechanics under simplified and controlled conditions. Moreover, liposomes also provided the basic ingredient for obtaining another important and versatile membrane mimic, i.e. Supported Lipid Bilayers.

Supported Lipid Bilayers (SLBs)

It might happen that, when performing certain interaction and/or structural studies involving lamellar membranes, the three dimensional geometry of vesicles represents an unnecessary obstacle to the main purpose of the experiment; or in other cases, it might happen that the typical length scales of a measurement are negligible compared to the curvature of the membrane under investigation. For these cases, a planar model membrane seems a more desirable system and Supported Lipid Bilayers (SLBs) hence represent a valuable solution. As suggested by its name, a SLB (please refer to Figure 1.4 a) consists of a planar lipid bilayer supported on a rigid substrate. Over the years, multiple methods for SLB formation

have been developed; a simple and effective strategy, pioneered by McConnell et al. [55], involves the spreading of small lipid vesicles on hydrophilic solid supports (also called vesicle fusion [56]). Figure 2.2 describes the main steps necessary for obtaining a SLB through vesicle fusion, starting from the deposition of the vesicles on the surface, to their rupture, caused by the increase of their concentration on the surface, which generates mechanical stresses on their membranes. Numerous

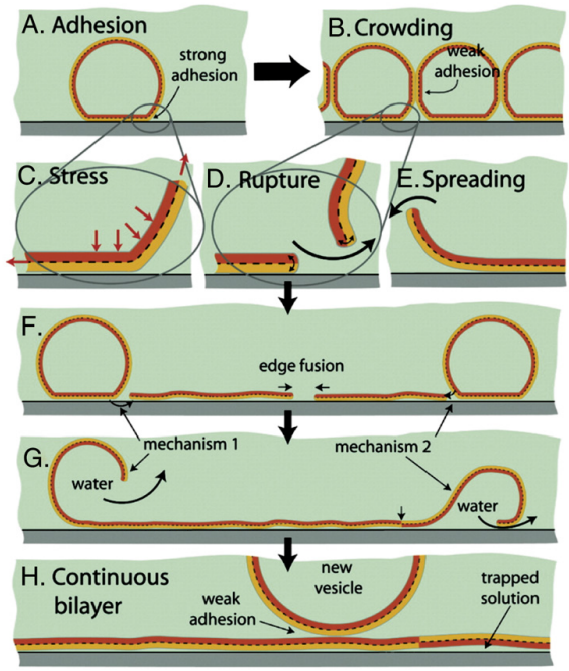

Figure 2.2: Stages of SLB formation by vesicle fusion: (A) adhesion, (B) crowding, (C-E) rupture and spreading of bilayer patches which can expose one of the two leaflets depending on the rupture and fusion processes, (F, G) coalescence of high energy edges and release of water/excess lipid, (H) formation of a continuous SLB. Figure adapted from [56].

physico-chemical parameters, such as temperature, surface charge, vesicle size etc..., influence the rupture of vesicles on the surface and hence the formation of SLBs, please refer to [57–60] for detailed investigations regarding this topic. By finely tuning the formation process, it is also possible to realize multicomponent SLBs, characterized by lipid heterogeneity, phase separations or presenting asymmetrical leaflets; also proteins and other biomolecules can be embedded within the lipid matrix of a SLB [61]. In addition to all the herein presented features, SLBs can be probed by a wide variety of surface-sensitive techniques [13] and hence represent stable and reliable membrane model systems for a plethora of interface studies.

Supported bicontinuous cubic phase lipid films

Analogously to SLBs, supported bicontinuous cubic phase lipid films represent synthetic mimics of natural cubic membranes. They consist of a film deposited on a rigid substrate, whose thickness can vary from hundreds of nanometres to tenths of micrometres and whose lipid constituents are self-assembled into a nonlamellar architecture. Despite most properties of nonlamellar lipid membranes (in particular cubic membranes) are not yet fully understood, very few studies in literature focused on the realization of these membrane models [62–65], most of the times obtaining thicknesses in the μm range, which are not representative of natural nonlamellar membranes. As mentioned in the previous chapter, three types of lipid cubic phase have been reported for lipid systems [66], corresponding to the primitive (P), double diamond (D) and gyroid (G) IPMS. The structure of a supported bicontinuous cubic phase lipid film can hence be obtained by the repetition in the 3D space of one of the three cubic units displayed in Figure 1.7. The result for the case of the double diamond (D) cubic architecture is shown in Figure 2.3. Natural cubic membranes are reported to occur in cells under starvation or as a

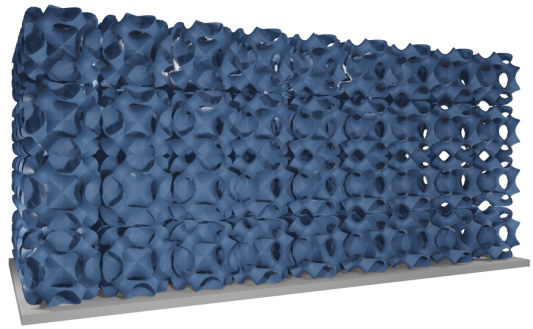

Figure 2.3: Schematic representation of a supported bicontinuous cubic phase lipid film; the cubic unit cell in this case is the so-called Double Diamond (D).

consequence of viral infections; therefore, studying the interactions of these highly curved membranes with the extracellular environment is of fundamental importance for better understanding the role and the mechanisms underpinning the formation of these intriguing lipid architectures. In this context, the possibility of relying on supported nonlamellar membrane mimics, which allow performing interaction studies under controlled conditions, represents a desirable choice for approaching the complexity that characterizes these highly curved biological interfaces.

2.2 Atomic Force Microscopy (AFM)

Since its invention, occurred in 1986 by Binning et al. [67], Atomic Force Microscopy (AFM) allowed imaging and manipulating matter at the atomic, molecular and cellular scales [68]. In particular, the possibility to operate AFM in aqueous media and at physiological temperatures makes it possible to study biological samples in their native environment, without the need of drying them on a substrate, therefore compromising their structure and stability. In AFM, a micrometer-sized cantilever presenting a molecularly sharp tip at its end is moved by a piezoelectric scanner and used to scan the sample. Tip-sample interactions deflect the cantilever; by exploiting a system of lasers, mirrors and photodiodes, it is possible to record these deflections and hence obtain the topography of the sample. Figure 2.4 reports a schematic representation of the structure of an AFM. In order to be probed by AFM, samples need to be adsorbed on a rigid substrate. Over the years, different operating modes have been developed, I refer to Dufrêne et al. [69], for a comprehensive description of the most important imaging modes of AFM. All the

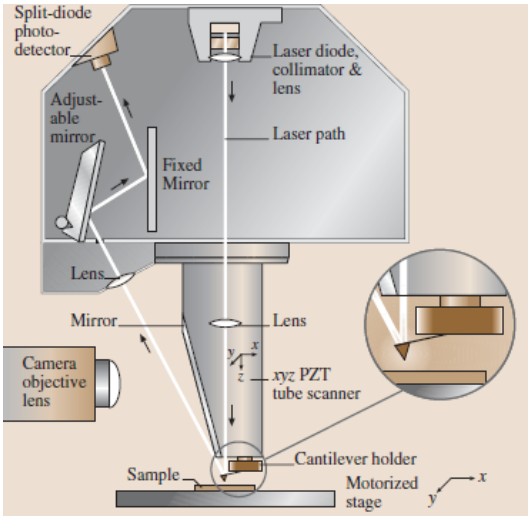

Figure 2.4: Description of the working principle of a typical AFM, as can be seen from the image, a laser beam is focused by a lens towards the tip of the cantilever which is scanning the surface, the beam is reflected and with the help of a system of mirrors is recorded in a photodetector. Figure adapted from [70].

AFM images presented in the following chapters have been obtained by operating the microscope in the so-called *PeakForce Tapping* mode, where the tip oscillations are performed at frequencies well below the cantilever resonance. This operating mode combines the benefits of both *Contact* and *Tapping* mode. Samples were always probed within a fluid cell, filled with the most appropriate solution, in order

to preserve their native structure (please refer to the specific manuscripts for more detailed information).

2.3 AFM-based Force Spectroscopy

AFM-based Force Spectroscopy (AFM-FS) allows probing the mechanical properties of biological samples at the nanoscale level, with high accuracy. Differently from classical AFM imaging, in a typical AFM-FS experiment, the tip is used to indent the sample and the forces experienced during the indentation are recorded as a function of the tip-sample separation. These data are then plotted in the so-called force-indentation curves, which hence contain information about the mechanical properties of the indented sample (refer to Chapters 3 and 5 for more information). The analysis of these curves is often challenging and requires adequate fitting models in order to extract quantitative information. When probing samples that display lateral homogeneity, multiple indentation models are available in literature, they depend on the characteristics of both tip and sample, as well on the nature of their interaction; please refer to Krieg et al. [68] for a comprehensive description of the most important indentation models.
In the herein presented work, AFM-FS has been applied to lipid membranes presenting both lamellar (in the form of vesicles and SLBs) and nonlamellar (in the form of thin supported lipid films) structures. In some cases, an accurate analysis allowed extracting precise information on the samples nanomechanics; in other situations, the absence of a correct theoretical model for analysing the force-indentation curves, forced us to develop alternative strategies for estimating the mechanical properties of the samples.

2.4 Neutron and X-Ray Reflectivity and Grazing Incidence Small Angle Scattering

Neutron and X-Ray Reflectivity (NR and XR, respectively) represent efficient tools for investigating the nuclear and electronic density profiles along the depth of nanometric thin films. For this reason, they are extensively used for studying the structures of liquid-liquid interfaces, polymers and biomembranes. In a typical reflectivity experiment, a beam of neutrons or X-rays impinges on the sample (which is adsorbed on a rigid substrate) with a certain angle and gets reflected towards a detector. Given the short wavelengths of both neutrons and X-rays, the presence of nanometer thick films at an interface generates interference effects that modulate the reflectivity signal observed at the detector. Figure 2.5 schematic-

ally describes the reflection of a beam from a thin layer between two semi-infinite media, detailing all the main parameters that influence the observed interference patterns. The reflections of neutrons and light have a lot of common features and

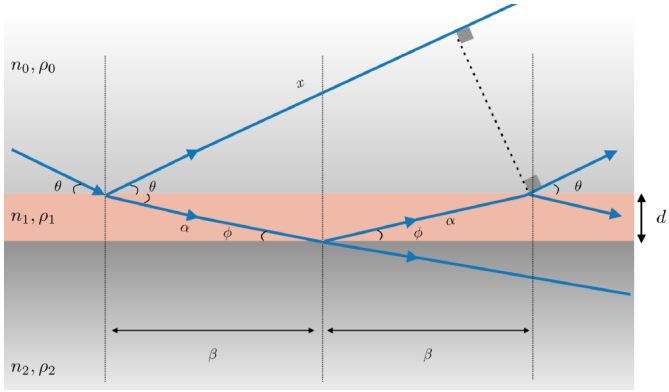

Figure 2.5: Reflection of a beam (neutron or X-rays) for a single thin film between two semi-infinite media.

follow the same fundamental equations [71]; indeed, the propagation of both types of radiation obeys to a second-order partial differential equation expressed in Equation 2.1, where k is the wave vector, while A represents, for light and X-rays the electric E or magnetic B field and the wavefunction Φ for neutrons.

$$(\nabla^2 + k^2)A = 0 \tag{2.1}$$

Introducing the Q vector as the modulus of the resultant between the incident, k_i, and the scattered/reflected, k_f, wavevectors (Equation 2.2)

$$|Q| = |k_f - k_i| = \frac{4\pi n}{\lambda} sin(\theta) \tag{2.2}$$

where 2θ is the scattering angle, n the refractive index and λ the wavelength; we can express the interference condition as:

$$\Delta(2\phi) = 2\pi \tag{2.3}$$

where 2ϕ represents the phase change. Equation 2.3 can be rewritten as

$$\Delta\Big(\frac{4\pi n}{\lambda} sin(\theta)\Big) = \frac{2}{\pi d} \tag{2.4}$$

or

$$\Delta(Q) = \frac{2}{\pi d} \tag{2.5}$$

Equation 2.5 tells that the Q-space distance between reflectivity successive maxima or minima (in the reflectivity curves), provides a direct measure of the film's thickness d. In this way, NR and XR allow studying the structure of adsorbed thin films along the axis perpendicular to the substrate. Please refer to [72] for a detailed description of the principles and applications of neutron/X-ray reflectivity. More recently, the introduction of Grazing Incidence Small Angle Scattering (GISAS) allowed probing the structure of the previously-mentioned systems even along their lateral directions. GISAS requires a set-up similar to the one used in reflectivity and that is why most of the GISAS beamline are also able to perform reflectivity measurements. With this type of experiments it is possible to investigate the in-plane structure of the sample. Figure 2.6 displays the geometry of a typical GISAS measurement; as it can be seen, along the z-axis, the GISAS measurement is equivalent to the previously-mentioned reflectivity, its main advantage resides in probing features on the xy plane. Compared to Equation 2.5, in this experiments

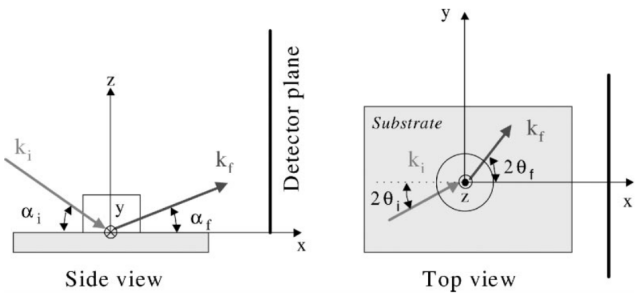

Figure 2.6: Sketch of the grazing-incidence geometry; the scheme presented in the Side view is also compatible with a simple reflectivity experiment. Adapted from [73].

all the three components of the Q vector are obtained, as detailed in Equation 2.6:

$$Q = \frac{2\pi}{\lambda} \begin{bmatrix} cos(\alpha_f)cos(2\theta_f) - cos(\alpha_i)cos(2\theta_i) \\ cos(\alpha_f)sin(2\theta_f) - cos(\alpha_i)sin(2\theta_i) \\ sin(\alpha_f) + sin(\alpha_i) \end{bmatrix} \tag{2.6}$$

Please refer to [73, 74] for a comprehensive description of the GISAS technique and for the complete theoretical derivation of the equations.

2.5 Small Angle X-Ray Scattering

In a typical Small Angle Scattering (SAS) experiment, a collimated beam of either neutrons or X-rays is directed towards the sample; once the interaction took place,

the elastically scattered radiation is recorded by a mono- or bi-dimensional detector. Figure 2.7 display a schematic example of a typical SAS instrument.

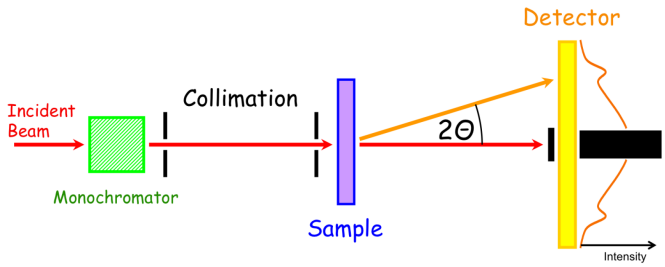

Figure 2.7: Scheme of a SAS instrument. The incident beam passes through a collimator and a monochromator, which are parts of the instrument that allow for a collimated beam with a narrow wavelength range hitting the sample. The scattered intensity is detected as a function of the scattering angle 2θ, which can be then converted into Q using Equation 2.2.

The scattered intensity pattern can be converted into a monodimensional curve that presents the scattering intensity ($I(Q)$) on the y-axis as a function of the scattering vector Q (Equation 2.2). Depending on whether neutrons or X-rays are employed as the radiation source, the experiment gets called Small Angle Neutron/X-ray Scattering (SANS or SAXS). The scattered intensity $I(Q)$ contains information about the structure, the shape, size and interactions between the different scattering centres of the sample. Equation 2.7 gives the expression for $I(Q)$, where K, the amplitude accounts for instrumental factors, N_P and V_P are the numerical density and the volume fraction of the scattering particles, respectively and B a term accounting for the incoherent background contribution [75, 76].

$$I(Q) = KN_PV_P^2(\Delta\rho)^2P(Q)S(Q) + B \tag{2.7}$$

Of particular importance are $P(Q)$ and $S(Q)$, the former is called "form factor" and provides information about the shape of the individual scatterer while the latter is called "structure factor" and is related to the spatial correlation between the different scatterers. Finally, $\Delta\rho$ is the contrast term, which quantifies the difference between the probe-sample and the probe-surrounding medium interactions. In a typical SAXS experiment, $\Delta\rho$ arises from the different electron densities of the sample and the continuous medium [75, 76].

2.6 Ellipsometry

Ellipsometry measures the polarization change in the light reflected or transmitted from a material. To describe the change in polarization, the amplitude ratio Ψ and the phase difference Δ are the most commonly used parameters.
Light can be described as an electromagnetic wave with its own electric and magnetic fields. The propagation of the wave's electric field in space and time is defined as the polarization. When two orthogonal light waves of arbitrary amplitude and phase combine together, the resulting light will be "elliptically polarized" and this is where ellipsometry gets the name from.
The electric fields parallel and perpendicular to the plane of incidence are called $p-$ and $s-$ polarized, respectively; in a typical ellipsometry experiment, the variation of these parameters upon reflection or transmission is measured. Briefly, a beam of light, having a known polarization, is directed towards the sample surface (at a specific angle), after it gets reflected or transmitted, the output polarization is measured. The change in polarization is commonly defined by the expression in Equation 2.8.

$$\rho = tan(\Psi e^{i\Delta}) \tag{2.8}$$

Figure 2.8 conceptually describes a typical ellipsometry measurement. Ellipsometry

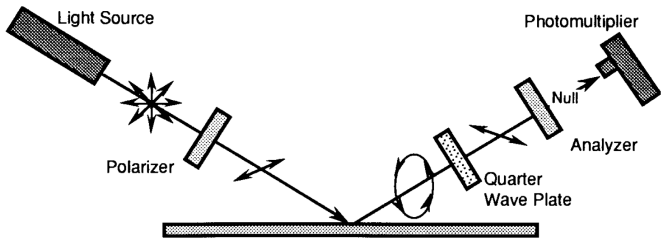

Figure 2.8: Conceptual scheme of an ellipsometry measurement. After being polarized by a polarizer, a beam of light hits the sample and its polarization state gets altered. The variation in the light polarization is measured using an analyser (non-mentioned parts are technical components that might vary from an instrument to another). Figure adapted from [77].

is mainly used to study thin films, it allows obtaining information on properties such as the film thickness and its optical constants. In order to extract these parameters, a regression analysis is usually applied, where a model is constructed in order to predict the Fresnel's coefficients of the film (related to both its thickness and optical properties) and then verify their actual values by comparing the calculated and experimental signal. For a comprehensive theoretical and practical description of ellipsometry, please refer to the work by Tompkins H. G. [77]. The

huge potential of this technique is in the thickness range that it is able to measure; indeed, ellipsometry can probe films whose thickness ranges from sub-nanometres to few microns.

Part II

Nanomechanics of lamellar lipid membranes

Chapter 3

The mechanical response of fluid and gel phase nanovesicles

As anticipated in the introduction, studying the mechanical properties of lipid membranes is fundamentally important for improving the current understanding on multiple biological processes. This chapter focuses on lamellar membranes; more precisely, on nano-sized lipid vesicles and SLBs, describing and elucidating the nanomechanics of these two different lipid systems.

Key biological processes that involve lipid vesicles were reported to be influenced by the mechanical properties of these membranous compartments, including exo/endocytosis, trafficking and the onset of several pathological conditions [18, 19, 25, 26]. For this reason, numerous efforts have been put into the mechanical characterization of synthetic nanovesicles and their membranes, since they represent versatile mimics for the study of biogenic membrane-bound organelles. Multiple Force Spectroscopy (FS) techniques such as micropipette aspiration, optical tweezers and Atomic Force Microscopy (AFM) allow for accurately probing the nanomechanics of these membranous systems at the nanoscale [78]. However, disentangling the contributions of all the parameters involved in the mechanical response of a lipid vesicle still represents a challenging task and an unsolved issue, hindering multiple research fields. AFM-FS offers the possibility to simultaneously determine the morphology and the mechanical properties of individual vesicles. In a typical AFM-FS experiment, a sharp tip is used to indent the sample and the forces experienced during the indentation are recorded as a function of its indentation depth. The relationship between the two parameters is described by the so-called force-indentation curves; Figure 3.1 reports two representative force-indentation

curves that can be obtained when indenting a SLB (Figure 3.1 a) and a lipid nanovesicle (Figure 3.1 b). The stiffness of a lipid vesicle, K, can be defined as the

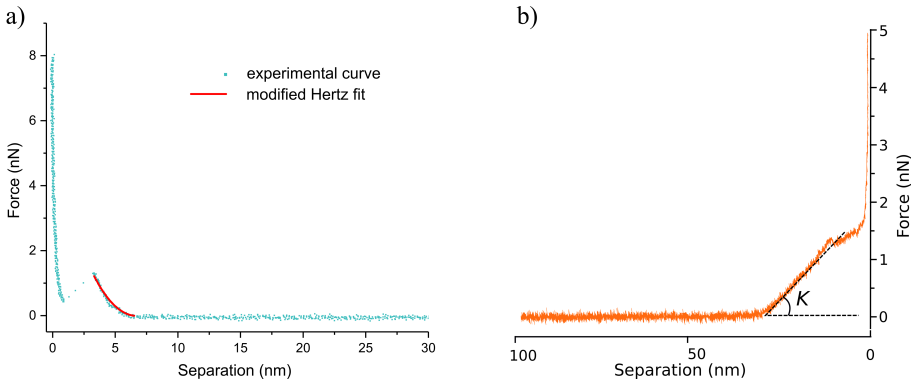

Figure 3.1: Representative force-indentation curves from an AFM-FS experiment. a) Force-indentation curve obtained on a SLBs (light-blue trace) fitted with a modified Hertz model [36] (red trace). b) Force-indentation curve obtained on a lipid vesicle; by fitting the linear part, it is possible to calculate its slope, which represents the vesicle stiffness, K. Figure adapted from [79].

linear resistance of an elastic body (i.e. the vesicle itself) to a deformation by an applied force [21]; it accounts for multiple contributions, the most important being membrane elasticity and the vesicle internal pressurization. As mentioned in the introduction, several theories have been proposed in the literature with the aim of disentangling the different contributions participating to the overall mechanical response of a vesicle; however, none of them seems to thoroughly describe the mechanical behaviour of both fluid and gel phase lipid vesicles. Indeed, the phase transition that lipid bilayers undergo at their melting temperature, T_m, alters the intermolecular interactions, producing a softening or stiffening of the membrane, thus making it even more difficult to derive a universal model for describing the mechanics of both fluid and gel phase bilayers. In this framework, models deriving from the TST seem better suited for describing the behaviour of gel phase vesicles; on the other hand, models based on the Canham-Helfrich theory better describe the properties of fluid phase vesicles. In the herein presented work [79], we combine AFM-FS experiments on lipid vesicles (either in the fluid or gel phase) with AFM-FS measurements on SLBs from the same lipid constituents, with the aim of better understanding the contributions of membrane and internal pressure to the overall vesicle mechanical response. SLBs are planar membrane models, characterized by a simpler mechanical response than vesicles; indeed, the absence of curvature and pressure allows for the application of well-established indentation mechanics models [68], through which it is possible to calculate the main biophysical descriptors

of membrane elasticity.

After probing by means of AFM-FS four different SLBs, namely DOPC, POPC (both in fluid phase), DPPC and DSPC (both in gel phase), the application of a modified Hertz fit [36] allows calculating their Young Modulus; then, by exploiting the Theory of Elasticity, their bending modulus, κ_{SLB} is obtained. Calculating the bending modulus of lipid membranes is of particular interest in soft matter, since bending represents one of the most important deformations taking place during multiple biological processes; this is also the reason that makes κ the most widely employed biophysical descriptor of membrane elasticity. The very same lipid bilayers are then probed by AFM-FS in their vesicular configuration and force-indentation curves are used to calculate the stiffness of the indented vesicles, obtaining results in good agreement with the literature [44, 60]. In order to obtain estimates of the vesicle's bending moduli (κ_V), the Reissner equation (Equation 1.6) is used.

To better understand how membrane and pressure contribute to the measured stiffness, we develop a model that describes an adsorbed lipid vesicle as a system of two springs in series, with spring constants K_1 and K_2. As can be seen in Figure 3.2, K_1 accounts for the mechanical response of the membrane while K_2 for those phenomena related to volume/surface variations induced by the indentation process (the most important being internal pressurization). As a consequence of this

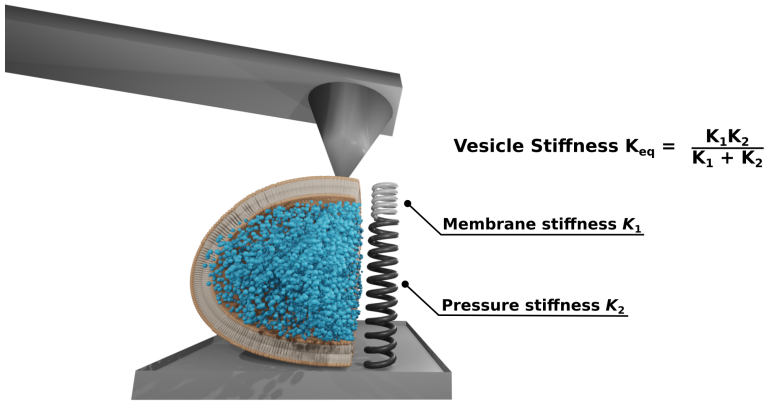

Figure 3.2: Spring-based model developed to describe the mechanical response of a vesicle to indentation. The stiffness of a vesicle accounts for the contributions of both membrane rigidity (mostly κ) and internal pressurization and can be described by a system of two springs in series. Figure adapted from [79].

model, the slope of the linear part in the force-indentation curves (Figure 3.1 b) represents the equivalent spring constant of the system, K_{eq}, whose value is given

by:

$$K_{eq} = \frac{K_1 K_2}{K_1 + K_2} \tag{3.1}$$

From Equation 3.1, it is immediately clear that the value of K_{eq} is always lower than those of K_1 and K_2. In the Reissner equation (Equation 1.6), the expression within the parentheses corresponds to the stiffness of the shell, i.e. K_1 (from TST hypothesis); however, when 1.6 is used to analyse AFM data, the value of K_{eq} (the one directly measured from the force-indentation curves) is usually plugged in into the equation. This procedure unavoidably leads to an underestimation of κ_V. Figure 3.3 a shows the values of κ_V obtained by substituting K_{eq} into Equation 1.6, compared with the ones obtained on SLBs (κ_{SLB}). The results perfectly support the spring-based model; indeed, in very soft vesicles, like the ones consisting of fluid phase bilayers, $K_1 << K_2$, hence Equation 3.1 can be simplified in $K_{eq} \approx K_1$, yielding results in good agreement with values measured on SLBs. On the other hand, as K_1 becomes proportional to K_2 (in the case of stiffer bilayers, such as gel phase ones), the approximation is not valid anymore and K_{eq} will be lower than K_1; in these cases, the application of the Reissner equation will generate disagreement with the results on SLBs.

Exploiting the fact that the literature on SLB mechanics is solid and well-established, it is reasonable to assume that the values of κ_{SLB} are the closest to the true bilayers bending moduli. Plugging in these values into Equation 1.4 and then using the obtained values of E to solve Equation 1.6 for the quantity within parentheses would allow obtaining the correct stiffness of the shell, K_1 (i.e. the membrane of the vesicle). At this point, knowing both K_{eq} and K_1, allows calculating K_2 (from Equation 3.1). Results are displayed in Figure 3.3 b and fully support the predictions of the spring-based model. Indeed, for vesicles with very soft membranes (like DOPC), $K_1 << K_2$ and so $K_1 \approx K_{eq}$; while for vesicles with stiffer bilayers (DPPC and DSPC), K_1 and K_2 are comparable, meaning that both springs will deform upon indentation, although to different extents. The first information that can be derived from these results is that K_2 has very similar values across all the different liposomes, despite their bilayers being in different phase states. Since the dominant phenomenon related to volume/surface variations is the vesicle pressurization state, we can also conclude that all the vesicles seem to be equally pressurized. Overall, this study shows that lipid vesicles, having comparable size but different bilayer compositions, possess similar internal pressurization, making membrane elasticity (the bending modulus in particular) the key determinant for the observed differences in stiffness. In fluid phase vesicles, this translates into a mechanical response being completely dominated by pressure, in agreement with findings from Vorselen et al. [44]; in gel phase vesicles, contributions from mem-

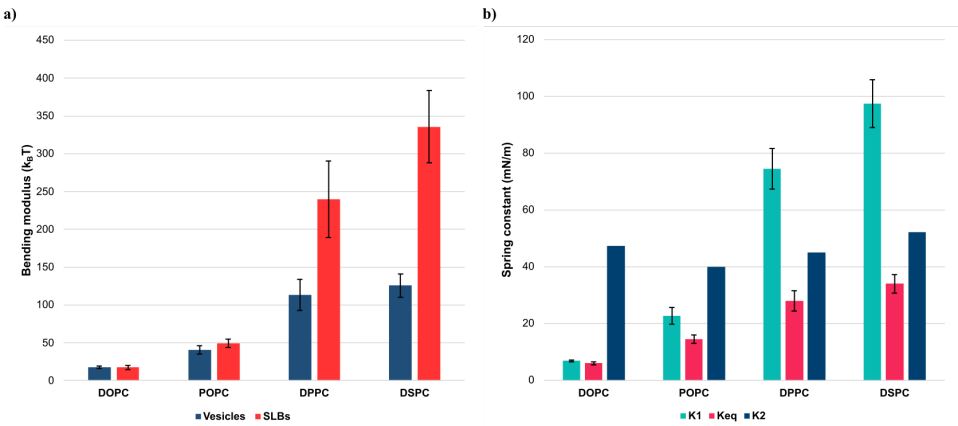

Figure 3.3: Results from AFM-FS experiments on vesicles and SLBs. a) Bending moduli obtained for lipid vesicles (blue) and SLBs (red). b) Values of the spring constants that describe the mechanical response of a lipid vesicle to indentation; K_1 is the spring constant associated to membrane elasticity (turquoise), K_2 is the spring constant associated with the vesicle internal pressurization (blue) while K_{eq} is the spring constant measured from AFM-FS experiments (magenta) and is given by the combination of K_1 and K_2.

brane elasticity and internal pressurization are comparable and both influence the measured vesicle stiffness.

The herein presented spring-based model could also provide an interpretation for the slope change that is often observed in the large-indentation regime of the force-distance curves performed on gel phase vesicles. When a vesicle undergoes larger deformations, leakage phenomena might occur; from a mathematical point of view, they can be described as variations in the value of K_2. On the other hand, the value of K_1 is not affected by larger indentations (the extent of the indentation should not affect the membrane elasticity). Referring again to Equation 3.1, we can see that when the value of K_2 varies but still largely exceeds K_1, the new K_{eq} will still be well-approximated by K_1 and so for fluid phase vesicles no appreciable changes in the curves' slope will take place. This does not hold true when K_1 and K_2 are comparable (gel phase vesicles); in these cases, the change in K_2 will produce a non-negligible change in K_{eq} which will likely be reflected in the slope change of the curve at large indentations. Figure 3.4 shows the results obtained by averaging (red trace) a representative ensemble of force-indentation curves (grey traces) for each vesicle type; for those vesicles where K_1 is comparable with K_2 (DPPC and DSPC), a slope change is observed; on the other hand, DOPC and POPC have values of K_1 far lower than their K_2; as a consequence, almost no slope changes can be observed in their curves.

The presented results enrich the current understanding on the mechanics of lamellar

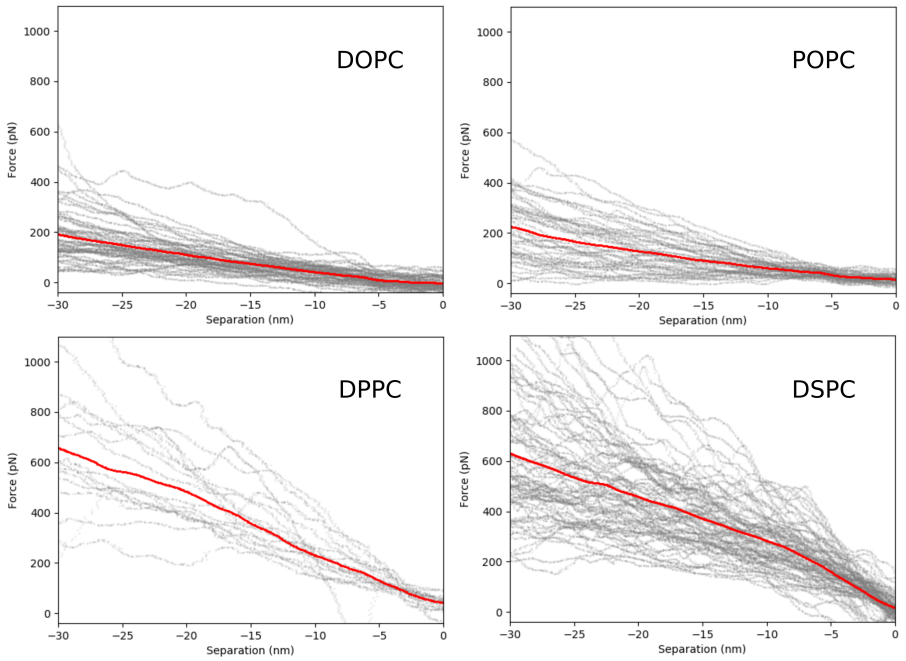

Figure 3.4: Average curves for the four different liposome types. Red traces are the average curves of the reported grey traces. When going from DOPC to DSPC, K_1 and K_2 become comparable and variations in K_2 due to leakages of internal fluid during the indentation may have a stronger impact on K_{eq} and on the observed curve slope. Figure adapted from [79].

membranes in both their planar and vesicular configurations; moreover, they help to shed light on the main factors regulating the mechanical response of different lipid vesicles to nanoscale deformations. Our spring-based model also represents a simple yet versatile starting point for the development of more accurate and complicated mechanical descriptions, able to take into account the effect of phase transitions on the mechanics of both fluid and gel phase lipid vesicles.

Chapter 4

Vesicle stiffness and membrane heterogeneity influence nanoscale interactions

This chapter deals with how lipid vesicles interact with surfaces and nanomaterials. The mechanical properties of these membranous compartments are known to regulate their response to external stimuli, hence playing a crucial role in most of their interactions at the nanoscale. The stiffness of a vesicle determines its overall mechanical response to an applied deformation; as a consequence, the ability of a lipid vesicle to deform once interacting with another object depends on this mechanical parameter. In this framework, measuring the stiffness of lipid vesicles and studying how it affects nanoscale interactions is relevant for multiple research fields. From a fundamental point of view, it could help reaching a better understanding on the mechanics of membranous compartments, on how it affects their circulation in the bloodstream and how their stability is affected by the presence of pathological conditions. From an applicative standpoint, characterizing the stiffness and the mechanical properties of lipid vesicles (either synthetic or natural) could help solving several issues related to the pharmacokinetics and internalization of numerous vesicle-based drug delivery systems and could pave the way for the development of efficient vesicle-based diagnostic tools.

The interaction of vesicles with their outer environment is also dependent on membrane heterogeneity; indeed, the presence of lipid rafts or phase segregations could generate micro/nano domains which possess completely different properties with respect to the surrounding lipid matrix. This phenomenon could result in interac-

tions targeting only specific regions of the bilayer, hence affecting the selectivity of numerous biological processes and the efficiency of several internalization mechanisms.
In the following sections, we describe how the stiffness of lipid vesicles affects their adsorption on surfaces and how it mediates the interaction of nanomaterials (namely gold nanoparticles, AuNPs) with their membrane; moreover, by employing multicomponent membranous systems, we show that the presence of lipid rafts contributes to the selective adsorption of AuNPs on specific regions of the bilayer.

4.1 Stiffness determines vesicle shape upon adsorption

The adhesion of lipid vesicles to a surface is related to their ability to deform, hence to their stiffness. This means that also the interaction of vesicles with biological surfaces is regulated by this parameter. In a recent study, Dai et al. [45] found that softer liposomes display an increased adhesion to the extracellular matrix (ECM), due to their higher deformability upon adsorption, which ultimately causes an increase in the contact area. The deformability of membrane delimited compartments upon adhesion can influence other important phenomena, such as their mobility and stability on surfaces.
In this section we show how the stiffness of lipid vesicles regulates their adsorption on a substrate and their consequent deformation. Results are then used to develop an AFM-based high-throughput mechanical characterization for both synthetic and biogenic lipid vesicles.
Within a liquid medium, lipid nanovesicles have a spherical shape with a diameter D_L and a corresponding surface area A_L. When a vesicle adsorbs on a substrate, its adhesion is mainly driven by electrostatic interactions, occurring between the surface and the membrane. In particular, since most biogenic lipid vesicles, such as EVs, are known to have negative ζ-potentials, they will be necessarily attracted by positively charged surfaces. Once adsorbed on a surface, the vesicle deforms from its initial spherical shape, adopting a more oblate morphology which can be described by a spherical cap. Since the stretching of the membrane is negligible, the membrane area of the vesicle on the surface, A_S, will be equal to A_L. The extent of the deformation depends on parameters such as the bending modulus and the pressurization, which are the most important contributions to vesicle stiffness; this means that the geometry of an adsorbed vesicle is mainly dependent on its stiffness. From these observations, the herein presented characterization method estimates the stiffness of a vesicle by calculating its contact angle, a parameter

used to quantify the vesicle deformation upon adhesion. According to these principles, softer vesicles will adopt more oblate shapes compared to stiffer ones and hence they will display lower contact angles. Figure 4.1 schematically summarizes all these observations. Being related to the morphometry of the adsorbed ves-

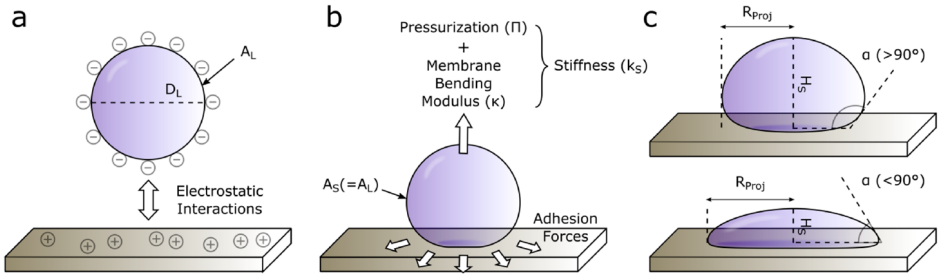

Figure 4.1: Schematic representation of the adsorption of a lipid vesicle on a substrate and its consequent deformation. Since the deformation upon adhesion depends on vesicle stiffness, softer vesicles adopt more oblate shapes than stiffer ones. It is possible to quantify the extent of the deformation by measuring the vesicle contact angle. Figure adapted from Ridolfi et al. [80].

icles, the contact angle can be simply determined from AFM images; indeed, under the assumptions of membrane area conservation and vesicle adopting spherical cap geometries upon adsorption, its value is given by Equation 4.1, where R_{cap} is the projected radius of the adsorbed vesicle and H_s its height; both parameters that can be obtained from a typical AFM image.

$$\alpha = 90 - sin^{-1}(\frac{R_{cap} - H_s}{R_{cap}}) \tag{4.1}$$

The assumption of membrane area conservation also allows calculating the diameter that the vesicle would have had in solution, prior to adsorption; this can be done by applying the equation:

$$D_L = 2\sqrt{\frac{A_S}{4\pi}} \tag{4.2}$$

The stiffness of a lipid vesicle is considered to be an extensive property (i.e. it varies with vesicle size); however, stiffness is reported not to vary a lot within vesicles of the same type and having relatively narrow size distributions. Based on this, populations of compositionally similar vesicles should have similar α values across different sizes. This hypothesis was tested by measuring the contact angle values for different liposomes, all of which had the same phosphatidylcholine headgroups (meaning same ζ-potentials). Once the contact angles are put into a scatterplot as a function of vesicle size (D_L), they generate an horizontal cluster of points; Figure 4.2 a reports a representative contact angle vs diameter scatterplot obtained from

POPC vesicles. As displayed in Figure 4.2 a, lipid vesicles of different size but same

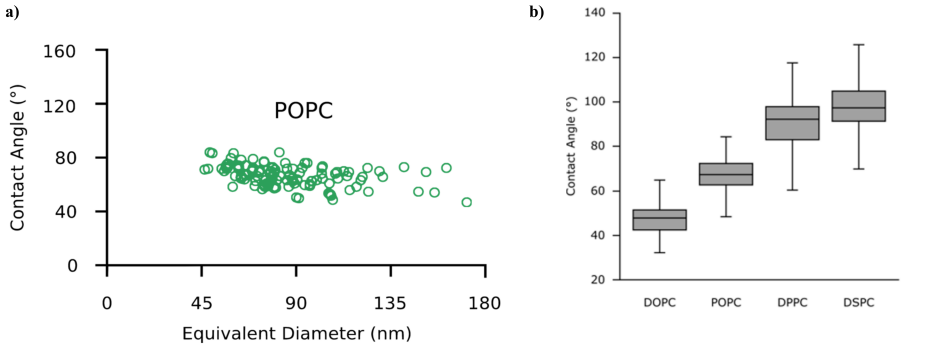

Figure 4.2: The contact angle of liposomes. a) Representative contact angle vs diameter scatterplot obtained for POPC liposomes. b) Contact angle distributions obtained for different liposome types; softer liposomes display lower contact angles than stiffer ones. Figure adapted from Ridolfi et al. [80].

composition have similar contact angles and hence similar stiffness values, confirming our previous assumption. Moreover, the scatterplot of Figure 4.2 a describes a peculiar mechanical fingerprint that can be regarded as representative of the typical vesicle-like behaviour. Figure 4.2 b reports the distributions of contact angles obtained for all the probed liposome types; softer liposomes seem to have lower contact angles than stiffer ones, meaning that they underwent larger deformations and adopted more oblate shapes after adsorption.

After testing this characterization on synthetic vesicles, the contact angle distributions of EVs from three different natural sources were also measured. Figure 4.3 reports some representative AFM images and the contact angle distributions of each EV sample. As can be seen from the scatterplots of Figure 4.3, also EVs display the mechanical fingerprint typical of the vesicle-like behaviour, i.e. a narrow contact angle distribution over a relatively wide range of sizes. In addition to the usual horizontal cluster, the scatterplot in Figure 4.3 d presents a vertical cluster of points corresponding to spherical objects having similar sizes but very different contact angle values; this is because the sample was affected by a mycoplasma contamination and hence it contained non-vesicular objects, characterized by a different mechanical fingerprint. In addition to estimating the stiffness of EVs, in this context, the contact angle characterization also revealed the presence of a contamination and hence proved to be a versatile tool for assessing the purity of vesicle dispersions.

To compare results from this AFM imaging-based characterization with more rigorous AFM-FS measurements, the stiffness of the same liposomes (DOPC, POPC,

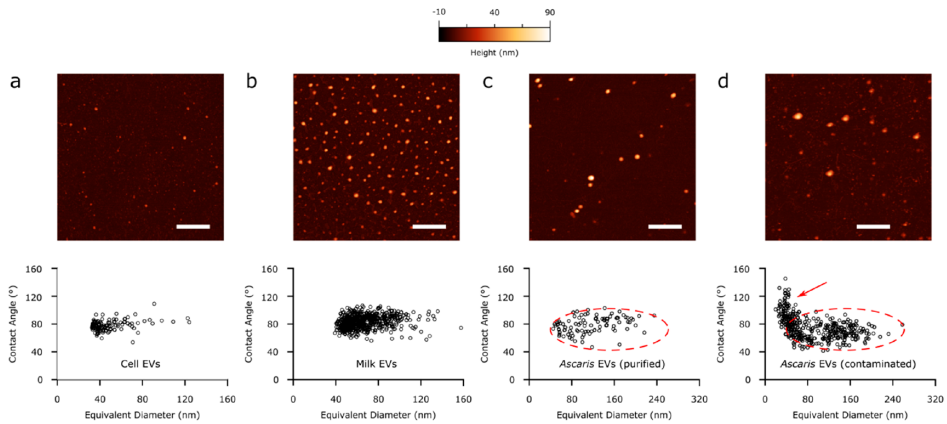

Figure 4.3: Representative AFM images (top row) and contact angle vs diameter scatterplots (bottom row) of natural EV samples from different sources. (a) EVs purified from HCT116 cell culture. (b) EVs purified from bovine milk. (c) EVs purified from Ascaris suum ES fractions. (d) Mycoplasma-contaminated Ascaris suum EVs. All purified EV samples show a relatively small dispersion of contact angles around the same average value at all sizes, resulting in horizontally elongated clusters. Contaminants (red arrow in panel d) do not follow this behaviour and appear as an additional vertical cluster with large contact angle variations. Ascaris EVs in both purified and contaminated samples appear in the same zone of the plot (panels c and d, dashed ovals). All scale bars are 1 μm. Figure adapted from Ridolfi et al. [80].

DPPC and DSPC) was directly measured by means of AFM-FS. As can be seen from the graph in Figure 4.4, there is a strikingly linear correlation between vesicle stiffness by AFM-FS and contact angle. This holds true for all the probed liposomes and means that it is indeed possible to quantitatively estimate vesicle stiffness (K) directly from AFM imaging experiments. Extrapolating the stiffness of Ascaris from the calibration curve of Figure 4.4 (built on liposomes' data) results in an expected stiffness value of 21 ± 4 mN/m. It was also possible to measure the stiffness of this EV sample by AFM-FS, obtaining an average value of 20 ± 5 mN/m, in very good agreement with the predicted one. The same procedure was replicated for Milk EVs and yielded strikingly similar results ($K = 20 \pm 7$ mN/m). These findings suggest that the strong correlation between α and K is also valid for EVs and that it is thus possible to estimate their stiffness directly from AFM images.

The herein presented characterization represents a valuable strategy for assessing both the morphological and mechanical properties of nanosized vesicle preparations. Although not having the accuracy of AFM-FS analysis, it allows estimating the size and stiffness of large numbers of vesicles in a relatively short amount of time (few AFM images can yield the contact angle, thus the stiffness, of hundreds

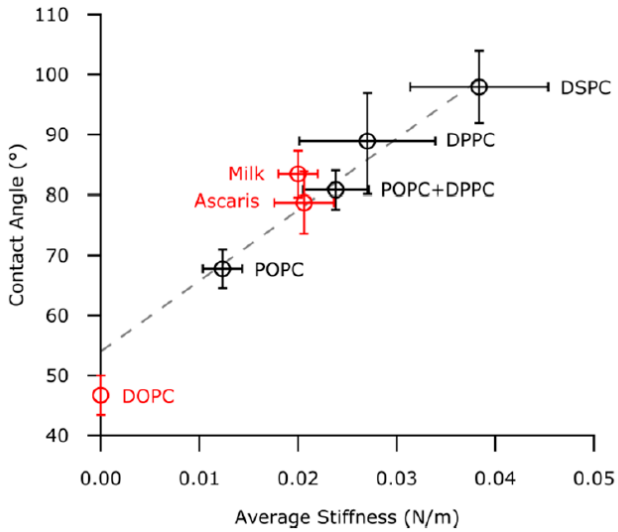

Figure 4.4: Correlation between average contact angle α (measured from AFM images) and average stiffness by AFM-FS. The calibration curve (dashed grey line, $R^2 = 0.97$) was built by measuring both the parameters on four different liposomes (black points). The stiffness by AFM-FS of Ascaris and milk EVs (red points) is almost coincident with the values extracted from their average α, using the calibration curve built on liposome-results. Figure adapted from Ridolfi et al. [80].

of vesicles). Moreover, the method can be applied to biogenic vesicle samples (such as EVs) to assess their stiffness and reveal the presence of potential non-vesicular contaminations. The characterization has been successfully applied in multiple EV-related studies, providing information about EV purity, morphology and stiffness [81, 82].

4.2 Vesicle stiffness mediates the adsorption of gold nanoparticles on the membrane

Representing the overall mechanical response to external stimuli, the stiffness of a lipid vesicle not only influences its shape upon adhesion; it also mediates the adsorption of nanomaterials, such as nanoparticles and biomolecules, on the vesicle membrane. Moreover, given the huge attention recently gained by vesicle-based drug delivery systems, studying how vesicle stiffness affects the bilayer ability to interact with external objects turns out to be of fundamental importance for optimizing processes such as internalization and encapsulation.
This section describes how the adsorption of citrated AuNPs on the membrane of nanosized vesicles is mediated by the stiffness of these lipid compartments. The

obtained results are then exploited for developing a facile, cost-effective and high-throughput method for measuring the mechanical properties of vesicles presenting unknown composition.

In order to assess how stiffness mediates the adsorption of AuNPs on the vesicle membrane, water dispersed liposomes obtained from different lipid molecules, more precisely, DOPC, POPC, POPC/DPPC (50/50 %mol), DPPC, DPPC/DSPC (50/50 %mol) and DSPC, were sampled. From DOPC to DSPC, the stiffness of the resulting liposomes increases due to the different hydrocarbon chains of the lipid constituents; indeed, higher numbers of double bonds and shorter chains generate softer vesicles. The composition affects the melting temperature T_m and hence the physical state of the bilayer at room temperature, with DOPC and POPC being in their fluid phase while DPPC and DSPC in their gel phase [83, 84]. Similarly to what has been shown in the previous chapter, AFM-FS was employed to calculate the stiffness of the mentioned liposome types, obtaining values in good agreement with the literature [37, 44, 45]. Figure 4.5 reports representative force-indentation curves (one for each lipid type) obtained from the AFM-FS experiments, together with the numerical values for the measured stiffnesses. To investigate the adsorp-

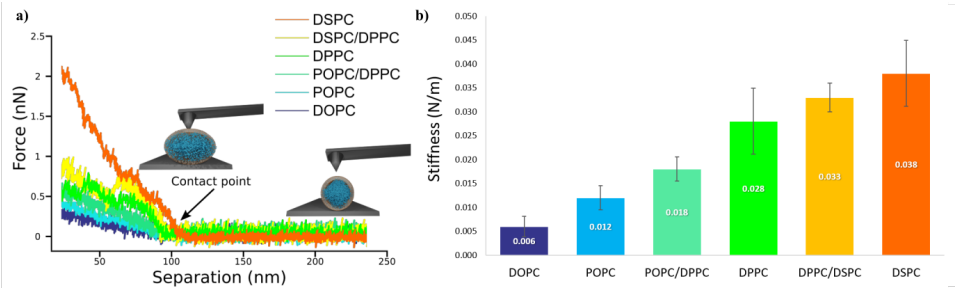

Figure 4.5: AFM-FS characterization of vesicles stiffness. a) Representative AFM force-indentation curves (only the initial part of the vesicle indentation) for the different vesicle batches, together with a graphical representation of the AFM-FS experiment. Liposome samples are DOPC; POPC, POPC/DPPC (50/50 mol%), DPPC, DPPC/DSPC (50/50 mol%) and DSPC vesicles; b) stiffness values (Nm^{-1}) of the different vesicles, determined through AFM-FS. All error bars represent the uncertainties obtained by bootstrapping (1000 repetitions of 5 draws, with replacement). Figure adapted from Caselli et al. [85].

tion of AuNPs on the vesicle membranes, a water dispersion of citrated AuNPs was used; these NPs are characterized by a 15 nm diameter which, due to the plasmonic properties of AuNPs, confers a peculiar red colour to the dispersion [86]. After mixing the AuNP dispersion with the different liposomes water dispersions, the spectral variations in the optical properties of AuNPs were measured by UV-Vis spectrophotometry. While the UV-Vis spectrum of AuNPs is characterized by a defined surface plasmon resonance peak at 522 nm (which is associated with the

colour red), the spectra of the AuNP-liposome dispersions changed according to a continuous trend; more precisely, their plasmon resonance peaks shifted towards higher wavelengths in the case of softer vesicles. Moreover, for very soft liposomes, a high-wavelength shoulder is recorded in the absorbance spectrum, resulting in a secondary peak at $\approx$ 625 nm (Figure 4.6). The variation in the plasmon resonance peaks is related to the different aggregation extent of AuNPs on the liposome membranes; indeed, when tightly packed in clusters, the AuNPs spatial proximity produces a coupling of their primary plasmons. This nanoscale phenomenon, macroscopically translates into a colour change of the NP-liposome dispersions, which shift from the original red colour towards darker shades of violet and blue, as displayed by the cuvettes in the inset of Figure 4.6. The mechanism that underpins

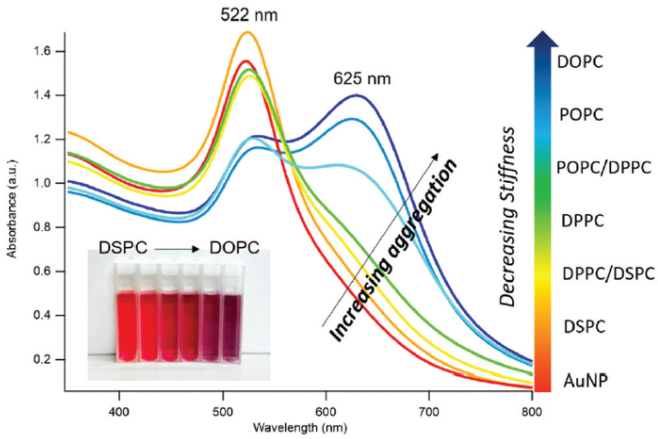

Figure 4.6: UV-Vis spectra of AuNPs incubated with synthetic vesicles at specific concentrations; the shift in the plasmon resonance peak and the emergence of a high-wavelength shoulder are more pronounced the softer the lipid vesicles. Inset: Visual appearance of the samples; the different aggregation of AuNPs on the liposome membranes generate a change in the colour of the solutions. Figure adapted from Caselli et al. [85].

the adsorption and aggregation of AuNPs on lipid membranes is complex and takes place in multiple steps; therefore, we remind to the works by Montis et al. [87] and Salassi et al. [88] for a thorough description.

The combination of results from AFM-FS and UV-Vis spectrophotometry experiments confirms that vesicle stiffness has a primary role in mediating the adsorption of AuNPs on the vesicle membranes, it also tells that the adsorption phenomenon interests all the vesicles, irrespectively of their membrane physical state; this is in contrast with previous studies, predicting no adsorption at all for gel phase bilayers [89, 90]. The difference between NP adsorption on a soft vesicle, presenting lipids in their fluid phase, and on a stiff vesicle, having its lipid in the gel phase, resides

in the aggregation of AuNPs; NP-clusters are formed on softer vesicles while isolated NPs adsorb on stiffer ones (this is also confirmed by the SAXS experiments, reported in the manuscript [85]). Another important observation regards the parameters contributing to the observed stiffness; as detailed in the previous chapter, both internal pressure and membrane rigidity contribute to the stiffness of a vesicle and disentangling their individual effects is not easy. In the herein reported experiments, vesicles presenting similar size distributions (irrespectively of their compositions) were used (please refer to the Supplementary Information in the original manuscript), meaning that their internal pressure was the same; moreover, all the different lipid types presented the very same polar head groups, which ensure that the chemical affinity for the AuNPs was identical for all the probed vesicles. Taken together, these observations lead to the conclusion that the adsorption of AuNPs on the vesicles membrane is mostly dependent on membrane rigidity.
The presented relationship between AuNPs aggregation and vesicle stiffness was then used to build up a UV-Vis spectrophotometry-based assay for assessing the mechanical properties of unknown vesicles. To this purpose, the aggregation of AuNPs was quantified by introducing a "Stiffness Index" (S.I.), accounting for the main spectral variations induced by mixing the liposomes with the AuNPs. The S.I. is related to the stiffness of the vesicles (measured by AFM-FS) through a sigmoidal relation, described in Equation 4.3, with the parameters a, b, c and d obtained by fitting the experimental values of S.I. and stiffness.

$$S.I. = a + \left\{ \frac{b}{\left(1 + exp\left(\frac{c - Stiffness}{d}\right)\right)} \right\} \tag{4.3}$$

Figure 4.7 reports all the experimental points together with the sigmoidal fitting curve. Equation 4.3 represents a functional relation for quantitatively estimating the stiffness of vesicles with unknown composition and properties, through a simple and highly reproducible optical assay. Moreover, the method is able to discriminate systems with very close stiffnesses, as DOPC and POPC, requiring minimal amounts of sample. It is also worth noticing that the sigmoidal law exhibits the highest variation of S.I. in the central region of the selected set of stiffnesses (see grey dashed curve in Figure 4.7, representing the first derivative of the sigmoidal fit); this provides maximum sensitivity in the region where the rigidities of natural membranes usually fall (i.e., between 0.02-0.025 N/m [80]). To test this hypothesis, the characterization was used for estimating the stiffness of an EV sample, yielding results in very good agreement with the ones found by probing the same vesicles by means of AFM-FS (green point in Figure 4.8). The successful application of this method to an EV sample demonstrates that through a simple optical method,

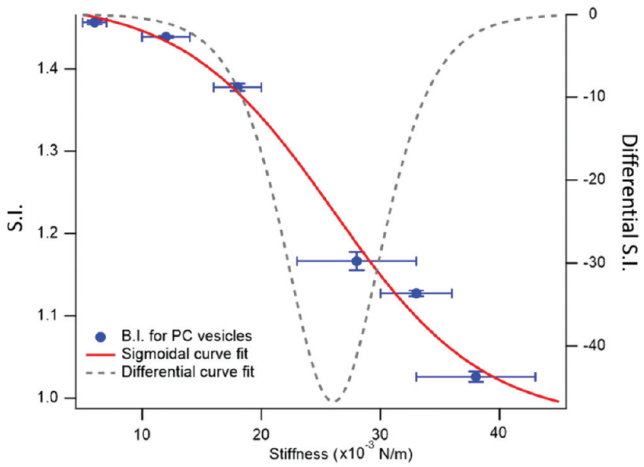

Figure 4.7: S.I. values plotted as a function of membrane stiffness (blue points); the red curve is the sigmoidal curve fit, while the grey dashed curve is the first derivative of the sigmoidal function. Figure adapted from Caselli et al. [85].

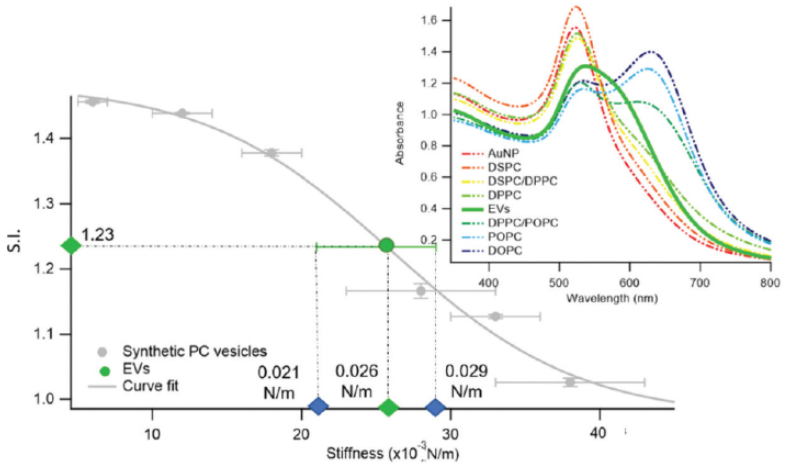

Figure 4.8: Sigmoidal trend of the S.I. as a function of vesicle stiffness. The S.I. of EVs (1.23 ± 0.01), evaluated through UV-Vis spectrophotometry, and stiffness, predicted by the sigmoidal law ($0.026 N/m$), are reported as green points in the graph. The green error bar represents the stiffness interval obtained through AFM-FS for EVs. The right inset reports the UV-Vis spectra of AuNPs (6.7 nM) in the presence of synthetic PC vesicles (dashed curves) and EVs (solid green curve) at a vesicles' concentration of 0.35 nM. Figure adapted from Caselli et al. [85].

involving cheap reagents and a standard wet lab facility, it is possible to assess the mechanical properties of complex vesicle systems from natural origins. Moreover,

the method requires minimal sample volumes (as small as 15 μl), has an impressive reproducibility and is able to provide an ensemble-average stiffness, where possible variabilities across the population (typical in biological samples) are considered. The herein presented experiments demonstrate that the stiffness of lipid vesicles and in particular their membrane elasticity plays a fundamental role in mediating their interaction with nanomaterials, such as nanoparticles, hence highlighting the central role of membrane mechanics in interface interactions.

4.3 Membrane heterogeneity influences nanoparticle adsorption

In contrast with the synthetic lipid membranes examined so far, biological membranes are characterized by lateral compositional heterogeneity. The self-organization of lipids and proteins induces subcompartmentalization in the membranes and has important effects on the their biological functions [91, 92]. One of the most relevant examples of lateral organization is represented by lipid rafts, micro- and/or nanodomains enriched in lipids such as cholesterol, sphingomyelin saturated glycerophospholipids and glycosphingolipids; these lipids segregate in the so-called liquid-ordered phase (L_o), immiscible with the surrounding liquid-crystalline disordered phase (L_d) [27]. Lipid rafts have been associated with important biological functions, they participate in the formation and targeting of biogenic vesicles (like EVs), they act as structural platforms for organizing the protein machinery and represent centres for the assembly of signalling molecules [15, 91, 93].
The structural perturbation introduced by lipid rafts promotes the selective adsorption of materials on the membranes and hence represents an important driving force in numerous interactions at the nanoscale. In this section, by employing synthetic multicomponent SLBs, we show how the presence of lipid rafts influences the adsorption of AuNPs on the membrane. According to Sheavly et al. [94], NPs adsorption causes the bilayer to bend, this entails an energy penalty that increases the free energy associated with the process. As schematically represented in Figure 4.9, this energetic penalty is significantly reduced along the phase boundaries, where the local curvature of the membrane, generated by the thickness mismatch between the two lipid domains, minimizes the free energy associated with the NPs adsorption. Multiple works in literature related the presence of phase segregations with the selective adsorption of nanomaterials (in particular NPs) along the domain boundaries [94, 95]; however, a direct proof of this interaction was still missing to date.
In order to address this issue, we employed multicomponent SLBs, consisting of

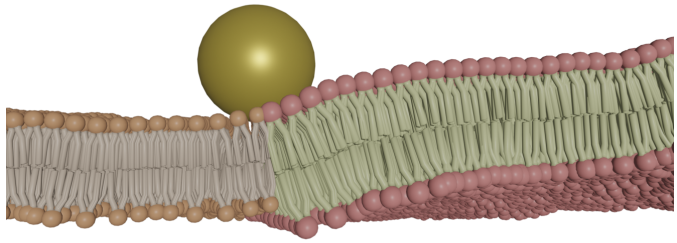

Figure 4.9: The energetic penalty associated with the bending of the bilayer, as a consequence of NP adsorption, is significantly reduced along the phase boundaries, where the thickness mismatch between the two lipid domains, induces a local curvature that promotes the interaction.

DOPC/DSPC/Cholesterol (39/39/22 mol%) which were obtained via vesicle fusion (please refer to material and methods). SLBs were characterized by Neutron Reflectivity (NR), yielding an average thickness of $\approx$ 5 nm. Moreover, fitting the reflectivity profile of the SLB, revealed a negligible hydration of the lipid chains, meaning that the substrate was almost completely covered by the bilayer (Figure 4.10 A and B). Since NR only provides information on the average structure along the direction perpendicular to the bilayer, AFM was used to resolve the in-plane bilayer heterogeneity, i.e. the lipid rafts. As displayed in Figure 4.10 C, AFM images further confirmed that the surface was completely covered with a lipid bilayer, characterized by the presence of nanometric domains, presenting different heights. The analysis of the AFM images and the application of appropriate masks (alternatively selecting the two regions with different height) allowed obtaining their height distributions. The analysis revealed that the bilayer consisted of two distinct lipid phase-like domains, whose height distributions were centred at height values of 3.7 nm and 4.7 nm, corresponding to the L_d and L_o phases, respectively (Figure 4.10 D). The thicker domains consist of DSPC and Cholesterol while DOPC is present in the thinner regions.

Once the system was fully characterized, AuNPs were injected and left interacting with the bilayer. AFM has the sufficient resolution to simultaneously resolve both the domain boundaries and the AuNPs, hence providing direct proof of the preferential adsorption phenomenon. To probe the adsorption of AuNPs on the bilayer, $600x600nm^2$ AFM images were acquired. As displayed in Figure 4.11 A, AuNPs adsorbed on the SLB, preferentially targeting the segregated phase boundaries. To obtain quantitative information about AuNPs preferential adsorption, the edges of

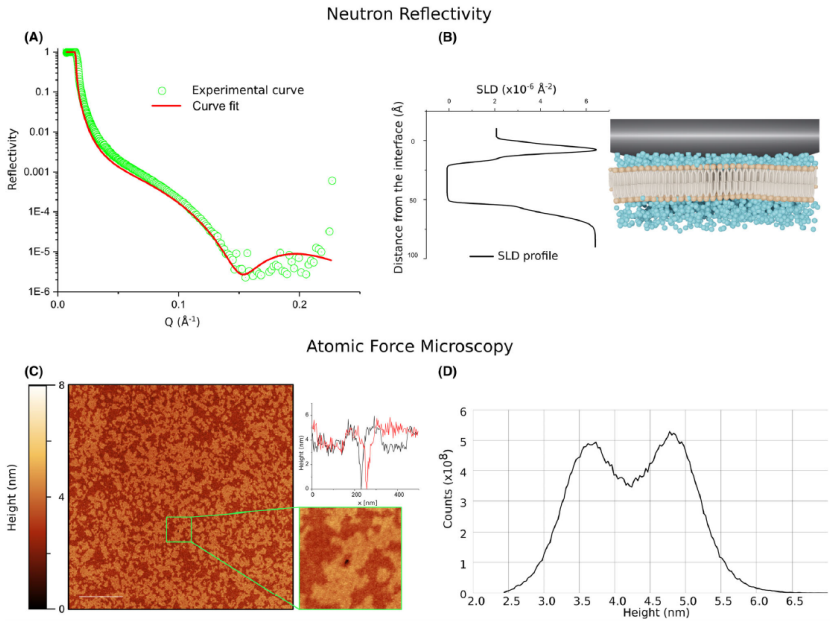

Figure 4.10: Characterisation of the multicomponent DOPC/DSPC/cholesterol (39/39/22 mol%) SLB. (A) Neutron Reflectivity curve. (B) Scattering length density (SLD) profile, describing variations of the SLD along the perpendicular to the bilayer. (C) AFM topography of the SLB. Both the L_o (brighter thicker regions) and L_d phases (darker thinner regions) are present as segregated domains. The scalebar is 1 μm. The 500 × 500 nm micrograph (bottom inset) displays the small hole in the bilayer; two perpendicular height profiles were traced, horizontally and vertically, across the whole image, confirming the presence of the two distinct lipid phases covering the surface. (D) Height distribution obtained from the AFM image; the two distinct peaks, centred at hd = 3.7 nm and ho = 4.7 nm, describe the different heights that characterize the L_d and L_o phase, respectively. Figure adapted from [96].

both rafts and NPs were mapped using *Gwyddion 2.53*, an image processing software; results are displayed in Figure 4.11 B. This procedure allowed obtaining a clearer indication about the AuNP-raft boundary relative position. As displayed in Figure 4.11 B, AuNPs preferentially targeted the boundaries of the two lipid phases; indeed, the lines describing their shapes are always in contact with the edges of the lipid rafts. More precisely, the ratio between the number of NPs adsorbed along the boundaries and the total amount of NPs present on the SLB tells that 91% of the NPs are located along the edges. Moreover, by comparing the height of the adsorbed AuNPs (14 ± 2 nm, obtained via AFM) with their nominal diameter (16 nm), it is possible to infer that NPs, after adsorbing, penetrate the bilayer and reach the SiO_2 surface. This observation support the idea that rafts' boundaries could serve as regions of increased permeability [97–99], where the membrane can easily wrap around the adsorbed NPs.

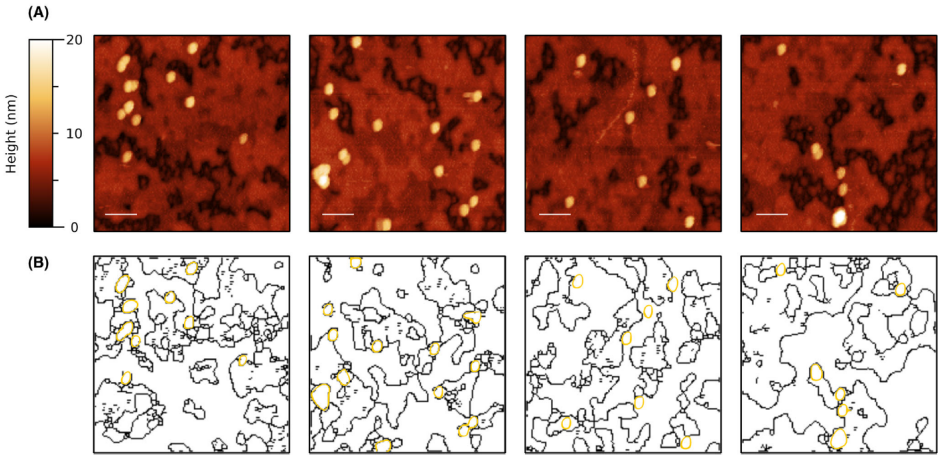

Figure 4.11: (A) Representative AFM micrographs displaying the selective adsorption of AuNPs along the boundaries of the lipid rafts (brighter regions of the SLB). From the images it is also possible to distinguish between isolated and clustered NPs. All scalebars are 100 nm. (B) Contour images obtained from the micrographs. Black lines represent the rafts edges while gold circles are the AuNPs. The gold NPs edges are always in contact with at least one of the lines describing the lipid segregated phase boundaries. Figure adapted from [96].

The herein presented work provides the direct proof that phase boundaries represent energetically favourable niches for the NP-lipid interactions, hence promoting NP preferential adsorption and subsequent internalization. The obtained results further enrich the understanding on NP-membrane interaction, suggesting that in addition to the mechanical properties of lipid membranes, also their compositional heterogeneity plays a crucial role in regulating interactions at the nanoscale.

Part III

Nanomechanics and structural stability of nonlamellar lipid membranes

Chapter 5

Structural and mechanical characterization of cubic phase lipid membranes

Inverse bicontinuous cubic phase membranes are ubiquitous in Nature and participate in numerous biological processes, like food digestion and protein storage. Three types of bicontinuous cubic phases have been reported for lipid systems, corresponding to the primitive (P), double diamond (D) and gyroid (G) Schwarz's IPMS [66] (see the Introduction for a more detailed description). Compared to planar membranes, these nonlamellar interfaces feature considerably higher membrane surface to volume ratios as well as a defined geometry with connected aqueous cavities, which can be exploited for the encapsulation of hydrophobic, hydrophilic and bioactive molecules, proteins and nanoparticles [100, 101]. For these reasons, they are widely employed as protein crystallization scaffolds and as nanoparticle-based drug delivery systems.

Despite their biotechnological potential, the properties of these highly curved interfaces are still poorly understood; in particular, their nanomechanics represents a totally unexplored field, meaning that the response of cubic membranes to nanoscale deformations, such as the ones involved in biological processes, is completely unknown. This is also due to the lack of appropriate synthetic lipid models which would allow characterizing these membranes under controlled and simplified conditions.

In this chapter, we report on the realization of thin supported lipid bicontinuous cubic (Q_{II}) phase films and on their structural and mechanical characterization.

Analogously to SLBs, information on the properties of these synthetic membrane models could enrich the understanding of their natural counterparts.
To obtain Q_{II} phase films with thicknesses approaching the ones of natural membranes, Glycerol monooleate (GMO), a natural food grade, biocompatible and biodegradable lipid [102, 103], was dissolved in chloroform at a concentration of 10 mg/ml and subsequently spin-coated on the experimental substrates. According to this procedure, the GMO molecules in the film, once hydrated at room temperature and atmospheric pressure, self-assemble into the double diamond cubic (Q_{II}^{D}) architecture (presenting the $Pn-3m$ space group symmetry); Figure 5.1 schematically describes the experimental steps that lead to the fabrication of the film. The

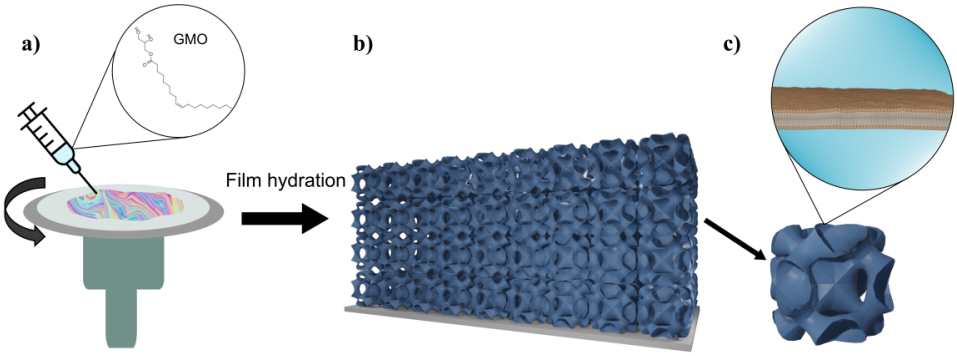

Figure 5.1: Fabrication of thin supported Q_{II} phase films. a) The GMO/chloroform solution is deposited on top of a rigid substrate which is then put under rotation using a spin coater. b) The resulting iridescent film can be hydrated to allow GMO to self-assemble into the expected cubic architecture. c) At room temperature, atmospheric pressure and in excess of water, the resulting lipid film is characterized by the repetition of multiple Q_{II}^{D} (also called Pn3m) unit cells in the 3D space. Figure adapted from [104].

film structure was probed by means of SAXS; Figure 5.2 a shows the diffractogram of the GMO-based lipid film prepared from a 10 mg/ml GMO:chloroform solution, compared with the ones obtained from more concentrated GMO solutions and the respective bulk phase. Differently from the more concentrated solutions, no Bragg peaks are visible in the diffractogram of the 10 mg/ml GMO film. This is most likely due to the limited number of cubic domains present in the thin layer. Indeed, using more concentrated GMO:chloroform solutions (which yield thicker films by spin coating) resulted in progressively more defined Bragg peaks. In particular, the single peak from the 100 mg/ml GMO film corresponds to a lattice parameter of 90 Å while the lattice parameters determined for the 1000 mg/ml GMO film and bulk phase are 92.6 ± 0.2 Å and 92.8 ± 0.3 Å, respectively. Peaks positions are consistent with a well-ordered Q_{II}^{D} architecture, mostly independent from the film thickness. These results suggest that the same lipid arrangement should also be

present in the 10 mg/ml GMO film.

The hypothesis about the 10 mg/ml GMO film being too thin to reveal any Bragg peak at SAXS was supported by Ellipsometry studies, which revealed a thickness in the nanometres range. Results were obtained from three different replicates and are displayed in Figure 5.2 b. At this point, AFM imaging (performed in li-

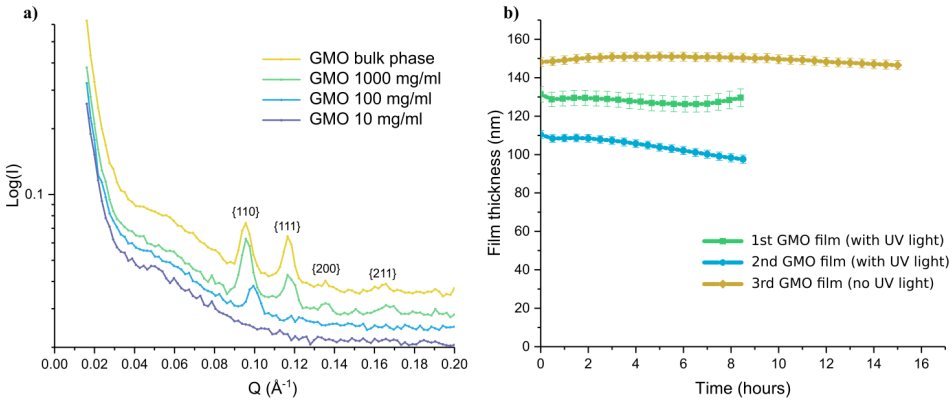

Figure 5.2: Structural characterization of the 10 mg/ml Q_{II}^D film. a) SAXS characterization of lipid Q_{II}^D phase films at different GMO concentrations. No Bragg peak is visible in the more diluted sample (purple curve); peaks become more pronounced as the initial GMO concentration is increased (until reaching the bulk phase). Peak positions are compatible with a Q_{II}^D phase, at all concentrations. The Miller indexes used for the lattice parameter calculation are reported on top of each peak. b) Ellipsometry analysis of the 10 mg/ml GMO film. Film thickness ranges from 110 to 150 nm. As can be seen from the 1^{st} and 2^{nd} acquisitions (green squares and blue circles), the film is destabilized by prolonged exposures to UV light while it remains stable and preserves its original thickness for more than 15 hours (gold diamonds), when probed by just visible light. Figure adapted from [104].

quid) was employed for determining the local surface structure of the nanometric film. Results are displayed in Figure 5.3 a and b, and demonstrate that also the 10 mg/ml lipid film presents a cubic architecture, directly exposed to the water interface. From the raw AFM images, it was possible to calculate the 2D autocorrelation function (ACF) and then use it for determining a lattice parameter of 97.6 $\pm$ 0.3 Å; in good agreement with the results obtained by SAXS on thicker systems. Scanning larger areas also allowed for an independent thickness characterization; as can be seen in Figure 5.3 c and d, the thickness measured by AFM is in perfect accord with the one estimated by ellipsometry.

The combination of SAXS, ellipsometry and AFM proved that it is possible to realize thin Q_{II} phase lipid films with thicknesses approaching the ones found in natural membranes; hence obtaining reliable and versatile platforms for studying the properties of biological nonlamellar membranes under controlled conditions.

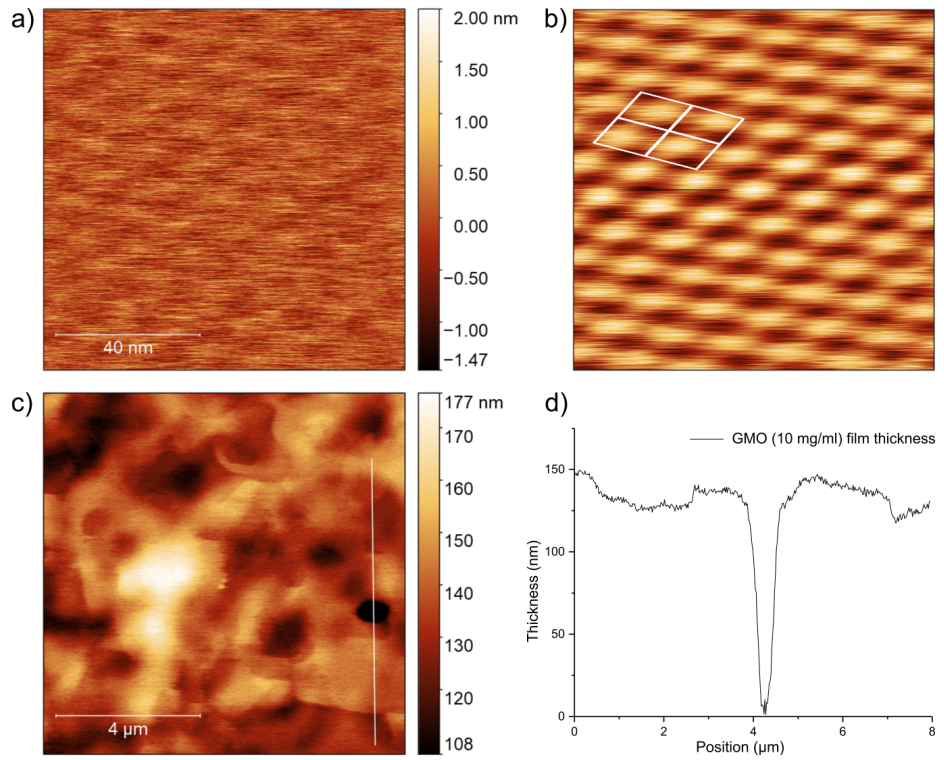

Figure 5.3: AFM imaging characterization of the 10 mg/ml GMO lipid film. a) The topography of the film surface revealed the presence of a cubic architecture, exposed to the water interface; b) the 2D ACF allows noise reduction and calculation of the lattice parameter (more information on that can be found in the manuscript). The white frame describes the unit cell lattice pattern; c) 10x10 μm^2 image describing a continuous and relatively homogeneous film; d) height profile along the white line in panel c. Thanks to an occasional discontinuity in the film, the thickness was estimated to be $\approx$ 150 nm). Figure adapted from [104].

The herein presented thin Q_{II}^{D} phase lipid films were then employed to investigate the mechanical response of cubic membranes to nanoscale deformations, by means of AFM-FS. As already mentioned in the previous chapters, during an AFM-FS experiment, a sharp tip is used to indent the sample and study its mechanical response to deformations. The relationship between force and indentation depth is recorded and plotted in the so-called force-indentation curves. The mechanical response recorded for the thin Q_{II}^{D} phase lipid films is completely different from the one of a SLB (represented in Figure 3.1 a); indeed, as displayed in the force-indentation curve of Figure 5.4 a, after an initial, approximately linear regime, all the recorded curves were characterized by a sequence of indentation peaks. Each peak describes the mechanical failure and subsequent penetration of a single cubic unit cell. In-

terestingly, the force involved in this phenomenon seems to be independent of the penetration depth, as if the resistance offered by each cubic unit is unaffected by the presence of the others. While no previous study reported about this peculiar behaviour of cubic lipid membranes, several engineering and material science investigations obtained very similar results from mechanical compression tests performed on cubic-inspired macroscopic 3D-printed structures [105–107]. These architectures are gaining increasing attention due to their combination of light weight, high impact and stress resistance, which represents a promising solution for multiple structural challenges [105–108]. Despite being characterized by completely different length scales, it seems that Q_{II}^{D} lipid membranes and these cubic-inspired 3D-printed macroscopic structures share the same topology-dependent mechanics; meaning that some of the mechanical properties studied on the macroscopic structures could remain valid for their nanoscale lipid counterparts, thus helping the development of potential bioinspired nanomaterials.

It is also possible to obtain structural information on the Q_{II}^{D} architecture of the

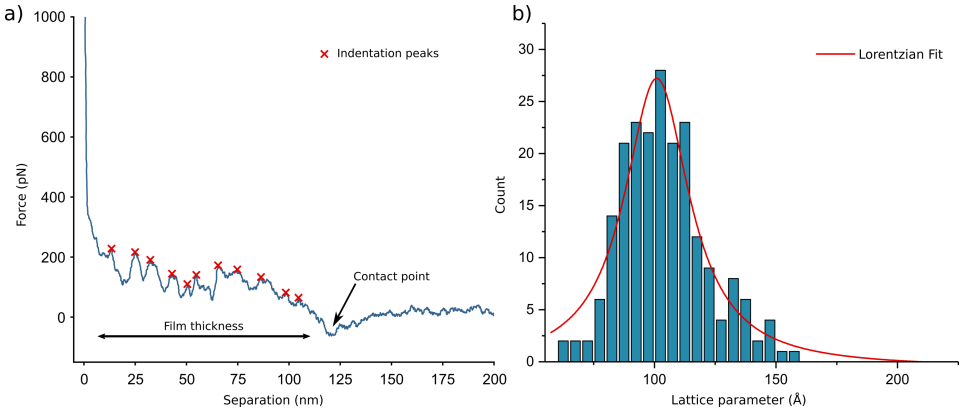

Figure 5.4: AFM-FS analysis of the lipid Q_{II}^{D} phase film. a) Representative AFM-FS curve obtained from the indentation of the cubic film; red crosses identify the indentation peaks, which correspond to the mechanical failure of single successive cubic unit cells. b) Distribution of the lattice parameters obtained from Equation 5.1; the distribution was fitted with a Lorentzian function and the centre was located at a lattice parameter value of $\approx$ 100 Å, in agreement with previous SAXS and AFM imaging analyses. Figure adapted from [104].

thin lipid films by analysing the position of the indentation peaks along the recorded force-indentation curves. From a single force-indentation curve, it is possible to estimate both the film thickness (from the determination of the contact point) and the number of indentation peaks, i.e. the number of cubic unit cells that were penetrated before reaching the substrate (more details on this are presented in the manuscript). Since each peak corresponds to the penetration of a single cubic unit

cell, whose height corresponds to the lattice parameter of the whole architecture, Equation 5.1 can be used to estimate the average lattice parameter, directly from the AFM-FS analysis.

$$\frac{Film\,thickness}{n^{\circ}\,of\,peaks\,(unit\,cells)} = Average\,cubic\,unit\,height = Average\,lattice\,parameter \tag{5.1}$$

Repeating this procedure for all the 211 recorded force-indentation curves yields a monomodal distribution of values (Figure 5.4 b) which can be fitted with a Lorentzian function centred at ≈100 Å, in agreement with values of lattice parameter from both the SAXS and the AFM imaging analyses. This result provides the first example of AFM-FS being used for characterizing the structure of nonlamellar lipid mesophases, thus offering an alternative solution to the more commonly used scattering and cryo-electron microscopy-based techniques.

The herein reported results show how the fabrication of thin supported Q_{II} phase lipid films could provide useful membrane models for studying the properties of natural nonlamellar lipid assemblies, under controlled conditions. After characterizing the film structure with multiple techniques, AFM-FS allowed obtaining the first nanomechanical characterization of Q_{II} membranes. Compared to classical rheological studies, which could only provide bulk characterizations, the herein reported analysis probed the cubic architectures via forces and deformations occurring at the nanoscale level, resembling the ones involved in biological membrane interactions [109]. The nanomechanics of these cubic membranes seems to be length scale independent and strictly related to their topology; this suggests that macroscopic cubic structures could be successfully employed for studying the properties of their nanometric membranous lipid counterparts.

Chapter 6

Shape and geometry affect membrane stability upon nanoscale interactions

Most of the interactions occurring at the nanoscale are mediated by biological barriers, such as lipid membranes. For this reason, understanding how the stability of biological and synthetic lipid interfaces is affected and affects these interactions could lead to significant advancements in multiple research fields, from enriching the knowledge about the onset of pathological conditions to optimizing the bioactivity and cytotoxicity of various nanomaterials (e.g. NPs) for drug delivery applications [110–112].

The effects of NP shape and curvature on their internalization pathways have been widely investigated [113–116]; in particular, it has been found that NP shape regulates the area available for the adsorption, therefore modulating the adhesion force with surfaces [117] while curvature determines the energetic costs of wrapping and internalization mechanisms [115, 116]. On the other hand, effects related to shape and curvature of lipid membranes, when interacting with nanomaterials, have been less investigated. Despite being commonly associated with lamellar structures, lipid membranes can present different shapes and curvatures; such as the case of nonlamellar architectures. These highly curved lipid arrangements occur spontaneously in Nature as a consequence of pathological conditions (e.g. starvation, viral infections) or during specific phases of a cell life cycle (e.g. membrane fusion). Although their fundamental biological role, most properties of these nonlamellar membranes, remain elusive and poorly characterized nowadays.

This chapter describes how the shape and geometry of lipid membranes affect their stability upon interaction with nanomaterials, in particular with AuNPs presenting different shapes. In order to probe the effect of these parameters in such interactions, lamellar and nonlamellar synthetic lipid membrane mimics have been employed. Stacks of lamellar planar membranes allowed modelling the commonly encountered flat membrane configurations, while supported cubic phase lipid films served as mimics of their respective nonlamellar biological counterparts. Both the systems were challenged with AuNPs presenting different shapes, namely nanospheres (AuNSs) and nanorods (AuNRods). AuNSs capped with mearcaptoundecyl-N,N,N-trimethyl ammonium bromide (TMA) had a diameter of 3.4 ± 0.6 nm while AuNRods were capped with Cetyltrimethyl ammonium bromide (CTAB) and presented sizes of 18 ± 4 and 4 ± 1 nm. Effects related to the interaction of these positively charged NPs on the structural stability of the two lipid systems were then analysed by means of neutron scattering techniques, revealing new insights into the role of membrane shape and curvature during interactions at the nanoscale.

Both lamellar (L_α) and nonlamellar (Q^D_{II}) lipid films were prepared by spin-coating n-hexane solution of GMO/DOPC (50/50 mol %) and GMO, respectively on silicon blocks and subsequently hydrated with excess water (either H_2O or D_2O, depending on the measurement); before each characterization, films were left equilibrating for 12 hours. Confocal microscopy analysis revealed a homogeneous thickness of 10 ± 2 μm for both the films (more details in the manuscript), while neutron reflectivity (NR) measurements confirmed the formation of highly ordered lamellar (Figure 6.1 a) and cubic (Figure 6.1 b) architectures. In the lamellar film, the positions of the two peaks determine an average water interlayer thickness of 26-29 Å. On the other hand, peaks position for the cubic architecture points to a lattice parameter of 95 ± 5 Å, corresponding to a water channel diameter of ≈ 44 Å[118]. AuNSs were then injected and left interacting with the lipid matrices for 8 hours; after that, NR profiles were acquired to determine the effects of the interaction. The impact of AuNSs on the two lipid systems can be assessed from the green traces of Figure 6.1; in both cases, the interaction did not affect the position of the peaks, which is unchanged from the initial red traces. However, an intensity drop in the reflectivity profile of the lamellar architecture can be observed, suggesting partial disruption of the bilayers. On the other hand, the reflectivity of the cubic architecture displays similar intensity even after AuNSs interaction, meaning that the cubic film almost completely preserved its pristine structure. To assess whether AuNSs could induce any structural modification of the cubic architecture on longer time scales, Grazing Incidence Small Angle Neutron Scattering (GISANS) measurements were performed over 24 hours. Compared to classic NR, GISANS allows

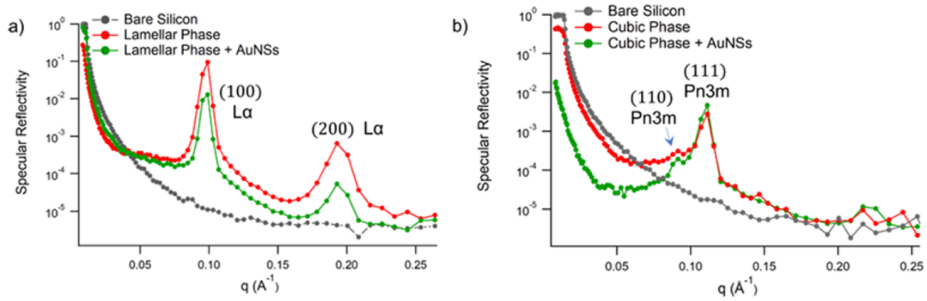

Figure 6.1: Neutron Reflectivity (NR) analysis of the two lipid systems following the interaction with AuNSs. a) GMO/DOPC film in the absence (red trace) and in the presence of AuNSs (green trace), together with reflectivity of the bare silicon (grey trace). b) GMO film in the absence (red trace) and in the presence of AuNSs (green trace), together with reflectivity of the bare silicon (grey trace). Figure adapted from [119].

monitoring the lipid arrangement and its possible alterations along the directions parallel to the film plane. Results are displayed in the Q_z vs Q_y plots of Figure 6.2. The GISANS pattern for the neat GMO film (Figure 6.2 a) is characterized by isolated and well-defined spots, whose position is representative of the crystallographic planes identified by the (110) and (111) Miller indexes, associated to the Pn-3m space group symmetry. Spot position is compatible with a lattice parameter of 102 Å, in good agreement with the one obtained in the previous NR investigations. When AuNSs are left interacting with the cubic architecture for longer periods of time, they smear out the point-like GISANS pattern, previously observed for the neat GMO film. This is related to an increase in the structural disorder of the cubic mesophase, either due to a partial disruption of the Pn-3m symmetry or to a loss of its spatial orientation. Interestingly, spot position in Figure 6.2 b is now compatible with a lattice parameter 2 nm smaller than the previous one, suggesting that AuNSs also produced a shrinkage of the cubic architecture, perhaps as a consequence of film dehydration by the NPs. All the reported results suggest that AuNSs possess a disruptive effect, when interacting with lipid membranes of different architecture; however, bicontinuous cubic membranes display an higher resistance than lamellar ones against AuNSs disruption, which still takes place, although on longer time scales.

Compared to AuNSs, AuNRods have a much more intense impact on the structural stability of lipid membranes; Figure 6.3 displays NR profiles for the GMO/DOPC and GMO lipid films (red traces), together with the ones acquired following AuNRods interaction (blue traces). Following the injection of AuNRods, no Bragg peaks can be observed in the NR profiles of both lipid systems, meaning that their archi-

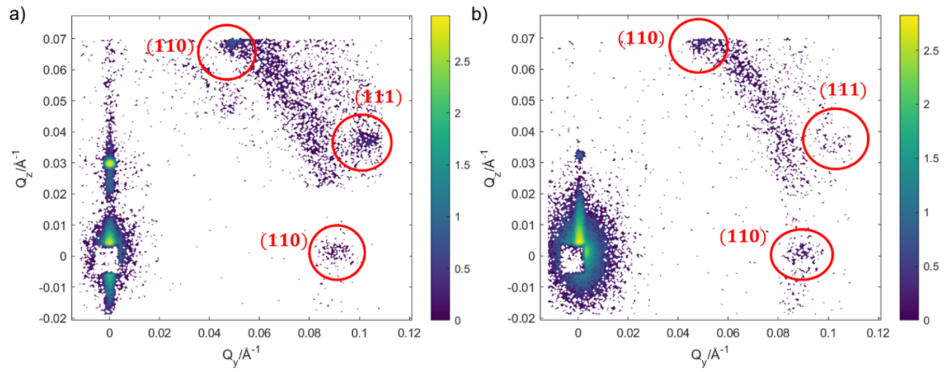

Figure 6.2: a) GISANS pattern of the neat GMO cubic film, in the absence of NPs; b) GISANS pattern of the GMO cubic film following the interaction with AuNSs. Intensities are reported in logarithmic scale. The reflectivity profiles of the cubic film in the presence of AuNSs has been acquired after 8 hours of incubation, employing a counting time for the acquisition of 24 hours, leading to a lipid film/AuNSs total interaction time of 32 hours. Figure adapted from [119].

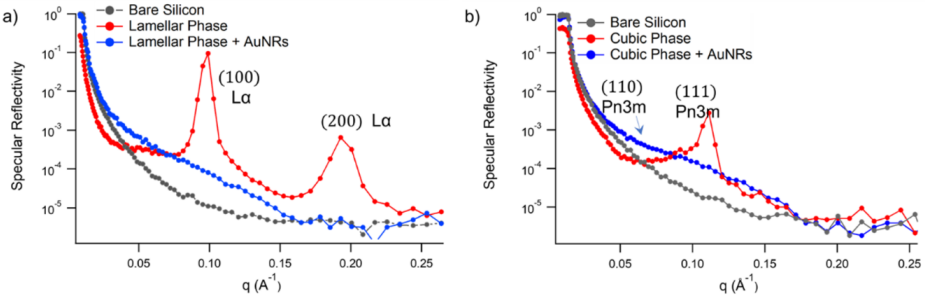

Figure 6.3: Neutron Reflectivity (NR) profiles of the two lipid systems following the interaction with AuNRods. a) GMO/DOPC film in the absence (red trace) and in the presence of AuNRods (blue trace), together with reflectivity of the bare silicon surfaces (grey trace). b) GMO film in the absence (red trace) and in the presence of AuNRods (blue trace), together with reflectivity of the bare silicon surface (grey trace). Figure adapted from [119].

tectures have been almost completely disrupted by the interaction. It is therefore impossible to assess any difference in the stability of the two lipid arrangements, against the disruption generated by AuNRods. However, this does not rule out the hypothesis that different disruption mechanisms might be at play over shorter time scales. To gain further insights into the faster disruption process induced by AuNRods, Neutron Reflectivity kinetics studies were employed for investigating the phenomenon. This type of measurements allows monitoring the structural alteration produced by AuNRods over shorter time scales [120]. Figure 6.4 reports representative Q_z, Q_x plots extracted from 5 hours long time-lapse acquisitions.

Both lamellar and cubic films present well-defined Bragg sheets (whose position is related to the two different lipid architectures); as can be seen, the longer the interaction time, the more the Bragg sheets get smeared out, ultimately disappearing completely. It is worth noticing that this process is characterized by different time scales in the two lipid architectures. In the case of lamellar membranes, the Bragg sheets completely vanish from the plots within 12 minutes, while in the cubic architecture they can still be detected even after 2 hours. These results are in line with

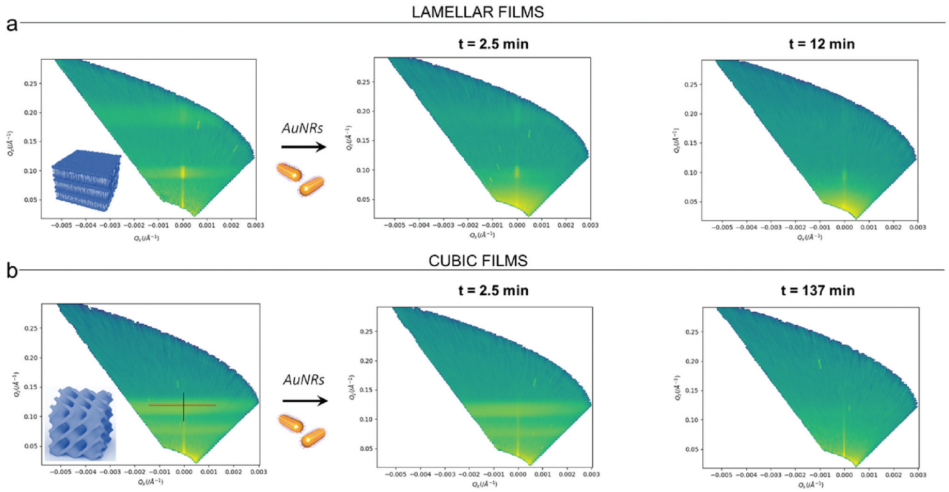

Figure 6.4: Neutron Reflectivity kinetics studies. Measurements of lamellar and cubic films in the presence of AuNRods have been acquired each 2.5 minutes over 5 hours, starting soon after the injection of AuNRods into the measurement chamber. a) Effect of AuNRods on the lamellar structure of GMO/DOPC films, any sign of lipid arrangements vanishes completely after 12 minutes. b) Effect of AuNRods on the cubic structure of GMO films; Bragg sheets are still detectable (though with very low intensity) even after 2 hours. Figure adapted from [119].

findings about the interaction of AuNSs and confirm that cubic membranes possess increased structural stability against the disruptive action of AuNPs. Confocal Laser Scanning Microscopy (CLSM) analysis allowed investigating the disruption of the lipid films at micrometric length scales and showed that the process follows two distinct pathways in the two lipid architectures, irrespectively of the NP shape (given the different length scale probed by this technique, results are briefly described in the following lines while we refer to the original manuscript for details about the CLSM characterization). The interaction of AuNPs with the lamellar films produces an initial swelling of the architecture, which increases the interlamellar distance and ultimately leads to the progressive peeling-off of the whole film, by gradually removing the outer surface layers. On the other hand, the disruption of the cubic architecture is characterized by a completely different mechanism; here

the AuNPs start to excavate the cubic membranes, thinning selected areas of the film and subsequently leading to the formation of cavities whose depth reaches the substrate level. On a microscopic length scale, this process produces a retraction of the cubic film according to a dewetting-like pattern. The shape of the NPs (namely AuNSs and AuNRods) does not change the two mechanisms; however, in both cases, AuNRods seem to accelerate the disruption, completely removing both the lipid films in shorter periods of time. Figure 6.5 schematically summarizes the disruptive mechanisms of both the lamellar and cubic films. The herein presented

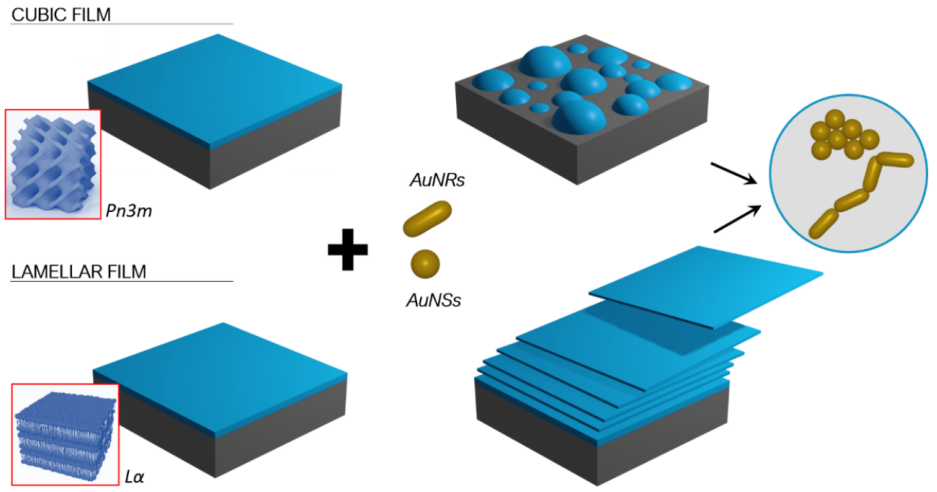

Figure 6.5: Schematic description of the two disruption processes occurring as a consequence of AuNPs interaction with lipid films. AuNPs induce the excavation and then the dewetting of the cubic films (top panel); on the other hand, they generate the progressive exfoliation of the lamellar film (bottom panel). The disruption of both lipid architectures is faster with AuNRods. Figure adapted from [119].

results demonstrate that membrane shape and geometry influence the structural stability of lipid architectures against nanoscale interactions. More specifically, results from our structural characterizations show that, compared to lamellar lipid architectures, the interconnected structure of cubic membranes features a higher resistance against the disruptive action of AuNPs, which enables the membrane to retain its initial structure for longer time periods.

Despite both the function and origin of cubic membranes in Nature being still poorly understood topics, some studies described the formation of such nonlamellar lipid assemblies as an adaptive strategy against the onset of pathological conditions [47]. In this framework, the presented results support this hypothesis and show that cubic phase membranes could serve as more resistant biological barriers against potentially harmful nanoscale interactions.

Chapter 7

Conclusions

Lipid membranes, either lamellar or nonlamellar, are fundamental building blocks of life; they actively participate in most biological processes and separate cells and cell-derived organelles from their outer environments. In doing so, they are subjected to stresses and deformations of different type and extent which perturb their equilibrium conformations. For these reasons, understanding the nanomechanics of lipid membranes and associated membranous compartments could provide new insights into all those interactions involving biological interfaces. However, the intrinsic complexity of most natural membranes and the lack of accurate theoretical descriptions are hindering the understanding and development of this field.
In the presented work, by employing multiple experimental techniques, ranging from AFM to neutron/X-ray scattering, and leveraging various membrane models, we probed the mechanical response of lamellar and nonlamellar lipid membranes to nanoscale deformations, resembling the ones that can be found in several natural processes, like vesicle-to-surface adsorption and interactions with nanomaterials, such as AuNPs.
Results on lamellar lipid assemblies (i.e. vesicles and SLBs) revealed that pressure, membrane elasticity and compositional heterogeneity should all be taken into consideration when analysing the mechanical response of a lipid nanovesicle to external stimuli, such as adsorption to surfaces and interaction with NPs.
Experiments aimed at probing vesicles stiffness also lead to the development of two high-throughput characterization methods for determining the stiffness of unknown vesicle preparations and were also successfully applied to natural systems, i.e. Extracellular vesicles.
On the other hand, the fabrication of thin bicontinous cubic phase lipid films allowed studying the structure and nanomechanics of these highly curved assemblies,

employing synthetic models that closely resemble some of the nonlamellar membranes found in Nature. Our AFM-FS analysis represents the first nanomechanical characterization of bicontinuous cubic phase membranes and revealed that these architectures possess an interesting length-scale independent mechanical response, strictly related to their topology. Moreover, by challenging both cubic and lamellar lipid assemblies with AuNPs of different shape and by comparing their response, we show that nonlamellar membranes possess an increased resistance to the disruption by external nanomaterials. These findings support previous hypotheses, according to which these mesophases represent a self-induced cellular defensive mechanism. Overall, the herein presented results help to better rationalize multiple aspects related to the mechanical response of lipid membranes at the nanoscale and provide valuable information for future thorough descriptions of these ubiquitous, fascinating yet complicated systems.

Bibliography

[1] Nick Lane. *The vital question: energy, evolution, and the origins of complex life.* WW Norton & Company, 2015.

[2] Alexis P Yelton, Luis R Comolli, Nicholas B Justice, Cindy Castelle, Vincent J Denef, Brian C Thomas, and Jillian F Banfield. Comparative genomics in acid mine drainage biofilm communities reveals metabolic and structural differentiation of co-occurring archaea. *BMC genomics*, 14(1):1–15, 2013.

[3] Zakaria A Almsherqi, Tomas Landh, Sepp D Kohlwein, and Yuru Deng. Cubic membranes: the missing dimension of cell membrane organization. *International review of cell and molecular biology*, 274:275–342, 2009.

[4] Xiaokang Zhang, Peng Ge, Xuekui Yu, Jennifer M Brannan, Guoqiang Bi, Qinfen Zhang, Stan Schein, and Z Hong Zhou. Cryo-em structure of the mature dengue virus at 3.5-å resolution. *Nature structural & molecular biology*, 20(1):105–110, 2013.

[5] D Fennell Evans and Håkan Wennerström. The colloidal domain: where physics, chemistry, biology, and technology meet. 1999.

[6] Jacob N Israelachvili, D John Mitchell, and Barry W Ninham. Theory of self-assembly of hydrocarbon amphiphiles into micelles and bilayers. *Journal of the Chemical Society, Faraday Transactions 2: Molecular and Chemical Physics*, 72:1525–1568, 1976.

[7] Jacob N Israelachvili. *Intermolecular and surface forces.* Academic press, 2015.

[8] GC Shearman, O Ces, RH Templer, and JM Seddon. Inverse lyotropic phases of lipids and membrane curvature. *Journal of Physics: Condensed Matter*, 18(28):S1105, 2006.

[9] Stephen T Hyde et al. Identification of lyotropic liquid crystalline mesophases. *Handbook of applied surface and colloid chemistry*, 2:299–332, 2001.

[10] James R Edgar. Q&a: What are exosomes, exactly? *BMC biology*, 14(1):1–7, 2016.

[11] Rumiana Dimova and Carlos Marques. *The Giant Vesicle Book*. CRC Press, 2019.

[12] Abolfazl Akbarzadeh, Rogaie Rezaei-Sadabady, Soodabeh Davaran, Sang Woo Joo, Nosratollah Zarghami, Younes Hanifehpour, Mohammad Samiei, Mohammad Kouhi, and Kazem Nejati-Koshki. Liposome: classification, preparation, and applications. *Nanoscale research letters*, 8(1):1–9, 2013.

[13] Luke A Clifton, Richard A Campbell, Federica Sebastiani, José Campos-Terán, Juan F Gonzalez-Martinez, Sebastian Björklund, Javier Sotres, and Marité Cárdenas. Design and use of model membranes to study biomolecular interactions using complementary surface-sensitive techniques. *Advances in colloid and interface science*, 277:102118, 2020.

[14] Guillaume Van Niel, Gisela d'Angelo, and Graça Raposo. Shedding light on the cell biology of extracellular vesicles. *Nature reviews Molecular cell biology*, 19(4):213–228, 2018.

[15] S Busatto, A Zendrini, A Radeghieri, L Paolini, M Romano, M Presta, and P Bergese. The nanostructured secretome. *Biomaterials science*, 8(1):39–63, 2020.

[16] Rong Xu, Alin Rai, Maoshan Chen, Wittaya Suwakulsiri, David W Greening, and Richard J Simpson. Extracellular vesicles in cancer—implications for future improvements in cancer care. *Nature reviews Clinical oncology*, 15(10):617–638, 2018.

[17] Leonid Margolis and Yoel Sadovsky. The biology of extracellular vesicles: The known unknowns. *PLoS biology*, 17(7):e3000363, 2019.

[18] Daan Vorselen, Susan M van Dommelen, Raya Sorkin, Melissa C Piontek, Jürgen Schiller, Sander T Döpp, Sander AA Kooijmans, Brigitte A van Oirschot, Birgitta A Versluijs, Marc B Bierings, et al. The fluid membrane determines mechanics of erythrocyte extracellular vesicles and is softened in hereditary spherocytosis. *Nature communications*, 9(1):1–9, 2018.

[19] Bradley Whitehead, LinPing Wu, Michael Lykke Hvam, Husnu Aslan, Mingdong Dong, Lars Dyrskjøt, Marie Stampe Ostenfeld, Seyed Moein Moghimi, and Kenneth Alan Howard. Tumour exosomes display differential mechanical and complement activation properties dependent on malignant state: implications in endothelial leakiness. *Journal of extracellular vesicles*, 4(1):29685, 2015.

[20] Raya Sorkin, Rick Huisjes, Filip Bošković, Daan Vorselen, Silvia Pignatelli, Yifat Ofir-Birin, Joames K Freitas Leal, Jürgen Schiller, Debakshi Mullick, Wouter H Roos, et al. Nanomechanics of extracellular vesicles reveals vesiculation pathways. *Small*, 14(39):1801650, 2018.

[21] Michael LeClaire, James Gimzewski, and Shivani Sharma. A review of the biomechanical properties of single extracellular vesicles. *Nano Select*, 2(1):1–15, 2021.

[22] Jiali Zhai, Sampa Sarkar, Charlotte E Conn, and Calum J Drummond. Molecular engineering of super-swollen inverse bicontinuous cubic and sponge lipid phases for biomedical applications. *Molecular Systems Design & Engineering*, 5(8):1354–1375, 2020.

[23] Sten Andersson, ST Hyde, Kare Larsson, and Sven Lidin. Minimal surfaces and structures: from inorganic and metal crystals to cell membranes and biopolymers. *Chemical Reviews*, 88(1):221–242, 1988.

[24] TKM Landh. Cubic cell membrane architectures: Taking another look at membrane-bound cell spaces. 1998.

[25] Ida Dulińska, Marta Targosz, Wojciech Strojny, Małgorzata Lekka, Paweł Czuba, Walentyna Balwierz, and Marek Szymoński. Stiffness of normal and pathological erythrocytes studied by means of atomic force microscopy. *Journal of biochemical and biophysical methods*, 66(1-3):1–11, 2006.

[26] S Majid Hosseini and James J Feng. How malaria parasites reduce the deformability of infected red blood cells. *Biophysical journal*, 103(1):1–10, 2012.

[27] R Koynova and B Tenchov. Transitions between lamellar and non-lamellar phases in membrane lipids and their physiological roles. *OA Biochemistry*, 1(1):1–9, 2013.

[28] Rob Phillips, Jane Kondev, Julie Theriot, Hernan G Garcia, and Nigel Orme. *Physical biology of the cell*. Garland Science, 2012.

[29] David Boal and David H Boal. *Mechanics of the Cell*. Cambridge University Press, 2012.

[30] Lev Davidovich Landau and Eugin M Lifshitz. *Course of Theoretical Physics Vol 7: Theory and Elasticity*. Pergamon press, 1959.

[31] Eric Reissner. Stresses and small displacements of shallow spherical shells. i. *Journal of Mathematics and Physics*, 25(1-4):80–85, 1946.

[32] LD Landau and EM Lifshits. Theory of elasticity [in russian], 1965.

[33] Heinrich Hertz. Über die berührung fester elastischer körper. *Journal für die reine und angewandte Mathematik*, 92(156-171):22, 1882.

[34] Joseph Boussinesq. *Application des potentiels à l'étude de l'équilibre et du mouvement des solides élastiques: principalement au calcul des déformations et des pressions que produisent, dans ces solides, des efforts quelconques exercés sur une petite partie de leur surface ou de leur intérieur: mémoire suivi de notes étendues sur divers points de physique, mathematique et d'analyse*, volume 4. Gauthier-Villars, 1885.

[35] Ian N Sneddon. Fourier transforms.- new york. *Toronto/London*, 1951.

[36] Emilios K Dimitriadis, Ferenc Horkay, Julia Maresca, Bechara Kachar, and Richard S Chadwick. Determination of elastic moduli of thin layers of soft material using the atomic force microscope. *Biophysical journal*, 82(5):2798–2810, 2002.

[37] Sai Li, Frederic Eghiaian, Christian Sieben, Andreas Herrmann, and Iwan AT Schaap. Bending and puncturing the influenza lipid envelope. *Biophysical journal*, 100(3):637–645, 2011.

[38] Annalisa Calo, David Reguera, Gerard Oncins, Marie-Annick Persuy, Guenhaël Sanz, Simona Lobasso, Angela Corcelli, Edith Pajot-Augy, and Gabriel Gomila. Force measurements on natural membrane nanovesicles reveal a composition-independent, high young's modulus. *Nanoscale*, 6(4):2275–2285, 2014.

[39] Oumaima Et-Thakafy, Nicolas Delorme, Cedric Gaillard, Cristelle Mériadec, Franck Artzner, Christelle Lopez, and Fanny Guyomarc'h. Mechanical properties of membranes composed of gel-phase or fluid-phase phospholipids probed on liposomes by atomic force spectroscopy. *Langmuir*, 33(21):5117–5126, 2017.

[40] Peter B Canham. The minimum energy of bending as a possible explanation of the biconcave shape of the human red blood cell. *Journal of theoretical biology*, 26(1):61–81, 1970.

[41] Wolfgang Helfrich. Elastic properties of lipid bilayers: theory and possible experiments. *Zeitschrift für Naturforschung C*, 28(11-12):693–703, 1973.

[42] Patricia Bassereau, Benoit Sorre, and Aurore Lévy. Bending lipid membranes: experiments after w. helfrich's model. *Advances in colloid and interface science*, 208:47–57, 2014.

[43] Rumiana Dimova. Recent developments in the field of bending rigidity measurements on membranes. *Advances in colloid and interface science*, 208:225–234, 2014.

[44] Daan Vorselen, Fred C MacKintosh, Wouter H Roos, and Gijs JL Wuite. Competition between bending and internal pressure governs the mechanics of fluid nanovesicles. *Acs Nano*, 11(3):2628–2636, 2017.

[45] Zhuo Dai, Miaorong Yu, Xin Yi, Zeming Wu, Falin Tian, Yunqiu Miao, Wenyi Song, Shufang He, Ejaj Ahmad, Shiyan Guo, et al. Chain-length-and saturation-tuned mechanics of fluid nanovesicles direct tumor delivery. *ACS nano*, 13(7):7676–7689, 2019.

[46] Yuru Deng, Zakaria A Almsherqi, Mary ML Ng, and Sepp D Kohlwein. Do viruses subvert cholesterol homeostasis to induce host cubic membranes? *Trends in cell biology*, 20(7):371–379, 2010.

[47] Qi Xiao, Zhichun Wang, Dewight Williams, Pawaret Leowanawat, Mihai Peterca, Samuel E Sherman, Shaodong Zhang, Daniel A Hammer, Paul A Heiney, Steven R King, et al. Why do membranes of some unhealthy cells adopt a cubic architecture? *ACS central science*, 2(12):943–953, 2016.

[48] Carlos Rodríguez-Abreu, Miguel García-Roman, and Hironobu Kunieda. Rheology and dynamics of micellar cubic phases and related emulsions. *Langmuir*, 20(13):5235–5240, 2004.

[49] Raffaele Mezzenga, Cedric Meyer, Colin Servais, Alexandre I Romoscanu, Laurent Sagalowicz, and Ryan C Hayward. Shear rheology of lyotropic liquid crystals: a case study. *Langmuir*, 21(8):3322–3333, 2005.

[50] Chiara Speziale, Reza Ghanbari, and Raffaele Mezzenga. Rheology of ultraswollen bicontinuous lipidic cubic phases. *Langmuir*, 34(17):5052–5059, 2018.

[51] Aldo Jesorka and Owe Orwar. Liposomes: technologies and analytical applications. *Annu. Rev. Anal. Chem.*, 1:801–832, 2008.

[52] Subhash C Basu and Manju Basu. *Liposome methods and protocols*. Number 199. Springer Science & Business Media, 2002.

[53] Theresa M Allen. Liposomes. *Drugs*, 54(4):8–14, 1997.

[54] Theresa M Allen and Pieter R Cullis. Liposomal drug delivery systems: from concept to clinical applications. *Advanced drug delivery reviews*, 65(1):36–48, 2013.

[55] Adrienne A Brian and Harden M McConnell. Allogeneic stimulation of cytotoxic t cells by supported planar membranes. *Proceedings of the National Academy of Sciences*, 81(19):6159–6163, 1984.

[56] Gregory J Hardy, Rahul Nayak, and Stefan Zauscher. Model cell membranes: Techniques to form complex biomimetic supported lipid bilayers via vesicle fusion. *Current opinion in colloid & interface science*, 18(5):448–458, 2013.

[57] Ralf P Richter and Alain R Brisson. Following the formation of supported lipid bilayers on mica: a study combining afm, qcm-d, and ellipsometry. *Biophysical journal*, 88(5):3422–3433, 2005.

[58] Ralf P Richter, Rémi Bérat, and Alain R Brisson. Formation of solid-supported lipid bilayers: an integrated view. *Langmuir*, 22(8):3497–3505, 2006.

[59] Bastien Seantier and Bengt Kasemo. Influence of mono-and divalent ions on the formation of supported phospholipid bilayers via vesicle adsorption. *Langmuir*, 25(10):5767–5772, 2009.

[60] Tania Kjellerup Lind, Marite Cardenas, and Hanna Pauliina Wacklin. Formation of supported lipid bilayers by vesicle fusion: effect of deposition temperature. *Langmuir*, 30(25):7259–7263, 2014.

[61] Volker Kiessling, Marta K Domanska, David Murray, Chen Wan, and Lukas K Tamm. Supported lipid bilayers. *Wiley encyclopedia of chemical biology*, pages 1–12, 2007.

[62] Aleksandra P Dabkowska, Maria Valldeperas, Christopher Hirst, Costanza Montis, Gunnar K Pálsson, Meina Wang, Sofi Nöjd, Luigi Gentile, Justas Barauskas, Nina-Juliane Steinke, et al. Non-lamellar lipid assembly at interfaces: controlling layer structure by responsive nanogel particles. *Interface focus*, 7(4):20160150, 2017.

[63] Martyn Rittman, Martina Frischherz, Flame Burgmann, Patrick G Hartley, and Adam Squires. Direct visualisation of lipid bilayer cubic phases using atomic force microscopy. *Soft Matter*, 6(17):4058–4061, 2010.

[64] Martyn Rittman, Heinz Amenitsch, Michael Rappolt, Barbara Sartori, Benjamin MD O'Driscoll, and Adam M Squires. Control and analysis of oriented thin films of lipid inverse bicontinuous cubic phases using grazing incidence small-angle x-ray scattering. *Langmuir*, 29(31):9874–9880, 2013.

[65] Adam M Squires, James E Hallett, Charlotte M Beddoes, Tomas S Plivelic, and Annela M Seddon. Preparation of films of a highly aligned lipid cubic phase. *Langmuir*, 29(6):1726–1731, 2013.

[66] K Larsson. Cubic lipid-water phases: structures and biomembrane aspects. *The Journal of Physical Chemistry*, 93(21):7304–7314, 1989.

[67] Gerd Binnig, Calvin F Quate, and Ch Gerber. Atomic force microscope. *Physical review letters*, 56(9):930, 1986.

[68] Michael Krieg, Gotthold Fläschner, David Alsteens, Benjamin M Gaub, Wouter H Roos, Gijs JL Wuite, Hermann E Gaub, Christoph Gerber, Yves F Dufrêne, and Daniel J Müller. Atomic force microscopy-based mechanobiology. *Nature Reviews Physics*, 1(1):41–57, 2019.

[69] Yves F Dufrêne, Toshio Ando, Ricardo Garcia, David Alsteens, David Martinez-Martin, Andreas Engel, Christoph Gerber, and Daniel J Müller. Imaging modes of atomic force microscopy for application in molecular and cell biology. *Nature nanotechnology*, 12(4):295–307, 2017.

[70] Bharat Bhushan. Introduction to nanotechnology. In *Springer handbook of nanotechnology*, pages 1–19. Springer, 2017.

[71] E Fermi. *Reflection of neutrons on mirrors*, volume 56. Manhattan District, 1946.

[72] Jean Daillant and Alain Gibaud. *X-ray and neutron reflectivity: principles and applications*, volume 770. Springer, 2008.

[73] Rémi Lazzari. Isgisaxs: a program for grazing-incidence small-angle x-ray scattering analysis of supported islands. *Journal of Applied Crystallography*, 35(4):406–421, 2002.

[74] P Müller-Buschbaum. A basic introduction to grazing incidence small-angle x-ray scattering. In *Applications of Synchrotron Light to Scattering and Diffraction in Materials and Life Sciences*, pages 61–89. Springer, 2009.

[75] Terence Cosgrove. *Colloid science: principles, methods and applications*. John Wiley & Sons, 2010.

[76] André Guinier, Gérard Fournet, and Kenneth L Yudowitch. Small-angle scattering of x-rays. 1955.

[77] Harland G Tompkins. *A user's guide to ellipsometry*. Courier Corporation, 2006.

[78] Melissa C Piontek, Rafael B Lira, and Wouter H Roos. Active probing of the mechanical properties of biological and synthetic vesicles. *Biochimica et Biophysica Acta (BBA)-General Subjects*, page 129486, 2019.

[79] Andrea Ridolfi, Lucrezia Caselli, Matteo Baldoni, Costanza Montis, Francesco Mercuri, Debora Berti, Francesco Valle, and Marco Brucale. Stiffness of fluid and gel phase lipid nanovesicles: Weighting the contributions of membrane bending modulus and luminal pressurization. *Langmuir*, 37(41):12027–12037, 2021.

[80] Andrea Ridolfi, Marco Brucale, Costanza Montis, Lucrezia Caselli, Lucia Paolini, Anne Borup, Anders T Boysen, Francesca Loria, Martijn JC van Herwijnen, Marije Kleinjan, et al. Afm-based high-throughput nanomechanical screening of single extracellular vesicles. *Analytical chemistry*, 92(15):10274–10282, 2020.

[81] Roberto Frigerio, Angelo Musicò, Marco Brucale, Andrea Ridolfi, Silvia Galbiati, Riccardo Vago, Greta Bergamaschi, Anna Maria Ferretti, Marcella Chiari, Francesco Valle, et al. Extracellular vesicles analysis in the covid-19 era: Insights on serum inactivation protocols towards downstream isolation and analysis. *Cells*, 10(3):544, 2021.

[82] Barbara Bortot, Maura Apollonio, Enrico Rampazzo, Francesco Valle, Marco Brucale, Andrea Ridolfi, Blendi Ura, Riccardo Addobbati, Giovanni Di Lorenzo, Federico Romano, et al. Malignant-ascites-derived small extracellular vesicles in advanced ovarian cancer patients: insights into the dynamics of the extracellular matrix. *Molecular Oncology*, 2021.

[83] Rodney L Biltonen and Dov Lichtenberg. The use of differential scanning calorimetry as a tool to characterize liposome preparations. *Chemistry and physics of lipids*, 64(1-3):129–142, 1993.

[84] Susan Mabrey and Julian M Sturtevant. Investigation of phase transitions of lipids and lipid mixtures by sensitivity differential scanning calorimetry. *Proceedings of the National Academy of Sciences*, 73(11):3862–3866, 1976.

[85] Lucrezia Caselli, Andrea Ridolfi, Jacopo Cardellini, Lewis Sharpnack, Lucia Paolini, Marco Brucale, Francesco Valle, Costanza Montis, Paolo Bergese, and Debora Berti. A plasmon-based nanoruler to probe the mechanical properties of synthetic and biogenic nanosized lipid vesicles. *Nanoscale Horizons*, 2021.

[86] Sujit Kumar Ghosh and Tarasankar Pal. Interparticle coupling effect on the surface plasmon resonance of gold nanoparticles: from theory to applications. *Chemical reviews*, 107(11):4797–4862, 2007.

[87] Costanza Montis, Lucrezia Caselli, Francesco Valle, Andrea Zendrini, Francesco Carlà, Ralf Schweins, Marco Maccarini, Paolo Bergese, and Debora Berti. Shedding light on membrane-templated clustering of gold nanoparticles. *Journal of colloid and interface science*, 573:204–214, 2020.

[88] Sebastian Salassi, Lucrezia Caselli, Jacopo Cardellini, Enrico Lavagna, Costanza Montis, Debora Berti, and Giulia Rossi. A martini coarse grained model of citrate-capped gold nanoparticles interacting with lipid bilayers. *Journal of Chemical Theory and Computation*, 2021.

[89] Kouta Sugikawa, Tatsuya Kadota, Kazuma Yasuhara, and Atsushi Ikeda. Anisotropic self-assembly of citrate-coated gold nanoparticles on fluidic liposomes. *Angewandte Chemie International Edition*, 55(12):4059–4063, 2016.

[90] Feng Wang, Dennis E Curry, and Juewen Liu. Driving adsorbed gold nanoparticle assembly by merging lipid gel/fluid interfaces. *Langmuir*, 31(49):13271–13274, 2015.

[91] Daniel Lingwood and Kai Simons. Lipid rafts as a membrane-organizing principle. *science*, 327(5961):46–50, 2010.

[92] Erdinc Sezgin, Ilya Levental, Satyajit Mayor, and Christian Eggeling. The mystery of membrane organization: composition, regulation and roles of lipid rafts. *Nature reviews Molecular cell biology*, 18(6):361–374, 2017.

[93] Kai Simons and Elina Ikonen. Functional rafts in cell membranes. *nature*, 387(6633):569–572, 1997.

[94] Jonathan K Sheavly, Joel A Pedersen, and Reid C Van Lehn. Curvature-driven adsorption of cationic nanoparticles to phase boundaries in multicomponent lipid bilayers. *Nanoscale*, 11(6):2767–2778, 2019.

[95] Eric S Melby, Arielle C Mensch, Samuel E Lohse, Dehong Hu, Galya Orr, Catherine J Murphy, Robert J Hamers, and Joel A Pedersen. Formation

of supported lipid bilayers containing phase-segregated domains and their interaction with gold nanoparticles. *Environmental Science: Nano*, 3(1):45–55, 2016.

[96] Andrea Ridolfi, Lucrezia Caselli, Costanza Montis, Gaetano Mangiapia, Debora Berti, Marco Brucale, and Francesco Valle. Gold nanoparticles interacting with synthetic lipid rafts: an afm investigation. *Journal of Microscopy*, 280(3):194–203, 2020.

[97] Peter I Kuzmin, Sergey A Akimov, Yuri A Chizmadzhev, Joshua Zimmerberg, and Fredric S Cohen. Line tension and interaction energies of membrane rafts calculated from lipid splay and tilt. *Biophysical journal*, 88(2):1120–1133, 2005.

[98] W Rawicz, BA Smith, TJ McIntosh, SA Simon, and E Evans. Elasticity, strength, and water permeability of bilayers that contain raft microdomain-forming lipids. *Biophysical journal*, 94(12):4725–4736, 2008.

[99] Khizar H Sheikh and Suzanne P Jarvis. Crystalline hydration structure at the membrane–fluid interface of model lipid rafts indicates a highly reactive boundary region. *Journal of the American Chemical Society*, 133(45):18296–18303, 2011.

[100] Hanna MG Barriga, Margaret N Holme, and Molly M Stevens. Cubosomes: the next generation of smart lipid nanoparticles? *Angewandte Chemie International Edition*, 58(10):2958–2978, 2019.

[101] TG Meikle, CJ Drummond, Frances Separovic, and CE Conn. Membrane-mimetic inverse bicontinuous cubic phase systems for encapsulation of peptides and proteins. In *Advances in Biomembranes and Lipid Self-Assembly*, volume 25, pages 63–94. Elsevier, 2017.

[102] Chandrashekhar V Kulkarni, Wolfgang Wachter, Guillermo Iglesias-Salto, Sandra Engelskirchen, and Silvia Ahualli. Monoolein: a magic lipid? *Physical Chemistry Chemical Physics*, 13(8):3004–3021, 2011.

[103] ST Hyde and Sten Andersson. A cubic structure consisting of a lipid bilayer forming an infinite periodic minimum surface of the gyroid type in the glycerolmonooleat-water system. *Zeitschrift für Kristallographie-Crystalline Materials*, 168(1-4):213–220, 1984.

[104] Andrea Ridolfi, Ben Humphreys, Lucrezia Caselli, Costanza Montis, Tommy Nylander, Debora Berti, Marco Brucale, and Francesco Valle. Nanoscale

structural and mechanical characterization of thin bicontinuous cubic phase lipid films. *Colloids and Surfaces B: Biointerfaces*, 2021.

[105] MM Sychov, LA Lebedev, SV Dyachenko, and LA Nefedova. Mechanical properties of energy-absorbing structures with triply periodic minimal surface topology. *Acta Astronautica*, 150:81–84, 2018.

[106] Diab W Abueidda, Mohamed Elhebeary, Cheng-Shen Andrew Shiang, Siyuan Pang, Rashid K Abu Al-Rub, and Iwona M Jasiuk. Mechanical properties of 3d printed polymeric gyroid cellular structures: Experimental and finite element study. *Materials & Design*, 165:107597, 2019.

[107] Zhao Qin, Gang Seob Jung, Min Jeong Kang, and Markus J Buehler. The mechanics and design of a lightweight three-dimensional graphene assembly. *Science advances*, 3(1):e1601536, 2017.

[108] Yuze Huang, Mir Behrad Khamesee, and Ehsan Toyserkani. A comprehensive analytical model for laser powder-fed additive manufacturing. *Additive Manufacturing*, 12:90–99, 2016.

[109] Gang Bao and Subra Suresh. Cell and molecular mechanics of biological materials. *Nature materials*, 2(11):715–725, 2003.

[110] Amir M Farnoud and Saeed Nazemidashtarjandi. Emerging investigator series: interactions of engineered nanomaterials with the cell plasma membrane; what have we learned from membrane models? *Environmental Science: Nano*, 6(1):13–40, 2019.

[111] Elvin Blanco, Haifa Shen, and Mauro Ferrari. Principles of nanoparticle design for overcoming biological barriers to drug delivery. *Nature biotechnology*, 33(9):941–951, 2015.

[112] Catherine J Murphy, Ariane M Vartanian, Franz M Geiger, Robert J Hamers, Joel Pedersen, Qiang Cui, Christy L Haynes, Erin E Carlson, Rigoberto Hernandez, Rebecca D Klaper, et al. Biological responses to engineered nanomaterials: needs for the next decade. *ACS central science*, 1(3):117–123, 2015.

[113] Kai Loon Chen and Geoffrey D Bothun. Nanoparticles meet cell membranes: probing nonspecific interactions using model membranes, 2014.

[114] Amir Houshang Bahrami. Orientational changes and impaired internalization of ellipsoidal nanoparticles by vesicle membranes. *Soft Matter*, 9(36):8642–8646, 2013.

[115] Sabyasachi Dasgupta, Thorsten Auth, and Gerhard Gompper. Shape and orientation matter for the cellular uptake of nonspherical particles. *Nano letters*, 14(2):687–693, 2014.

[116] Robert Vácha, Francisco J Martinez-Veracoechea, and Daan Frenkel. Receptor-mediated endocytosis of nanoparticles of various shapes. *Nano letters*, 11(12):5391–5395, 2011.

[117] Qingxin Mu, Guibin Jiang, Lingxin Chen, Hongyu Zhou, Denis Fourches, Alexander Tropsha, and Bing Yan. Chemical basis of interactions between engineered nanoparticles and biological systems. *Chemical reviews*, 114(15):7740–7781, 2014.

[118] Renata Negrini and Raffaele Mezzenga. Diffusion, molecular separation, and drug delivery from lipid mesophases with tunable water channels. *Langmuir*, 28(47):16455–16462, 2012.

[119] Lucrezia Caselli, Andrea Ridolfi, Gaetano Mangiapia, Pierfrancesco Maltoni, Jean-François Moulin, Debora Berti, Nina-Juliane Steinke, Emil Gustafsson, Tommy Nylander, and Costanza Montis. Interaction of nanoparticles with lipid films: the role of symmetry and shape anisotropy. *Phys. Chem. Chem. Phys.*, 2021.

[120] R Kampmann, M Haese-Seiller, V Kudryashov, B Nickel, C Daniel, W Fenzl, A Schreyer, E Sackmann, and J Rädler. Horizontal tof-neutron reflectometer refsans at frm-ii munich/germany: first tests and status. *Physica B: Condensed Matter*, 385:1161–1163, 2006.

Appendix

Manuscript n°1

LANGMUIR

pubs.acs.org/Langmuir Article

Stiffness of Fluid and Gel Phase Lipid Nanovesicles: Weighting the Contributions of Membrane Bending Modulus and Luminal Pressurization

Andrea Ridolfi,* Lucrezia Caselli, Matteo Baldoni, Costanza Montis, Francesco Mercuri, Debora Berti, Francesco Valle,* and Marco Brucale*

Cite This: *Langmuir* 2021, 37, 12027−12037 Read Online

ACCESS | Metrics & More | Article Recommendations | Supporting Information

ABSTRACT: The mechanical properties of biogenic membranous compartments are thought to be relevant in numerous biological processes; however, their quantitative measurement remains challenging for most of the already available force spectroscopy (FS)-based techniques. In particular, the debate on the mechanics of lipid nanovesicles and on the interpretation of their mechanical response to an applied force is still open. This is mostly due to the current lack of a unified model being able to describe the mechanical response of both gel and fluid phase lipid vesicles and to disentangle the contributions of membrane rigidity and luminal pressure. In this framework, we herein propose a simple model in which the interplay of membrane rigidity and luminal pressure to the overall vesicle stiffness is described as a series of springs; this approach allows estimating these two contributions for both gel and fluid phase liposomes. Atomic force microscopy-based FS, performed on both vesicles and supported lipid bilayers, is exploited for obtaining all the parameters involved in the model. Moreover, the use of coarse-grained full-scale molecular dynamics simulations allowed for better understanding of the differences in the mechanical responses of gel and fluid phase bilayers and supported the experimental findings. The results suggest that the pressure contribution is similar among all the probed vesicle types; however, it plays a dominant role in the mechanical response of lipid nanovesicles presenting a fluid phase membrane, while its contribution becomes comparable to the one of membrane rigidity in nanovesicles with a gel phase lipid membrane. The results presented herein offer a simple way to quantify two of the most important parameters in vesicle nanomechanics (membrane rigidity and internal pressurization), and as such represent a first step toward a currently unavailable, unified model for the mechanical response of gel and fluid phase lipid nanovesicles.

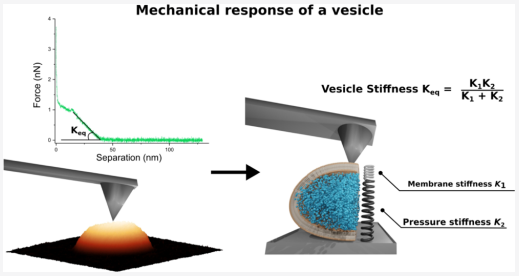

INTRODUCTION

Lipid membranes are fundamental components of most biological systems, delimiting the inner and outer compartments of cells, organelles, and viruses, hosting a significant portion of an organism's interactome and constituting a critical component of extracellular vesicles (EVs).[1] Several key biological processes were revealed to be affected by the mechanical characteristics of involved membranous compartments, including, for example, exo-/endocytosis, trafficking, and in some cases pathological onset.[2−5] Given this central role, the scientific community has devoted extended efforts for better understanding the mechanics of synthetic nanovesicles and their membranes, which represent widely used mimics for the study of biogenic membrane-bound organelles.

To this end, force spectroscopy (FS) techniques such as micropipette aspiration,[6] electrodeformation,[7] optical tweezers,[8] and atomic force microscopy (AFM)[9,10] are often employed, as they allow probing the mechanical properties at the nanoscale with high accuracy.[11] However, since it is difficult to identify and disentangle the contributions of all the parameters involved at this length scale, studying the mechanics of nanosized objects is still challenging for most of the above-mentioned techniques. In particular, the accurate determination of the nanomechanical characteristics of natural and synthetic lipid vesicles with sizes <500 nm remains a largely open issue, hindering multiple research fields.

AFM-based FS (AFM-FS) has been recently applied for studying the mechanics of both natural and synthetic lipid vesicles.[12−16] The main advantage offered by AFM-FS is the possibility to simultaneously determine the exact morphology

Received: June 22, 2021
Revised: September 13, 2021
Published: October 6, 2021

https://doi.org/10.1021/acs.langmuir.1c01660
Langmuir 2021, 37, 12027−12037

Table 1. Bending Modulus Values Reported in Literature for Fluid and Gel Phase Lipid Bilayers, Calculated Using Different Techniques

references	lipid	technique	temperature (°C)	κ ($\times 10^{19}$J)	κ (k_BT)
Liu and Nagle, 2004[53]	DOPC	scattering experiments	30	0.8	19.1
Levine, et al., 2014[54]	DOPC	atomistic simulations	25	1.1	27.7
Et-Thakafy, et al., 2017[14]	DOPC	AFM-FS on vesicles	25	0.9	21.9
Et-Thakafy, et al., 2017[14]	DOPC	AFM-FS on SLBs	25	0.9	21.4
Picas, et al., 2012[55]	DOPC	AFM-FS on SLBs	25	0.7	18.0
present study	DOPC	AFM-FS on vesicles	28	0.8	17.7
present study	DOPC	AFM-FS on SLBs	28	0.7	17.5
Dimova, 2014[56]	POPC	X-ray scattering	30	0.9	20.3
Nagle, 2017[57]	POPC	X-ray scattering	30	1.1	25.7
Henriksen, et al., 2006[58]	POPC	micropipette aspiration	25	1.6	38.5
present study	POPC	AFM-FS on vesicles	28	1.6	40.5
present study	POPC	AFM-FS on SLBs	28	2.0	49.2
Et-Thakafy, et al., 2017[14]	DPPC	AFM-FS on SLBs	25	2.0	49.3
Yi, et al., 2009[59]	DPPC	neutron spin echo	30	2.1	49.6
Picas, et al., 2012[55]	DPPC	AFM-FS on SLBs	25	2.3	56.6
Et-Thakafy, et al., 2017[14]	DPPC	AFM-FS on vesicles	25	15.5	376.7
Delorme and Fery, 2006[60]	DPPC	AFM-FS on vesicles	25	13.5	330.0
present study	DPPC	AFM-FS on vesicles	28	4.7	113.4
present study	DPPC	AFM-FS on SLBs	28	10.0	240.1
Yi, et al., 2009[59]	DSPC	neutron spin echo	40	3.4	79.1
Daillant, et al., 2005[52]	DSPC	X-ray scattering	∼50	11.2	275.0
present study	DSPC	AFM-FS on vesicles	28	5.2	125.9
present study	DSPC	AFM-FS on SLBs	28	14.0	335.8

and mechanical properties of individual vesicles. In a typical AFM-FS experiment, the forces experienced by the tip during the indentation of a vesicle are recorded as a function of the tip−sample separation distance; these data are then plotted as force versus distance curves. Based on the Canham−Helfrich theory (CHT),[17,18] Vorselen et al. theorized that the initial mechanical response of a lipid vesicle to indentation is elastic and follows a linear correlation between the applied perpendicular force and the penetration depth.[19] The resulting mechanical response can be broadly described in terms of Hooke's law, $F = -Kx$, where K, the stiffness (K) of the vesicle, can be estimated from the slope of the observed linear regime. Stiffness is an extensive property resulting from multiple contributions, the most important being the intrinsic membrane elasticity and the luminal pressure (the internal pressure that originates from the fluid confined within a vesicle).

In order to quantify a vesicle's membrane intrinsic elasticity, its contribution to the experimentally accessible quantity K has to be disentangled from the others. Among the various biophysical descriptors, the bilayer bending modulus (κ) is a widely used parameter in membrane biophysics to quantify the energy required to deform a membrane from its spontaneous curvature;[20] moreover, its evaluation is of fundamental importance for understanding the effect of the membrane bending rigidity in biological processes such as vesicle fusion and budding.

Several theories and models have been proposed in the AFM-FS literature to derive κ from the measured K values, obtaining different degrees of agreement with the results from other techniques (examples can be found in Table 1). The description is further complicated by the dual nature that lipid membranes display above and below their melting temperature (T_m); at $T > T_m$, lipid bilayers are generally found in the so-called fluid phase, in which their acyl chains present an increased lateral mobility compared to the case of $T < T_m$, where membranes display the so-called gel phase, characterized by a limited lateral mobility and a tighter packing degree between the acyl chains of the two leaflets. One of the most straightforward theories used to describe the mechanics of adsorbed lipid vesicles is the thin shell theory (TST),[21] which models the lipid vesicle as being solely constituted by a homogeneous shell of thickness h and curvature radius R, provided that the ratio h/R is sufficiently small.[22] Following this approach, TST does not account for the luminal pressurization, hence ascribing all the energetic contributions of vesicle indentation to the membrane elasticity. Moreover, by describing the membrane as a single homogeneous shell, simple TST models ignore the fact that in fluid phase bilayers, the two leaflets are free to slide upon each other. Reissner[23] generalized the TST and proposed an analytical solution for the case of shallow segments of thin elastic spherical shells, which takes into consideration the presence of transverse shear deformations.[22]

More recently, both experimental and theoretical studies[19,25,26] found that the pressure contribution to the indentation response of nanosized fluid phase liposomes accounts for a great part of the overall deformation energy. Based on these findings, they developed a CHT-based model that allows calculating both the bending modulus and the luminal pressure of nanosized fluid phase lipid vesicles from their stiffness K and tether force (i.e., the force at which a lipid tube of uniform diameter is elongated away from the vesicle by the AFM tip). This model has been employed for studying the mechanical properties of EVs,[27] revealing that specific pathological conditions can induce a change in their membrane rigidity.[4]

In this context, it is immediately apparent that the two above-presented models differ irreconcilably in their treatment of the lipid bilayer, which is modeled either as a single

https://doi.org/10.1021/acs.langmuir.1c01660
Langmuir 2021, 37, 12027−12037

homogeneous shell in one case (TST) or as a pair of independently sliding monolayers in the other. These different scenarios seem at first glance most suited to describe vesicles constituted by lipids in their gel and fluid phases, respectively, thus suggesting that the applicability of the two models might be dictated by the state of the lipid membrane under investigation.

An orthogonal experimental strategy to determine via AFM-FS the κ values of membranes is to drastically simplify the problem and deposit them on a rigid substrate, obtaining supported lipid bilayers (SLBs),[28−30] whose indentation mechanics is considerably simpler to model with respect to intact vesicles. This is mainly due to the fact that the mechanical response of SLBs is not affected by internal pressure-related phenomena, hence making it possible to univocally relate the SLB indentation forces to the rigidity of the bilayer. To this purpose, various contact mechanics models have been developed to extract κ from AFM-FS experiments on SLBs.[9] Despite the extensive number of reports both on SLBs and vesicles, there is still disagreement between the κ values measured on the same membranes in the two experimental configurations. This issue further complicates the interpretation of experimental data and ultimately hinders a complete understanding of several membrane-related processes in terms of stiffness.

In an attempt to reconcile the different interpretations outlined above, we propose a simple model where the contributions of membrane rigidity and luminal pressure to the overall stiffness of a nanosized vesicle are described as a series of springs. This approach permits us to quantitatively estimate the individual contributions to the stiffness of fluid or gel phase nanosized vesicles by using a single model. We test this approach on a library of synthetic liposomes, composed of phospholipids having the same polar head group [phosphatidylcholine (PC)] but different acyl chains. This allows exploring different lipid lateral interaction energies, spanning the bilayer phase space between fluid and gel phases. All the bilayers are probed by AFM-FS both as SLBs and vesicles, allowing us to quantitatively distinguish the contributions of the membrane bending modulus and luminal pressure to the overall stiffness of the liposomes. Particle-based simulations performed on realistic models of lipid bilayers mimicking the experimental setup are then employed to support the AFM-FS results and provide new insights into the origin of the observed different mechanical responses.

EXPERIMENTAL SECTION

Vesicle Preparation. Different lipids with a PC polar headgroup [DOPC (1,2-dioleoyl-*sn*-glycero-3-phosphocholine) (>99%), POPC (1-palmitoyl-2-oleoyl-*glycero*-3-phosphocholine) (≥98.0%), DPPC (1,2-dipalmitoyl-*sn*-glycero-3-phosphocholine) (>99%), and DSPC (1,2-1,2-distearoyl-*sn*-glycero-3-phosphocholine) (>99%)] were purchased from Sigma-Aldrich (St. Louis, MO, USA). All chemicals were used as received. Lipid dry powders were dispersed in defined amounts of chloroform to prepare stock solutions. Lipid films were obtained by evaporating appropriate amounts of lipid stock solutions in chloroform under a stream of nitrogen, followed by overnight drying under vacuum. The films were swollen by a suspension in warm (50 °C) water (Milli-Q grade water was used in all preparations) to a final lipid concentration of 4 mg/mL, followed by vigorous vortex mixing. The resultant multilamellar liposomes in water were subjected to 10 freeze−thaw cycles and extruded 10 times through two stacked polycarbonate membranes with 100 nm pore size at room temperature, to obtain unilamellar liposomes with a narrow and reproducible size distribution. The filtration was performed with the Extruder [Lipex Biomembranes, Vancouver (Canada)] through Nuclepore membranes (please refer to Caselli et al.[31] for further details about the vesicle preparation and characterization).

Surface Cleaning Procedure. All reagents were purchased from Sigma-Aldrich Inc. (www.sigmaaldrich.com). Liposomes and SLBs were evaluated on microscopy borosilicate glass coverslips (Menzel Gläser) and on SiO_2 wafers, respectively. The substrates were first immersed in a 3:1 mixture of 96% H_2SO_4 and 30% v/v aqueous H_2O_2 ("oxidizing piranha") solution for 2 h in order to remove any organic residue present on their surface. Their surfaces were then cleaned in a sonicator bath (Elmasonic Elma S30H) for 30 min in acetone followed by 30 min in isopropanol and 30 min in ultrapure water (Millipore Simplicity UV). After this procedure, the substrates can be stored in ultrapure water, preserving their pristine conditions for weeks.

Surface Preparation for AFM-FS on Intact Vesicles. Cleaned glass coverslips were treated with air plasma for 15 min (air plasma cleaner, PELCO easiGlow) and incubated overnight in ultrapure water in order to maximize the silanol surface density. Slides were then functionalized by vapor-phase silanization with (3-aminopropyl)-triethoxysilane (APTES). Small batches of three to five slides were put in a desiccator with 30 μL of APTES and 10 μL of triethylamine (TEA), then a gentle static vacuum was induced by briefly engaging a rotary pump. Glass slides were then kept under these conditions for 8 h. TEA was used to promote APTES−silanol binding.[32] After that, functionalized glass coverslips can be stored in sealed Petri dishes, preserving the same surface properties for several weeks (please see the Supporting Information for surface characterization).

Surface Preparation for AFM-FS on SLBs. Cleaned silicon wafers were treated with air plasma for 15 min (air plasma cleaner, PELCO easiGlow), incubated in ultrapure water for 10 min in order to maximize the number of reactive surface silanols, and then dried with nitrogen.

SLB Formation via Vesicle Fusion. A 100 μL droplet of 200 mM $CaCl_2$ diluted 1:10 in 100 mM NaCl was spotted on a SiO_2 slide. A 10 μL droplet of the chosen vesicular dispersion was then added to the previous droplet and left incubating at room temperature for 30 min in order to promote vesicle adsorption on the surface. After that, the droplet was replaced (keeping the sample under constant hydration) by a 100 μL droplet of ultrapure water, which was then left incubating for additional 15 min. After the system equilibrated, the large droplet was gently removed, and the slide was placed in the AFM fluid cell for the measurements. This procedure is reported to promote the formation of continuous and homogeneous SLBs.[33]

AFM Setup. All AFM experiments were performed on a Bruker MultiMode 8 (equipped with NanoScope V controller electronics, a sealed fluid cell, and a type JV piezoelectric scanner) using Bruker SNL-A probes (with a triangular cantilever; nominal tip curvature radius, 2−12 nm; and nominal elastic constant, 0.35 N/m) calibrated with the thermal noise method.[34] The temperature within the fluid cell was 28 °C.

AFM Imaging. Imaging was performed in the PeakForce mode. In order to minimize vesicle deformation or rupture upon interaction with the probe, the applied force setpoint was kept in the 150−250 pN range. The lateral probe velocity was not allowed to exceed 5 μm/s. Feedback gain was set at higher values than those usually employed for optimal image quality in order to ensure minimal probe-induced vesicle deformation upon lateral contact along the fast scan axis (a comprehensive explanation of this procedure was given elsewhere[35]). The average height value of all bare substrate zones was taken as the baseline zero height reference. Image background subtraction was performed using Gwyddion 2.53.16.[36]

AFM-FS on Vesicles. In order to perform the mechanical characterization of vesicles via AFM-FS, the samples were first scanned to locate individual vesicles. The chosen vesicle was then imaged at a higher resolution (~500 × 500 nm scan, 512 × 512 points); its height profile along the slow scan axis was fitted with a circular arc taking into account values only 10 nm above the bare substrate (typical fit, $R^2 \geq 0.95$). This procedure yielded, for each

https://doi.org/10.1021/acs.langmuir.1c01660
Langmuir 2021, 37, 12027−12037

vesicle, an apparent fitted curvature radius R_C and a vesicle height value H, which were corrected as described elsewhere.[19] To avoid intrinsic piezo inaccuracy and drift, which imply a certain degree of uncertainty on both the XY position at which the force curve was constructed relative to the original image and on the maximum applied force, multiple force curves were constructed. In particular, we recorded a series of force/distance curves at multiple XY positions (typically around 64−100 curves arranged in a square array covering the vesicle initial location) for each individual vesicle. All force/distance curves were recorded at a frequency of one full approach/retraction cycle per second and a ramp size of 200−250 nm. In most cases, only a few curves showed the full mechanical fingerprint of an intact vesicle on both the approach and retraction cycles, showing a linear deformation upon applying pressure and a tether elongation plateau upon probe retraction. Of these, we first discarded those with probe-vesicle contact points occurring at probe−surface distances below the vesicle height, as measured by imaging. We then discarded traces in which the tether elongation plateau occurring during probe retraction did not extend beyond the initial contact point (further details can be found in ref 35). The remaining traces were used to calculate the vesicle stiffness (K). Multiple valid curves referring to the same vesicle resulted in very narrow distributions of K (with the average measured values taken as representative for each vesicle), while different vesicles of the same type showed much larger variations.

AFM-FS on SLBs. When performing AFM-FS on SLBs, the accuracy of the XY position at which each force curve is performed becomes less important in comparison to vesicles. We nevertheless recorded a series of force/distance curves at multiple XY positions (typically around 64−100 curves arranged in a square array covering large regions of the SLB) in order to minimize the impact of (putative) local anisotropies of either the substrate or the bilayer on the measured mechanical properties. All force/distance curves were recorded at a frequency of one full approach/retraction cycle per second and a ramp size of 200−250 nm. The recorded curves were then analyzed to extract the bending modulus (κ) values.

Particle-Based Molecular Dynamics Simulations. Particle-based molecular dynamics (MD) simulations were performed on realistic models of SLBs using the Martini coarse-grained potential.[37−39] Simulations were performed with the LAMMPS program package[40] and run on the CNR-ISMN high-performance computing facility.

The model system was composed of a 2D periodic support surface, a finite-size model of SLBs in water solution, and a model of a mechanical probe. Models of DPPC and DOPC lipid bilayers in water solution were considered. Upon equilibration onto the substrate in water, lipid bilayer models relax into a round-like shape, with a diameter of about 24 nm. A model of a mechanical probe mimicking the AFM tip was built as a disc of SG4 beads, similar to the support surface. A radius of the AFM tip model of 9 nm was considered. The mechanical properties of SLB were simulated by reproducing the displacement of the AFM tip toward the surface, which was kept fixed in simulations. A first trajectory was obtained by displacing the AFM tip toward the SLB at a constant velocity of 0.1 nm/ns. This first fast trajectory allowed us to obtain starting configurations for subsequent accurate sampling of force versus distance curves. Further details are provided in the Supporting Information section.

RESULTS AND DISCUSSION

We employed AFM-FS to measure the mechanical response of a series of lipid bilayers in their planar (SLB) and vesicular configurations. All the FS experiments were performed under the same experimental conditions (deposition protocol, solution, temperature, and substrate; see the Experimental Section). All the probed lipids have the same polar head group (PC) but differ in the length and degree of unsaturation of their hydrocarbon chains. As a general rule, short and unsaturated hydrocarbon tails generate softer lipid bilayers, while long fully saturated tails have a higher packing degree, which increases the overall bilayer rigidity. It is known from the literature that the bending modulus of lipid bilayers used in this study increases in the following order: DOPC < POPC < DPPC < DSPC[31,41,42] (with DOPC and POPC being in their fluid phase and DPPC and DSPC in their gel phase under the experimental conditions employed herein). All the four lipids were used to form liposomes and SLBs and then measured via AFM-FS.

Measurement of Vesicle Stiffness. We first measured the stiffness of several different vesicles composed of each of the lipids in the above-mentioned set (details can be found in previous works[31,35]). Despite stiffness being an extensive property, the very similar average size and narrow polydispersity of the measured liposomes resulted in a relatively small variance within each sample (as it can be seen from the small overlap between the error bars in Figure 1 and from their numerical values in the second column of Table 3). The liposomes follow the expected stiffness ranking, with DOPC liposomes being the softest and DSPC liposomes the stiffest, and the stiffness values are in close agreement with those reported in the literature for similar-sized vesicles.[19,43]

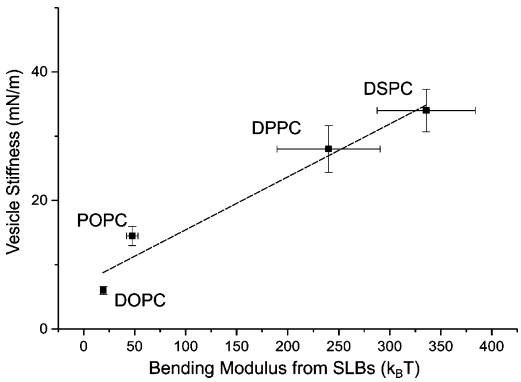

Figure 1. Linear correlation between the average vesicle stiffness K and the average SLB bending modulus κ_{SLB}. Error bars for vesicle stiffness describe the standard deviation of the mean, while the ones for κ_{SLB} of SLBs represent the uncertainties obtained by bootstrapping (1000 repetitions of 5 draws, with replacement).

Measurement of SLB Bending Modulus. We then performed AFM-FS measurements on SLBs obtained from the rupture of the same set of liposomes. The mechanical response of SLBs to indentation is much simpler to model with respect to that of vesicles; indeed, their bidimensional geometry and the absence of internal pressure contributions allow one to unambiguously probe the membrane rigidity in itself. Once the bilayer adsorbs on the substrate, it can be effectively modeled as a layer of a continuous material and hence the AFM tip can be used to apply a perpendicular force to the SLB, resulting in its compression. Fitting an appropriate contact mechanics model to the recorded indentation traces allows extracting quantitative nanomechanical information about the SLB. Among the numerous contact mechanics models developed to describe the indentation of a flat material by probes of various shapes and sizes,[9] we found that the modified Hertz model[44] proposed by Dimitriadis et al.[45] is the one that best

https://doi.org/10.1021/acs.langmuir.1c01660
Langmuir 2021, 37, 12027−12037

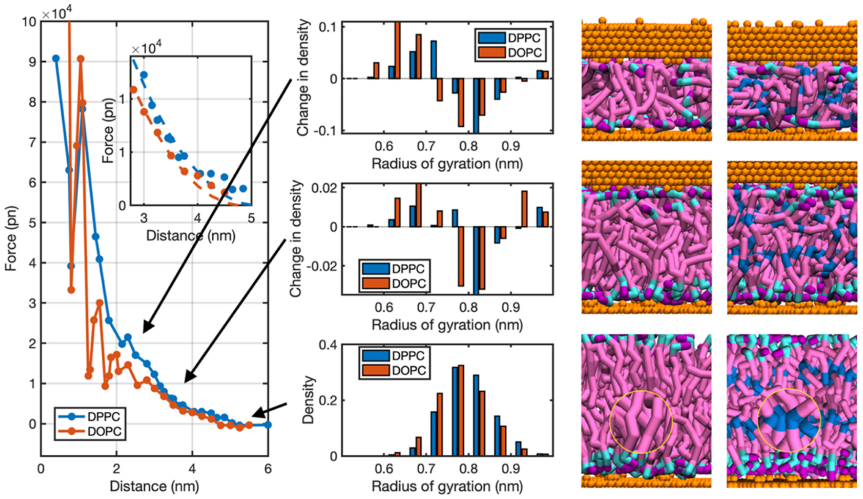

Figure 2. Simulated force/distance curves for DOPC (orange curve) and DPPC (blue curve) SLBs; dashed lines, in the inset, are the modified Hertz fits, also used for fitting the AFM-FS curves on SLBs. Distribution of the radius of gyration for configurations extracted from the points indicated by the arrow and the corresponding snapshots extracted from MD simulations. The blue segments indicate the coarse-grained beads (Martini C3 particle), describing the double-bond moiety in the structure of DOPC.

fits all our SLB indentation profiles (Figure S1). According to this model, the Young modulus of the probed bilayer can be calculated from eq 1

$$F = \frac{16}{9} E R_{tip}^{1/2} \delta^{3/2} [1 + 0.884\chi + 0.781\chi^2 + 0.386\chi^3 + 0.0048\chi^4] \quad (1)$$

where the force F is related to the Young modulus E, tip radius R_{tip}, and indentation depths δ and χ, which is equal to $\sqrt{R\delta/h}$, with h being the thickness of the bilayer (evaluated by AFM imaging experiments on different SLBs and in good agreement with the literature,[14,46−51] please refer to Figure S3 for further details). According to Saavedra et al.,[64] probing SLBs with tips having radii of ∼2 nm leads to the penetration of the lipid membrane with minimal compression and an absence of any clear mechanical event associated to membrane rupture in the force/distance traces; under these conditions, the estimation of E is not possible. However, all of our SLB indentation curves contained a clear compression region before a sharp force drop corresponding to the mechanical failure of the bilayer, suggesting that R_{tip} was always above 2 nm in our experiments. To estimate the value of R_{tip}, a subset of SLB indentation curves for each lipid was fitted, leaving the tip radius as a free parameter; this always yielded R_{tip} values in the 7−8 nm range, which would therefore allow for a correct estimation of E. TST provides a relation between the Young modulus E and the bending modulus κ; such an expression can be used to obtain the SLB bending modulus κ_{SLB} and is described in eq 2, where ν is the Poisson modulus (assumed to be 0.5[12,14] for all the following calculations).

$$\kappa = \frac{Eh^3}{12(1-\nu)} \quad (2)$$

The values obtained for the bending moduli of the whole SLB series are (17.5 ± 2.8) k_BT for DOPC, (49.2 ± 5.2) k_BT for POPC, (240.1 ± 50.4) k_BT for DPPC, and (335.8 ± 48.1) k_BT for DSPC; remarkably, they follow the same trend observed for the stiffness of the respective liposomes and are in good agreement with the vast majority of literature results, in that fluid phase bilayers typically show bending moduli around 1 order of magnitude lower than those of gel phase bilayers.[52] Table 1 reports a comparison of our results with several bending modulus values reported in the literature both for fluid and gel phase bilayers.

Vesicle Stiffness and SLB Bending Modulus Are Linearly Correlated. While the κ_{SLB} values obtained as described above are intensive (i.e., size-independent) mechanical properties, specific for each bilayer type, and the stiffness values K, measured on their vesicular configuration, are extensive properties and might be influenced by the size and/or geometry artifacts. Nevertheless, it is possible to obtain a strong indication of K being representative of the vesicles' mechanical response by plotting it against κ_{SLB} for the whole series of lipids (see Figure 1). The resulting linear correlation between mechanical descriptors, obtained from two series of independent measurements, performed with the same setup, on the same lipid bilayers, in either planar or vesicular geometry, can be considered as indicative of two facts: first, the average stiffness K is indeed a good descriptor of mechanical differences occurring across the panel of lipids, as hypothesized previously (see the section, "Measurement of Vesicle Stiffness"). Second,—despite K being a complex parameter emerging from the interplay of several concurring phenomena including vesicle geometry, bilayer bending modulus, and its resistance to pressurization—all of its determinants appear to be effectively recapitulated in just one parameter, κ.

This observation can be rationalized as follows: K values were measured on vesicles having similar sizes, same polar head group, and in the absence of an osmotic imbalance; under these conditions, any systematic difference between the mechanical responses exhibited by vesicles of different

https://doi.org/10.1021/acs.langmuir.1c01660
Langmuir 2021, 37, 12027−12037

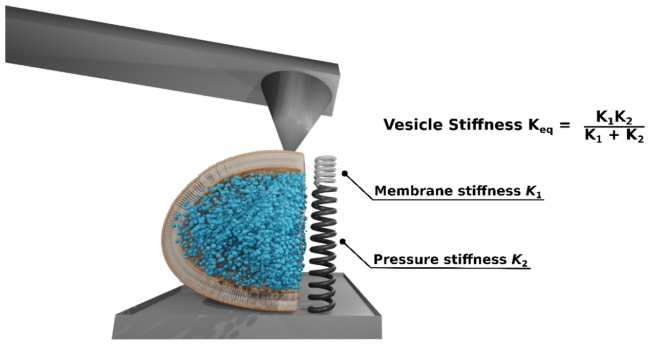

Figure 3. Spring-based model developed to describe the mechanical response of a vesicle to indentation. The stiffness of a vesicle accounts for the contributions of both membrane rigidity (mostly κ) and internal pressurization and can be described by a system of two springs in series. As a consequence, AFM-FS indentation experiments sample the overall spring constant of the whole system, which is lower than both the single spring constants K_1 and K_2.

compositions will necessarily arise from the different degrees of interaction exhibited by their constituent lipids. Different interlipidic interaction energies will ultimately determine both κ and the various phenomena contributing to K, thus resulting in the observed direct proportionality between κ_{SLB} and K. Moreover, the linear relation displayed in Figure 1 is in good agreement with Dai et al.,[61] who theorized a linear relation between the stiffness and the bending modulus of lipid nanovesicles.

MD Simulations. Coarse-grained simulations were performed on model systems of SLBs, with the aim of reproducing their response to the indentation by the AFM tip. A representative snapshot of a configuration extracted from MD simulations for the evaluation of the mechanical properties of SLBs is shown in Figure S2 (refer also to Figure S4 for further details). The two considered lipids, DOPC and DPPC, are representative of the fluid and gel states of SLBs, respectively.

The simulated force/distance curves are qualitatively very similar to the ones obtained from the AFM-FS measurements on SLBs. Moreover, the modified Hertz fit applied to the experimental force/distance curves can still be used for describing the simulated ones with remarkable accuracy (see Figure 2). The offset in the absolute value of computed forces with respect to the experiments is related to the details of the simulations (the size and shape of the simulated mechanical probe, etc.). Namely, the flat shape of the probe used in MD simulations (see Figure S2 in the Supporting Information) partially accounts for the larger overall computed force with respect to values measured for DPPC and DOPC SLBs in AFM-FS experiments.[54,62−64] This effect can be related to the higher contact area of the probe used in simulations with respect to a curved tip shape. However, the shape of the probe used to simulate force spectra allowed us to sample the dynamics of a large portion of the SLB.

In agreement with the experimental results, the DPPC SLB displays a stiffer mechanical response with respect to the DOPC SLB. At small indentations (tip−surface distances between 6 and 3 nm), the SLBs undergo an essentially elastic deformation which only entails minimal perturbations to the equilibrium configuration for both DOPC and DPPC (see Figure 2); differences in the response of the two simulated SLBs can be mainly ascribed to the different cohesive energies (hydrophobic interactions) of the bilayers. At larger indentations (tip−surface distances of ∼2.5 nm), a qualitative difference emerges for the two considered lipid species. The stiffness of the DPPC SLB still exceeds the one of the DOPC SLB, as expected; however, starting from a tip−surface distance of about 2.5 nm, the DOPC SLB undergoes a more evident structural rearrangement with respect to DPPC (see Figure 2, rightmost panels). This behavior can be related to the presence of saturated chains in the fatty acid moieties of DPPC, in contrast with the unsaturated chains of DOPC. These structural features are reproduced by the potential parameters used in simulations and lead to the observed differences in the mechanical properties of the two considered species. The occurrence of C−C double bonds in the unsaturated fatty acid chains of DOPC provides these molecules with a higher propensity to deform under a mechanical stress, with respect to those of DPPC (see Figure 2). The magnitude of this local distortion can also be visualized when computing the average radius of gyration for the individual lipid molecules constituting the bilayer. In this context, the radius of gyration provides a measure of the linearity of the molecular structure. As shown in Figure 2, the radius of gyration of DOPC molecules exhibits a significant drop in tip−surface distances below 2.5 nm, signaling molecular deformations toward a coil-like structure. These deformations affect the structure of the whole bilayer and the resulting mechanical response, as evidenced by the kinks in the computed force−displacement curves for DOPC in the range between 1 and 2 nm. Based on these results, differences in the mechanical behavior of the two considered SLBs, representative of gel and fluid phase bilayers, can be related to the interplay between intermolecular cohesion energy and intramolecular deformation. It is also worth noting that, at very large stress values, irreversible (plastic) structural deformations, falling beyond the range of elastic deformations considered by the employed model, occur. On a qualitative level, results from these simulations confirm that the different cohesion energies of fluid and gel phase lipids and the molecular structure can explain their different mechanical behaviour, as observed by AFM-FS.

A Mechanical Model for Both Fluid and Gel Phase Vesicles. The two most widely employed models for vesicles' mechanics are limited to the study of either fluid or gel phase bilayers. However, in the previous paragraphs, we have shown

https://doi.org/10.1021/acs.langmuir.1c01660
Langmuir 2021, 37, 12027−12037

that the experimentally determined vesicle stiffness K is directly proportional to the SLB bending modulus κ_{SLB}, irrespective of the phase state of the constituent bilayers, thus suggesting that their mechanical behavior can be interpreted within a unified theoretical framework.

In order to gain more insights into the relationship between the mechanical responses of a lipid bilayer in its vesicular and SLB forms, we developed a simple model that allows separating the contributions of membrane elasticity and luminal pressure from the mechanical response of a fluid or gel phase lipid vesicle subjected to an applied perpendicular force. As schematized in Figure 3, we model an adsorbed lipid vesicle as a system of two springs in series, with spring constants K_1 and K_2. The spring constant K_1 accounts for the mechanical response of the membrane, while K_2 accounts for those phenomena arising as a consequence of the volume/surface variations induced by the indentation process (the most relevant being internal pressurization).

More specifically, the slope observed in the linear part of the AFM force/distance curves (Figure S5) represents the equivalent spring constant of the system, K_{eq}, which is related to K_1 and K_2 by eq 3.

$$K_{eq} = \frac{K_1 K_2}{K_1 + K_2} \tag{3}$$

The relation expressed by eq 3 implies that the value of K_{eq} is lower than the values of both K_1 and K_2.

TST Underestimates the Mechanical Response of Gel Phase Lipid Vesicles. As detailed above, TST models a vesicle as a hollow homogeneous shell with no internal pressure.[65] Reissner[24] derived a TST-based analytical solution (eq 4) for describing the relation between force and shell indentation[66]

$$F = \left(\frac{4Eh^2}{R^2 \sqrt{3(1-\nu^2)}} \right) \delta \tag{4}$$

where E is the Young modulus, h the bilayer thickness, δ the penetration depth, R the shell (vesicle) radius of curvature, and ν the Poisson modulus. Equation 4 is analogous to Hooke's law, where the term within the parentheses represents, for small penetration depths, the stiffness of the vesicle. Once K is known, E and κ can be determined, applying eqs 4 and 2. Equation 4 is designed for hollow shells; hence it assumes that the stiffness (the proportionality constant between F and δ) is only ascribed to the vesicle membrane.

According to the just-defined spring-based model, if we use the stiffness obtained from the AFM measurements, K_{eq} (a combination of K_1 and K_2) to estimate the Young modulus from eq 4, we could obtain unexpected results. Notably, since K_{eq} is lower than K_1, the mechanical contribution of the membrane and hence the values of E and κ_V (the bending modulus calculated with the vesicular configuration) are necessarily underestimated. Table 2 shows the bending moduli obtained by substituting K_{eq} into the Reissner equation for the panel of investigated liposomes and compares them with the values of the bending modulus obtained for the SLBs; the errors represent the uncertainties obtained by bootstrapping (1000 repetitions of 5 draws, with replacement).

As hypothesized, the κ_V values obtained via TST from vesicle indentation are lower than the ones obtained via the modified Hertz model from the corresponding SLBs (κ_{SLB}).

Table 2. Comparison between the Bending Modulus Values Obtained for Vesicles and SLBs

	κ_V from TST (k_BT)	κ_{SLB} from modified Hertz model (k_BT)
DOPC	17.7 ± 1.7	17.5 ± 2.8
POPC	40.5 ± 5.5	49.2 ± 5.6
DPPC	113.4 ± 20.2	240.1 ± 50.5
DSPC	125.9 ± 15.4	335.8 ± 48.1

Interestingly, the higher the vesicle stiffness, the higher the difference between κ_V and κ_{SLB}. These results support the predictions of this spring-based model; indeed, when probing very soft liposomes, such as DOPC, $K_{eq} \sim K_1$, and the Reissner formula yields results that are in good accord with the values measured on SLBs. However, as the K_1 of the probed liposomes increases and becomes proportional to K_2, the approximation is not valid anymore; K_{eq} will be lower than the other two spring constants, yielding values of κ_V lower than the respective κ_{SLB}.

Estimating the Membrane-Associated Spring Constant. Since the SLB indentation can be modeled as a 2D process, the complexity related to the 3D geometry of vesicles can be circumvented, and the contributions from the vesicle internal pressure neglected. Moreover, since the literature on SLB mechanics is well established, and there are very few uncertainties regarding data interpretation, we herein assume that the κ_{SLB} values are the ones that most closely represent the intrinsic bending rigidity of the membranes. Leveraging this assumption, if we now replace the κ_{SLB} values back in eq 2, we obtain the respective Young moduli E that can be then substituted in eq 4, in order to extract the correct values for the spring constant associated with the vesicle membrane (corresponding to the expression within parentheses in eq 4), K_1. Table 3 displays the K_1 values that we obtained for the probed vesicles and compares them with the respective K_{eq} values, calculated directly from the AFM force/distance curves.

Table 3. Spring Constant Values that Describe the Mechanical Response of a Lipid Vesicle to Indentation

	K_1 derived from SLB assumption (mN/m)	K_{eq} from the AFM curves (mN/m)	K_2 obtained by substituting K_1 and K_{eq} in (3) (mN/m)
DOPC	6.9 ± 0.3	6.0 ± 0.6	~47.3
POPC	22.7 ± 2.9	14.5 ± 1.5	~40.0
DPPC	74.4 ± 7.2	28.0 ± 3.6	~44.9
DSPC	97.4 ± 8.4	34.0 ± 3.3	~52.2

The results in Table 3 strongly support the predictions derived from the spring-based model; indeed, for very soft fluid phase vesicles (such as DOPC), we can assume that $K_1 \ll K_2$, hence obtaining $K_{eq} \sim K_1$, which means that the stiffness measured from the AFM force/distance curves (K_{eq}) is close to the actual value of the membrane stiffness (K_1). When dealing with stiffer membranes, as in the case of gel phase bilayers (DPPC and DSPC), K_1 increases and becomes comparable with K_2; in this new configuration, both the springs of the model deform (although to different extents) under application of a force. In this second scenario, the stiffness calculated from the AFM force/distance curves (K_{eq}) results from the combination of both springs (hence from the contributions of both the membrane and luminal pressure). Using the newly obtained values of K_1, we can exploit eq 3 to derive the values of K_2 for each different liposome. These

https://doi.org/10.1021/acs.langmuir.1c01660
Langmuir 2021, 37, 12027−12037

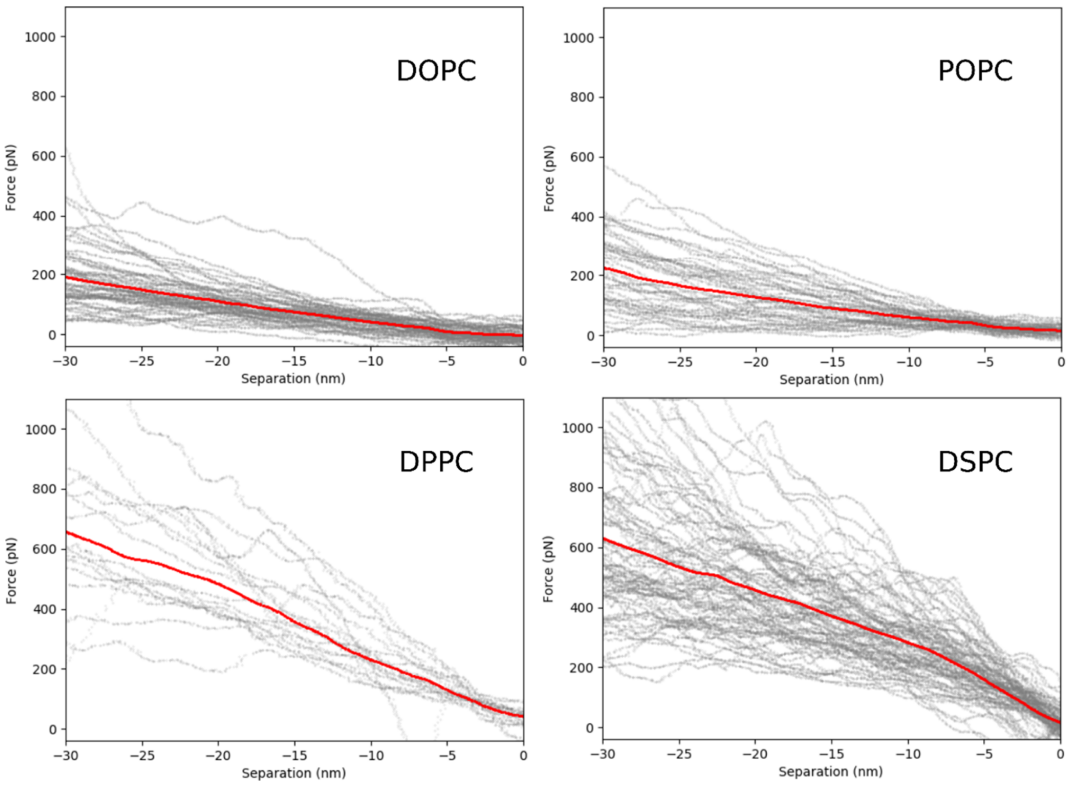

Figure 4. Average curves for the four different liposome types. Each average curve (red curve) was calculated by computing the average value of the single force/distance curves at each separation value. As can be seen, when going from DOPC to DSPC, K_1 and K_2 become comparable, and variations in K_2 due to leakages of internal fluid during the indentation may have a stronger impact on K_{eq} and on the observed curve slope.

values are shown in the third column of Table 3 and should recapitulate the mechanical contribution arising from changes in the volume/surface of the vesicles, the most relevant being the internal pressurization. Surprisingly, the estimated K_2 values are very similar for most of the probed liposomes, irrespective of their membrane phase state. Only DSPC vesicles display a slightly increased pressurization, compared to the other ones. These results suggest that the mechanical contributions from the internal pressurization of most of the probed vesicles are very similar across different liposome types. Looking at the K_2 values for the fluid phase liposomes (DOPC and POPC), it can be seen that the pressure plays a predominant role in the general mechanical response of these vesicles (with DOPC having a K_2 that is 1 order of magnitude higher than K_1), which is in perfect accord with the findings of Vorselen et al.,[19] according to which the internal pressure of fluid phase liposomes provides the most relevant contribution to the vesicles' mechanical response. The obtained results also highlight the different contributions of membrane elasticity and internal pressure to the overall vesicle stiffness, in fluid and gel phase liposomes; in the first ones, the greater contribution to the vesicle stiffness is from the internal pressure, while in the second ones, the contributions of membrane and pressure become comparable, and the vesicle mechanical response is given by their combination.

The Difference between K_1 and K_2 Could Explain the Slope Change Often Observed at Large Indentation Lengths in the AFM Force/Distance Curves. When the penetration depth is further increased (to values much larger than the membrane thickness), different events may take place: the AFM tip can puncture the bilayer (as often suggested by a sudden drop in the force signal in several vesicle indentation curves), the vesicles may lose part of their luminal content (depressurization) or even burst under excessive pressure. The manifestation of these events varies across different vesicle types; from the analysis of the force curves obtained during the AFM-FS measurements on vesicles, we found that the ratio between K_1 and K_2 could provide an interpretation of the variability in the mechanical response characterizing the second part of the force/distance curves. Figure 4 displays the force curves collected during a representative ensemble of indentation cycles performed on four different vesicle types (gray curves). Different from the calculation of the vesicle stiffness, this time, the curves were processed exploiting a custom Python script that allowed for the automatic determination of the contact point, for the subsequent alignment and for the estimation of the average curves (red traces). Due to this, occasional misalignment issues might occur, which, however, do not significantly affect the following qualitative interpretation of the results. The average curves are

https://doi.org/10.1021/acs.langmuir.1c01660
Langmuir 2021, 37, 12027−12037

obtained by averaging the values of the displayed gray curves at each separation point. As seen in Figure 4, the straightness of the red curves decreases from DOPC to DSPC, with the latter displaying a pronounced slope change.

These different behaviors can be rationalized by analyzing how K_{eq} changes when the value of K_2 is decreased. For those cases in which the overall stiffness is dominated by K_2, $K_{eq} \sim K_1$ and hence a variation in K_2 has a negligible effect on the observed curve slope (K_{eq}), as the new value of K_2 still largely exceeds K_1 (see eq 3). On the other hand, when K_2 is comparable with K_1, its variation has a stronger impact on K_{eq}, generating an appreciable change in the slope of the curve.

A decrease in K_2 could come as a consequence of larger indentations, which imply an increase in the internal pressurization of the vesicles, an event that could trigger the release of part of the internal fluid with a subsequent loss of volume. As a result, the vesicle would consequently have less fluid inside its lumen, hence being less pressurized, that is, its K_2 would have a lower value. On the other hand, since K_1 represents the membrane stiffness, which should not be affected by depressurization phenomena, its value is assumed to remain constant during the whole indentation process. According to these predictions, in Figure 4, the effect of depressurization on the curves' slope is negligible for DOPC (the curves retain the initial slope also for larger indentations), but it becomes gradually more important approaching the stiffer gel phase liposomes, where the curves display larger variability for higher indentation values. The onset of a second linear regime in the force/distance curves has also been recorded in the AFM studies of Vorselen et al.[19] and Calò et al.,[12] while Vella et al.[67] obtained a similar response from indentation tests on inflated spherical shells; most of these studies point to the pressure as the main responsible factor for the observed effect. This aspect might also explain why in stiffer liposomes, variations in the measured values of both stiffness and bending modulus are higher than those found for softer ones.

CONCLUSIONS

Lipid membranes are involved in a plethora of relevant biological processes; for this reason, characterizing their mechanical properties can help understand the fundamental interactions between interfaces at the nanoscale. FS techniques can be used to probe the mechanical properties of nanosized membranous envelopes such as vesicles, viruses, and other organelles; despite the high accuracy of these techniques, the data interpretation still stirs a debate, ultimately leading to a disagreement of the results obtained with different techniques.

By performing AFM-FS on a set of fluid and gel phase SLBs, we characterized their mechanical response in terms of bending modulus, which is an intrinsic descriptor of the membrane rigidity. Coarse-grained MD simulations performed on realistic SLBs models confirmed and supported the AFM-FS results, showing that the differences, experimentally observed between fluid and gel phase bilayers, can be ascribed to the interplay between intermolecular cohesion energy and intramolecular deformation.

Leveraging these results, we probed (by means of AFM-FS) the same set of fluid and gel phase lipid bilayers, in the liposome configuration, and found that the mechanical response of a lipid vesicle to an applied deformation can be modeled by a system of two springs in series. One of the springs accounts for the effect of membrane elasticity while the other for the effects arising from large volume/surface variations, whose greater contribution comes from the luminal pressure.

Exploiting this spring-based model, we find that despite not accounting for internal pressure contributions, the TST can still be used to extract the bending modulus values of very soft vesicles (such as DOPC), for which the spring constant representing membrane stiffness has a negligible value compared to the one representing the luminal pressure. When these two contributions become comparable, the mechanical response of vesicles is a combination of the two springs and cannot be correctly analyzed by means of TST only. By assuming that the correct values of the bending modulus are the ones obtained from the AFM-FS on SLBs, we find that the pressurization of most of the probed vesicles (which had a similar size) is similar, independent of the lipids forming the bilayer. Moreover, our mechanical model provides an interesting interpretation of the change in the slope displayed in the force curves of stiffer liposomes, showing that when the two spring constants are comparable, a change in the internal pressure would have a more appreciable effect on the vesicle stiffness, as probed through AFM-FS.

Our findings shed light on the nanomechanics of lipid vesicles and provide a possible explanation to the discrepancy that is often observed among the results of the bending modulus obtained from intact vesicles and SLBs. Future works will be aimed at quantifying the extent of the internal pressure contribution, in order to correct and hence extend the applicability of TST-based models to the description of both gel and fluid phase vesicles. Ultimately, when applied to natural vesicles, such as EVs, the simple but clear-cut insights afforded by our model might help to better understand the fundamental biological processes that involve vesicular deformation and/or reorganization.

ASSOCIATED CONTENT

Supporting Information

The Supporting Information is available free of charge at https://pubs.acs.org/doi/10.1021/acs.langmuir.1c01660.

AFM-FS measurements performed on both vesicles and SLBs and details about the MD simulations (PDF)

AUTHOR INFORMATION

Corresponding Authors

Andrea Ridolfi − *Consorzio Interuniversitario per lo Sviluppo dei Sistemi a Grande Interfase, 50019 Firenze, Italy; Istituto per lo Studio dei Materiali Nanostrutturati, Consiglio Nazionale delle Ricerche, 40129 Bologna, Italy; Dipartimento di Chimica "Ugo Schiff", Università degli Studi di Firenze, 50019 Firenze, Italy;* orcid.org/0000-0003-4224-9333; Email: andrea.ridolfi@unifi.it

Francesco Valle − *Consorzio Interuniversitario per lo Sviluppo dei Sistemi a Grande Interfase, 50019 Firenze, Italy; Istituto per lo Studio dei Materiali Nanostrutturati, Consiglio Nazionale delle Ricerche, 40129 Bologna, Italy;* Email: francesco.valle@cnr.it

Marco Brucale − *Consorzio Interuniversitario per lo Sviluppo dei Sistemi a Grande Interfase, 50019 Firenze, Italy; Istituto per lo Studio dei Materiali Nanostrutturati, Consiglio Nazionale delle Ricerche, 40129 Bologna, Italy;* orcid.org/0000-0001-7244-4389; Email: marco.brucale@cnr.it

Authors

Lucrezia Caselli − *Consorzio Interuniversitario per lo Sviluppo dei Sistemi a Grande Interfase, 50019 Firenze, Italy; Dipartimento di Chimica "Ugo Schiff", Università degli Studi di Firenze, 50019 Firenze, Italy*

Matteo Baldoni − *Istituto per lo Studio dei Materiali Nanostrutturati, Consiglio Nazionale delle Ricerche, 40129 Bologna, Italy*

Costanza Montis − *Consorzio Interuniversitario per lo Sviluppo dei Sistemi a Grande Interfase, 50019 Firenze, Italy; Dipartimento di Chimica "Ugo Schiff", Università degli Studi di Firenze, 50019 Firenze, Italy*

Francesco Mercuri − *Istituto per lo Studio dei Materiali Nanostrutturati, Consiglio Nazionale delle Ricerche, 40129 Bologna, Italy;* orcid.org/0000-0002-3369-4438

Debora Berti − *Consorzio Interuniversitario per lo Sviluppo dei Sistemi a Grande Interfase, 50019 Firenze, Italy; Dipartimento di Chimica "Ugo Schiff", Università degli Studi di Firenze, 50019 Firenze, Italy;* orcid.org/0000-0001-8967-560X

Complete contact information is available at: https://pubs.acs.org/10.1021/acs.langmuir.1c01660

Notes

The authors declare no competing financial interest.

■ ACKNOWLEDGMENTS

This research received funding from the Horizon 2020 Framework Programme under the grants FETOPEN-801367 "evFOUNDRY" and FETPROACT-EIC-05-2019 "Bio-Organic Wetsuits". We thank the SPM@ISMN research facility for supporting the AFM experiments.

■ REFERENCES

(1) Van Niel, G.; D'Angelo, G.; Raposo, G. Shedding Light on the Cell Biology of Extracellular Vesicles. *Nat. Rev. Mol. Cell Biol.* **2018**, *19*, 213−228.

(2) Dulińska, I.; Targosz, M.; Strojny, W.; Lekka, M.; Czuba, P.; Balwierz, W.; Szymoński, M. Stiffness of Normal and Pathological Erythrocytes Studied by Means of Atomic Force Microscopy. *J. Biochem. Biophys. Methods* **2006**, *66*, 1−11.

(3) Hosseini, S. M.; Feng, J. J. How Malaria Parasites Reduce the Deformability of Infected Red Blood Cells. *Biophys. J.* **2012**, *103*, 1−10.

(4) Vorselen, D.; van Dommelen, S. M.; Sorkin, R.; Piontek, M. C.; Schiller, J.; Döpp, S. T.; Kooijmans, S. A. A.; van Oirschot, B. A.; Versluijs, B. A.; Bierings, M. B.; van Wijk, R.; Schiffelers, R. M.; Wuite, G. J. L.; Roos, W. H. The Fluid Membrane Determines Mechanics of Erythrocyte Extracellular Vesicles and Is Softened in Hereditary Spherocytosis. *Nat. Commun.* **2018**, *9*, 4960.

(5) Whitehead, B.; Wu, L.; Hvam, M. L.; Aslan, H.; Dong, M.; Dyrskjøt, L.; Ostenfeld, M. S.; Moghimi, S. M.; Howard, K. A. Tumour Exosomes Display Differential Mechanical and Complement Activation Properties Dependent on Malignant State: Implications in Endothelial Leakiness. *J. Extracell. Vesicles* **2015**, *4*, 29685.

(6) Rand, R. P.; Burton, A. C. Mechanical Properties of the Red Cell Membrane: I. Membrane Stiffness and Intracellular Pressure. *Biophys. J.* **1964**, *4*, 115−135.

(7) Dimova, R.; Riske, K. A. Electrodeformation, Electroporation, and Electrofusion of Giant Unilamellar Vesicles. In *Handbook of Electroporation*; SpringerLink, 2017; Vol. *1*, pp 235−252.

(8) van Mameren, J.; Wuite, G. J. L.; Heller, I. Introduction to Optical Tweezers: Background, System Designs, and Commercial Solutions. *Methods Mol. Biol.* **2018**, *1665*, 3−23.

(9) Krieg, M.; Fläschner, G.; Alsteens, D.; Gaub, B. M.; Roos, W. H.; Wuite, G. J. L.; Gaub, H. E.; Gerber, C.; Dufrêne, Y. F.; Müller, D. J. Atomic Force Microscopy-Based Mechanobiology. *Nat. Rev. Phys.* **2019**, *1*, 41.

(10) Parisse, P.; Rago, I.; Ulloa Severino, L.; Perissinotto, F.; Ambrosetti, E.; Paoletti, P.; Ricci, M.; Beltrami, A. P.; Cesselli, D.; Casalis, L. Atomic Force Microscopy Analysis of Extracellular Vesicles. *Eur. Biophys. J.* **2017**, *46*, 813−820.

(11) Piontek, M. C.; Lira, R. B.; Roos, W. H. Active Probing of the Mechanical Properties of Biological and Synthetic Vesicles. *Biochim. Biophys. Acta, Gen. Subj.* **2021**, *1865*, 129486.

(12) Calò, A.; Reguera, D.; Oncins, G.; Persuy, M.-A.; Sanz, G.; Lobasso, S.; Corcelli, A.; Pajot-Augy, E.; Gomila, G. Force measurements on natural membrane nanovesicles reveal a composition-independent, high Young's modulus. *Nanoscale* **2014**, *6*, 2275−2285.

(13) Sorkin, R.; Huisjes, R.; Bošković, F.; Vorselen, D.; Pignatelli, S.; Ofir-Birin, Y.; Freitas Leal, J. K.; Schiller, J.; Mullick, D.; Roos, W. H.; Bosman, G.; Regev-Rudzki, N.; Schiffelers, R. M.; Wuite, G. J. L. Nanomechanics of Extracellular Vesicles Reveals Vesiculation Pathways. *Small* **2018**, *14*, 1801650.

(14) Et-Thakafy, O.; Delorme, N.; Gaillard, C.; Mériadec, C.; Artzner, F.; Lopez, C.; Guyomarc'h, F. Mechanical Properties of Membranes Composed of Gel-Phase or Fluid-Phase Phospholipids Probed on Liposomes by Atomic Force Spectroscopy. *Langmuir* **2017**, *33*, 5117−5126.

(15) Takechi-Haraya, Y.; Goda, Y.; Sakai-Kato, K. Atomic Force Microscopy Study on the Stiffness of Nanosized Liposomes Containing Charged Lipids. *Langmuir* **2018**, *34*, 7805−7812.

(16) Di Santo, R.; Romanò, S.; Mazzini, A.; Jovanović, S.; Nocca, G.; Campi, G.; Papi, M.; De Spirito, M.; Di Giacinto, F.; Ciasca, G. Recent Advances in the Label-Free Characterization of Exosomes for Cancer Liquid Biopsy: From Scattering and Spectroscopy to Nanoindentation and Nanodevices. *Nanomaterials* **2021**, *11*, 1476.

(17) Canham, P. B. The Minimum Energy of Bending as a Possible Explanation of the Biconcave Shape of the Human Red Blood Cell. *J. Theor. Biol.* **1970**, *26*, 61−81.

(18) Helfrich, W. Elastic Properties of Lipid Bilayers: Theory and Possible Experiments. *Z. Naturforsch., C: Biochem., Biophys., Biol., Virol.* **1973**, *28*, 693−703.

(19) Vorselen, D.; Mackintosh, F. C.; Roos, W. H.; Wuite, G. J. L. Competition between Bending and Internal Pressure Governs the Mechanics of Fluid Nanovesicles. *ACS Nano* **2017**, *11*, 2628−2636.

(20) Boal, D. *Mechanics of the Cell*, 2nd ed.; Cambridge University Press, 2012.

(21) Landau, L. D.; Lifshitz, E. M. *Theory of Elasticity*, 3rd ed.; Course of Theoretical Physics, 1986.

(22) Wan, F. Y. M.; Gregory, R. D.; Milac, T. I. A Thick Hollow Sphere Compressed by Equal and Opposite Concentrated Axial Loads: An Asymptotic Solution. *SIAM J. Appl. Math.* **1998**, *59*, 1080−1097.

(23) Reissner, E. Stresses and Small Displacements of Shallow Spherical Shells I. *J. Math. Phys.* **1946**, *25*, 80−85.

(24) Reissner, E. Stresses and Small Displacements of Shallow Spherical Shells. I. *J. Math. Phys.* **1946**, *25*, 80−85.

(25) Vorselen, D.; Piontek, M. C.; Roos, W. H.; Wuite, G. J. L. Mechanical Characterization of Liposomes and Extracellular Vesicles, a Protocol. *Front. Mol. Biosci.* **2020**, *7*, 139.

(26) Tang, X.; Shi, X.; Gan, Y.; Yi, X. Nanomechanical Characterization of Pressurized Elastic Fluid Nanovesicles Using Indentation Analysis. *Extreme Mech. Lett.* **2020**, *34*, 100613.

(27) Kalluri, R.; LeBleu, V. S. The Biology, Function, and Biomedical Applications of Exosomes. *Science* **2020**, *367*, No. eaau6977.

(28) Richter, R. P.; Bérat, R.; Brisson, A. R. Formation of Solid-Supported Lipid Bilayers: An Integrated View. *Langmuir* **2006**, *22*, 3497−3505.

(29) Hardy, G. J.; Nayak, R.; Zauscher, S. Model Cell Membranes: Techniques to Form Complex Biomimetic Supported Lipid Bilayers

via Vesicle Fusion. *Curr. Opin. Colloid Interface Sci.* **2013**, *18*, 448−458.
(30) Clifton, L. A.; Campbell, R. A.; Sebastiani, F.; Campos-Terán, J.; Gonzalez-Martinez, J. F.; Björklund, S.; Sotres, J.; Cárdenas, M. Design and Use of Model Membranes to Study Biomolecular Interactions Using Complementary Surface-Sensitive Techniques. *Adv. Colloid Interface Sci.* **2020**, *277*, 102118.
(31) Caselli, L.; Ridolfi, A.; Cardellini, J.; Sharpnack, L.; Paolini, L.; Brucale, M.; Valle, F.; Montis, C.; Bergese, P.; Berti, D. A Plasmon-Based Nanoruler to Probe the Mechanical Properties of Synthetic and Biogenic Nanosized Lipid Vesicles. *Nanoscale Horiz.* **2021**, *6*, 543−550.
(32) Kanan, S. M.; Tze, W. T. Y.; Tripp, C. P. Method to Double the Surface Concentration and Control the Orientation of Adsorbed (3-Aminopropyl)Dimethylethoxysilane on Silica Powders and Glass Slides. *Langmuir* **2002**, *18*, 6623−6627.
(33) Ridolfi, A.; Caselli, L.; Montis, C.; Mangiapia, G.; Berti, D.; Brucale, M.; Valle, F. Gold Nanoparticles Interacting with Synthetic Lipid Rafts: An AFM Investigation. *J. Microsc.* **2020**, *280*, 194−203.
(34) Hutter, J. L.; Bechhoefer, J. Calibration of Atomic-Force Microscope Tips. *Rev. Sci. Instrum.* **1993**, *64*, 1868−1873.
(35) Ridolfi, A.; Brucale, M.; Montis, C.; Caselli, L.; Paolini, L.; Borup, A.; Boysen, A. T.; Loria, F.; Van Herwijnen, M. J. C.; Kleinjan, M.; Nejsum, P.; Zarovni, N.; Wauben, M. H. M.; Berti, D.; Bergese, P.; Valle, F. AFM-Based High-Throughput Nanomechanical Screening of Single Extracellular Vesicles. *Anal. Chem.* **2020**, *92*, 10274−10282.
(36) Nečas, D.; Klapetek, P. Gwyddion: An Open-Source Software for SPM Data Analysis. *Cent. Eur. J. Phys.* **2012**, *10*, 181−188.
(37) Marrink, S. J.; Tieleman, D. P. Perspective on the Martini Model. *Chem. Soc. Rev.* **2013**, *42*, 6801−6822.
(38) Alessandri, R.; Grünewald, F.; Marrink, S. J. The Martini Model in Materials Science. *Adv. Mater.* **2021**, *33*, 2008635.
(39) Summerfield, A.; Baldoni, M.; Kondratuk, D. V.; Anderson, H. L.; Whitelam, S.; Garrahan, J. P.; Besley, E.; Beton, P. H. Ordering, Flexibility and Frustration in Arrays of Porphyrin Nanorings. *Nat. Commun.* **2019**, *10*, 2932.
(40) Plimpton, S. Fast Parallel Algorithms for Short-Range Molecular Dynamics. *J. Comput. Phys.* **1995**, *117*, 1−19.
(41) Fernandez-Puente, L.; Bivas, I.; Mitov, M. D.; Méléard, P. Temperature and Chain Length Effects on Bending Elasticity of Phosphatidylcholine Bilayers. *Epl* **1994**, *28*, 181−186.
(42) Marsh, D. Elastic Curvature Constants of Lipid Monolayers and Bilayers. *Chem. Phys. Lipids* **2006**, *144*, 146−159.
(43) Li, S.; Eghiaian, F.; Sieben, C.; Herrmann, A.; Schaap, I. A. T. Bending and Puncturing the Influenza Lipid Envelope. *Biophys. J.* **2011**, *100*, 637−645.
(44) Hertz, H. Ueber Die Berührung Fester Elastischer Körper. *J. Reine Angew. Math.* **1882**, *92*, 156−171.
(45) Dimitriadis, E. K.; Horkay, F.; Maresca, J.; Kachar, B.; Chadwick, R. S. Determination of Elastic Moduli of Thin Layers of Soft Material Using the Atomic Force Microscope. *Biophys. J.* **2002**, *82*, 2798−2810.
(46) Åkesson, A.; Lind, T.; Ehrlich, N.; Stamou, D.; Wacklin, H.; Cárdenas, M. Composition and Structure of Mixed Phospholipid Supported Bilayers Formed by POPC and DPPC. *Soft Matter* **2012**, *8*, 5658.
(47) Leonenko, Z. V.; Finot, E.; Ma, H.; Dahms, T. E. S.; Cramb, D. T. Investigation of Temperature-Induced Phase Transitions in DOPC and DPPC Phospholipid Bilayers Using Temperature-Controlled Scanning Force Microscopy. *Biophys. J.* **2004**, *86*, 3783.
(48) Bilotto, P.; Lengauer, M.; Andersson, J.; Ramach, U.; Mears, L. L. E.; Valtiner, M. Interaction Profiles and Stability of Rigid and Polymer-Tethered Lipid Bilayer Models at Highly Charged and Highly Adhesive Contacts. *Langmuir* **2019**, *35*, 15552−15563.
(49) Charitat, T.; Bellet-Amalric, E.; Fragneto, G.; Graner, F. Adsorbed and Free Lipid Bilayers at the Solid-Liquid Interface. *Eur. Phys. J. B* **1999**, *8*, 583.
(50) Berquand, A.; Lévy, D.; Gubellini, F.; Le Grimellec, C.; Milhiet, P.-E. Influence of Calcium on Direct Incorporation of Membrane Proteins into In-Plane Lipid Bilayer. *Ultramicroscopy* **2007**, *107*, 928−933.
(51) Tristram-Nagle, S.; Petrache, H. I.; Nagle, J. F. Structure and Interactions of Fully Hydrated Dioleoylphosphatidylcholine Bilayers. *Biophys. J.* **1998**, *75*, 917−925.
(52) Daillant, J.; Bellet-Amalric, E.; Braslau, A.; Charitat, T.; Fragneto, G.; Graner, F.; Mora, S.; Rieutord, F.; Stidder, B. Structure and Fluctuations of a Single Floating Lipid Bilayer. *Proc. Natl. Acad. Sci. U.S.A.* **2005**, *102*, 11639−11644.
(53) Liu, Y.; Nagle, J. F. Diffuse Scattering Provides Material Parameters and Electron Density Profiles of Biomembranes. *Phys. Rev. E: Stat., Nonlinear, Soft Matter Phys.* **2004**, *69*, 040901.
(54) Levine, Z. A.; Venable, R. M.; Watson, M. C.; Lerner, M. G.; Shea, J.-E.; Pastor, R. W.; Brown, F. L. H. Determination of Biomembrane Bending Moduli in Fully Atomistic Simulations. *J. Am. Chem. Soc.* **2014**, *136*, 13582−13585.
(55) Picas, L.; Rico, F.; Scheuring, S. Direct Measurement of the Mechanical Properties of Lipid Phases in Supported Bilayers. *Biophys. J.* **2012**, *102*, L01−L03.
(56) Dimova, R. Recent Developments in the Field of Bending Rigidity Measurements on Membranes. *Adv. Colloid Interface Sci.* **2014**, *208*, 225−234.
(57) Nagle, J. F. Experimentally Determined Tilt and Bending Moduli of Single-Component Lipid Bilayers. *Chem. Phys. Lipids* **2017**, *205*, 18−24.
(58) Henriksen, J.; Rowat, A. C.; Brief, E.; Hsueh, Y. W.; Thewalt, J. L.; Zuckermann, M. J.; Ipsen, J. H. Universal Behavior of Membranes with Sterols. *Biophys. J.* **2006**, *90*, 1639−1649.
(59) Yi, Z.; Nagao, M.; Bossev, D. P. Bending Elasticity of Saturated and Monounsaturated Phospholipid Membranes Studied by the Neutron Spin Echo Technique. *J. Phys.: Condens. Matter* **2009**, *21*, 155104.
(60) Delorme, N.; Fery, A. Direct Method to Study Membrane Rigidity of Small Vesicles Based on Atomic Force Microscope Force Spectroscopy. *Phys. Rev. E: Stat., Nonlinear, Soft Matter Phys.* **2006**, *74*, 030901.
(61) Hochmuth, F. M.; Shao, J. Y.; Dai, J.; Sheetz, M. P. Deformation and Flow of Membrane into Tethers Extracted from Neuronal Growth Cones. *Biophys. J.* **1996**, *70*, 358−369.
(62) Redondo-Morata, L.; Giannotti, M. I.; Sanz, F. Influence of Cholesterol on the Phase Transition of Lipid Bilayers: A Temperature-Controlled Force Spectroscopy Study. *Langmuir* **2012**, *28*, 12851−12860.
(63) Gumí-Audenis, B.; Sanz, F.; Giannotti, M. I. Impact of Galactosylceramides on the Nanomechanical Properties of Lipid Bilayer Models: An AFM-Force Spectroscopy Study. *Soft Matter* **2015**, *11*, 5447−5454.
(64) Saavedra, V. O.; Fernandes, T. F. D.; Milhiet, P.-E.; Costa, L. Compression, Rupture, and Puncture of Model Membranes at the Molecular Scale. *Langmuir* **2020**, *36*, 5709−5716.
(65) LeClaire, M.; Gimzewski, J.; Sharma, S. A Review of the Biomechanical Properties of Single Extracellular Vesicles. *Nano Sel.* **2021**, *2*, 1−15.
(66) Berry, J. D.; Mettu, S.; Dagastine, R. R. Precise Measurements of Capsule Mechanical Properties Using Indentation. *Soft Matter* **2017**, *13*, 1943−1947.
(67) Vella, D.; Ajdari, A.; Vaziri, A.; Boudaoud, A. The Indentation of Pressurized Elastic Shells: From Polymeric Capsules to Yeast Cells. *J. R. Soc. Interface* **2012**, *9*, 448−455.

https://doi.org/10.1021/acs.langmuir.1c01660
Langmuir 2021, 37, 12027−12037

Supplementary Information

Stiffness of fluid and gel phase lipid nanovesicles: weighting the contributions of membrane bending modulus and luminal pressurization

Andrea Ridolfi [a,b,c,], Lucrezia Caselli [a,c], Matteo Baldoni [b], Costanza Montis [a,c], Francesco Mercuri [b], Debora Berti [a,c], Francesco Valle [a,b,*] and Marco Brucale [a,b,*].*

[a] Consorzio Interuniversitario per lo Sviluppo dei Sistemi a Grande Interfase, 50019 Firenze, Italy.

[b] Consiglio Nazionale delle Ricerche, Istituto per lo Studio dei Materiali Nanostrutturati, 40129 Bologna, Italy.

[c] Dipartimento di Chimica "Ugo Schiff", Università degli Studi di Firenze, 50019 Firenze, Italy.

** corresponding authors*

Figure S1

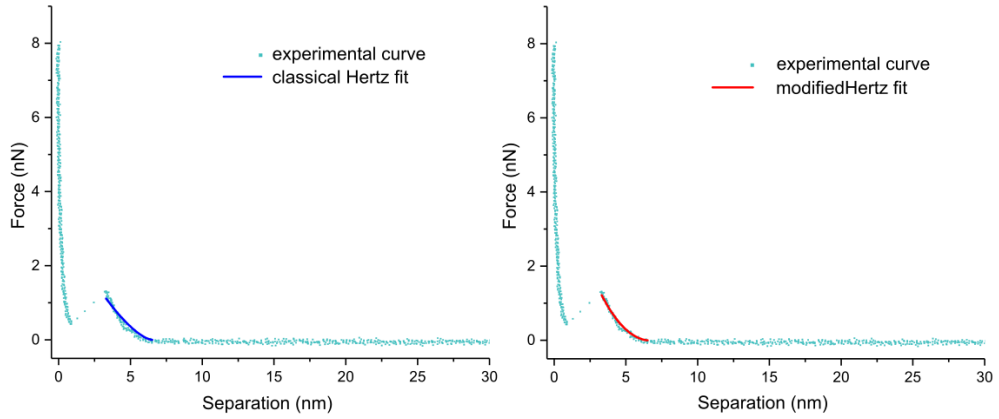

Difference between the classical and the corrected Hertz fitting model (proposed by Dimitriadis et al.); as can be seen, the classical Hertz fit underestimates the Young Modulus, indeed the fitted curve (obtained from the indentation of a POPC SLB) is less steep than the original one. On the other hand, the modified Hertz fit presents a much better accord with the experimental data. This is probably due to the low thickness of the lipid bilayers and to the related substrate contributions; both being phenomena not taken under sufficient consideration by the Hertz theory. The more recent model, proposed by Dimitriadis et al. (1) instead, accounts for those cases in which the substrate contributions become relevant, as a consequence of the low layer thickness.

Additional details about the particle-based molecular dynamics (MD) simulations

The support surface was composed by seven stacked layers of SGA beads arranged in a hexagonal (honeycomb) lattice, with a 2:1 mapping with respect to graphite. The interaction within the particles constituting the support layer was defined in terms of a deep LJ potential only. This allows to exclude

the mechanical part of the potential from the total energy. The interaction of the support layer with all other particles was defined by using the parameters of SN0 beads. The surface roughness was introduced by randomly removing a variable number of particles from the support layers, from 90% for the topmost layer to 0% in the central layer. A model substrate of about 30x30 nm with periodicity in 2 dimensions was first relaxed by MD in vacuum.

The model system constituted by the SLB model in water solution and the AFM tip model, at a distance of about 8 nm from the surface, was first relaxed by equilibrium MD for about 40 ns in the NPT ensemble, keeping the particle of the AFM tip fixed (see also Fig. S2).

From this initial run, configurations were extracted at intervals of 0.75 nm along the trajectory. These configurations were used as starting points for equilibrium MD simulations (about 50 ns), keeping the AFM tip model fixed and evaluating the mean force between the tip and the SLB over the last 5 ns.

Figure S2

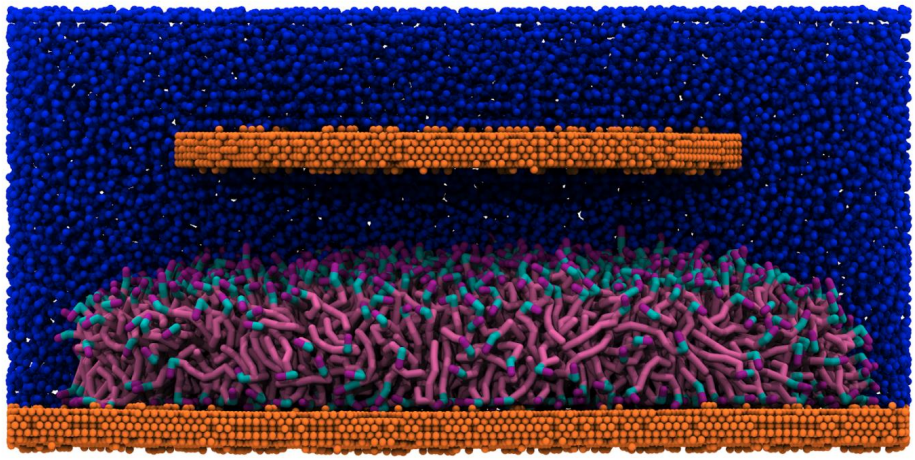

Side view (section) of the model system used in MD simulations of a DPPC SLB. Particles of the support layer (bottom) and of the mechanical probe (top) are in orange; water particles are in blue. The lateral size of the model shown is 30 nm. The figure shows a snapshot from one of the equilibration runs carried out to evaluate the force between the mechanical probe and the SLB

Figure S3

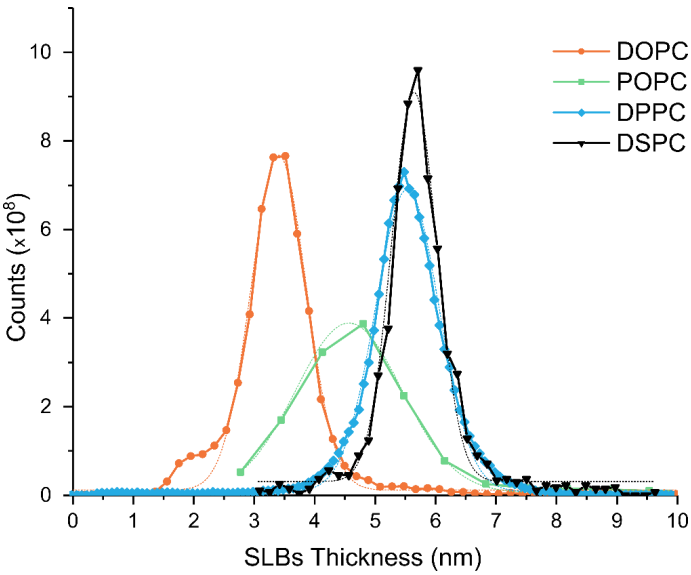

AFM images of SLBs were analyzed and processed using Gwyddion(2), following the procedures described elsewhere(3), in order to extract the height distributions of the SLBs from the four different lipid types. Peaks of the distributions were then fitted to obtain an average value of the SLB thickness. Dotted lines display the Gaussian distributions that were used for extracting the thickness values. Numerical results from the fits are displayed in Table S1.

Figure S4

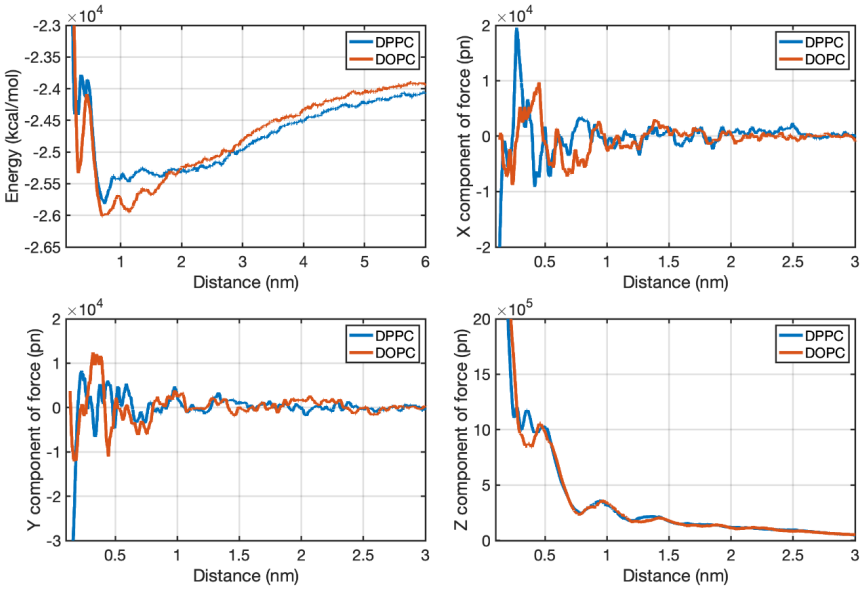

Total energy and components of the force between the mechanical probe model and the SLB for the initial (non-equilibrium) trajectories. DPPC: blue curves; DOPC: orange curves.

Figure S5

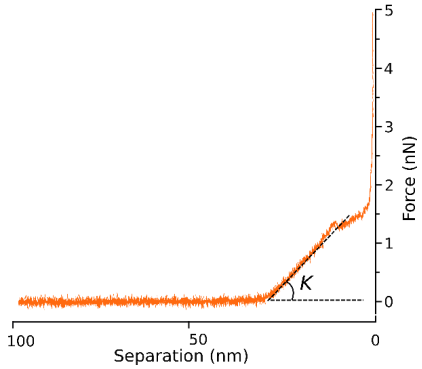

Representative AFM force-indentation curve obtained from an AFM-FS measurement on a lipid vesicle. The slope of the initial linear part can be fitted in order to obtain the value of the vesicle stiffness *K*.

Figure S6

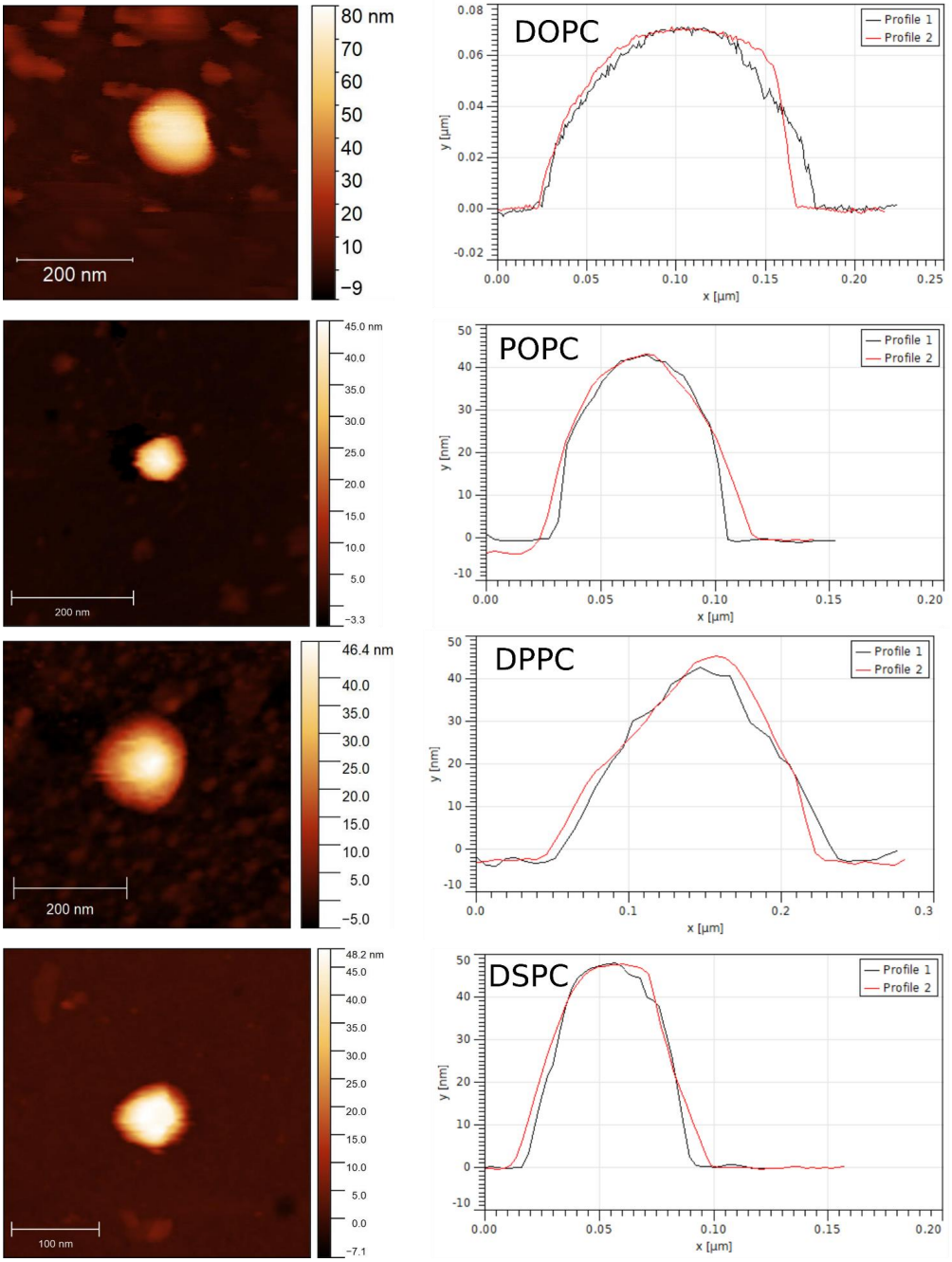

Representative AFM images of the probed liposomes (one for each lipid type). On the right, the height profiles (black is the slow scan axis while red the fast scan axis) from which it is possible to calculate the radius of the adsorbed vesicle (refer to Ridolfi et al. (4) for more details).

Figure S7

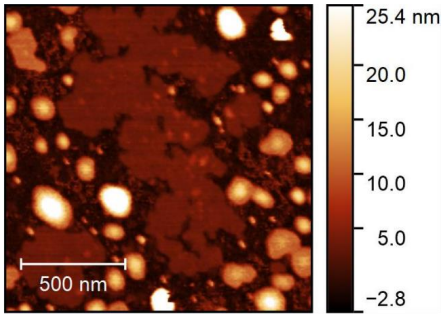
25.4 nm
20.0
15.0
10.0
5.0
−2.8
500 nm

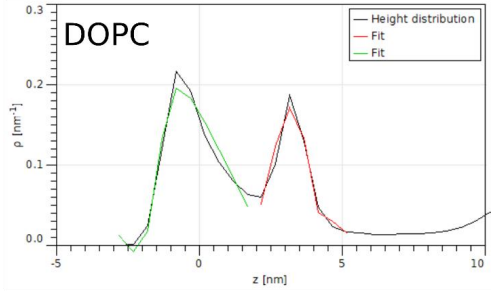
DOPC
Height distribution
Fit
Fit
ρ [nm⁻¹]
z [nm]

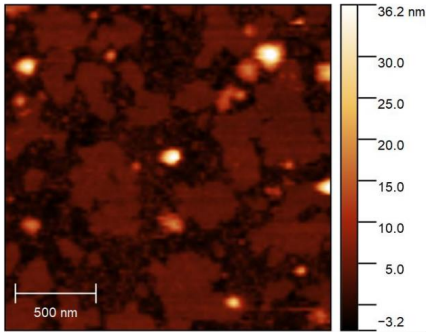
36.2 nm
30.0
25.0
20.0
15.0
10.0
5.0
−3.2
500 nm

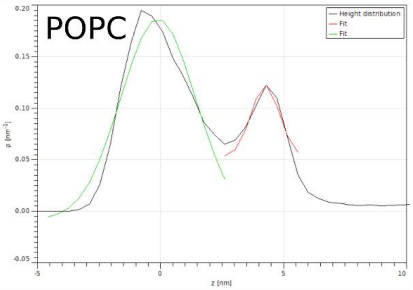
POPC
Height distribution
Fit
Fit
ρ [nm⁻¹]
z [nm]

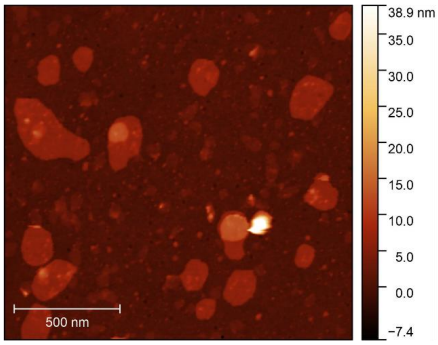
38.9 nm
35.0
30.0
25.0
20.0
15.0
10.0
5.0
0.0
−7.4
500 nm

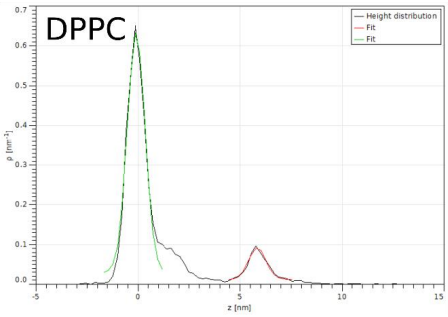
DPPC
Height distribution
Fit
Fit
ρ [nm⁻¹]
z [nm]

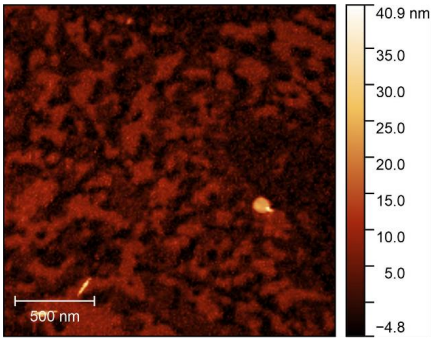
40.9 nm
35.0
30.0
25.0
20.0
15.0
10.0
5.0
−4.8
500 nm

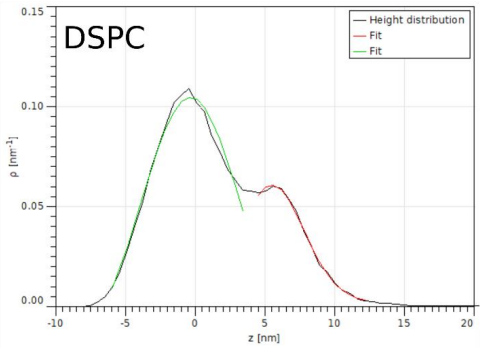
DSPC
Height distribution
Fit
Fit
ρ [nm⁻¹]
z [nm]

Representative SLB images for each of the probed lipids. On the right, the height distributions were fitted with Gaussian curves (red curve for the SLB, green curve for the substrate). The distance between the two peaks is close to the average thickness values used in the manuscript and reported in Table S1.

Table S1:

Thickness values of the different Supported Lipid Bilayers obtained by fitting a Gaussian distribution to the profile of Figure S4. The indicated thicknesses and errors refer to the values of mean and standard deviation of the respective distribution.

Lipid	SLB thickness (nm)
DOPC	3.429 ± 0.007
POPC	4.407 ± 0.009
DPPC	5.584 ± 0.004
DSPC	5.679 ± 0.009

Table S2:

Curvature radii of the liposomes measured in this study; at least 15 vesicles for each lipid were measured via AFM-FS. The curvature radius (R_c) of each vesicle was measured by fitting the profile of the adsorbed vesicle, using Gwyddion(2). Mean curvature radii and their standard deviations are also reported below.

DOPC	R_c (nm)	POPC	R_c (nm)	DPPC	R_c (nm)	DSPC	R_c (nm)
Vesicle 1	80.7	Vesicle 1	84.2	Vesicle 1	80.7	Vesicle 1	81.7
Vesicle 2	84.3	Vesicle 2	115.6	Vesicle 2	105.5	Vesicle 2	58.2
Vesicle 3	116.8	Vesicle 3	104.2	Vesicle 3	94.7	Vesicle 3	40.8
Vesicle 4	84.1	Vesicle 4	72.4	Vesicle 4	191.8	Vesicle 4	81.6
Vesicle 5	78.0	Vesicle 5	19.5	Vesicle 5	156.6	Vesicle 5	36.1
Vesicle 6	80.3	Vesicle 6	33.2	Vesicle 6	72.8	Vesicle 6	49.4
Vesicle 7	46.4	Vesicle 7	89.6	Vesicle 7	49.6	Vesicle 7	62.0
Vesicle 8	102.8	Vesicle 8	52.2	Vesicle 8	68.1	Vesicle 8	44.3
Vesicle 9	53.3	Vesicle 9	38.5	Vesicle 9	57.3	Vesicle 9	52.1
Vesicle 10	57.1	Vesicle 10	39.1	Vesicle 10	45.1	Vesicle 10	73.5
Vesicle 11	76.1	Vesicle 11	49.5	Vesicle 11	30.8	Vesicle 11	54.3
Vesicle 12	74.4	Vesicle 12	59.9	Vesicle 12	34.9	Vesicle 12	89.4
Vesicle 13	91.5	Vesicle 13	61.1	Vesicle 13	47.4	Vesicle 13	103.7

Vesicle 14	76.7	Vesicle 14	37.7	Vesicle 14	51.5	Vesicle 14	81.5
Vesicle 15	90.6	Vesicle 15	53.3	Vesicle 15	35.5	Vesicle 15	79.0
Vesicle 16	65.3	Vesicle 16	60.8	Vesicle 16	49.3		
Vesicle 17	67.4	Vesicle 17	65.0	Vesicle 17	62.1		
Vesicle 18	68.5			Vesicle 18	71.8		
Vesicle 19	66.8			Vesicle 19	79.6		
Vesicle 20	77.7			Vesicle 20	39.7		
mean (nm)	76.9	**mean (nm)**	60.9	**mean (nm)**	71.2	**mean (nm)**	65.8
st. dev (nm)	16.4	**st. dev (nm)**	25.8	**st. dev (nm)**	40.9	**st. dev (nm)**	20.0

References

1. Dimitriadis, E.K., F. Horkay, J. Maresca, B. Kachar, and R.S. Chadwick. 2002. Determination of elastic moduli of thin layers of soft material using the atomic force microscope. *Biophys. J.* 82:2798–2810.

2. Nečas, D., and P. Klapetek. 2012. Gwyddion: An open-source software for SPM data analysis. *Cent. Eur. J. Phys.* 10:181–188.

3. Ridolfi, A., L. Caselli, C. Montis, G. Mangiapia, D. Berti, M. Brucale, and F. Valle. 2020. Gold nanoparticles interacting with synthetic lipid rafts: an AFM investigation. *J. Microsc.* 00:1–10.

4. Ridolfi, A., M. Brucale, C. Montis, L. Caselli, L. Paolini, A. Borup, A.T. Boysen, F. Loria, M.J.C. Van Herwijnen, M. Kleinjan, P. Nejsum, N. Zarovni, M.H.M. Wauben, D. Berti, P. Bergese, and F. Valle. 2020. AFM-Based High-Throughput Nanomechanical Screening of Single Extracellular Vesicles. *Anal. Chem.* 92:10274–10282.

Manuscript n°2

analytical chemistry

pubs.acs.org/ac Article

AFM-Based High-Throughput Nanomechanical Screening of Single Extracellular Vesicles

Andrea Ridolfi, Marco Brucale,* Costanza Montis, Lucrezia Caselli, Lucia Paolini, Anne Borup, Anders T. Boysen, Francesca Loria, Martijn J. C. van Herwijnen, Marije Kleinjan, Peter Nejsum, Natasa Zarovni, Marca H. M. Wauben, Debora Berti, Paolo Bergese, and Francesco Valle*

Cite This: *Anal. Chem.* 2020, 92, 10274−10282 Read Online

ACCESS | Metrics & More | Article Recommendations | Supporting Information

ABSTRACT: The mechanical properties of extracellular vesicles (EVs) are known to influence their biological function, in terms of, e.g., cellular adhesion, endo/exocytosis, cellular uptake, and mechanosensing. EVs have a characteristic nanomechanical response which can be probed via force spectroscopy (FS) and exploited to single them out from nonvesicular contaminants or to discriminate between subtypes. However, measuring the nanomechanical characteristics of individual EVs via FS is a labor-intensive and time-consuming task, usually limiting this approach to specialists. Herein, we describe a simple atomic force microscopy based experimental procedure for the simultaneous nanomechanical and morphological analysis of several hundred individual nanosized EVs within the hour time scale, using basic AFM equipment and skills and only needing freely available software for data analysis. This procedure yields a "nanomechanical snapshot" of an EV sample which can be used to discriminate between subpopulations of vesicular and nonvesicular objects in the same sample and between populations of vesicles with similar sizes but different mechanical characteristics. We demonstrate the applicability of the proposed approach to EVs obtained from three very different sources (human colorectal carcinoma cell culture, raw bovine milk, and *Ascaris suum* nematode excretions), recovering size and stiffness distributions of individual vesicles in a sample. EV stiffness values measured with our high-throughput method are in very good quantitative accord with values obtained by FS techniques which measure EVs one at a time. We show how our procedure can detect EV samples contamination by nonvesicular aggregates and how it can quickly attest the presence of EVs even in samples for which no established assays and/or commercial kits are available (e.g., *Ascaris* EVs), thus making it a valuable tool for the rapid assessment of EV samples during the development of isolation/enrichment protocols by EV researchers. As a side observation, we show that all measured EVs have a strikingly similar stiffness, further reinforcing the hypothesis that their mechanical characteristics could have a functional role.

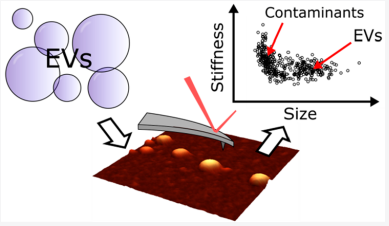

Extracellular vesicles (EVs) are cell-released, submicrometer membranous particles involved in numerous physiological and pathological functions.[1,2] Due to their almost ubiquitous relevance, they are focalizing the interest of a rapidly growing, highly multidisciplinary research community including oncologists, neurologists, bioengineers, parasitologists, cell biologists, food scientists, and biophysicists.[3−9] Because of the diverse biogenesis/release mechanisms of EVs and their enormous heterogeneity, the EV community is making a continuous effort to reach a consensus regarding several fundamental issues, including EV nomenclature.[10]

The vast majority of experimental research on EVs of any type starts with their isolation, purification, and enrichment—which are nontrivial endeavors, often needing sample-specific protocol optimization to limit contamination by nonvesicular material or excessive EV size polydispersion.[11−14] Furthermore, the analysis of EV samples is made difficult by a general scarcity of established tools for characterizing EVs with highly varied size, origin, function, membrane lipid/protein composition, and cargo content.[10,15] Some of the most powerful EV characterization techniques (e.g., cryo-EM) are highly demanding in terms of costs, time, and expertise. Hence, there is a need to develop methods for rapid, label-free assessment of EV samples, which are able to discern between vesicular and nonvesicular particles in the submicrometer range and are applicable to EVs isolated from highly diverse sources. In this context, single-vesicle measurements seem especially promising.[16]

One relatively constant feature of EVs isolated from different sources is their mechanical behavior, which is known to be influential on cellular adhesion, endo/exocytosis, cellular

Received: December 18, 2019
Accepted: July 7, 2020
Published: July 7, 2020

https://dx.doi.org/10.1021/acs.analchem.9b05716
Anal. Chem. 2020, 92, 10274−10282

uptake, and mechanosensing.[17] EVs have been shown to give a characteristic mechanical response to an applied load: a highly linear force/distance elastic deformation regime, which is also typical of synthetic liposomes but is otherwise very uncommon in nonvesicular objects.[18−21] This characteristic behavior can be recognized by probing the mechanical response of individual vesicles deposited on a substrate via atomic force microscope (AFM)-based force spectroscopy (FS).[22] The linear deformation regime slope reflects the vesicle's overall stiffness (k_S), i.e., its resistance to deformation, and can be quantitatively measured via AFM-FS nanoindentation experiments. Specific types of EV were observed to have characteristic k_S values, which can vary in the presence of pathological processes.[21,23] Due to this, it seems reasonable to consider mechanical response in general, and k_S in particular, as the basis for a method capable of discriminating EVs from contaminants or even between different types of EVs.

The observed linear mechanical response of vesicles is best rationalized by the Canham−Helfrich (CH) model,[24,25] in which the overall stiffness k_S is the sum of two contributing factors: membrane rigidity, quantified by its bending modulus (κ), and luminal pressurization (Π). Wuite and co-workers recently demonstrated that AFM-FS can be employed to separately determine the κ and Π values of individual liposomes,[26] that the same approach is applicable to EVs,[21] and that it can detect quantitative mechanical behavior variations linked to biological function.[17] This elegant and powerful AFM-FS approach is however quite labor-intensive, requiring the experimental determination of k_S, tether elongation force (F_T), and curvature radius (RC) for each individual vesicle. In particular, obtaining clear F_T readings involves the establishment of a single mechanical link between the vesicle's membrane and the AFM probe and can be problematic on EVs with abundant membrane proteins and/or lipopolysaccharides content. Finally, it is necessary to pool the readings of at least several tens of individual vesicles to obtain a reasonably clear picture of an EVs population's overall mechanical characteristics. Combined together, these considerations imply that the FS-based strategy mentioned above is in our opinion the best currently available method to obtain a quantitative mechanical characterization of individual vesicles but is also poorly suited to a quick, routine screening of unknown EV samples mainly aimed at achieving a broad picture of their size distribution and purity.

We herein propose a method for the rapid nanomechanical assessment of EV populations based on simple AFM imaging performed in liquid and successive morphometric analysis easily performed with freely available software. Following the procedure detailed in the following sections, it is possible to define the size and mechanical characteristics of a few hundred individual vesicles in the hour time scale in ideal experimental conditions. Although the mechanical readout provided by our procedure is semiquantitative, it is able to discriminate between subpopulations of vesicular and nonvesicular objects deposited on the same substrate and between populations of vesicles with similar sizes but different mechanical characteristics. Moreover, we show a calibration procedure that can be used to estimate the k_S of EVs without performing FS experiments.

As a proof of concept, we demonstrate the applicability of our method to EV samples isolated from three purposedly very different natural sources: human colorectal carcinoma (HCT116) cell culture, raw bovine milk, and the excretory/secretory products of the parasitic nematode *Ascaris suum*. Being so dissimilar, the selected sources must be subjected to very different isolation/enrichment procedures to obtain EV samples. Nevertheless, our method is able to assess the presence of vesicles and/or contaminants in aliquots of each sample and to yield a distribution of size and nanomechanical characteristics of hundreds of individual EVs within several hours. It is worthwhile to add that we were able to quickly verify the presence of vesicles with the "typical" nanomechanical characteristics of EVs in the *Ascaris suum* samples, whose characterization is otherwise still challenging, e.g., due to the current lack of specific protein markers. This suggests that our method could help the iterative optimization of isolation/enrichment protocols of other currently uncharacterized EVs.

EXPERIMENTAL SECTION

Full details about synthetic and natural vesicles preparation, characterization, and surface immobilization are given in the Supporting Information (see below).

We refer the reader to the Supporting Information section also for experimental details on AFM setup, AFM imaging conditions, and AFM force spectroscopy measurements.

Quantitative AFM Morphometry of Vesicles. The mechanical characterization of vesicles via quantitative AFM morphometry was performed as follows. Representative AFM micrographs (typically 5 × 5 μm, 512 × 512 points) were first acquired as described above. Since all the following image analysis steps rely on a correct zero-height baseline assignment, special care was taken to ensure that the image was devoid of image flattening artifacts by masking all positive features appearing on the surface and excluding them from linear background interpolation. In some cases, it was necessary to iterate the masking/subtraction procedure several times to obtain the required background flatness.

Figure S2a exemplifies a correctly processed AFM image of DPPC liposomes: after background subtraction, height profiles measured along the diagonals of the whole image (Figure S2b) are extremely flat, and the average height of empty areas is zero. Moreover, height profiles measured along the X and Y axis for individual vesicles are symmetrical and almost superimposable (Figure S2c), denoting that probe-induced deformation of vesicles along the fast scan axis is marginal.

Putative vesicles are then singled out from the background by marking all pixels exceeding a height threshold (Figure S2a). The employed threshold value was 10 nm in all cases except for DOPC samples, for which we employed a 5 nm threshold (for reasons explained below). Objects touching any edge of the image were automatically excluded from successive analysis. We then manually excluded objects evidently corresponding to clusters of two or more adjoining globular objects or to imaging artifacts such as vesicles that detached themselves from the surface between successive scan lines, resulting in nonglobular shapes with sharp drops along the slow scan axis (Figure S2d). The radius of the largest possible inscribed disc was then calculated for each object (Figure S2d, white circles); those with an inscribed circle radius <10 nm were discarded to exclude spikes and streaks from successive analysis.

Figure S2e shows a representative AFM image of a single putative DPPC vesicle. Our morphometrical analysis starts with the consideration that the shape observed in AFM micrographs is the combination of the vesicle's true shape,

https://dx.doi.org/10.1021/acs.analchem.9b05716
Anal. Chem. 2020, 92, 10274−10282

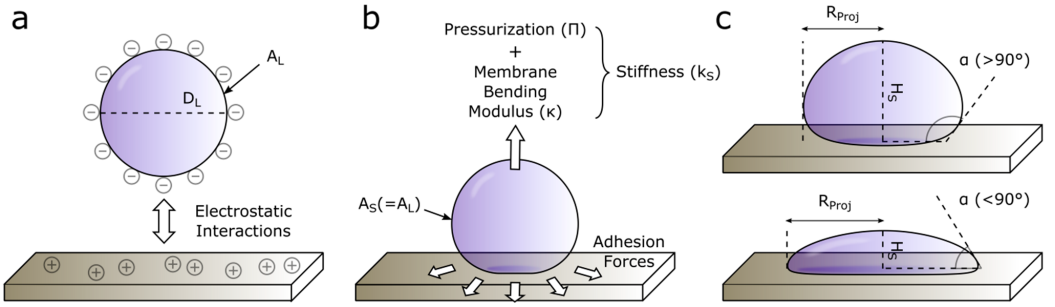

Figure 1. Schematic depiction of the surface adhesion process of a vesicle. (a) In liquid, the vesicle's average shape is a sphere with diameter D_L ("diameter in liquid") and corresponding total membrane area A_L ("area in liquid"). All vesicles utilized in this study have a negative ζ-potential in ultrapure water and are thus electrostatically attracted to substrates coated with poly-L-lysine. (b) When the vesicle first contacts the substrate, adhesive forces tend to maximize surface/membrane contact, causing the deformation of its previously spherical shape into an increasingly oblate spheroid. Membrane stretching is assumed to be negligible throughout the whole process, and thus the total membrane area of the vesicle on the surface (A_S) is equal to A_L (see panel a). The vesicle resists deformation to a degree quantified by its membrane bending modulus κ and internal pressurization Π, which jointly contribute to overall stiffness (k_S). (c) The equilibrium geometry of the adsorbed vesicle is thus a function of its stiffness k_S (see panel b) and can be quantified in terms of height H_S and projected radius R_{Proj}. These two values can be used to calculate the vesicle's contact angle α, which describes the entity of its oblate deformation independently from its size; α will be >90° when $H_S > R_{Proj}$ (top) and <90° in the opposite case (bottom). Comparatively stiffer vesicles will experience smaller deformations and will thus have larger measured α (top) than softer ones (bottom).

probe convolution, feedback artifacts, and the intrinsic AFM limitation of not being able to follow the shape of objects with fractal dimension above 1 along the Z axis.[27] Images can be optimized for minimal feedback artifacts (as discussed above), and their quantitative analysis can take probe convolution into account (see Figure S3). The observed AFM morphology is thus assumed to be a close "pseudo-3D" rendition of the examined object, resulting from the combination of the object's true height values measured along the Z axis and its projection on the XY plane. According to this, a globular object's true maximum surface height H_S and projected surface radius R_{Proj} can be quantitatively measured from its AFM image (Figure S2e): H_S is simply its maximum Z value, while R_{Proj} corresponds to its maximum inscribed disc radius corrected for tip convolution (see Figures S3 and S4).

We then assume that the spheroid shape of a surface-adhered vesicle can be approximated to that of a spherical cap[28] with a height equal to H_S and a projected surface radius equal to R_{Proj} (Figure S2f). The vesicle's projected radius R_{Proj} is used as the best approximation of its curvature radius (R_{Cap}) if $R_{Proj} < H_S$ (Figure S2f, left panel) and of its base radius (A_{Cap}) if $R_{Proj} > H_S$ (Figure S2f, right panel). The corresponding vesicle−surface contact angle (α, see Figure S2f) and total membrane area (A_S, see Figure 1) can be obtained via simple trigonometry calculations (see the Supporting Information). Finally, we estimate the vesicle's size in solution by assuming that even if its shape (originally spherical) was distorted upon interaction with the surface, its membrane underwent negligible stretching,[29] thus allowing us to calculate the diameter of a sphere of area A_L equal to the A_S value recovered from AFM imaging (Figure 1).

RESULTS AND DISCUSSION

Nanomechanical Screening of Vesicles via AFM Imaging. The rationale for our mechanical screening methodology is schematized in Figure 1. In the absence of external perturbations, the average shape of a vesicle in solution is spherical (Figure 1a) and can be geometrically characterized in terms of its diameter (D_L) and total surface area (A_L). Most, if not all, EVs have a negative surface charge[30−32] and can adhere to positively charged surfaces by electrostatic interactions exerting an attractive force between its membrane and the substrate.[28] Upon interaction, adhesion forces deform the initially spherical vesicle into an increasingly oblate shape. This deformation is opposed by both membrane rigidity and luminal pressurization, which jointly contribute to the vesicle's observed stiffness (Figure 1b). The extent to which a surface-adhered vesicle is deformed at equilibrium is thus a function of its stiffness, with higher k_S values resulting in smaller geometrical distortions and softer vesicles assuming more oblate shapes.[33] The vesicle−surface contact angle (α) can be employed as a size-independent quantitative descriptor of the adhered vesicle's deformation (Figure 1c).

With the opportune precautions (see the Supporting Information), simple AFM imaging in liquid can be used to determine the unperturbed equilibrium geometry of EVs deposited on a substrate in terms of their height H_S and surface-projected radius R_{Proj} (Figure 1c). These values can be used to calculate each vesicle's contact angle α and (assuming membrane area conservation during deformation) its original solution diameter D_L.

It is worthwhile to note that the membrane area conservation assumption[26,34] we use is just a useful simplification of the complex interplay of phenomena occurring when a vesicle electrostatically adheres to a surface; an alternative approach reported in the literature is to instead assume volume conservation.[35−38] Although theoretically incompatible, both approaches yielded accurate vesicular size characterization in different AFM-based studies.[17,39] We chose the area conservation assumption on the basis of the fact that in our hands it yielded the best accord between AFM morphometry and other vesicle sizing techniques (see below); most importantly, analyzing our data assuming volume conservation would imply hypothesizing that, upon surface adhesion, vesicles were able to stretch their surface area by very

https://dx.doi.org/10.1021/acs.analchem.9b05716
Anal. Chem. 2020, 92, 10274−10282

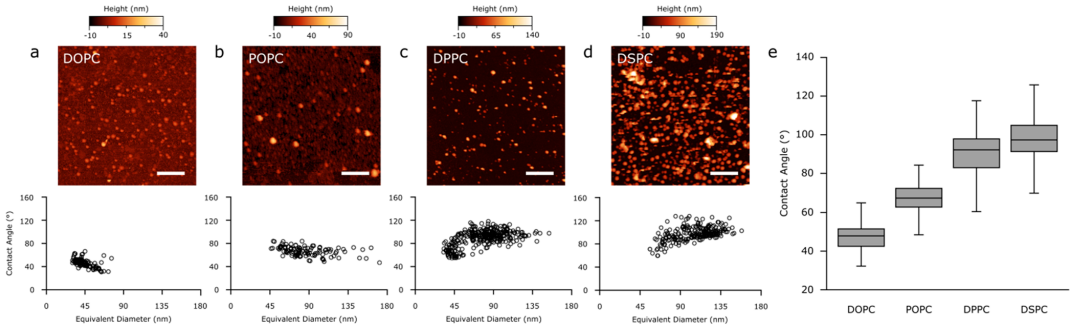

Figure 2. (a–d) Representative AFM images (top) and contact angle vs equivalent diameter scatterplots (bottom) of (a) DOPC, (b) POPC, (c) DPPC, and (d) DSPC liposomes. All scale bars are 1 μm. (e) Box plot comparison of liposome contact angle distributions. Gray boxes extend between the first (bottom edge) and third (top edge) quartile values, with black lines indicating median values. Whiskers correspond to the lowest (bottom) and highest (top) value found within the distribution. *t* tests performed on all pairs of distributions give *p*-values $\leq$0.0001.

large amounts (up to ~250%) without rupturing, which we rejected as unphysical.

It is also important to note that CH theory assumes κ to be an intrinsic property of vesicles formed by the same type of membrane, while k_S is expected to vary with vesicle size.[40] However, we hypothesize that k_S variations observed within populations of vesicles of the same type will be relatively small in the relatively narrow size distribution most relevant to EV research (30–500 nm in diameter). If this is true, populations of compositionally similar vesicles should show a limited dispersion of α values across different vesicle sizes, possibly small enough to resolve their distributions.

Vesicles of the Same Type Have a Characteristic Average Contact Angle Value. To verify the above hypothesis on the simplest possible vesicular objects, we first prepared solutions of synthetic liposomes having a negative ζ-potential (DOPC, POPC, DPPC, and DSPC) in ultrapure water, deposited them on PLL-coated substrates, captured their adhered morphology with in-liquid AFM imaging, and then calculated α and D_L values for several hundreds of individual vesicles. For each type of liposome, we plotted the calculated values of all individual vesicles as points on α versus D_L graphs (Figure 2a–d). The α values of DOPC and POPC vesicles seem to be weakly negatively correlated with their size, while DPPC and DSPC plots suggest the opposite trend. It is interesting to note that in all cases, most of the deviation from a horizontal, flat distribution occurs in smaller (D_L < 50 nm) vesicles, while larger ones seem to converge toward an average α value. Despite these deviations, all the examined liposome types show a relatively narrow global distribution of contact angle values at all observed diameters D_L, suggesting that the adhesion geometry of a population of vesicles with identical composition can be broadly summarized by their average α value (Figure 2e).

The Contact Angle of Adhered Vesicles Is Linked to Their Stiffness. Liposomes in the chosen series (DOPC, POPC, DPPC, and DSPC) have increasing κ values,[41−43] which in the absence of osmotic imbalances across the membrane result in a correspondingly increasing k_S trend.

We first verified this assumption via AFM-FS experiments, measuring an increasing trend of κ in the range of 9–20 k_BT and a correspondingly increasing trend of k_S values in the 10–40 mN/m range for the POPC-DPPC-DSPC series, in accordance with previously reported values obtained with this technique.[26,40] We then compared these measurements to the image analysis results described above; Figure 2e shows a comparison of the contact angle distributions for each type of liposome. All α value distributions are roughly symmetrical around a median value, which is different for each liposome and increases along the series. As hypothesized, stiffer vesicles become less oblate than softer ones upon adhesion, and their α values are on average correspondingly larger. All distributions plotted in Figure 2e are significantly different (*t* tests, all pairs, $P \leq 0.0001$). This suggests that comparing the distribution of contact angles observed via AFM imaging enables the mechanical differentiation of vesicular samples having similar size distributions.

Data reported in Figure 2 also suggest that the chosen liposome series spans over the entire range of practically measurable α values.

DOPC is the softest liposome we could successfully deposit on the employed PLL-functionalized substrates. The size distribution of intact DOPC vesicles on the surface (Figure 2a) is significantly lower than those of the other three liposomes, while it was measured to be similar to that of the POPC sample in solution (see Figure S5), suggesting that larger DOPC vesicles were either ruptured by adhesion forces or were so compliant as to be mistaken for punctured vesicles and not included in successive analysis. Moreover, even clearly intact vesicles were extremely oblate in shape, with very low H_S values. This made it necessary to lower the height threshold used to detect features during image analysis (see materials and methods). The threshold cannot of course be lowered indefinitely due to intrinsic roughness and instrumental noise; in practice, this sets ~30° as the lowest reliably measurable α values on soft vesicular objects. At the opposite end of the range, DPPC and DSPC α distributions are substantially overlapping, even if their reported κ values are quite different.[44,45] This could be explained by the fact that very stiff vesicles, only experiencing limited deformation upon interaction with the substrate, might have an insufficient contact area to provide stable adhesion, and due to this, they might detach from the surface more readily than softer vesicles when probed by the AFM tip. We indeed observed a high proportion of detachment artifacts (vesicles suddenly "disappearing" in successive scan lines) in DSPC samples.

https://dx.doi.org/10.1021/acs.analchem.9b05716
Anal. Chem. 2020, 92, 10274−10282

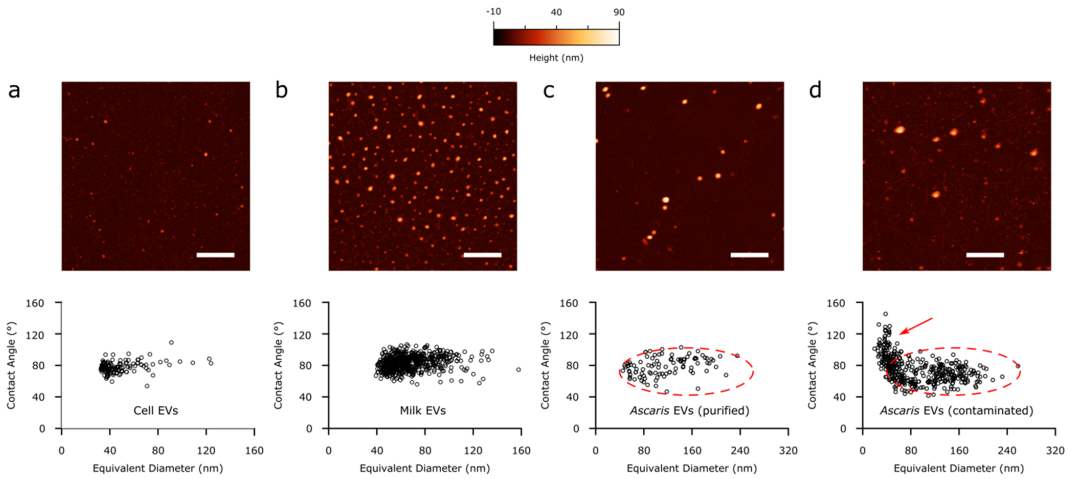

Figure 3. Representative AFM images (top row) and contact angle vs equivalent diameter scatterplots (bottom) of natural EV samples enriched from different sources. (a) EVs purified from HCT116 cell culture. (b) EVs purified from bovine milk. (c) EVs purified from *Ascaris suum* ES fractions. (d) Mycoplasma-contaminated *Ascaris suum* EVs. All purified EV samples show a relatively small dispersion of contact angles around the same average value at all sizes, resulting in horizontally elongated clusters with very weak or absent correlation between α and D_L. Nonvesicular contaminants (red arrow in panel d) do not follow this behavior and appear as an additional cluster with large contact angle variations. *Ascaris* EVs in both purified and contaminated samples appear in the same zone of the plot (panels b and c, dashed ovals).

Therefore, the α distribution of DSPC is probably biased toward lower values due to the difficulty of measuring stiffer (and weakly anchored) vesicles.

Taken together, the above considerations seem to imply that negatively charged vesicles having a stiffness between those of DOPC and DSPC should have a practically measurable α range of 30−140° when deposited on PLL-functionalized substrate and that their average α value should be a function of their k_S.

Measuring the Contact Angle of Natural EVs. The same procedure can be applied to samples containing natural vesicles. As reported by Vorselen et al.,[21] the mechanical behavior of EVs qualitatively follows that of synthetic liposomes of similar size, even in the presence of molecular cargo and integral membrane proteins. Due to this, we expect samples containing a population of EVs with small size and compositional variance to have a correspondingly small α dispersion.

We first tested the above hypothesis applying the same procedure used for liposomes on a commercially available "exosome standard" containing EVs isolated from HCT116 cell culture (see materials and methods). As expected, the resulting α versus D_L plot (Figure 3a) shows all vesicles falling in a relatively narrow range of α values regardless of their size, resulting in a horizontally elongated cluster which is indicative of vesicle-like mechanical behavior. We then repeated the analysis on natural EV samples isolated from bovine milk (Figure 3b) and from the parasitic nematode *Ascaris suum* excretory/secretory products (Figure 3c). In both cases, EVs cluster around a characteristic α value at all sizes, confirming that the purely vesicular nature of the examined samples can be mechanically assessed as previously described for liposomes.

Interestingly, the α values of all examined natural EVs seem to fall in a relatively narrow range, which corresponds to k_S values between those of POPC and DPPC liposomes: $\alpha = 83° \pm 8°$ for HCT116 EVs, $87° \pm 7°$ for bovine milk EVs, and $81° \pm 10°$ for *Ascaris* EVs. This observation is compatible with the fact that different natural vesicles can show strikingly similar mechanical properties.[17] By combining typical EV size constraints (diameter ∼40−300 nm) with observed typical EV α values (60°−100°) it is thus possible to draw the boundaries of an area in α vs D_L plot (Figure 4) which could be linked to the presence of "typical" EVs in a sample.

Contact Angle Values Can Be Used to Discriminate between EVs and Impurities. Importantly, EV-enriched samples from natural sources can contain nonvesicular contaminants which could silently bias ensemble-averaged, routine characterization techniques such as, e.g., dynamic light scattering, ζ-potential, quartz crystal microbalance, flow cytometry, and Western blot. Some types of contaminants, having a markedly different morphology from EVs (e.g., membrane patches, fibrils, pili, flagella), can be discerned from EVs by appropriate microscopy techniques, including AFM. However, a purely qualitative visual inspection approach could mistakenly identify as EVs any spurious object having the expected size distribution and a generally spherical shape (e.g., nanosized crystals, protein aggregates, polymer particles).

We propose that plotting α versus D_L distributions of an EV sample can help in assessing its purity. As discussed above, the α/D_L plot of a sample only containing compositionally similar EVs will give a horizontally elongated cluster of points characterized by an average α value. Deviations from this general behavior can be thus taken as indicative of the presence of nonvesicular contaminants.

To test the above hypothesis, we applied our purely morphometric analysis on an EV sample previously recognized as contaminated. Figure 3d shows the α/size plot of a contaminated *Ascaris suum* EV sample tested with a mycoplasma kit and found positive. The resulting "L-shaped" distribution differs significantly from a corresponding *Ascaris*

https://dx.doi.org/10.1021/acs.analchem.9b05716
Anal. Chem. 2020, 92, 10274−10282

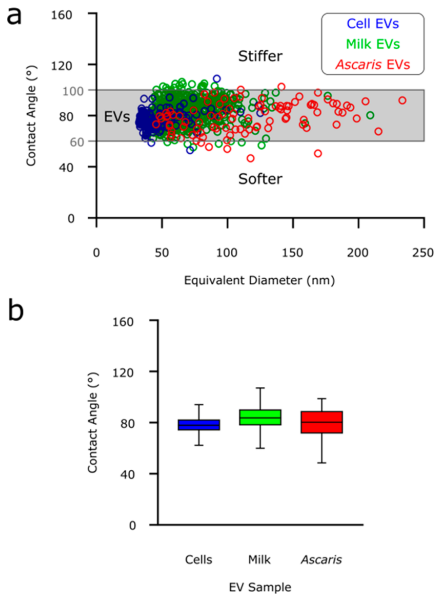

Figure 4. (a) General scheme of a contact angle vs equivalent diameter plot. The area highlighted in gray delimits values corresponding to typical mechanical behavior and size distribution of EVs deposited on a PLL substrate in ultrapure water. Individual EVs from natural sources are plotted together as blue (HCT116 cell EVs), green (milk EVs), and red (Ascaris EVs) circles. (b) Box plot comparison of EVs contact angle distributions. Boxes extend between the first (bottom edge) and third (top edge) quartile values, with black lines indicating median values. Whiskers correspond to the lowest (bottom) and highest (top) value found within the distribution. EVs from all three examined sources show a very similar stiffness.

EV sample tested negative for mycoplasma and bacteria growth (Figure 3c). Besides the expected horizontal band of points with a narrow distribution of α values (which is indicative of vesicles), an additional vertical cluster of objects with a very broad contact angle distribution is present at $D_L \sim 40$ nm. This vertical cluster of points corresponds to globular objects which were included in the morphological analysis because they could not be excluded by qualitative visual inspection alone, but which are mechanically not behaving as a single type of vesicle, thus reflecting nonvesicular contaminants in the sample. The average α value and size distributions of the horizontal clusters of Figures 3c and 3d are comparable (red dashed ovals), confirming that the two samples contain the same type of EVs. Our AFM approach can thus distinguish EVs from contaminants on the basis of their mechanical behavior and determine their respective size distributions, facilitating their characterization and successive separation.

AFM intermittent contact phase imaging or similar techniques could in principle be used to directly discriminate between globular objects with similar morphology but different physicochemical characteristics. However, we foresee that the results of these analyses would prove extremely prone to variations due to the specific AFM apparatus employed, and the results quite difficult to generalize. In our hands, the same peakforce images that allowed discriminating between EVs and contaminants using our purely morphological analysis did not provide sufficient contrast in the in-phase and quadrature channels to directly differentiate them.

Quantitative Estimation of EV Stiffness from AFM Images. To compare the results of our AFM imaging-based screening with more rigorous, FS-based nanomechanical characterization, we performed AFM-FS experiments (see Figure S1) on a series of increasingly stiffer synthetic liposomes (POPC; POPC:DPPC 1:1 mixture; DPPC; DSPC) deposited on PLL-functionalized substrates, obtaining distributions of their k_S values. We then plotted their average α versus average k_S (Figure 5), evidencing a strongly linear correlation (R^2 = 0.97). This suggests that it is possible to quantitatively estimate k_S directly from AFM imaging experiments performed on the same substrate used for a calibration line similar to Figure 5.

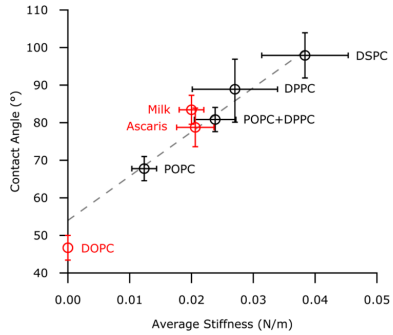

Figure 5. Quantitative correlation between average contact angle (α, measured via AFM imaging) and average stiffness (k_S, measured via AFM-FS) of vesicles deposited on PLL-functionalized glass. Black points correspond to the series of four synthetic liposomes which was used to quantify the α vs k_S dependency, showing a strong linear correlation (dashed gray line, R^2 = 0.97). Red points correspond to data not included in the linear fit (DOPC and natural EVs). All error bars represent the uncertainties obtained by bootstrapping (1000 repetitions of 5 draws, with replacement). DOPC was plotted at a k_S value of zero (see main text). The k_S of *Ascaris* and milk EVs (as measured via AFM-FS) is practically coincident with the value obtained by interpolating their average α on the liposome series fit and in both cases compatible with k_S values previously reported for other EVs from natural sources.

It is worthwhile to note that it was impossible for us to perform the full AFM-FS characterization (in terms of k_S, κ, and Π) on some of the samples. In particular, we did not observe measurable linear deformation regimes in any of the DOPC nanoindentation curves, making it impossible to measure its k_S via FS. Moreover, we could not measure F_T on *Ascaris* and milk EVs since the vast majority of retraction curves showed complex unfolding/detachment behaviors rather than clean tether elongation plateaus (see Figure S1). Nevertheless, we could easily obtain α/size plots for both samples and then estimate their expected stiffness values via extrapolation or interpolation of the linear fit shown in Figure 5.

Extrapolating the expected k_S of DOPC from its average α yields a nonphysical (negative) value. We interpreted this as a sign of a very low k_S value. Interestingly, individual approach/retraction cycles performed on intact DOPC vesicles often show clear tether elongation plateaus on the retraction curve at

https://dx.doi.org/10.1021/acs.analchem.9b05716
Anal. Chem. 2020, 92, 10274−10282

a specific F_T but no linear indentation slope on the corresponding approach curve. This suggests that the low k_S of DOPC results in very shallow indentation "slopes" which cannot be distinguished from instrumental noise. Interestingly, if we place DOPC in the α vs k_S plot (Figure 5) by assigning it a k_S value equal to 0 and then include it in the linear calibration, the correlation remains highly linear (R^2 = 0.98), further reinforcing the observation that α and k_S are strongly interdependent across a wide range of values.

We then performed the same α-based k_S extrapolation on *Ascaris* EVs, resulting in an expected stiffness value of 21 ± 4 mN/m. In this case, however, it was also possible to check extrapolation validity by directly measuring k_S via AFM-FS; the experimentally determined stiffness of 20 ± 5 mN/m coincides with the extrapolated value and is intriguingly similar to previous k_S measurements performed on other types of natural vesicles.[21,40] *Ascaris* EVs' experimental point in Figure 5, plotted at their average α (from image analysis) and k_S (from FS), is intercepted by the linear fit calculated on synthetic liposomes. The same experimental procedure was then replicated on milk EVs, obtaining strikingly similar results (k_S = 20 ± 7 mN/m, see Figure 5). Taken together, these observations suggest that the same strong correlation between α and k_S observed in liposomes is also valid for EVs and that it is thus possible to obtain a quantitative estimate of their stiffness directly from AFM image analysis, without resorting to more time-consuming FS studies. According to this reasoning, the "most typical" natural EV α value of 80° (Figure 4) corresponds to a k_S value of ∼20 mN/m.

Conclusion and Perspectives. We have herein described an AFM-based experimental strategy for the nanomechanical and morphological screening of nanosized vesicles. By the application of a set of simple experimental precautions and image analysis steps to AFM scans performed in liquid, the proposed procedure makes it possible to discriminate between vesicular and nonvesicular objects in a sample. Furthermore, it allows quantitative size and stiffness estimates for each observed vesicle. Although unable to reach the level of detail afforded by FS-based mechanical assessment methods[21,26] previously employed on EVs, the approach proposed here has the advantages of being considerably faster and easier to perform and of having limited instrumental requirements. Our results also suggest that our approach remains applicable in cases where FS-based approaches might fail.

When studied with our methodology, EVs isolated from three very different natural sources showed a similar stiffness, which is strikingly close to those previously measured on EVs from other sources.[17,21] This supports the hypothesis that the mechanical characteristics of EVs might be generally tuned for optimal diffusion velocity and deformability.[46,47] Given the wide spectrum of functions performed by EVs, ranging from cell homeostasis regulation to environmental stress-dependent signaling to extracellular matrix remodeling, the above hypothesis, if confirmed, would prove rather puzzling. We cannot of course exclude that EVs isolated from other sources might have more pronounced mechanical differences than those analyzed in our study, which would facilitate their mechanical differentiation.

Being based on the quantitative measurement of contact angles of vesicles adhered to a surface, our method could be extended to other substrates in addition to the PLL-functionalized glass slides employed in this study. This could be functional in modulating surface/vesicle adhesion forces, thus making it possible to better explore vesicles softer than DOPC or stiffer than DSPC by bringing them into the measurable α range or by extending it to the study of positively charged artificial vesicles. Its ability to quickly give a quantitative readout of the interaction between a vesicular object and a nanoengineered surface could be a valid support in developing more quantitative and more reproducible bionanomaterial research studies focusing on or involving the bionanointerface.[48]

Lastly, the geometrical parameters H_S and R_{Proj} can be also used to calculate the volume of each individual adsorbed vesicle in an AFM image. Similarly to how α is linked to k_S, any measured loss of volume induced by surface adhesion may be linked to Π; it might be thus possible to estimate lumen pressurization without resorting to complex FS experiments. We plan to explore this possibility in forthcoming studies.

In summary, we described a simple AFM-based characterization strategy that can be implemented for the nanomechanical and morphological screening of samples enriched in nanosized EVs. We showed that this method can be used to discriminate between EVs and non-EV contaminants and that it enables the high-throughput quantitative nanomechanical measurement of individual EVs, offering a simple way to implement a multiparametric characterization of EVs with nanomechanical information.

■ ASSOCIATED CONTENT

Supporting Information

The Supporting Information is available free of charge at https://pubs.acs.org/doi/10.1021/acs.analchem.9b05716.

Additional details on (i) synthetic and natural vesicles preparation, purification, and deposition; (ii) trigonometry calculations; (iii) mechanical characterization of individual vesicles by AFM force spectroscopy; (iv) AFM imaging and morphometry analysis; (v) influence of AFM probe on the nanomechanical characterization of vesicles; (vi) robustness of the image analysis procedure with respect to imaging quality; dynamic light scattering (DLS), and zeta potential characterization of liposomes; (vii) characterizations of EVs from natural sources (PDF)

■ AUTHOR INFORMATION

Corresponding Authors

Marco Brucale − *Consorzio Interuniversitario per lo Sviluppo dei Sistemi a Grande Interfase, 50019 Firenze, Italy; Consiglio Nazionale delle Ricerche, Istituto per lo Studio dei Materiali Nanostrutturati, 40129 Bologna, Italy;* orcid.org/0000-0001-7244-4389; Email: marco.brucale@cnr.it

Francesco Valle − *Consorzio Interuniversitario per lo Sviluppo dei Sistemi a Grande Interfase, 50019 Firenze, Italy; Consiglio Nazionale delle Ricerche, Istituto per lo Studio dei Materiali Nanostrutturati, 40129 Bologna, Italy;* orcid.org/0000-0001-5793-7206; Email: francesco.valle@cnr.it

Authors

Andrea Ridolfi − *Consorzio Interuniversitario per lo Sviluppo dei Sistemi a Grande Interfase, 50019 Firenze, Italy; Consiglio Nazionale delle Ricerche, Istituto per lo Studio dei Materiali Nanostrutturati, 40129 Bologna, Italy; Dipartimento di Chimica "Ugo Schiff", Università degli Studi di Firenze, 50019 Firenze, Italy*

https://dx.doi.org/10.1021/acs.analchem.9b05716
Anal. Chem. 2020, 92, 10274−10282

Costanza Montis − *Consorzio Interuniversitario per lo Sviluppo dei Sistemi a Grande Interfase, 50019 Firenze, Italy; Dipartimento di Chimica "Ugo Schiff", Università degli Studi di Firenze, 50019 Firenze, Italy;* orcid.org/0000-0001-6960-3772

Lucrezia Caselli − *Dipartimento di Chimica "Ugo Schiff", Università degli Studi di Firenze, 50019 Firenze, Italy*

Lucia Paolini − *Consorzio Interuniversitario per lo Sviluppo dei Sistemi a Grande Interfase, 50019 Firenze, Italy; Dipartimento di Medicina Molecolare e Traslazionale, Università degli Studi di Brescia, 25123 Brescia, Italy;* orcid.org/0000-0002-4410-5272

Anne Borup − *Department of Clinical Medicine, Faculty of Health, Aarhus University, 8200 Aarhus, Denmark*

Anders T. Boysen − *Department of Clinical Medicine, Faculty of Health, Aarhus University, 8200 Aarhus, Denmark;* orcid.org/0000-0002-0192-1413

Francesca Loria − *HansaBiomed Life Sciences, 12618 Tallinn, Estonia*

Martijn J. C. van Herwijnen − *Department of Biochemistry & Cell Biology, Faculty of Veterinary Medicine, Utrecht University, 3584 CM Utrecht, The Netherlands*

Marije Kleinjan − *Department of Biochemistry & Cell Biology, Faculty of Veterinary Medicine, Utrecht University, 3584 CM Utrecht, The Netherlands*

Peter Nejsum − *Department of Clinical Medicine, Faculty of Health, Aarhus University, 8200 Aarhus, Denmark*

Natasa Zarovni − *HansaBiomed Life Sciences, 12618 Tallinn, Estonia*

Marca H. M. Wauben − *Department of Biochemistry & Cell Biology, Faculty of Veterinary Medicine, Utrecht University, 3584 CM Utrecht, The Netherlands*

Debora Berti − *Consorzio Interuniversitario per lo Sviluppo dei Sistemi a Grande Interfase, 50019 Firenze, Italy; Dipartimento di Chimica "Ugo Schiff", Università degli Studi di Firenze, 50019 Firenze, Italy;* orcid.org/0000-0001-8967-560X

Paolo Bergese − *Consorzio Interuniversitario per lo Sviluppo dei Sistemi a Grande Interfase, 50019 Firenze, Italy; Dipartimento di Medicina Molecolare e Traslazionale, Università degli Studi di Brescia, 25123 Brescia, Italy;* orcid.org/0000-0002-4652-2168

Complete contact information is available at: https://pubs.acs.org/10.1021/acs.analchem.9b05716

Author Contributions

The manuscript was written through contributions of all authors. All authors have given approval to the final version of the manuscript.

Notes

The authors declare no competing financial interest.

■ ACKNOWLEDGMENTS

This research has received funding from the Horizon 2020 Framework Programme under the grant FETOPEN-801367 evFOUNDRY. P.N. was supported by a grant from Independent Research Fund Denmark (DFF-6111-00521). We thank the SPM@ISMN research facility for support in the AFM experiments.

■ REFERENCES

(1) van Niel, G.; D'Angelo, G.; Raposo, G. *Nat. Rev. Mol. Cell Biol.* **2018**, *19*, 213−228.
(2) Yanez-Mo, M.; et al. *J. Extracell. Vesicles* **2015**, *4*, 27066.
(3) Galieva, L. R.; James, V.; Mukhamedshina, Y. O.; Rizvanov, A. A. *Front. Neurosci.* **2019**, *13*, 13.
(4) Mardahl, M.; Borup, A.; Nejsum, P. *Adv. Parasitol.* **2019**, *104*, 39−112.
(5) Ostenfeld, M. S.; et al. *Cancer Res.* **2014**, *74*, 5758−5771.
(6) Roy, S.; Hochberg, F. H.; Jones, P. S. *J. Extracell. Vesicles* **2018**, *7*, 1438720.
(7) van Herwijnen, M. J. C.; Driedonks, T. A. P.; Snoek, B. L.; Kroon, A. M. T.; Kleinjan, M.; Jorritsma, R.; Pieterse, C. M. J.; Hoen, E. N. M. N.; Wauben, M. H. M. *Front Nutr* **2018**, *5*, 5.
(8) Vescovi, R.; et al. *Cancer Immunol. Res.* **2019**, *7*, 12−28.
(9) Xu, R.; Rai, A.; Chen, M. S.; Suwakulsiri, W.; Greening, D. W.; Simpson, R. J. *Nat. Rev. Clin. Oncol.* **2018**, *15*, 617−638.
(10) Thery, C. *J. Extracell. Vesicles* **2018**, *7*, 1535750.
(11) Cocucci, E.; Meldolesi, J. *Trends Cell Biol.* **2015**, *25*, 364−372.
(12) Jeppesen, D. K.; Hvam, M. L.; Primdahl-Bengtson, B.; Boysen, A. T.; Whitehead, B.; Dyrskjot, L.; Orntoft, T. F.; Howard, K. A.; Ostenfeld, M. S. *J. Extracell. Vesicles* **2014**, *3*, 25011.
(13) Montis, C.; Zendrini, A.; Valle, F.; Busatto, S.; Paolini, L.; Radeghieri, A.; Salvatore, A.; Berti, D.; Bergese, P. *Colloids Surf., B* **2017**, *158*, 331−338.
(14) Shao, H. L.; Im, H.; Castro, C. M.; Breakefield, X.; Weissleder, R.; Lee, H. H. *Chem. Rev.* **2018**, *118*, 1917−1950.
(15) Paolini, L.; Zendrini, A.; Radeghieri, A. *Biomarkers Med.* **2018**, *12*, 383−391.
(16) Chiang, C. Y.; Chen, C. C. Toward characterizing extracellular vesicles at a single-particle level. *J. Biomed. Sci.* **2019**, *26*. DOI: 10.1186/s12929-019-0502-4.
(17) Sorkin, R.; Huisjes, R.; Boskovic, F.; Vorselen, D.; Pignatelli, S.; Ofir-Birin, Y.; Leal, J. K. F.; Schiller, J.; Mullick, D.; Roos, W. H.; Bosman, G.; Regev-Rudzki, N.; Schiffelers, R. M.; Wuite, G. J. L. *Small* **2018**, *14*, 1801650.
(18) Calo, A.; Reguera, D.; Oncins, G.; Persuy, M. A.; Sanz, G.; Lobasso, S.; Corcelli, A.; Pajot-Augy, E.; Gomila, G. *Nanoscale* **2014**, *6*, 2275−2285.
(19) Parisse, P.; Rago, I.; Severino, L. U.; Perissinotto, F.; Ambrosetti, E.; Paoletti, P.; Ricci, M.; Beltrami, A. P.; Cesselli, D.; Casalis, L. *Eur. Biophys. J.* **2017**, *46*, 813−820.
(20) Sharma, S.; Rasool, H. I.; Palanisamy, V.; Mathisen, C.; Schmidt, M.; Wong, D. T.; Gimzewski, J. K. *ACS Nano* **2010**, *4*, 1921−1926.
(21) Vorselen, D.; van Dommelen, S. M.; Sorkin, R.; Piontek, M. C.; Schiller, J.; Dopp, S. T.; Kooijmans, S. A. A.; van Oirschot, B. A.; Versluijs, B. A.; Bierings, M. B.; van Wijk, R.; Schiffelers, R. M.; Wuite, G. J. L.; Roos, W. H. *Nat. Commun.* **2018**, *9*, 9.
(22) Krieg, M.; Fläschner, G.; Alsteens, D.; Gaub, B. M.; Roos, W. H.; Wuite, G. J. L.; Gaub, H. E.; Gerber, C.; Dufrêne, Y. F.; Müller, D. J. *Nature Reviews Physics* **2019**, *1*, 41−57.
(23) Whitehead, B.; Wu, L.; Hvam, M. L.; Aslan, H.; Dong, M.; Dyrskjøt, L.; Ostenfeld, M. S.; Moghimi, S. M.; Howard, K. A. *J. Extracell. Vesicles* **2015**, *4*, 29685−29685.
(24) Canham, P. B. *J. Theor. Biol.* **1970**, *26*, 61−81.
(25) Helfrich, W. *Z. Naturforsch., C: J. Biosci.* **1973**, *28*, 693−703.
(26) Vorselen, D.; MacKintosh, F. C.; Roos, W. H.; Wuite, G. J. L. *ACS Nano* **2017**, *11*, 2628−2636.
(27) Valle, F.; Brucale, M.; Chiodini, S.; Bystrenova, E.; Albonetti, C. *Micron* **2017**, *100*, 60−72.
(28) Seifert, U.; Lipowsky, R. *Phys. Rev. A: At., Mol., Opt. Phys.* **1990**, *42*, 4768−4771.
(29) Jackman, J. A.; Choi, J. H.; Zhdanov, V. P.; Cho, N. J. *Langmuir* **2013**, *29*, 11375−11384.
(30) Buzas, E. I.; Toth, E. A.; Sodar, B. W.; Szabo-Taylor, K. E. *Semin. Immunopathol.* **2018**, *40*, 453−464.
(31) Deregibus, M. C.; Figliolini, F.; D'antico, S.; Manzini, P. M.; Pasquino, C.; De Lena, M.; Tetta, C.; Brizzi, M. F.; Camussi, G. *Int. J. Mol. Med.* **2016**, *38*, 1359−1366.
(32) Konoshenko, M. Y.; Lekchnov, E. A.; Vlassov, A. V.; Laktionov, P. P. *BioMed Res. Int.* **2018**, *2018*, 1.

(33) Reviakine, I.; Gallego, M.; Johannsmann, D.; Tellechea, E. *J. Chem. Phys.* **2012**, *136*, 084702.
(34) Piontek, M. C.; Lira, R. B.; Roos, W. H. *Biochim. Biophys. Acta, Gen. Subj.* **2019**, 129486.
(35) Et-Thakafy, O.; Delorme, N.; Gaillard, C.; Meriadec, C.; Artzner, F.; Lopez, C.; Guyomarc'h, F. *Langmuir* **2017**, *33*, 5117−5126.
(36) Yokota, S.; Kuramochi, H.; Okubo, K.; Iwaya, A.; Tsuchiya, S.; Ichiki, T. *PLoS One* **2019**, *14*, e0224091.
(37) Chernyshev, V. S.; Rachamadugu, R.; Tseng, Y. H.; Belnap, D. M.; Jia, Y.; Branch, K. J.; Butterfield, A. E.; Pease, L. F., 3rd; Bernard, P. S.; Skliar, M. *Anal. Bioanal. Chem.* **2015**, *407*, 3285−3301.
(38) Skliar, M.; Chernyshev, V. S.; Belnap, D. M.; Sergey, G. V.; Al-Hakami, S. M.; Bernard, P. S.; Stijleman, I. J.; Rachamadugu, R. *Biochem. Biophys. Res. Commun.* **2018**, *501*, 1055−1059.
(39) Skliar, M.; Chernyshev, V. S. *J. Visualized Exp.* **2019**, *151*, e59254.
(40) Li, S.; Eghiaian, F.; Sieben, C.; Herrmann, A.; Schaap, I. A. T. *Biophys. J.* **2011**, *100*, 637−645.
(41) Dimova, R. *Adv. Colloid Interface Sci.* **2014**, *208*, 225−234.
(42) Nagle, J. F. *Faraday Discuss.* **2013**, *161*, 11−29.
(43) Yi, Z.; Nagao, M.; Bossev, D. P. *J. Phys.: Condens. Matter* **2009**, *21*, 155104.
(44) Fernandezpuente, L.; Bivas, I.; Mitov, M. D.; Meleard, P. *Europhys. Lett.* **1994**, *28*, 181−186.
(45) Marsh, D. *Chem. Phys. Lipids* **2006**, *144*, 146−159.
(46) Dai, Z.; Yu, M. R.; Yi, X.; Wu, Z. M.; Tian, F. L.; Miao, Y. Q.; Song, W. Y.; He, S. F.; Ahmad, E.; Guo, S. Y.; Zhu, C. L.; Zhang, X. X.; Li, Y. M.; Shi, X. H.; Wang, R.; Gan, Y. *ACS Nano* **2019**, *13*, 7676−7689.
(47) Yu, M. R.; Song, W. Y.; Tian, F. L.; Dai, Z.; Zhu, Q. L.; Ahmad, E.; Guo, S. Y.; Zhu, C. L.; Zhong, H. J.; Yuan, Y. C.; Zhang, T.; Yi, X.; Shi, X. H.; Gan, Y.; Gao, H. J. *Proc. Natl. Acad. Sci. U. S. A.* **2019**, *116*, 5362−5369.
(48) Faria, M.; Bjornmalm, M.; Thurecht, K. J.; Kent, S. J.; Parton, R. G.; Kavallaris, M.; Johnston, A. P. R.; Gooding, J. J.; Corrie, S. R.; Boyd, B. J.; Thordarson, P.; Whittaker, A. K.; Stevens, M. M.; Prestidge, C. A.; Porter, C. J. H.; Parak, W. J.; Davis, T. P.; Crampin, E. J.; Caruso, F. *Nat. Nanotechnol.* **2018**, *13*, 777−785.

https://dx.doi.org/10.1021/acs.analchem.9b05716
Anal. Chem. 2020, 92, 10274−10282

Supplementary Material for

AFM-based High-Throughput Nanomechanical Screening of Single Extracellular Vesicles

Andrea Ridolfi[1,2,3], Marco Brucale*[1,2], Costanza Montis[1,3], Lucrezia Caselli[3], Lucia Paolini[1,4], Anne Borup[5], Anders T. Boysen[5], Francesca Loria[6], Martijn J. C. van Herwijnen[7], Marije Kleinjan[7], Peter Nejsum[5], Natasa Zarovni[6], Marca H. M. Wauben[7], Debora Berti[1,3], Paolo Bergese[1,4], Francesco Valle*[1,2]

[1] Consorzio Interuniversitario per lo Sviluppo dei Sistemi a Grande Interfase (CSGI), Firenze, Italy

[2] Consiglio Nazionale delle Ricerche, Istituto per lo Studio dei Materiali Nanostrutturati (CNR-ISMN), Bologna, Italy

[3] Dipartimento di Chimica "Ugo Schiff", Università degli Studi di Firenze, Firenze, Italy

[4] Dipartimento di Medicina Molecolare e Traslazionale, Università degli Studi di Brescia, Brescia, Italy

[5] Department of Clinical Medicine, Faculty of Health, Aarhus University, Aarhus, Denmark

[6] HansaBiomed Life Sciences, Tallinn, Estonia

[7] Department of Biochemistry & Cell Biology, Faculty of Veterinary Medicine, Utrecht University, Utrecht, The Netherlands

Table of contents:

Experimental details, materials and methods

Liposomes Preparation and Characterization

Different lipids with PC polar headgroup (DOPC (1,2-dioleoyl-sn-glycero-3-phosphocholine), POPC (1-palmitoyl-2-oleoyl-glycero-3-phosphocholine), DPPC (1,2-dipalmitoyl-sn-glycero-3-phosphocholine), DSPC (1,2-1,2-distearoyl-sn-glycero-3-phosphocholine)) were purchased from Sigma Aldrich (St. Louis, MO, USA); lipid dry powders were dispersed in defined amounts of chloroform, to prepare stock solutions. Lipid films were obtained by evaporating appropriate amounts of lipid stock solutions in chloroform under a stream of nitrogen, followed by overnight drying under vacuum. The films were swollen by suspension in warm (50 °C) milliQ water to a final lipid concentration of 4 mg/mL, followed by vigorous vortex mixing. The dispersions were then tip-sonicated for 15min to obtain a dispersion of unilamellar lipid vesicles. The size distribution and Zeta Potential of the vesicles was determined through Dynamic Light Scattering and Zeta Potential measurements, respectively (see Figure S5).

Natural Vesicles Isolation and Purification

EVs from Human Colorectal Carcinoma cell line HCT116 were obtained from HansaBioMed Life Sciences Ltd. (Cat. HBM-HCT-30/2); EVs from other natural sources were enriched as described below. All EV data were acquired and reported following MISEV 2018 and MIRABEL international guidelines [Faria 2018; Thery 2018]. Relevant data were also submitted to the EV-TRACK [Van Deun 2017] knowledge base (EV-TRACK ID: EV190077).

EVs from bovine milk

Raw milk (100 ml) was collected from the cooled tank from a local dairy farm (Tolakker, Utrecht, The Netherlands), transferred to 50 ml polypropylene tubes and centrifuged for 10 minutes at 22°C at 3000 xg (Beckman Coulter Allegra X-12R, Fullerton, CA, USA). After removal of the cream layer, the milk supernatant was harvested without disturbing the pellet and transferred to new tubes. A second centrifugation step at 3000 xg followed, after which the milk supernatant was collected and stored at -80°C until further processing. Thawed milk supernatant (80 ml) was transferred to polyallomer SW40 tubes (Beckman Coulter) and centrifuged at 5000 xg for 30 minutes at 4°C and subsequently at 10000 xg (Beckman Coulter Optima L-90K with a SW40Ti rotor). For the precipitation of caseins, the milk supernatant was acidified to pH 4.6 by adding Hydrochloric acid (HCl, 1M) while stirring. Caseins were pelleted by centrifugation at 360 xg (Beckman Coulter Allegra X-12R) after which casein-free milk supernatant was collected. Next, 6.5 ml of the milk 10000 xg supernatant was loaded on top of a 60% – 10% Optiprep gradient (OptiprepTM, Progen Biotechnik GmbH, Heidelberg, Germany) made in a SW40 tube. Gradients were ultracentrifuged at 197000 xg (Beckman Coulter Optima L-90K with a SW40Ti rotor) for 15-18 h. After centrifugation, fractions of 500 µl were harvested and densities were measured in order to identify the EV-containing fractions with 1.06-1.19 g/ml, which were pooled. Optiprep was exchanged for PBS by using size exclusion chromatography on the EV-containing fractions pooled in a 20 ml column (Bio-Rad Laboratories, Hercules, CA, USA) packed with 15 ml Sephadex g100 (Sigma-Aldrich, St. Louis, MO, USA). Fractions of 1 ml with eluted from the column by washing with PBS (GibcoTM, Invitrogen, Carlsbad, CA, USA). Eluates 3 to 9 were pooled as these contained EVs and samples were stored at -80°C until use.

EVs from Ascaris suum

Live adult *Ascaris suum* nematodes were obtained from pigs slaughtered at the Danish Crown abattoir in Herning, Denmark. Five worms, two males and three females, were put in a T175 flask and washed in 175 ml RPMI-1640 with 1X Antibiotic-Antimycotic (Thermo Fisher Scientific; Cat.: 15240062) and 1 µg/ml ciprofloxacin (Sigma; Cat.: 17850) (RPMI-Anti/Anti) in a total of four cycles of 15 minutes followed by three cycles of one hour of incubation at 37 °C. After washing, the worms were incubated in 175 ml RPMI-Anti/Anti for 72h in a 5% CO2 incubator at 37 °C. The media containing excretory/secretory (ES) products from the worms was exchanged and collected every 24 hours. The collected ES products were stored at -80 °C. ES products from all three days were thawed at 4 °C and pooled to be concentrated 720 times with Amicon® Ultra-15 Centrifugal Filter Unit 10 kDa cut-off (Merck; Cat.: UFC901024). The concentrate was used for EV separation.

To separate EVs, two different methods were used: ultracentrifugation (UC) and size exclusion chromatography (SEC). Ultracentrifugation procedure: 500 µl of the concentrated ES products were transferred to polycarbonate ultracentrifuge tubes with cap assembly (Beckman Coulter; Cat.: 355603) and diluted with PBS 1X to a final volume of 10 ml. Total volume was centrifuged at 10000 xg for 30 minutes at 4°C at 10000 xg for 30 minutes at 4 °C (Beckman Coulter Optima L-80 XP Ultracentrifuge, TI 50 rotor kept at 4°). Supernatant (approx. 10 ml) was transferred to a new polycarbonate ultracentrifuge tube and centrifuged at 100000 xg for 70 minutes at 4°C (Beckman Coulter Optima L-80 XP Ultracentrifuge, TI 50 rotor kept at 4°C). The pellet was then dissolved in 10 ml of PBS 1X and re-centrifuged at 100000 xg for 70 minutes at 4°C. Final pellet was resuspended in 2 ml PBS 1X, transferred to an Eppendorf tube and stored at -80°C. SEC procedure: EVs were separated using qEVoriginal/70 nm columns from iZON (iZON Science Ltd; Cat.: SP1) according to manufacturing instructions using PBS 1X as buffer. Twenty-four fractions of 500 µl were collected. The fractions 7-10 were pooled as EV-containing fraction and stored at -80°C.

EV characterization

EV preparations from bovine milk and *Ascaris suum* were characterized for purity from protein contaminants and titrated by Colorimetric Nanoplasmonic Assay (CONAN) assay (Supplementary Table ST1). EV size distribution was in addition determined by Nanoparticle Tracking Analysis (NTA) for samples from *Ascaris suum* E/S (Supplementary Figures S6-S8). Protein composition was analyzed by Western blot. It is to note that the biochemical characterization can be performed only on bovine milk derived EVs, since no specific protein markers have been identified for *Ascaris suum* samples so far. The presence of EV-associated markers, and non-EV markers is presented in Supplementary Figure S9. Characterization protocol details and results are reported below.

Surface Preparation and Sample Deposition

All AFM experiments were performed on poly-L-lysine (PLL) coated glass coverslips. All reagents were acquired from Sigma-Aldrich Inc (www.sigmaaldrich.com) unless otherwise stated. Microscopy glass slides (15mm diameter round coverslips, Menzel Gläser) were cleaned in a sonicator bath (Elmasonic Elma S30H) for 30 minutes in acetone, followed by 30 minutes in isopropanol and 30 minutes in ultrapure water (Millipore Simplicity UV). Clean slides were incubated overnight in a 0.0001% (w/v) PLL solution at room

temperature, thoroughly rinsed with ultrapure water and dried with nitrogen. The water contact angle (1µl droplets at ~25°C, measured with a GBX DigiDrop goniometer) of slides was 26°±1° prior to functionalization and 20°±2° after PLL deposition.

A 10 µl-droplet of the vesicle-containing solution under study was deposited on a PLL-functionalized glass slide and left to adsorb for 10 minutes at 4°C, then inserted in the AFM fluid cell (see below) without further rinsing. The concentration of each vesicle-containing solution was adjusted by trial and error in successive depositions in order to maximize the surface density of isolated, individual vesicles and minimize clusters of adjoining vesicles.

AFM setup

All AFM experiments were performed in ultrapure water at room temperature on a Bruker Multimode8 (equipped with Nanoscope V electronics, a sealed fluid cell and a type JV piezoelectric scanner) using Bruker SNL-A probes (triangular cantilever, nominal tip curvature radius 2-12 nm, nominal elastic constant 0.35 N/m) calibrated with the thermal noise method [Hutter 1993].

AFM Imaging

Imaging was performed in PeakForce mode. In order to minimize vesicle deformation or rupture upon interaction with the probe, the applied force setpoint was kept in the 150-250 pN range. Lateral probe velocity was not allowed to exceed 5µm/s. Feedback gain was set at higher values than those usually employed for optimal image quality in order to ensure minimal probe-induced vesicle deformation upon lateral contact along the fast scan axis.

This type of parameter optimization resulted in images with comparatively high noise levels in the empty areas of the surface (≤20nm peak to peak), but in which the height profiles of individual vesicles measured along both the slow and the fast scan axis could be fitted extremely well with circular arcs (Figure S1c). The average height value of all bare substrate zones was taken as the baseline zero height reference.

Image background subtraction was performed using Gwyddion 2.53 [Necas 2012]. Image analysis was performed with a combination of Gwyddion and custom Python scripts, but it can be easily carried out manually by only using functions included in Gwyddion and a spreadsheet.

AFM force spectroscopy

The mechanical characterization of vesicles via AFM force spectroscopy was performed following the approach recently described in [Vorselen 2017]. The sample was first scanned (see previous paragraph) to locate individual vesicles (Figure S1a). The chosen vesicle was then imaged (Figure S1b) at higher resolution (~500x500 nm scan, 512x512 points); its height profile along the slow scan axis was fitted with a circular arc only taking into account values 10nm above the bare substrate (typical fit $R^2 \geq 0.95$). This procedure yielded, for each vesicle, an apparent fitted curvature radius R_C and a vesicle height value H_S (Figure S1c), which were corrected as described elsewhere [Vorselen 2017].

In principle, it would be sufficient to record the force/distance plot of just one approach/retraction cycle for each vesicle measured at its highest point, while avoiding membrane puncturing. In our hands however, this was practically impossible due to intrinsic piezo inaccuracy and drift, which imply a certain degree of

uncertainty on both the XY position at which the force curve is performed relative to the original image, and on the maximum applied force.

To overcome this limitation, we recorded a series of force/distance curves at multiple XY positions (typically around 64-100 curves arranged in a square array covering the vesicle initial location Figure S1b, green crosses) for each individual vesicle. In most cases, only a few curves showed the full mechanical fingerprint of an intact vesicle on both the approach and retraction cycles (Figure S1d), showing a linear deformation upon applied pressure and a tether elongation plateau during probe retraction. Of these, we first discarded those with probe-vesicle contact points (P_C) occurring at probe-surface distances below vesicle height as measured by imaging ($P_C < H_S$, see previous paragraph). We then discarded traces in which the tether elongation plateau occurring during probe retraction did not extend beyond initial contact point. However, we relaxed this requirement for those natural vesicle samples on which obtaining clean tether plateaus was nearly impossible (see results and discussion section).

Remaining traces (typically 1-3 per vesicle) were analyzed to calculate vesicle stiffness (k_S) and tether elongation force (F_T). Multiple valid curves referring to the same vesicle resulted in very narrow distributions of both k_S and F_T (with average measured values taken as representative for each vesicle), while different vesicles of the same type showed much larger variations (see below). Membrane bending modulus (κ) and internal pressurization (Π) values were then calculated for each individual vesicle using its R_C, k_S and F_T values as described in [Vorselen 2017].

Trigonometry calculations

The contact angle value α is always calculated from H_S and R_{Cap} as follows:

(1) $$\alpha = 90 - \sin^{-1}((R_{Cap} - H_S)/R_{Cap})$$

H_S is directly obtained from AFM images; R_{Cap} and A_S are calculated from H_S and R_{Proj} as follows:

(2) If $R_{Proj} > H_S$, $R_{Proj} \approx A_{Cap}$; $R_{Cap} = \frac{H_S^2 + R_{Proj}^2}{2H_S}$; $A_S = \pi\left(2R_{Proj}^2 + H_S^2\right)$

(3) If $R_{Proj} < H_S$, $R_{Proj} \approx R_{Cap}$; $A_S = \pi H_S\left(4R_{Proj} - H_S\right)$

Finally, the vesicle's diameter in solution D_L, assuming $A_L = A_S$, is

(4) $$D_L = 2\sqrt{\frac{A_S}{4\pi}}$$

Supporting Figure S1

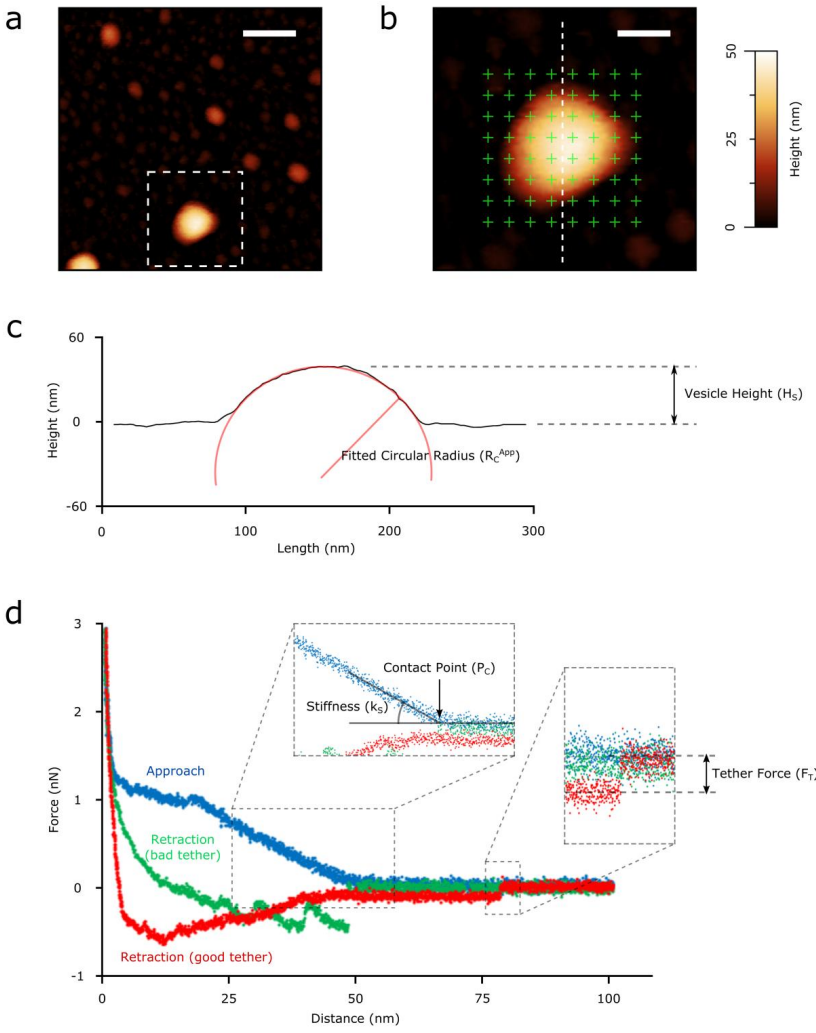

Mechanical characterization of individual vesicles by AFM force spectroscopy was performed following the approach recently suggested by Vorselen et al. [ref Vorselen 2017 in main text]. (a): As a first step, larger areas (scalebar 1µm) were scanned to locate individual isolated vesicles (in this case, a POPC vesicle). (b): The selected vesicle was then imaged at higher resolution (~500x500 nm scan, 512x512 points) to accurately characterize its morphology and to perform force spectroscopy approach/retraction cycles. To avoid intrinsic drifting problems of the piezo and also to gain a more robust estimate of the overall response of the vesicle, multiple indentations were performed following the points on a grid (green crosses) drawn on the vesicle and its surroundings. (c): The height profile along the slow scan axis is fitted with a circle to obtain the curvature radius R_C^{App} which is then corrected for tip convolution (see Figure S2)

and used in the normalization of the values of stiffness and internal pressure. Vesicle height H_S is also measured. (d): Typical force/distance curves recorded during approach and retraction FS cycles performed on a single vesicular object. In the approach (blue) curve, applied force remains zero until the tip first touches the vesicle at Contact Point P_C, then increases during vesicle indentation. All the curves that showed interactions at Distance values lower than the height H_S observed in the previous imaging step were discarded. According to CHM theory [main text refs Canham 1970; Helfrich 1973], the initial mechanical response of the vesicle to indentation is elastic and linear; the application of a linear fit to this portion of the curve yields the stiffness k_S of the vesicle. The red trace describes the retraction of the tip from the sample and is characterized by the formation of a membrane tether that is pulled by the tip beyond the initial contact point ending with a sharp return to the initial zero force value. The force value measured before this rapid variation is the tether elongation force F_T. All the retraction curves that did not resemble the event of tether formation described by the red trace were not considered in the analysis. Obtaining force curves unambiguously showing tether elongations is one of the main issues for the successful application of this FS method to EVs. As exemplified by the green trace, in most retraction traces following the indentation of an EV the presence of abundant membrane proteins and/or peptidoglycans causes the appearance of multiple unfolding/detachment/rupture events (absent in synthetic liposomes) which often avoid the formation and/or identification of single membrane tethers.

Supporting Figure S2

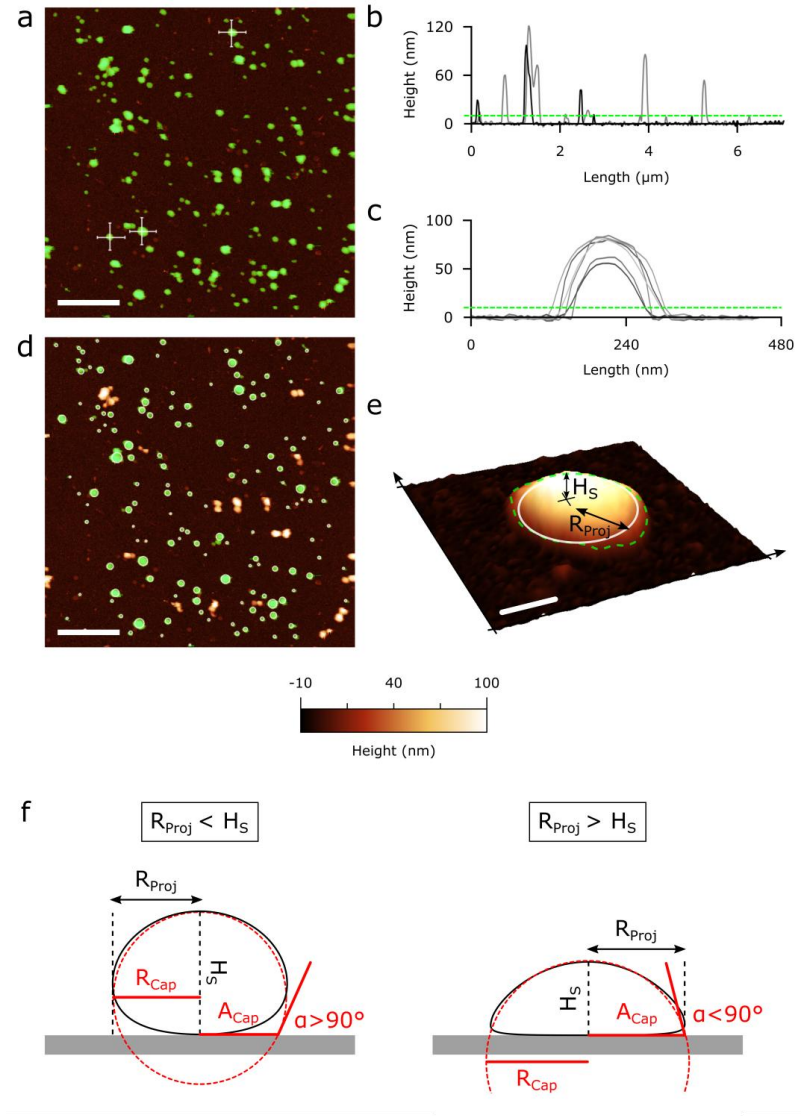

AFM imaging and morphometry analysis. (a): representative AFM micrograph of a DPPC liposome sample deposited on a PLL-functionalized substrate. Scalebar = 1µm. Correct background subtraction is crucial to successive image analysis steps (see materials and methods) and is first checked by plotting height profiles measured along the two diagonals of the whole image (b): after proper flattening, diagonal profiles must show a flat baseline centered at height=0 with positive features. To minimize probe-induced vesicle deformation, imaging should be preferentially performed at low applied load (<250 pN) and high feedback gain (see main text, materials and methods). (c): Profiles of putative vesicles measured along fast and slow

scan axes (panel a, white lines) should be roughly symmetrical and superimposable, indicating minimal mechanical perturbation due to scanning. Circular arcs are typically able to fit to random profiles of vesicles with an $R^2 \geq 0.99$ when discarding the substrate-proximal region (see below). (a,b,c): based on the observed signal/noise ratio, an height threshold (green mask in panel a, dashed line in panels b and c) is utilized to separate features subjected to successive analysis steps from the background. A threshold of 10 nm was used in most cases. (d): If present, manifestly non-globular impurities or imaging artifacts are manually excluded from the analysis. Mutually- or edge-touching globular objects are also discarded. For each remaining globule (green mask), the largest inscribable disc is then plotted (white circles), discarding objects having inscribed disc radii below 10 nm. (e): Each remaining object is considered a putative vesicle, and its morphology is parametrized with two quantities measured from its AFM image: the corrected (see Figure S2) radius R_{Proj} of the largest possible disc (white circle) inscribed within the boundary delimited by the height threshold (green dashed line), and the highest Z value occurring within it, H_S. Scalebar is 75 nm. (f): Geometrical approximation of the spheroid shape of a surface-adhered vesicle with a spherical cap having height H_S, surface radius A_{Cap} and spherical radius R_{Cap}. While H_S is always directly measured on the AFM image (see panel e), R_{Cap} and A_{Cap} are calculated from as follows: if $R_{Proj} < H_S$, R_{Proj} is taken as a good approximation of R_{Cap}; and when $R_{Proj} > H_S$, R_{Proj} is taken as a good approximation of A_{Cap}. In all cases, contact angle α is then calculated via simple trigonometry calculations (see above).

Supporting Figure S3

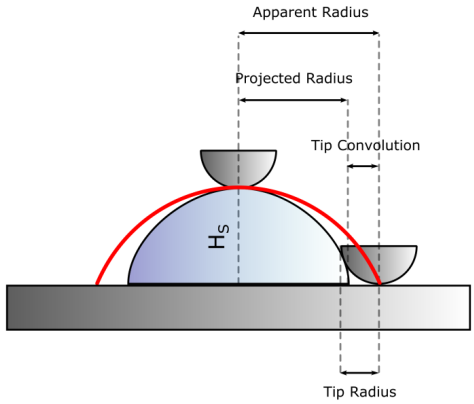

Influence of AFM probe on the nanomechanical characterization of vesicles. The position of a vesicle on a Contact Angle vs. Diameter plot is determined by the H_S and R_{Proj} values measured on its AFM image. While the measurement of H_S is only affected by force setpoint and feedback gain (see main text), R_{Proj} is affected by tip convolution. Due to this, maximum inscribed disc radii values measured on the AFM image should be regarded as 'apparent radii', resulting from the sum of R_{Proj} plus a tip contribution. This tip 'broadening' contribution is variable in entity, and linked to the exact shapes of the tip (its curvature radius at the apex being the most important) and the vesicle (in particular, H_S). A clear indication of excessively large tip convolution is a non-circular profile of several vesicular objects in an image; it is not advised to apply image analysis to images where this occurs. Circular profiles (see main text image 2c) can only result from the convolution of two objects having circular shapes along the scanning direction; recording two perpendicular circular profiles on the same object is thus indicative of the fact that the tip is effectively behaving as a hemisphere, and that the largest possible overestimation of R_{Proj} coincides with its apex curvature radius. In any case, the largest broadening effect occurs at the base of the vesicle, which is not included in our image analysis procedure since it only takes into account those portions of objects being above a height threshold (see main text Figure 2a, b and c). This reduces the maximum impact of tip convolution on successive analysis steps to a fraction of the probe's curvature radius. The nominal tip radii of most commercially available 'sharp' AFM tips (e.g. from 2 to 12 nm for the Bruker SNL probes employed in this study) limits the maximum possible overestimation of R_{Proj} to ~10 nm in the worst case scenario for vesicles with $\alpha \geq 90°$. Progressively shallower vesicles would be less affected; the total result being a ~5% underestimation of α for a 'typical' vesicle with $H_S = 50$ nm in the worst possible scenario.

These considerations suggest that, by using tips with apex curvature radii ≤10 nm and by taking the opportune precautions detailed in the materials and methods section of main text, one can in most cases neglect tip de-convolution. It is important to note that several pieces of information obtained from a Contact Angle vs. Diameter scatterplot (e.g. the presence of contaminants, the attribution of items in a horizontally elongated cluster to vesicle-like mechanical behavior, the relative position of clusters) are unaffected by tip convolution. We only advise tip convolution correction in those cases in which the quantitative readout of α is crucial (e.g. for the quantitative estimation of k_S), and if a reliably sharp tip is unavailable. In these cases, it would be possible to correct R_{Proj} values by simply adding an internal standard

to the sample. This internal standard could be constituted by monodisperse rigid spherical nanoparticles, which could be singled out and used to estimate XY tip convolution, or a synthetic liposome with a previously characterized α value. The latter would appear as an additional horizontal cluster in the α/size scatterplot; apparent R_{Proj} values would then be adjusted by different tip radius values until the reference cluster average α coincided with the expected value.

Supporting Figure S4

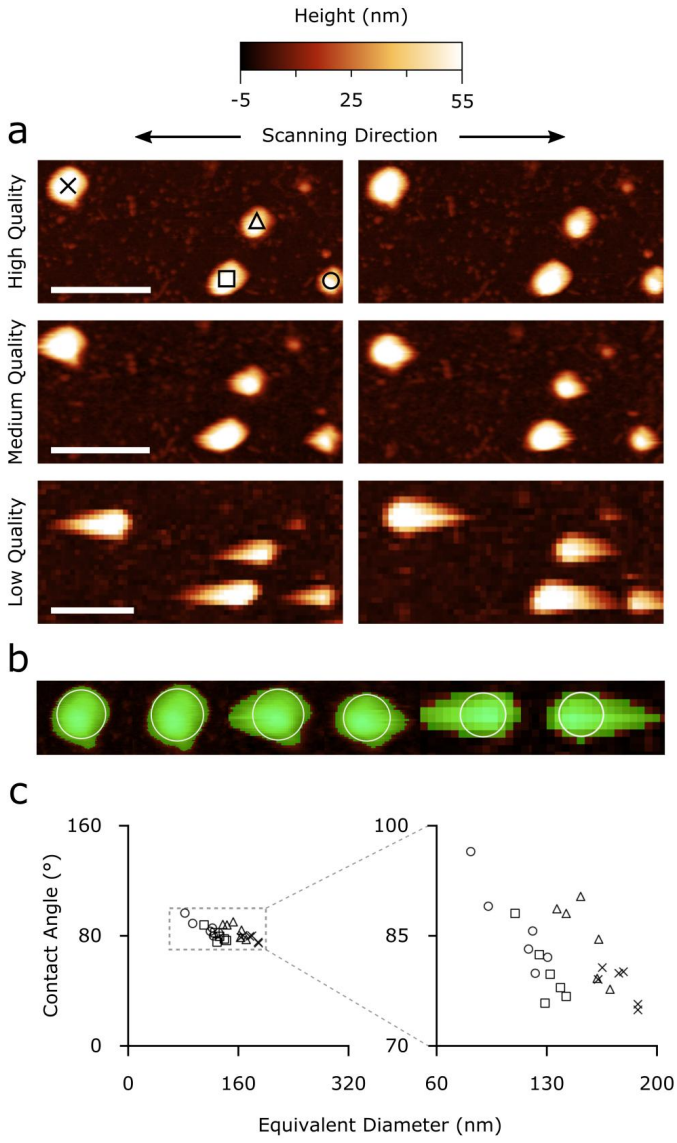

Robustness of the image analysis procedure with respect to imaging quality. Quantitative measurements of α are based on two parameters obtained from AFM images: vesicle height H_S and Projected Radius R_{Proj}. While it is of course advised to perform the analysis on AFM images of the best available quality (with respect to resolution, feedback setting, and applied force setpoint: see main text), we found that both H_S and R_{Proj} are only marginally affected by image quality. (a): The two main parameters affecting AFM image quality are feedback gain and resolution (here strictly intended as number of recorded points). We show six

AFM scans on the same four individual *Ascaris* EVs performed in different instrumental conditions. Images in the left and right column respectively correspond to 'trace' (toward cantilever apex) and 'retrace' (toward cantilever base) fast scan axis directions. Images in the top, middle and bottom rows were acquired with progressively worse imaging quality. Top row: 512x512 points, best feedback setting (vesicles have symmetrical profiles). Mid row: 256x256 points, suboptimal feedback setting (vesicles start to show slow feedback artifacts, elongated 'tails' start to appear in the scanning direction). Bottom row: 128x128 points, worse feedback setting (vesicles have long feedback artifacts in the scanning directions). All scalebars are 400nm. (b): Detail of the six scans performed on the vesicle marked with an "X" in panel a. The zone above the selected height threshold is highlighted in green; it is easy to notice how its horizontal deformation caused by feedback artifacts has a limited impact on the maximum inscribed disc radius used to calculate R_{Proj} (white circles). Similarly, reduced resolution has a very limited impact on the maximum height value corresponding to H_S. (c): α/size plot of the four vesicles shown in panel a. Each vesicle is marked with the same symbol used in panel a, and plotted at the six slightly different coordinates resulting from image analysis of the six scans of panel a. Pooling the six measurements performed on each vesicle and calculating their variance allows the dispersion of both α and D_L values induced by image quality to be estimated. R_{Proj} and H_S values obtained from the worst images cause deviations of ~5% in α and ~20% in D_L with respect to the best ones. Needless to say, it's advisable to always use the best attainable image quality, in particular for quantitative correlation studies such as the one described in main text under the heading "Quantitative estimation of EV stiffness from AFM images".

Supporting Figure S5

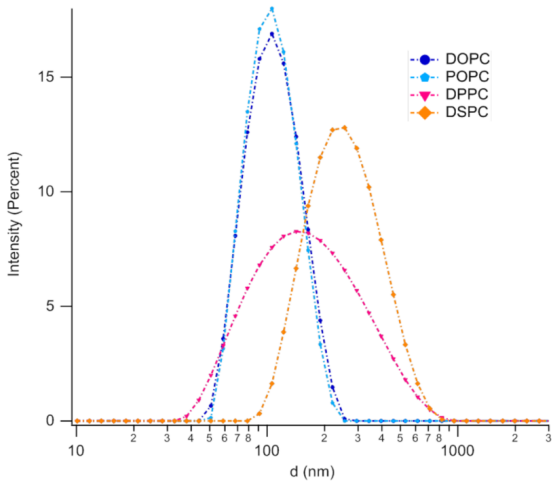

Lipid composition	Dh (nm)	PDI	Zeta Potential (mV)
DOPC	115 ± 5	0.09 ± 0.01	- 11 ± 3
POPC	110 ± 8	0.10 ± 0.05	- 9 ± 2
DPPC	170 ± 20	0.34 ± 0.05	- 10 ± 3
DSPC	290 ± 20	0.20 ± 0.03	- 11 ± 4

Dynamic Light Scattering (DLS) and Zeta Potential characterization of liposomes: (a) Graph reporting the size distribution, as contribution to the scattered intensity, of each lipid composition, as obtained from DLS measurements; (b) Table summarizing average hydrodynamic diameter (Dh) and polydispersity index (PDI) of the lipid vesicles, obtained from DLS analysis, and Zeta Potential values measured for each liposomal dispersion. DLS and Zeta Potential measurements have been performed on a Laser Doppler Micro-electrophoresis (Malvern Zeta Sizer Nano Z), enabling the calculation of electrophoretic mobility and, from this, zeta potential and zeta potential distribution, through the laser interferometric technique M3-PALS (Phase analysis Light Scattering). The measurements have been performed at 25°C. The reported values are an average of three measurements performed on each sample. Measurements were performed at the PSCM Lab (EPN Campus, Grenoble, France). From the reported data it is clearly highlighted that lipid vesicles from DPPC and DSPC (i.e., with a higher stiffness at r.t.) tend to be characterized by larger average sizes and higher polydispersity. All vesicles dispersions in water are characterized by similar, and slightly negative, zeta potential values.

Additional EV characterization

EV preparations purity assessment

EV preparations form bovine milk and Ascaris suum excretory/secretory products were checked for purity from protein contaminants by the COlorimetric NANoplasmonic (CONAN) assay, which exploits the nanoplasmonic properties of colloidal gold nanoparticles (AuNPs) and their peculiar interaction with proteins and lipid bilayers [Maiolo 2015]. The CONAN assay used in this work consisted of a 6 nM Milli-Q water solution of 14 nm diameter AuNPs. AuNPs were synthesized by the Turkevich's method. The experiments were conducted and data analyzed using the protocols described in [Zendrini 2019]. All the UV/vis/NIR absorption spectra were collected with an Ensight multimode plate reader (PerkinElmer), which allowed collection of the spectra on samples of 100 µL final volume.

The assay consists of an aqueous solution of bare AuNPs at 6 nM concentration. When mixed with pure EV formulations, the AuNPs cluster on the EV membrane, whereas in EV formulations which contain exogenous protein contaminants (EPCs) the AuNPs are preferentially cloaked by such EPCs (an AuNP-EPC corona forms), which prevents AuNPs from clustering to the EV membrane. When AuNPs cluster (are in tight proximity), their localized surface plasmon resonance (LSPR) red shifts and broadens, resulting in a color change of the AuNP solution from red to blue, which can be accurately monitored through UV−vis spectroscopy. The assay red shift is therefore directly related to the purity grade of the added EV formulation and can be conveniently quantified by describing the AuNP UV/vis/NIR absorption spectra with the nanoparticle Aggregation Index (AI), defined as the ratio between the absorbance intensity at the LSPR peak and the intensity at 650+850 nm [Busatto 2018; Mallardi 2018]. For all the analyzed EV formulations separated as described in the main text, the AI values resulted in around 20% of the reference AI of the initial assay (i.e., the dispersed AuNP solution). This proves the EV formulations contained negligible amounts of EPCs. Results reported indicate that the AI for the assayed EV formulation is around 20% of the AI of the starting assay. According to the limit of detection for protein contaminants reported in [Zendrini 2019], this indicates the samples contain an overall amount of exogenous contaminants ≤ 50 ng/µL.

EV titration

In the case negligible amount of proteins in EV preparations (< 50 ng/µL) the aggregation index (AI) of the CONAN assay is proportional to the EV number density. We exploited the assay to determine EV total molar concentration (Table ST1) measuring the AI of a POPC liposome calibration curve at known molar concentrations (from 0.8 to 12.5 nM) and interpolating EV AI to the curve. Full details are given in [Busatto 2018 and Zendrini 2019].

Supplementary Table S1

EV sample	EV total molar concentration (mol/L)
SEC+Myco	7.07 E-08
UC+Myco	5.64 E-08
SEC myco free	1.00 E-08
Bovine Milk	4.25 E-07

Table S1: EV total molar concentration. UC+Myco: Ascaris suum EV separated from mycoplasma contaminated medium. Separation protocol: Ultracentrifugation (UC). SEC+Myco: Ascaris suum EV separated from mycoplasma contaminated medium. Separation protocol: size exclusion chromatography (SEC). SEC+Myco: Ascaris suum EV separated from mycoplasma free medium. Separation protocol: size exclusion chromatography (SEC). Bovine milk: EV separated from bovine milk.

Nanoparticle Tracking Analysis

EVs size distribution of *Ascaris suum* samples was additionally determined with Nanoparticle Tracking Analysis (NTA). EV separated after ultracentrifugation protocol (UC) or size exclusion chromatography (SEC, fractions 7-10) (see main text for details) were analyzed with a Nanosight NS300 system (Malvern) coupled with a Nanosight syringe pump (Malvern) [using 405 nm wavelength (blue)]. Before any sample analysis, the system was quality checked by measuring a suspension of 100 nm polystyrene beads. In brief, PBS-diluted samples (final volume 1 ml) were injected into the sample chamber using a syringe and the microscope objective was adjusted in order to obtain a clear picture of particles within the beam. Analysis parameter: Flow rate: 10; Temperature: 23°C; Screen gain: 1; Viscosity: Water; Camera level: 10. For each sample, five measurements were performed with a duration of 60 seconds for each repeat/frame. The data were analyzed using NTA software version 3.2.

Supporting Figure S6

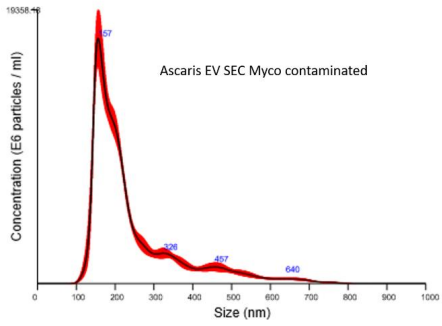

Average finite track length adjustment (FTLA) Concentration/Size graphs for NTA analysis of particles of Ascaris EVs separated with SEC. Medium contaminated with mycoplasma. Red error bars indicate +/- 1 standard error of the mean. Mode 157.5 +/- 3.5 nm. It is important to note that the size of mycoplasma

contaminants is, on average, smaller than 50 nm (as can be seen by looking at the vertical cluster in Fig. 3d of the main text); making it challenging to be revealed by NTA techniques, which usually present a limit of detection around 30 – 50 nm for EVs and protein aggregates [Bohren 2007].

Supporting Figure S7

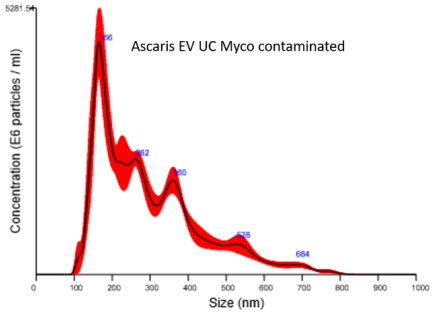

Average finite track length adjustment (FTLA) Concentration/Size graphs for NTA analysis of particles of Ascaris EVs separated with UC. Medium contaminated with mycoplasma (see fig S6 caption for additional discussion). Red error bars indicate +/- 1 standard error of the mean. Mode 164.7 +/- 8.4 nm.

Supporting Figure S8

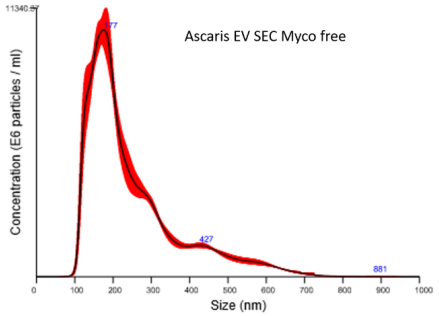

Average finite track length adjustment (FTLA) Concentration/Size graphs for NTA analysis of particles of Ascaris EVs separated with UC. Medium not contaminated with mycoplasma. Red error bars indicate +/- 1 standard error of the mean. Mode 166.4 +/- 6.3 nm

EV biochemical characterization

For biochemical analysis purified EV samples from bovine milk were pelleted at 100000 xg for 65 minutes (in a Beckman Coulter Optima Max-XP with a TLA-55 rotor) in polyallomer microcentrifuge tubes (Beckman) and the pellet was resuspended in sample buffer (62.5 mM Tris pH 6.8, 2% SDS, 10% Glycerol). Samples were run on a 12.5% SDS-PAGE gel in order to separate proteins. The separated proteins were transferred onto PVDF membranes and blocked in PBS containing 0.2% fish skin gelatin (Sigma-Aldrich) and 0.1%

Tween-20. Proteins were detected by immunoblotting using rabbit-anti-human-MFG-E8 (Sigma HPA002807, dilution 1:1000); mouse-anti-bovine-CD63 (BioRad MCA2042G, dilution 1:2000); mouse-anti-human CD9 (Biolegend 312102, clone HI9a, dilution 1:1000); mouse-anti-human-Flotillin (BD 610821, clone 18, dilution 1:500 and the sample was reduced with DTT + β-mercapthoethanol); mouse-a-human-TSG-101 (SC-7964, dilution 1:100 and the sample was reduced with DTT + β-mercapthoethanol); rabbit-anti-bovine Lactoglobulin-β-HRP (Ab112894, dilution 1:1000); rabbit-a-bovine Casein (GTX37769, dilution 1:500). Goat anti-mouse-HRP (Jackson Immuno Research, Suffolk, UK; 1:10000) was used as secondary antibody. HRP conjugated antibodies were detected using SuperSignal West Dura Chemiluminescent Substrate (Thermo Scientific, Landsmeer, Netherlands) and ChemiDoc XRS and Image Lab 5.1 (Bio-Rad) (Figure S8).

Supporting Figure S9

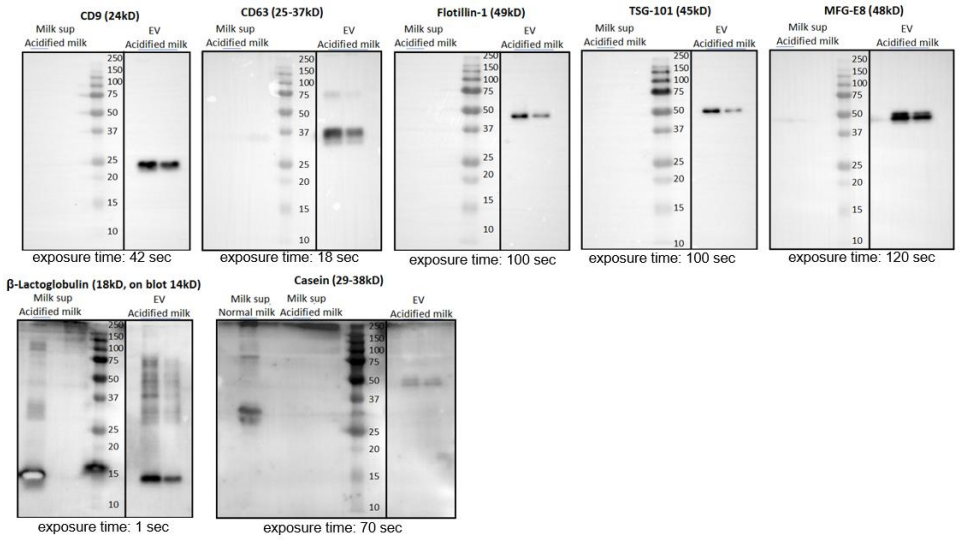

Western blot characterization of purified milk EVs for CD9, CD63, Flotillin-1, TSG-101 and MFG-E8. Non EV-enriched proteins β-Lactoglobulin and β casein were included for characterization. For casein, a non-acidified (normal milk) sample was included to show the presence of casein in milk, as compared to acidified milk. Note that β-Lactoglobulin is predicted to be 18 kDa (which was observed in milk supernatant) but the band is lower in EVs. EV samples were technical duplicates as these were isolated from the same raw milk sample.

Supplementary References

[Bohren 2007]: Bohren CF, Huffman DR. “Absorption and scattering by a sphere”, in: Bohren CF, Huffman DR, editors. Absorption and scattering of light by small particles. Weinheim: Wiley-VCH Verlag GmbH; 2007. pp. 83–129.

[Busatto 2018]: Busatto S, Giacomini A et al. “Uptake Profiles of Human Serum Exosomes by Murine and Human Tumor Cells through Combined Use of Colloidal Nanoplasmonics and Flow Cytofluorimetric Analysis” Anal. Chem 90, 7855-7861 (2018)

[Faria 2018]: M. Faria, M. Bjornmalm et al. “Minimum information reporting in bio-nano experimental literature” *Nat Nanotechnol 13* (2018)

[Hutter 1993]: J. L. Hutter, J. Bechhoefer, “Calibration of Atomic-Force Microscope Tips” Rev Sci Instrum 1993, 64. 1868-1873

[Maiolo 2015]: Maiolo D, Paolini L et al. “Colorimetric nanoplasmonic assay to determine purity and titrate extracellular vesicles” Anal. Chem 87, 4168-76 (2015)

[Mallardi 2018]: Mallardi A, Nuzziello N et al. “Counting of peripheral extracellular vesicles in Multiple Sclerosis patients by an improved nanoplasmonic assay and dynamic light scattering” Colloids Surf B Biointerfaces 168, 134-142 (2018)

[Necas 2012]: D. Necas, P. Klapetek, “Gwyddion: an open-source software for SPM data analysis” Cent Eur J Phys 2012, 10. 181-188

[Skliar 2018]: Skliar M, Chernyshev VS et al. “Membrane proteins significantly restrict exosome mobility” Biochem. Biophys. Res. Comm. 501, 1055e1059 (2018)

[Thery 2018]: C. Thery, K. W. Witwer et al. “Minimal information for studies of extracellular vesicles 2018 (MISEV2018): a position statement of the International Society for Extracellular Vesicles and update of the MISEV2014 guidelines” *J Extracell Vesicles 7* (2018)

[Van Deun 2017]: J. Van Deun, P. Mestdagh et al. “EV-TRACK: transparent reporting and centralizing knowledge in extracellular vesicle research” *Nat Methods 14* (2017)

[Vorselen 2017]: D. Vorselen, F. C. MacKintosh et al. “Competition between Bending and Internal Pressure Governs the Mechanics of Fluid Nanovesicles” Acs Nano 2017, 11. 2628-2636

[Zendrini 2019]: Zendrini A, Paolini L et al. “Augmented COlorimetric NANoplasmonic (CONAN) Method for Grading Purity and Determine Concentration of EV Microliter Volume Solutions” Front. Bioeng. Biotechnol., 7, 452 (2020)

Manuscript n°3

Volume 6
Number 7
July 2021
Pages 499–576

Nanoscale Horizons

The home for rapid reports of exceptional significance in nanoscience and nanotechnology

rsc.li/nanoscale-horizons

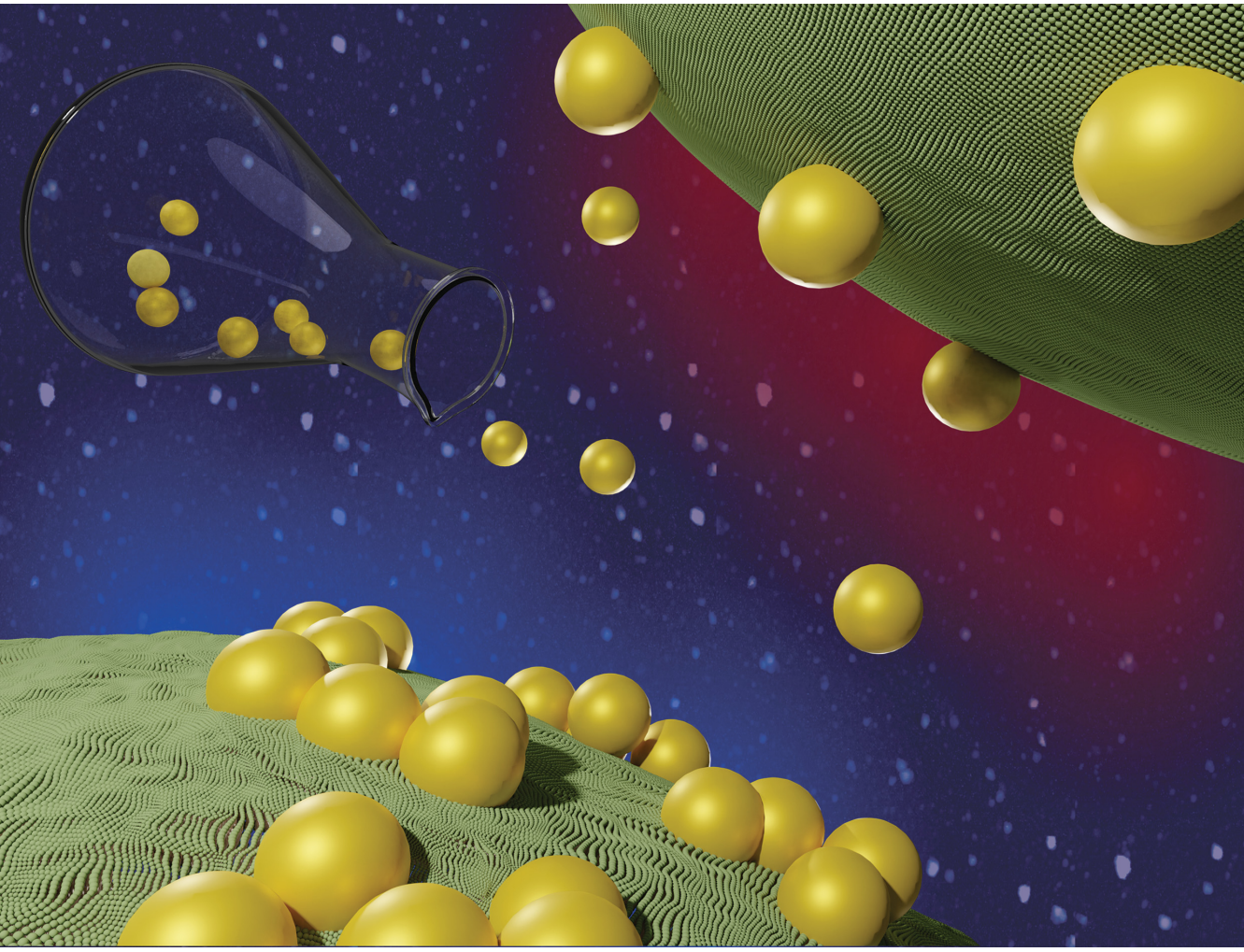

ISSN 2055-6756

ROYAL SOCIETY OF CHEMISTRY

COMMUNICATION
Costanza Montis, Debora Berti *et al.*
A plasmon-based nanoruler to probe the mechanical properties of synthetic and biogenic nanosized lipid vesicles

NCNST

Nanoscale Horizons

ROYAL SOCIETY OF CHEMISTRY

COMMUNICATION

View Article Online
View Journal | View Issue

Cite this: *Nanoscale Horiz.*, 2021, 6, 543

Received 8th January 2021,
Accepted 7th April 2021

DOI: 10.1039/d1nh00012h

rsc.li/nanoscale-horizons

A plasmon-based nanoruler to probe the mechanical properties of synthetic and biogenic nanosized lipid vesicles†

Lucrezia Caselli,[ab] Andrea Ridolfi,[abc] Jacopo Cardellini,[ab] Lewis Sharpnack,[d] Lucia Paolini,[be] Marco Brucale,[bc] Francesco Valle,[bc] Costanza Montis,*[ab] Paolo Bergese[bef] and Debora Berti*[ab]

Nanosized lipid vesicles are ubiquitous in living systems (*e.g.* cellular compartments or extracellular vesicles, EVs) and in formulations for nanomedicine (*e.g.* liposomes for RNA vaccine formulations). The mechanical properties of such vesicles are crucial in several physicochemical and biological processes, ranging from cellular uptake to stability in aerosols. However, their accurate determination remains challenging and requires sophisticated instruments and data analysis. Here we report the first evidence that the surface plasmon resonance (SPR) of citrated gold nanoparticles (AuNPs) adsorbed on synthetic vesicles is finely sensitive to the vesicles' mechanical properties. We then leverage this finding to show that the SPR tracking provides quantitative access to the stiffness of vesicles of synthetic and natural origin, such as EVs. The demonstration of this plasmon-based "stiffness nanoruler" paves the way for developing a facile, cost-effective and high-throughput method to assay the mechanical properties of dispersions of vesicles of nanometric size and unknown composition at a collective level.

New concepts

Citrated gold nanoparticles (AuNPs) undergo membrane-templated self-assembly when challenged with nanosized lipid vesicles. We show that the stiffness of the target vesicle finely modulates the extent of AuNPs aggregation, which can be easily monitored by UV-Vis spectrophotometry. Leveraging this discovery, we propose a novel experimental method to assess the mechanical properties of synthetic and natural vesicles. Through a "stiffness index", S.I., we quantify the extent of AuNPs aggregation and define its functional dependence on the mechanical properties of the vesicles. This method was validated on a set of synthetic lipid vesicles of known stiffness and then tested on a sample of biogenic extracellular vesicles (EVs). The "plasmon-based stiffness nanoruler" is a reproducible, sensitive, high-throughput, and readily accessible method, which overcomes many of the hurdles still hampering an accurate determination of the rigidity of nanovesicles.In addition, it can easily and readily probe the properties of tiny sample amounts, which represents a considerable advantage for biological samples, usually available in low quantities due to purification costs. This new method will advance our understanding of the role of rigidity of nanovesicles in modulating their biological behavior, from the pharmacokinetics of liposomal formulation for drug delivery to the uptake of natural vesicles and viruses.

Introduction

Membrane-delimited compartments (*e.g.*, cells, organelles and nanosized vesicles of biological origin, such as enveloped viruses[1] or extracellular vesicles (EVs)[2,3]) are among the basic units of living organisms. Importantly, they are also widespread structural motifs in bio-inspired nanomaterials, such as liposomes,[4] virosomes[5] or polymerosomes.[6] The mechanical properties of such membrane compartments regulate the response to external stimuli, which is crucial in a host of biologically-relevant interactions at the nanoscale.[7–11] A well-known example is the mechanical response of cells and membrane bound-organelles, which is the key in numerous biological processes (*e.g.* cell fusion, growth and differentiation, endo- and exocytosis, uptake of nanoparticles or viruses,[12–14] *etc.*) and in the onset of pathological cell conditions.[15–18] More recent reports have highlighted that the mechanical response of EVs (membrane-delimited nanoparticles secreted by all cell types and essential mediators of cell signalling[2,3,19]) is a biomarker for malignant conditions of parental cells.[20,21] In addition, the nanomechanics of pathogens, including viruses with a lipid envelope (*e.g.* Moloney murine leukemia virus and HIV[22]), was recently connected to their infectivity.[23] Mechanical properties

[a] *Department of Chemistry, University of Florence, Via della Lastruccia 3, Sesto Fiorentino, Florence 50019, Italy. E-mail: debora.berti@unifi.it, costanza.montis@unifi.it*
[b] *Consorzio Sistemi a Grande Interfase, Department of Chemistry, University of Florence, Sesto Fiorentino, Italy*
[c] *Consiglio Nazionale delle Ricerche, Istituto per lo Studio dei Materiali Nanostrutturati (CNRISMN), via Gobetti 101, Bologna 40129, Italy*
[d] *ESRF–The European Synchrotron, Grenoble 38043, France*
[e] *Department of Molecular and Translational Medicine, University of Brescia, Brescia, Italy*
[f] *Consorzio Interuniversitario Nazionale per la Scienza e la Tecnologia dei Materiali, Florence, Italy*

† Electronic supplementary information (ESI) available. See DOI: 10.1039/d1nh00012h

are also crucial for the interaction of synthetic nanostructures with the biological environment: the deformability of liposomes or polymeric vesicles for drug or vaccine delivery deeply affects their pharmacokinetics in the bloodstream and the internalization route.[24]

Although central in several research areas, the accurate assessment of the mechanical properties of synthetic or natural vesicles still poses a challenge.[25,26] Traditional methods, such as shape fluctuation optical analysis,[27] micropipette aspiration,[28] X-ray scattering[29,30] and neutron spin-echo,[31] provide insights into biologically-relevant descriptors of the mechanical response of the lipid membrane, such as the bilayer's bending rigidity.[27–31] However, these techniques are cost- and/or time-consuming and often yield discrepant results, as pointed out in several reports.[25,26,32–34] More recently, techniques that actively probe the mechanical properties at a whole-vesicle level, rather than those of the lipid shell, are gaining the central stage;[35] examples include optical tweezers and Atomic Force Microscopy (AFM) operating modes, such as Dynamic Mechanical Analysis, Quantitative Imaging and Lorentz Contact Resonance.[20] Most of these methods rely on contact mechanic models for interpreting the measured mechanical properties of the probed objects; however, there is still disagreement on which model is best suited for describing the nanomechanics of a lipid vesicle.[36] As a consequence, classical AFM-based force spectroscopy (AFM-FS) indentation experiments still represent a common choice for the nanomechanical analysis of vesicles,[37–39] since they allow determining the overall mechanical response of vesicles to applied deformations, *i.e.* their ''stiffness'', in a model-free approach. The measured stiffness includes contributions both from the membrane shell and the enclosed volume, accounting for the mechanical properties of the internal pool, volume variations upon deformation, osmotic imbalance, *etc.* Unfortunately, all these experimental methods probe a single particle at a time and require sophisticated instruments or/and highly experienced users.[35]

Here, we propose AuNPs as nanoprobes of the stiffness of membranous nano-objects, with typical submicron sizes. This approach overcomes many limitations of the currently available methods, measurements can be performed with a UV-Vis spectrophotometer and limited data analysis is required. In the following, this communication will (i) explore how the stiffness of liposomes modulates the surface plasmon resonance (SPR) of AuNPs adsorbed on their membrane and (ii) propose this previously unnoticed relationship as the working principle of a new, accessible and robust spectrophotometric method to evaluate the stiffness of both synthetic and natural lipid vesicles of unknown composition.

The SPR of AuNPs is finely sensitive to the chemical environment and the interparticle distance, which underpins their application as nanoscale probes.[40] The coupling between the SPR of proximal AuNPs, which results from AuNPs close approach or aggregation, was exploited for the first time by El-Sayed and co-workers as a plasmon ruler[41] and is nowadays used in a number of bioanalytical assays.[42,43] The CONAN (COlloidal NANoplasmonic) assay is a recent example, where the AuNPs SPR shift upon incubation with EVs is exploited to determine their purity and concentration;[44–46] in this latter case, the SPR shift arises from the spontaneous aggregation of AuNPs on the lipid membrane of vesicles (of both synthetic and natural origin, as EVs). This membrane-induced aggregation has been the focus of several recent investigations.[47–52] Specifically, the membrane-induced aggregation of AuNPs has been interpreted as on–off mechanism to date,[53,54] switchable by the physical state of the membrane: fluid-phase bilayers, characterized by free lipid diffusion and low rigidity, would promote aggregation, resulting in a marked change of AuNPs SPR profile. Conversely, the aggregation of AuNPs would be completely inhibited on tightly packed gel-phase membranes, characterized by a higher rigidity. At variance with the literature, we demonstrate that the SPR shift of AuNPs also interest gel-phase membranes and is rather modulated by the stiffness of the vesicles through a precise functional dependence: this allows defining a ''stiffness nanoruler'', able to discriminate vesicles within the same physical state (whether it is gel or fluid) on the basis of their mechanical behaviour. In analogy with the plasmon nanoruler, introduced as distance-sensor,[41] this plasmon-based descriptor leverages the unique sensitivity of AuNPs SPR to determine the mechanical properties of lipid vesicles. As a proof-of-principle of applicability to complex natural systems, we tested the assay on EVs, whose stiffness is of prominent relevance in cellular adhesion and uptake[55] and a characteristic that distinguish EVs deriving from malignant and non-malignant cells.[20,21]

Results and discussion

We prepared a library of unilamellar liposomes having a similar average diameter ($\sim$100 nm) and low polidispersity indexes (see ESI† for details on preparation and characterization) from a set of synthetic phosphatidylcholines (PC) differing for length and/or degree of unsaturation of the acyl chains (Fig. 1a). The free-standing bilayers, either in the gel or fluid phase at room temperature (Fig. 1a), display different rigidities.[56–59] Given their very similar size distributions and the absence of any osmotic imbalance between the lumen and the external medium, the rigidity of the lipid shells can be considered the sole responsible for the overall stiffnesses of the vesicles.

Fig. 1b reports representative AFM-FS force/distance plots of single-vesicle indentation events for each lipid.[60,61] The slope of the linear regime occurring immediately after the contact point represents the stiffness of the vesicles; the stiffnesses in Fig. 1c were obtained by averaging the values for multiple vesicles (see ESI† for further details). Taken together, the entire series of stiffness values measured on the selected library of synthetic PC standards can be regarded as a stiffness gauge in which the rigidity monotonically increases from DOPC to DSPC vesicles, in line with the literature.[25,62] This set will be used to validate the stiffness plasmon nanoruler.

The vesicles (20 μl of a water dispersion at a 0.35 nM vesicles' concentration) were then challenged with 100 μl of 6.7 nM water dispersion of negatively charged citrated AuNPs (13 ± 0.6 nm diameter, zeta potential: -36 ± 2 mV), to obtain a

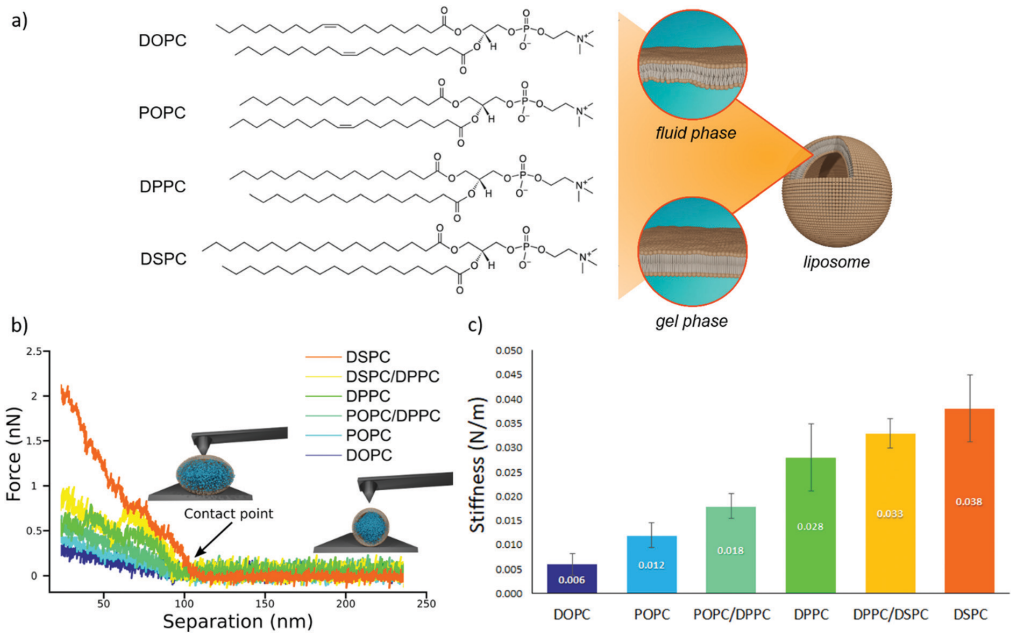

Fig. 1 AFM characterization of vesicles stiffnesses. (a) Chemical formulas of the four lipids used for the preparation of liposomes (1,2-distearoyl-*sn*-*glycero*-3-phosphocholine (DSPC), 1,2-dipalmitoyl-*sn*-*glycero*-3-phosphocholine (DPPC), 1-palmitoyl-2-oleoyl-*glycero*-3-phosphocholine (POPC) and 1,2-dioleoyl-*sn*-*glycero*-3-phosphocholine (DOPC)); depending on the molecular composition, the lipid bilayer enclosing a liposome exhibits a different degree of molecular packing at room temperature, which determines the phase (*i.e.*, fluid or gel) of the membrane. (b) AFM force-distance curves for the different vesicles batches, together with graphical representation of vesicles deformation induced by the AFM tip at two different separation distances. Liposomes samples are DOPC; POPC, POPC/DPPC (50/50 mol%), DPPC, DPPC/DSPC (50/50 mol%) and DSPC vesicles; (c) stiffness values (N m^{-1}) of the different vesicles, determined through AFM-FS; All error bars represent the uncertainties obtained by bootstrapping (1000 repetitions of 5 draws, with replacement).

final liposomes/AuNPs molar ratio of ~1/100. The changes in the SPR profile were monitored after 15 minutes of incubation at room temperature (Fig. 2a). These experimental conditions were carefully selected on the basis of our recent investigation on POPC liposomes interacting with citrated AuNPs.[52]

The AuNPs dispersion in the absence of lipid vesicles shows a well-defined SPR peak centred at 522 nm (red curve); upon mixing with liposomes, an immediate colour change is visible to the naked eye (inset, Fig. 2a), which clearly depends on the composition of the target membrane. Going from DSPC to DOPC, we observe colour shifts from red to increasingly dark shades of violet and blue. The variation in the SPR profile gradually increases as the stiffness of vesicles decreases. Specifically, from the stiffest vesicles (DSPC) to the softest ones (DOPC), the progressive emergence of a high-wavelength shoulder can be observed, eventually resulting in a secondary plasmon peak at about 625 nm (see Fig. 2a).

This new spectral feature is the hallmark of the aggregation of AuNPs, whose spatial proximity produces the coupling of the individual AuNPs plasmons.

To get insights into the structure of AuNPs aggregates, we performed Small Angle X-ray Scattering (SAXS) for DOPC, POPC, DPPC and DSPC liposomes challenged with AuNPs (Fig. 2b).

The power-law dependence in the low-q region highlights the presence of AuNPs clusters on fluid-phase bilayers, with a fractal dimension which increases as the stiffness of vesicles decreases (Fig. 2b, inset, and ESI†).[63] The spatial correlation between AuNPs was determined from the structure factor $S(q)$, inferred from the high-q region of the scattering profiles (Fig. 2b, inset, and ESI†). The position of the $S(q)$ correlation peaks for fluid-phase liposomes is consistent with AuNP–AuNP center-to-center distances comparable with the particle diameter and decreasing with vesicles' stiffness (14.5 nm and 14.1 nm for POPC and DOPC, respectively). For liposomes in the gel phase, no low-q upturn of intensity was detected and the positional correlation corresponds to significantly higher AuNP–AuNP distances (*i.e.*, 30.5 nm and 30.2 nm for DSPC and DPPC, respectively), hinting at the presence of multiple AuNPs adsorbed on the same liposomal surface, but not aggregated.

According to recent reports, the aggregation of AuNPs on lecithin vesicles is switched on and off by the membrane phase:[53,54] aggregation is inhibited on gel-phase bilayers (*e.g.* DPPC and DSPC at r.t.) and promoted by fluid-phase membranes (*e.g.* DOPC and POPC at r.t.), with no differences observed for bilayers in the same phase.[53,54] Conversely, the UV-Vis and SAXS data here shown provide additional insights, highlighting that – in

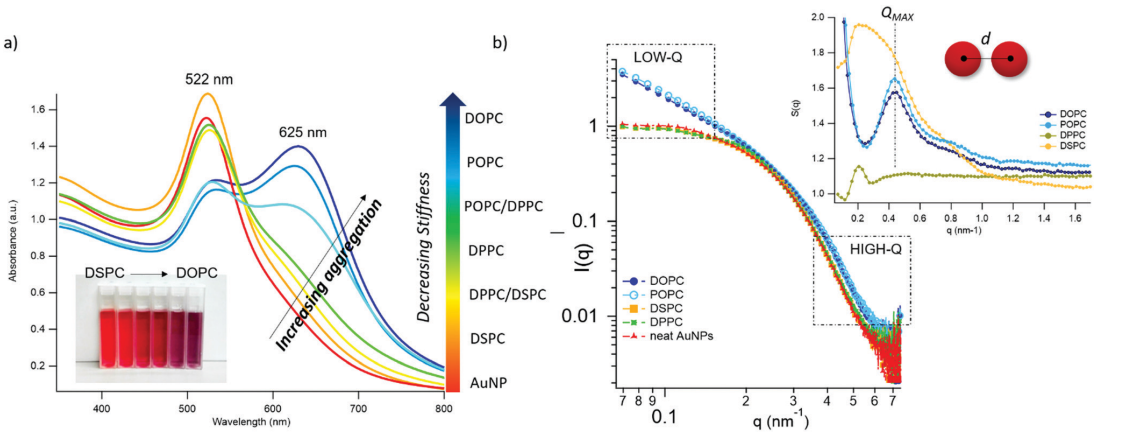

Fig. 2 AuNPs interaction with lipid bilayers of different stiffness. (a) UV-Vis spectra of AuNPs (6.7 nM) incubated with synthetic vesicles (0.2 nM) (liposomes/AuNPs number ratio 1/100). Inset: Visual appearance of the same samples. (b) SAXS profiles of NPs with and without vesicles (1 : 8 vesicles/AuNPs molar ratio). Under these conditions, the scattering from vesicles (subtracted from the scattering of AuNPs-vesicles mixtures) is negligible and the observed signal is only due to AuNPs. The power law dependence at low-q is connected to the presence of AuNPs clusters and to their morphology. The power-lawexponents for DOPC/AuNPs and POPC/AuNPs complexes, *i.e.* −1.54 and −1.50 respectively (see ESI†), are consistent with an increasing fractal dimension of clusters as the stiffness of vesicles decreases. The absence of such power-law for gel-phase liposomes is related to non-aggregated AuNPs, preserving their original diameter. The right inset is the structure factor ($S(q)$) *vs.* q, extracted from the high-q range of vesicles/AuNPs profiles (see ESI†).

these experimental conditions – AuNPs clustering on lipid vesicles is not abruptly switched-on by varying the membrane physical state: the slight – but still evident – differences in the AuNPs SPR induced by vesicles with the same physical state but different rigidities demonstrate that AuNPs aggregation is rather modulated by the membrane rigidity in a ''continuous fashion''.

This dependence can be exploited to set-up a UV-Vis spectroscopic assay to probe the mechanical properties of lipid vesicles. With this aim, we analysed the optical spectra to extract a quantitative descriptor. The so-called ''stiffness index'', S.I., (see Fig. 3a), accounting for the main variations in the AuNPs SPR profile, was used to build-up an empirical 'AuNPs spectral response' *vs.* 'vesicles' stiffness' scale. The S.I. for each AuNPs/vesicles hybrid is calculated dividing the area subtended by the absorbance spectrum in the 560–800 nm range by the area relative to the total spectral range (350–800 nm). The results are then normalized for the S.I. of neat AuNPs

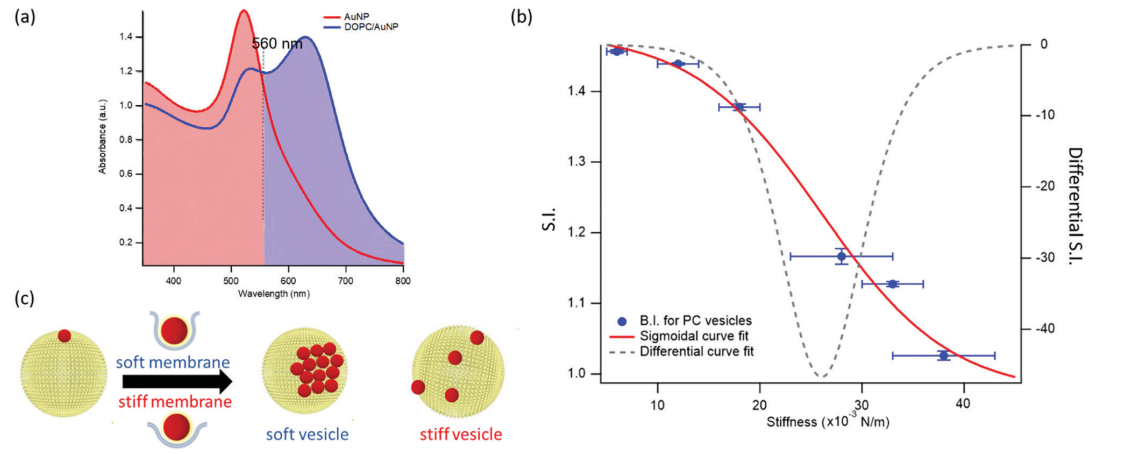

Fig. 3 Quantification of liposomes-induced variation in the AuNPs SPR profile. (a) Visual description of the stiffness index (S.I.); (b) S.I. values (blue spots) with relative errors bars plotted as a function of membrane stiffness. The red curve is the sigmoidal curve fit, while the grey dashed curve is the first derivative of the sigmoidal curve fit with respect to stiffness (see ESI† for details on fitting parameters). (c) Mechanism of interaction between AuNPs and vesicles characterized by different stiffness. The adhesion of an AuNP on a soft membrane is followed by a significant AuNP wrapping by the membrane, resulting into AuNPs aggregation on the vesicle surface. The AuNP docking on a stiffer membrane results in a lower wrapping extent, preventing AuNPs clustering.

(which is then equal to 1 by definition) to obtain positive integer values of S.I., which gradually increase with increasing AuNPs aggregation extent.

Fig. 3b reports the S.I. (blue dots) obtained for the liposome set plotted as a function of vesicles' stiffness, obtained from AFM-FS measurements (Fig. 1). Each point represents the average value obtained from five independent batches, which highlights a particularly high reproducibility (see Table S5 of ESI† for standard deviations of each vesicles' batch).

The dependence of the S.I. on stiffness can be expressed by a sigmoidal law, with the following expression:

$$\text{S.I.} = \frac{b}{1 + \exp\left(\frac{c - S}{d}\right)} + a \qquad (1)$$

with S the stiffness obtained from AFM-FS and a, b, c and d constant fitting parameters (see red profile in Fig. 3b for the best fitting curve and ESI† for further details).

For this set of synthetic vesicles, having superimposable size distributions and a luminal content identical to the external medium, the stiffness differences observed in AFM-FS are only due to a membrane contribution, which results from the different composition of the bilayers. As it is well-established, the mechanical response of a lipid bilayer is mainly controlled by its bending rigidity,[25] quantified by the bilayer bending modulus. Therefore, in these experimental conditions, it is the bilayer bending modulus that determines the overall stiffness of the vesicles and in turn the extent of AuNPs aggregation (*i.e.* the S.I.).

Interestingly, in a recent simulation Lipowsky and co-authors[64] report a sigmoidal correlation between the wrapping efficiency of spherical NPs interacting with model membranes and the bilayer bending modulus. This relation holds for fixed NPs radius and membrane-NPs adhesion energy, which perfectly matches our experimental conditions (*i.e.* NPs of defined size and vesicles with fixed PC headgroups).

This finding is fully in line with a recent report,[52] where AuNPs wrapping, modulated by the membrane bending modulus, is recognized as the main driver for the membrane-templated aggregation of AuNPs, through the mechanism sketched in Fig. 3c: briefly, AuNPs adsorb on the vesicle's surface due to Van der Waals attractive interactions and get partially wrapped by the membrane. This wrapping drives a ligand exchange between the membrane lipids and the AuNPs stabilizing agent, *i.e.* the citrate anion, whose release reduces the interparticle electrostatic energy barrier and leads to the aggregation of AuNPs. Importantly, the extent of AuNPs aggregation is modulated by the wrapping efficiency, which is related to the bending rigidity of the membrane. Our results, reporting the first experimental evidence of a sigmoidal relation between AuNPs aggregation and membrane bending rigidity, reconcile this latter mechanism with the theoretical predictions proposed by Lipowsky *et al.*, who first connected the wrapping ability of a membrane to its bending modulus through a sigmoidal law.

The dependence of the S.I. on the stiffness of vesicles (eqn (1)) allows a quantitative estimate of the mechanical properties of membrane-enclosed compartments of unknown composition. The method here proposed possess high reproducibility and sensitivity. In fact, it is able to robustly discriminate systems with very close stiffnesses (*i.e.* differences as small as 0.006 N m^{-1}), as POPC and DOPC liposomes, whose mechanical properties are usually not distinguishable with many other techniques.[62,65]

In addition, the presence of a sigmoidal law, which exhibits the highest variation of S.I. in the central region of the selected set of stiffnesses (see grey dashed curve of Fig. 3b, representing the first derivative of the sigmoidal fit) provides maximum sensitivity in the region where the rigidities of natural membranes usually fall (*i.e.* 0.02–0.025 N m^{-1}[66]).

We chose EVs to further validate the method and to provide evidence of its applicability on membranous nanoparticles, which are more challenging both in terms of compositional

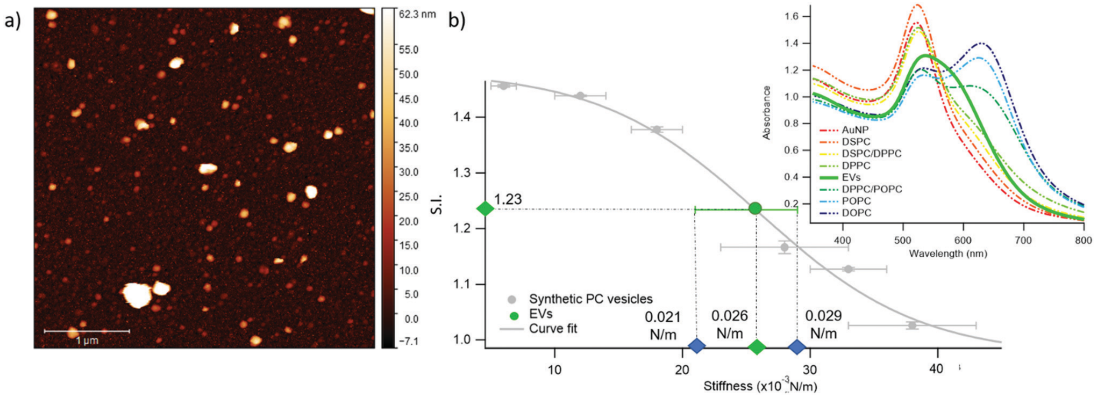

Fig. 4 Quantification of Extracellular Vesicles (EVs)-induced variation in the SPR profile of AuNPs. (a) Representative AFM image of EVs; (b) Sigmoidal trend of the S.I. as a function of membrane stiffness. The EVs' S.I. (1.23 ± 0.01), evaluated through UV-Vis spectroscopy, and stiffness, predicted by the sigmoidal law (0.026 N m^{-1}), are reported as green points in the graph. The green error bar represents the stiffness interval obtained through AFM-FS for EVs. The right inset reports the UV-Vis spectra of AuNPs (6.7 nM) in the presence of synthetic PC vesicles (dashed curves) and EVs (solid green curve) at a vesicles' concentration of 0.35 nM.

and structural complexity, as well as in analyte availability. Specifically, we assayed a sample of EVs from the murine cell line TRAMP-C2, with size and *z*-potential similar to the PC synthetic liposomes (see ESI† for details). The EVs were separated from the cell culture medium and characterized according to international guidelines;[67] in particular, we used the protocols described in Paolini *et al.* (medium EVs),[68] to obtain a pure – *i.e.* not containing exogenous proteins (which would otherwise affect the EVs interaction with AuNPs[44,48]) – EVs dispersion in water. The morphology of EVs was investigated by liquid imaging AFM (see Fig. 4a), showing the characteristic spherical cap shape of EVs adhered onto a substrate and an average diameter of 74.3 nm (refer to ESI† for further details).

The stiffness of EVs, determined through AFM-FS as previously described for PC liposomes, falls in the middle of the stiffness interval defined by the synthetic standards used for calibration (0.025 ± 0.004 N m^{-1}), in between the values obtained for DPPC and DPPC/POPC liposomes (see Fig. 1c). 20 μl of EVs (0.35 nM) were mixed with 100 μl of AuNPs in the same conditions (AuNPs/vesicles molar ratio, incubation time and temperature) previously employed for synthetic liposomes and the SPR profile change of AuNPs was recorded through UV-Vis spectroscopy (right inset of Fig. 4b).

In full agreement with the AFM analysis, this SPR profile variation, S.I. = 1.23 ± 0.01, is intermediate between the ones of DPPC, S.I. = 1.16 ± 0.01, and DPPC/POPC, S.I.= 1.377 ± 0.005. This result demonstrates that the correlation between AuNPs aggregation and vesicles' stiffness, observed in liposomes, also holds for the case of far more complex nanosized vesicles of biological origin. More importantly, the value of stiffness estimated from the S.I. of the AuNPs/EVs hybrid according to the calibration trend (*i.e.*, 0.0259 ± 0.0005 N m^{-1}) falls right in the middle of the EVs stiffness range determined through AFM (Fig. 4b): this striking agreement proves the predictive ability of this new optical method, showing that the nanoplasmonic properties of AuNPs can be effectively harnessed to assess the stiffness of membrane-confined objects with high sensitivity.

Conclusions

The determination of the stiffness of synthetic and natural vesicles is particularly challenging. Here, we show that the SPR of AuNPs can be exploited to quantify this property: combining UV-Vis Spectroscopy, Small Angle X-ray Scattering and AFM-based Force Spectroscopy, we prove that AuNPs aggregation, induced by the interaction with lipid membranes and quantified by an empirical index S.I., exhibits a clear dependence on the mechanical properties of synthetic vesicles. This dependence, expressed by a sigmoidal law, can be used to estimate the stiffness of biological membrane compartments, *e.g.* EVs, of unknown composition and properties. Similarly to the plasmon ruler developed by El-Sayed *et al.*,[41] where the SPR of AuNPs is used to probe their mutual distance, we define a "stiffness nanoruler", where the plasmon resonance is applied to probe the nanomechanics of a target membrane. The method requires cheap reagents and a standard wet lab facility, while keeping competitive reproducibility and sensitivity. From the sample side, it allows for examination of volumes as small as 15 μl (with a concentration of particles in the 10^{-8} M range) which is not accessible today to any other method. This allows to minimize the amounts of vesicles required, which is paramount for biological samples, where low amounts of analyte are yearned due to the origin of the samples (*e.g.* human biological fluids) and/or complex and time-consuming separation protocols. Moreover, differently from other methods – such as AFM and micropipette – which probe the stiffness of single objects, it provides the ensemble-averaged stiffness, *i.e.* accounting for possible variability across the population, with short-time (few minutes) data acquisition.

Conflicts of interest

There are no conflicts to declare.

Acknowledgements

This work has been supported by the European Community through the evFOUNDRY project (H2020-FETopen, ID: 801367) and the BOW project (H2020-EIC-FETPROACT-2019, ID: 952183). We also acknowledge MIUR-Italy ("Progetto Dipartimenti di Eccellenza 2018–2022, ref. B96C1700020008" allocated to Department of Chemistry "Ugo Schiff") and Ente Cassa di Risparmio di Firenze for the economic support. We thank the SPM@ISMN research facility for support in the AFM experiments. The European Synchrotron Radiation Facility (ESRF) is acknowledged for provision of beam-time.

References

1 W. Lucas and K. M. David, *Encyclopedia of Life Sciences*, 2010, pp. 1–7.
2 M. Yáñez-mó and E. Al, *J. Extracell. Vesicles*, 2015, **14**, 27066.
3 G. Raposo and P. D. Stahl, *Nat. Rev. Mol. Cell Biol.*, 2019, **20**, 509–510.
4 G. Bozzuto and A. Molinari, *Int. J. Nanomed.*, 2015, **10**, 975–999.
5 A. Huckriede, L. Bungener, T. Stegmann, T. Daemen, J. Medema, A. M. Palache and J. Wilschut, *Vaccine*, 2005, **23**, S26.
6 X. Zhang and P. Zhang, *Curr. Nanosci.*, 2016, **13**, 124–129.
7 M. Mendozza, L. Caselli, A. Salvatore, C. Montis and D. Berti, *Soft Matter*, 2019, **15**(44), 8951–8970.
8 A. E. Nel, L. Mädler, D. Velegol, T. Xia, E. M. Hoek, P. Somasundaran, F. Klaessig, V. Castranova and M. Thompson, *Nat. Mater.*, 2009, **8**(7), 543–557.
9 C. M. Beddoes, C. P. Case and W. H. Briscoe, *Adv. Colloid Interface Sci.*, 2015, **218**, 48–68.
10 P. K. K. Nagayama, *Particles at Fluid Interfaces and Membranes: Attachment of Colloid Particles*, Elsevier Science, 1st edn, 2001.
11 K. L. Chen and G. D. Bothun, *Environ. Sci. Technol.*, 2014, **48**, 873–880.

12 M. Simunovic, C. Prévost, P. Bassereau and P. Bassereau, *Philos. Trans. R. Soc., A*, 2016, **374**, 20160034.
13 P. B. Canham, *J. Theor. Biol.*, 1970, **26**, 61–81.
14 E. A. Evans, *Biophys. J.*, 1974, **14**, 923–931.
15 A. C. Dumitru, M. Poncin, L. Conrard, Y. F. Dufrêne, D. Tyteca and D. Alsteens, *Nanoscale Horiz.*, 2018, **3**, 293–304.
16 I. Safeukui, P. A. Buffet, G. Deplaine, S. Perrot, V. Brousse, A. Sauvanet, B. Aussilhou, P. H. David, S. Dokmak, A. Couvelard, D. Cazals-hatem, O. Mercereau-puijalon and N. Mohandas, *Blood Adv.*, 2018, **2**, 1–4.
17 C. Alibert, B. Goud and J. Manneville, *Biol. Cell.*, 2017, **109**, 167–189.
18 D. Vorselen, S. M. van Dommelen, R. Sorkin, M. C. Piontek, J. Schiller, S. T. Döpp, S. A. A. Kooijmans, B. A. van Oirschot, B. A. Versluijs, M. B. Bierings, R. van Wijk, R. M. Schiffelers, G. J. L. Wuite and W. H. Roos, *Nat. Commun.*, 2018, **9**, 1–9.
19 G. Van Niel, G. D. Angelo and G. Raposo, *Nat. Rev. Mol. Cell Biol.*, 2018, **19**, 213–228.
20 B. Whitehead, L. P. Wu, M. L. Hvam, H. Aslan, M. Dong, L. DyrskjØt, M. S. Ostenfeld, S. M. Moghimi and K. A. Howard, *J. Extracell. Vesicles*, 2015, **4**, 1–11.
21 L. Paolini, A. Zendrini and A. Radeghieri, *Biomarkers Med.*, 2018, **12**(4), 383–391.
22 C. Carrasco, M. Castellanos, P. J. De Pablo and M. G. Mateu, *Proc. Natl. Acad. Sci. U. S. A.*, 2008, **105**, 4150–4155.
23 W. H. Roos, *Semin. Cell Dev. Biol.*, 2018, **73**, 145–152.
24 P. Guo, D. Liu, K. Subramanyam, B. Wang, J. Yang, J. Huang, D. T. Auguste and M. A. Moses, *Nat. Commun.*, 2018, **9**(1), 1–9, DOI: 10.1038/s41467-017-02588-9.
25 J. F. Nagle, M. S. Jablin, S. Tristram-nagle and K. Akabori, *Chem. Phys. Lipids*, 2015, **185**, 3–10.
26 D. Bochicchio and L. Monticelli, *The Membrane Bending Modulus in Experiments and Simulations: A Puzzling Picture*, Elsevier Inc., 1st edn, 2016, vol. 23.
27 N. Bezlyepkina, R. L. Knorr, R. Lipowsky and R. Dimova, *Soft Matter*, 2010, **6**, 1472–1482.
28 J. R. Henriksen and J. H. Ipsen, *Eur. Phys. J. E: Soft Matter Biol. Phys.*, 2004, **167**, 149–167.
29 J. Pan, S. Tristram-nagle and J. F. Nagle, *Phys. Rev. E: Stat., Nonlinear, Soft Matter Phys.*, 2009, **80**, 021931.
30 C. Length, G. Fragneto, T. Charitat, E. Bellet-amalric and R. Cubitt, *Langmuir*, 2003, **19**, 7695–7702.
31 M. Mell, L. H. Moleiro, Y. Hertle, P. Fouquet, R. Schweins, T. Hellweg and F. Monroy, *Eur. Phys. J. E: Soft Matter Biol. Phys.*, 2013, **36**, 75.
32 D. Marsh, *Chem. Phys. Lipids*, 2006, **144**, 146–159.
33 J. F. Nagle, *Faraday Discuss.*, 2013, **161**, 11–29.
34 R. Dimova, *Adv. Colloid Interface Sci.*, 2014, **208**, 225–234.
35 M. C. Piontek, R. B. Lira and W. H. Roos, *Biochim. Biophys. Acta, Gen. Subj.*, 2019, 129486.
36 M. LeClaire, J. Gimzewski and S. Sharma, *Nano Sel.*, 2021, **2**, 1–15.
37 D. Vorselen, M. C. Piontek, W. H. Roos and G. J. L. Wuite, *Front. Mol. Biosci.*, 2020, **7**, 1–14.
38 S. Li, F. Eghiaian, C. Sieben, A. Herrmann and I. A. T. Schaap, *Biophys. J.*, 2011, **100**, 637–645.
39 A. Calò, D. Reguera, G. Oncins, M. A. Persuy, G. Sanz, S. Lobasso, A. Corcelli, E. Pajot-Augy and G. Gomila, *Nanoscale*, 2014, **6**, 2275–2285.
40 V. Amendola, R. Pilot and M. Frasconi, *J. Phys.: Condens. Matter*, 2017, **29**, 203002.
41 P. K. Jain, W. Huang and M. A. El-sayed, *Nano Lett.*, 2007, **7**, 2080–2088.
42 W. Zhao, M. M. Ali, S. D. Aguirre, M. A. Brook and Y. Li, *Anal. Chem.*, 2008, **80**, 8431–8437.
43 C. C. Chang, C. P. Chen, T. H. Wu, C. H. Yang, C. W. Lin and C. Y. Chen, *Nanomaterials*, 2019, **9**, 1–24.
44 D. Maiolo, L. Paolini, G. Di Noto, A. Zendrini, D. Berti, P. Bergese and D. Ricotta, *Anal. Chem.*, 2015, **87**(8), 4168–4176.
45 A. Zendrini, L. Paolini, S. Busatto, A. Radeghieri, M. Romano, M. H. M. Wauben, M. J. C. van Herwijnen, P. Nejsum, A. Borup, A. Ridolfi, C. Montis and P. Bergese, *Front. Bioeng. Biotechnol.*, 2020, **7**, 452.
46 A. Mallardi, N. Nuzziello, M. Liguori, C. Avolio and G. Palazzo, *Colloids Surf., B*, 2018, **168**, 134–142.
47 A. Ridolfi, L. Caselli, C. Montis, G. Mangiapia, D. Berti, M. Brucale and F. Valle, *J. Microsc.*, 2020, **280**(3), 194–203.
48 C. Montis, D. Maiolo, I. Alessandri, P. Bergese and D. Berti, *Nanoscale*, 2014, **6**(12), 6452–6457.
49 C. Montis, V. Generini, G. Boccalini, P. Bergese, D. Bani and D. Berti, *J. Colloid Interface Sci.*, 2018, **516**, 284–294.
50 J. Liu, *Langmuir*, 2016, **32**, 4393–4404.
51 F. Wang and J. Liu, *Nanoscale*, 2015, **7**, 15599–15604.
52 C. Montis, L. Caselli, F. Valle, A. Zendrini, F. Carlà, R. Schweins, M. Maccarini, P. Bergese and D. Berti, *J. Colloid Interface Sci.*, 2020, **573**, 204–214.
53 K. Sugikawa, T. Kadota, K. Yasuhara and A. Ikeda, *Angew. Chem., Int. Ed.*, 2016, **55**, 4059–4063.
54 F. Wang, D. E. Curry and J. Liu, *Langmuir*, 2015, **31**, 13271–13274.
55 R. Sorkin, R. Huisjes, F. Boškovic, D. Vorselen, S. Pignatelli, Y. Ofir-birin, J. K. F. Leal, J. Schiller, D. Mullick, W. H. Roos, G. Bosman, N. Regev-rudzki, R. M. Schiffelers and G. J. L. Wuite, *Small*, 2018, **1801650**, 1–8.
56 J. F. Nagle, J. Pan, S. Tristram-nagle and N. Kuc, *Biophys. J.*, 2008, **94**, 117–124.
57 R. Dimova, B. Pouligny and C. Dietrich, *Biophys. J.*, 2000, **79**, 340–356.
58 C. Lee, W. Lin and J. Wang, *Phys. Rev. E: Stat., Nonlinear, Soft Matter Phys.*, 2001, **64**, 020901.
59 K. R. Mecke and T. Charitat, *Langmuir*, 2003, **19**, 2080–2087.
60 U. C. Afm, S. Sharma, H. I. Rasool, V. Palanisamy, C. Mathisen, M. Schmidt, D. T. Wong and J. K. Gimzewski, *ACS Nano*, 2010, **4**, 1921–1926.
61 M. Krieg, G. Fl, D. Alsteens, B. M. Gaub, W. H. Roos, G. J. L. Wuite, H. E. Gaub, C. Gerber and Y. F. Dufr, *Nat. Rev. Phys.*, 2019, **1**, 41–57.
62 J. F. Nagle, *Chem. Phys. Lipids*, 2017, **205**, 18–24.
63 L. A. Feigin and D. S. Svergun, *Structure Anaysis by Small Angle X-Ray and Neutron Scattering*, Plenum Press, New York, Princeton, 1987.
64 M. Raatz, R. Lipowsky and T. R. Weikl, *Soft Matter*, 2014, **10**, 3570–3577.

65 G. Niggemann, M. Kummrow, W. Helfrich, G. Niggemann, M. Kummrow, W. H. The and B. Rigidity, *J. Phys. II*, 1995, **5**, 413–425.
66 A. Ridolfi, M. Brucale, C. Montis, L. Caselli, L. Paolini, A. Borup, A. T. Boysen, F. Loria, M. J. C. van Herwijnen, M. Kleinjan, P. Nejsum, N. Zarovni, M. H. M. Wauben, D. Berti, P. Bergese and F. Valle, *Analytical chemistry*, 2020, **92**(15), 10274–10282.
67 C. Théry and E. Al, *J. Extracell. Vesicles*, 2018, **7**, 1535750.
68 L. Paolini, S. Federici, G. Consoli, D. Arceri, A. Radeghieri, I. Alessandri and P. Bergese, *J. Extracell. Vesicles*, 2020, **9**(1), 1741174.

Electronic Supplementary Material (ESI) for Nanoscale Horizons.

Supporting Information for:

A plasmon-based nanoruler to probe the mechanical properties of synthetic and biogenic nanosized lipid vesicles

Lucrezia Caselli, Andrea Ridolfi, Jacopo Cardellini, Lewis Sharpnack, Lucia Paolini, Marco Brucale, Francesco Valle, Costanza Montis, Paolo Bergese and Debora Berti

Supplementary Materials and Methods

Materials

Tetrachloroauric (III) acid (≥ 99.9%) and trisodium citrate dihydrate (≥ 99.9%) for the synthesis of AuNPs were provided by Sigma-Aldrich (St. Louis, MO). 1,2-dioleoyl-sn-glycero-3-phosphocholine (DOPC) (>99%), 1-palmitoyl-2-oleoyl-sn-glycero-3-phosphocholine (POPC) (≥ 98.0%), 1,2-dipalmitoyl-sn-glycero-3-phosphocholine (DPPC) (>99%) and 1,2-distearoyl-sn-glycero-3-phosphocholine (DSPC) (>99%) for the liposomes preparation were provided by Sigma-Aldrich (St. Louis, MO). All chemicals were used as received. Milli-Q grade water was used in all preparations.

Synthesis of citrated AuNPs

Anionic gold nanospheres of 16 nm in size were synthesized according to the Turkevich-Frens method [1,2]. Briefly, 20 mL of a 1mM $HAuCl_4$ aqueous solution was brought to boiling temperature under constant and vigorous magnetic

stirring. 2 mL of 1% citric acid solution were then added and the solution was further boiled for 20 minutes, until it acquired a deep red color. The nanoparticles dispersion was then slowly cooled down to room temperature.

Preparation of liposomes

The proper amount of lipid was dissolved in chloroform and a lipid film was obtained by evaporating the solvent under a stream of nitrogen and overnight vacuum drying. The film was then swollen and suspended in warm (50 °C) milliQ-water by vigorous vortex mixing, in order to obtain a final 4 mg/ml lipid concentration. The resultant multilamellar liposomes in water were subjected to 10 freeze-thaw cycles and extruded 10 times through two stacked polycarbonate membranes with 100 nm pore size at room temperature, to obtain unilamellar liposomes with narrow and reproducible size distribution. The filtration was performed with the Extruder (Lipex Biomembranes, Vancouver (Canada)) through Nuclepore membranes.

Preparation of liposomes/AuNPs hybrids

The hybrid samples preparation procedure for Figure 2a of the main text is the following: 20 µL of liposomes (previously diluted to a final lipid concentration of 0.04 mg/ml) or extracellular vesicles were placed inside a 500 µL UV-Vis

plastic cuvette. Then 100 µL of citrated gold nanoparticles ($6.7 \cdot 10^{-9}$ M, see "Synthesis citrated Gold Nanoparticles" and "Supplementary Characterization of Gold Nanoparticles" of SI) were added, in order to have a final concentration (inside the cuvette) of ~$5 \cdot 10^{-11}$ M and of ~$5 \cdot 10^{-9}$ M for liposomes and AuNPs, respectively, and liposomes/AuNPs number ratio of ~1/100. This liposomes/AuNPs number ratio was selected on the basis of our previous publication [3], which highlights that the aggregation of AuNPs on POPC vesicles -and subsequent AuNPs SPR variations- is promoted by low liposomes amounts within the mix. Thus, such a ratio allows for maximizing the liposomes-induced AuNPs SPR spectral shift for an enhanced sensitivity of the plasmon-based nanoruler assay. Then, samples were incubated for 15 minutes, after that the UV-Vis spectra were recorded.

The hybrid samples preparation procedure for Figure 2b of the main text is the following: fixed volumes (768.9 µL) of AuNPs dispersion ($6.7 \cdot 10^{-9}$ M) were added to 20 µL of liposomes (see Table S4 of SI for liposomes concentration), in order to have a final AuNPs/liposomes number ratio of ~8. Samples were incubated for 15 minutes, then placed in glass capillaries of 1 mm diameter and Small-Angle X-Ray profiles acquired.

UV-vis spectroscopy

UV-Vis spectra were measured with a JASCO UV-Vis spectrophotometer.

Small Angle X-ray Scattering

SAXS measurements for the characterization of AuNPs were carried out on a S3-MICRO SAXS/WAXS instrument (HECUS GmbH, Graz, Austria) which consists of a GeniX microfocus X-ray sealed Cu Kα source (Xenocs, Grenoble, France) of 50 W power which provides a detector focused X-ray beam with λ = 0.1542 nm Cu Kα line. The instrument is equipped with two one-dimensional (1D) position sensitive detectors (HECUS 1D-PSD-50 M system). Each detector is 50 mm long (spatial resolution 54 μm/channel, 1024 channels) and covers the SAXS q-range ($0.003 < q < 0.6\,^{\circ}\text{Å}^{-1}$). The temperature was controlled by means of a Peltier TCCS-3 Hecus. The analysis of SAXS curves was carried out using Igor Pro.[4] SAXS measurement on AuNPs aqueous dispersion was carried out in a sealed glass capillary of 1.5 mm diameter. To analyze gold nanospheres' curves we chose a model function with a spherical form factor and a Schulz size distribution:[5], it calculates the scattering for a polydisperse population of spheres with uniform scattering length density. The distribution of radii is a Schulz distribution given by the following equation:

$$f(R) = (z+1)^{z+1} x^{z} \frac{exp[-(z+1)x]}{R_{avg}\Gamma(z+1)}$$

where R_{avg} is the mean radius, $x = R/R_{avg}$ and z is related to the polydispersity. The form factor is normalized by the average particle volume, using the 3rd moment of R:

$$\langle V \rangle = \frac{4\pi}{3}\langle R^{+3} \rangle = \frac{4\pi}{3}\langle R \rangle^{+3}\frac{(z+3)(z+2)}{(z+1)^2}$$

The scattering intensity is:

$$I(q) = \left(\frac{4\pi}{3}\right)^2 N_0 \Delta\rho^2 \int_0^\infty f(R)R^6F^2(qR)dR$$

where N_0 is the total number of particles per unit volume, $F(R)$ is the scattering amplitude for a sphere and $\Delta\rho$ is the difference in scattering length density between the particle and the solvent.

SAXS measurements for the characterization of AuNPs/liposomes hybrids were collected at beamline ID02 at the European Synchrotron Radiation Facility (ESRF, Grenoble, France) [6]. A scattering vector (of magnitude q) range of $0.007 \leq q \leq 0.2$ nm^{-1} was covered with two sample–detector distances (1 and 10 m) and a single-beam setting for an X-ray monochromatic radiation wavelength with a wavelength of $\lambda = 0.10$ nm (12.46 keV). The beam diameter was adjusted to 72.4 μm in the horizontal (x) direction and 42.3 μm in the vertical (y) direction (full width at half-maximum at the sample). Assuming a Gaussian distribution, the portion of the beam that is hitting outside the channel can be estimated. When the channel is centered, this is ~0.3% but closer to the edge and more beam overlaps the edge. The beamstop diameter was 2 mm. As a detector, a 2D Rayonix MX-

170HS with a pixel size of 44 × 44 μm2 was used, which was housed in an evacuated flight tube, at a sample-to-detector distance of alternatively 10 m (leading to an available q-range of 0.007-0.02 nm^{-1}) or 1 m (leading to an available q-range of 0.07-0.2 nm^{-1}). The exposure times for the background- and sample measurements were 0.5 s for the case of 1 m sample-to-detector distance and 0.3 s for the case of 10 m sample-to-detector distance. Measured scattering patterns were normalized to an absolute intensity scale after applying standard detector corrections and then azimuthally averaged to obtain the one-dimensional intensity profiles, denoted by I (q).

Atomic Force Microscopy (AFM)

Surface Preparation and Sample Deposition

All AFM experiments were performed on poly-L-lysine (PLL) coated glass coverslips. All reagents were acquired from Sigma-Aldrich Inc (www.sigmaaldrich.com) unless otherwise stated. Microscopy borosilicate glass slides (15mm diameter round coverslips, Menzel Gläser) were first immersed in a 3:1 mixture of 96% H_2SO_4 and 50% aqueous H_2O_2 ('oxidising piranha') solution for 2 h in order to remove any organic residue present on their surface; after that, they were cleaned in a sonicator bath (Elmasonic Elma S30H) for 30 minutes in acetone, followed by 30 minutes in isopropanol and 30 minutes in ultrapure water (Millipore Simplicity UV). Clean slides were incubated overnight

in a 0.0001% (w/v) PLL solution at room temperature, thoroughly rinsed with ultrapure water and dried with nitrogen. A 10 µl-droplet of the vesicle-containing solution under study was deposited on a PLL-functionalized glass slide and left to adsorb for 10 minutes at 4°C, then inserted in the AFM fluid cell (see below) without further rinsing. The concentration of each vesicle-containing solution was adjusted in order to maximize the surface density of isolated, individual vesicles and minimize clusters of adjoining vesicles.

AFM Setup

All AFM experiments were performed in ultrapure water at room temperature on a Bruker Multimode (equipped with Nanoscope V electronics, a sealed fluid cell and a type JV piezoelectric scanner) using Bruker SNL-A probes (triangular cantilever, nominal tip curvature radius 2-12 nm, nominal elastic constant 0.35 N/m, calibrated with the thermal noise method.

AFM Imaging

Imaging was performed in PeakForce mode. In order to minimize vesicle deformation or rupture upon interaction with the probe, the applied force setpoint was kept in the 150-250 pN range. Lateral probe velocity was not allowed to exceed 5µm/s. Feedback gain was set at higher values than those usually employed for optimal image quality in order to ensure minimal probe-induced vesicle deformation upon lateral contact along the fast scan axis (please refer to Ridolfi et al. [7] for further details). The average height value of all bare substrate

zones was taken as the baseline zero height reference. Image background subtraction was performed using Gwyddion 2.53.16 [8].

AFM-based Force Spectroscopy (AFM-FS)

The mechanical characterization of vesicles via AFM force spectroscopy was performed by first scanning the sample (see previous paragraph) to locate individual vesicles. The chosen vesicles were then imaged reducing the scan size for achieving higher accuracy. We recorded a series of force/distance curves at multiple XY positions (typically around 64-100 curves arranged in a square array covering the vesicle initial location) for each individual vesicle. In most cases, only a few curves showed the mechanical fingerprint of an intact vesicle response to indentation: a linear deformation upon applied pressure during probe penetration. Of these, we first discarded those curves with probe-vesicle contact points occurring at probe-surface distances below vesicle height as measured by imaging. Remaining traces (typically 1-3 per vesicle) were analyzed to calculate vesicle stiffness (k_S).

Transmission Electron Microscopy

Trasmission electron microscopy (TEM) images were acquired with a STEM CM12 Philips electron microscope equipped with an OLYMPUS Megaview G2 camera, at CeME (CNR Florence Research Area, Via Madonna del Piano, 10 - 50019 Sesto Fiorentino). A drop of citrated AuNPs, diluted ten times, was placed

on 200 mesh carbon-coated copper grids with a diameter of 3 mm and a thickness of 50 μm (Agar Scientific) and dried at room temperature. Then, the sample was analyzed at an accelerating voltage of 100 keV.

Dynamic Light Scattering

DLS measurements at $\theta = 90°$ were performed using a Brookhaven Instrument 90 Plus (Brookhaven, Holtsville, NY). Each measurement was an average of ten repetitions of one minute each and repeated ten times. The autocorrelation functions were analyzed through the cumulant fitting stopped to the second order or with Laplace inversion according to CONTIN algorithm, allowing an estimate of the hydrodynamic diameter of particles.

Z-Potential Measurements

Zeta potential measurements were performed using a Zeta Potential Analyzer (Zeta Plus, Brookhaven Instruments Corporation, Holtsville, NY). Zeta potentials were obtained from the electrophoretic mobility u, according to Helmholtz-Smoluchowski equation: $\zeta = (\eta/\varepsilon) \times u$ with η being the viscosity of the medium, ε the dielectric permittivity of the dispersing medium. The Zeta Potential values are reported as averages from ten measurements.

Supplementary Characterization of Gold Nanoparticles

Transmission Electron Microscopy

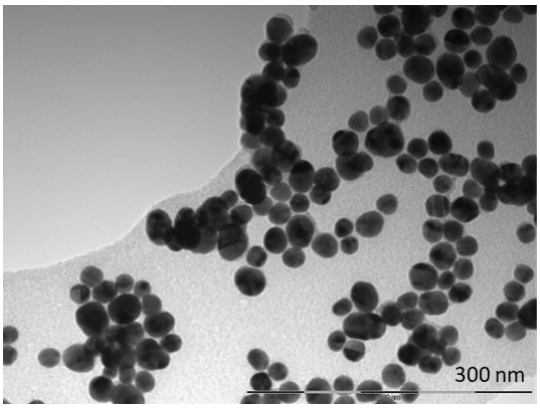

Figure S1 Representative Transmission electron microscopy (TEM) images of citrated gold nanoparticles acquired with a STEM CM12 Philips electron microscope, at CeME (CNR Florence Research Area, Via Madonna del Piano, 10 - 50019 Sesto Fiorentino). The sample was placed on a 200 mesh carbon-coated copper grid.

Small Angle X-ray Scattering

The analysis of SAXS curves was carried out using Igor Pro.[4] SAXS measurements on AuNPs aqueous dispersion were carried out in sealed glass capillaries of 1.5 mm diameter. To analyze gold nanospheres' curves we chose a model function with a spherical form factor and a Schulz size distribution:[5], it calculates the scattering for a polydisperse population of spheres with uniform scattering length density. The distribution of radii is a Schulz distribution given by the following equation:

$$f(R) = (z+1)^{z+1} x^z \frac{exp[-(z+1)x]}{R_{avg}\Gamma(z+1)}$$

where R_{avg} is the mean radius, $x = R/R_{avg}$ and z is related to the polydispersity. The form factor is normalized by the average particle volume, using the 3rd moment of R:

$$\langle V \rangle = \frac{4\pi}{3}\langle R^{+3} \rangle = \frac{4\pi}{3}\langle R \rangle^{+3} \frac{(z+3)(z+2)}{(z+1)^2}$$

The scattering intensity is:

$$I(q) = \left(\frac{4\pi}{3}\right)^2 N_0 \Delta\rho^2 \int_0^\infty f(R) R^6 F^2(qR) dR$$

where N_0 is the total number of particles per unit volume, $F(R)$ is the scattering amplitude for a sphere and $\Delta\rho$ is the difference in scattering length density between the particle and the solvent. The structural parameters (Table S1) of citrated gold nanoparticles were evaluated from the SAXS profile of their water dispersion (Figure S2) according to the models reported in the Materials and Methods section of SI.

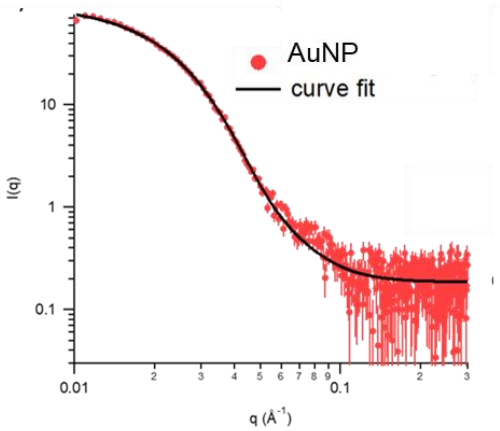

Figure S2 Experimental SAXS curve (red markers) obtained for AuNPs and curve fit (solid black line) according to the Schulz spheres model from the NIST package SANS Utilities. The size and polydispersity obtained from the fitting procedure are summarized in the Table S1 below.

	R_{core} (nm)	poly
AuNP	6.5	0.3

Table S1 Structural parameters of the nanoparticles obtained from the analysis of SAXS curves according to the the Schulz spheres model.

Dynamic Light Scattering and Z-Potential

AuNPs hydrodynamic diameter and surface charge in MilliQ water were evaluated through Dynamic Light Scattering and Zeta-Potential, respectively,

and reported in Table S2.

	D_h (nm)	Z-Potential (mV)
AuNPs	15.8 ± 0.3	-36 ± 2

Table S2 Hydrodynamic diameter obtained from Dynamic Light Scattering and Zeta Potential values of AuNPs.

UV-vis Spectroscopy

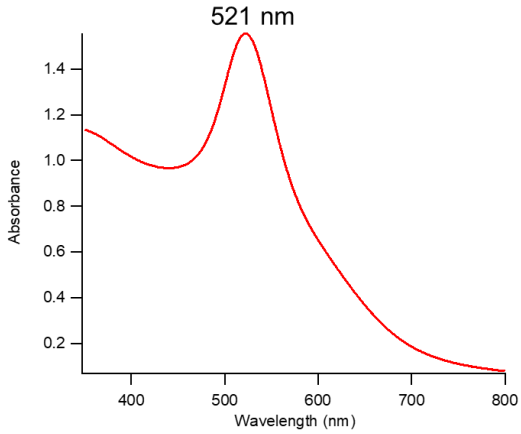

Figure S3 UV-Vis absorption spectra of AuNPs after 1:5 dilution in water. The plasmon absorption peak is at around 521 nm.

The size of AuNPs was further evaluated from UV-Vis Spectroscopy by the following equation [9]:

$$d = \exp\left(B_1 \frac{A_{spr}}{A_{450}} - B_2\right)$$

with d diameter of gold nanoparticles, A_{spr} absorbance at the surface plasma resonance peak, A_{450} absorbance at the wavelength of 450 nm and B_1 and B_2 are dimensionless parameters, taken as 3 and 2.2, respectively. The diameter value obtained is of 13.5 nm.

The concentration of citrated gold nanoparticles was determined via UV-Vis spectrometry, using the Lambert-Beer law ($E(\lambda) = \varepsilon(\lambda)lc$), taking the extinction values $E(\lambda)$ at the LSPR maximum, i.e. λ = 521 nm. The extinction coefficient $\varepsilon(\lambda)$ of gold nanoparticles dispersion was determined by the method reported in literature [10], by the following equation:

$$\ln(\varepsilon) = k\ln(d) + a$$

with d core diameter of nanoparticles, and k and a dimensionless parameters ($k = 3.32111$ and $a = 10.80505$). The arithmetic mean of the sizes obtained by optical and scattering analyses was selected, leading to a $\varepsilon(\lambda)$ of $2.8 \cdot 10^8$ $M^{-1}cm^{-1}$. The final concentration of the citrated AuNPs is therefore ~$5.6 \cdot 10^{-9}$ M.

Supplementary Characterization of Liposomes

Dynamic Light Scattering and Zeta-Potential

	D_h (nm)	Zeta P
DOPC	118.6 ± 0.2	-16 ± 1
POPC	103.8 ± 0.1	-19 ± 3
POPC/DPPC	92.1 ± 0.2	-22 ± 1
DPPC	115.7 ± 0.1	-13 ± 1
DPPC/DSPC	104 ± 0.2	-10 ± 1
DSPC	127.7 ± 0.2	-19 ± 1

Table S3 Hydrodynamic diameter obtained from Dynamic Light Scattering and Zeta Potential values of synthetic liposomes.

Evaluation of Liposomes concentration

The lipid concentration in the starting colloidal dispersion was estimated to be 4 mg/mL from the initial lipid and water amounts employed in the formation and swelling of lipid films (see "Preparation of liposomes" in the Materials and Methods section), assuming the absence of lipid loss due to the extrusion procedure. The liposomes concentration in the final dispersion was subsequently

calculated considering the hydrodynamic diameter of each liposomal batch (Table S3 of SI). In particular, from the liposomes' average diameter, the liposomal surface area (surface area=$4\pi r^2$) can be calculated; the doubled surface can be subsequently divided by the lipid cross section (0.5 nm^2) in order to obtain the lipid number per liposome, assuming that approximately one half of the lipids is localized in the external leaflet of a liposomes, since the bilayer thickness, about 4-5 nm, is negligible with respect to the liposomes' average diameter. Eventually, the total weighted lipid concentration was divided by the total number of lipids per liposome, yielding the real liposome concentration, which is reported in Table S4 for each liposomes' dispersion.

	Concentration (M)
DOPC	$3.2 \cdot 10^{-8}$
POPC	$3.1 \cdot 10^{-8}$
POPC/DPPC	$3.6 \cdot 10^{-8}$
DPPC	$3.1 \cdot 10^{-8}$
DPPC/DSPC	$3.8 \cdot 10^{-8}$
DSPC	$3.5 \cdot 10^{-8}$

Table S4 Final liposomes' concentration in each liposomal batch.

Supplementary Characterization of EVs

Zeta Potential

The Zeta Potential of EVs dispersion in milliQ water was measured as described in the "Material and Methods" section of SI and is equal to -21 ± 3 mV.

AFM characterization of synthetic and natural lipid vesicles

AFM Mechanical Characterization

According to the Canham-Helfrich theory, the mechanical response of a vesicle to an applied force is elastic; this behavior is reflected in the linear relationship between the force and tip penetration, in the AFM force-distance curves, right after the contact point (see Fig.1b in the main text). Calculating the slope of this linear part, gives the value of the vesicle stiffness, a mechanical parameter that accounts for multiple contributions, the most relevant being the intrinsic membrane rigidity (the bending modulus) and the vesicle luminal, i.e. internal, pressure. The latter contribution describes the vesicle pressurization following the deformation applied by the AFM tip. This deformation generates a volume variation that increases the pressure within the vesicle. While the bending modulus is an intrinsic descriptor of the lipid membrane bending rigidity, the internal pressure and hence the stiffness depend on the size of each vesicle. Indeed, the volume variation associated with a given tip penetration varies with

the vesicle size (i.e. the same penetration will result in higher volume variations for smaller vesicles); as a consequence, vesicles that are heterogenous in size will be subjected to different pressurizations following similar indentation events. However, both the measured liposomes and EVs are characterized by low polydispersity, this allows considering the stiffness a size-independent parameter. Moreover, since all the tested liposomes were characterized by similar size distributions and same polar headgroups, they will experience similar pressurizations and electrostatic attractions to the substrate; as a result, we can assume that changes in their stiffness are entirely ascribable to differences in their membrane rigidity, which can be recapitulated by the bending modulus. Membrane rigidity may vary depending on the phase behavior of the lipid bilayer, a temperature dependent parameter. All the measurements were performed at 28°C, where neat DOPC and POPC vesicles are in the fluid phase, while DPPC and DSPC ones are in the gel phase. In fluid-state membranes, lipid molecules can diffuse freely within the bilayer plane, while in gel- state membranes lipids are more tightly packed and their motion is more constrained. As a consequence, gel- phase bilayers are expected to be stiffer than fluid- phase ones. Our results from the Force Spectroscopy FS analysis (Figure 1c, main text) confirms this behavior, with DPPC and DSPC vesicles being substantially stiffer than DOPC and POPC ones. Two other important parameters that can affect the stiffness of a lipid bilayer are the chain length and its degree of saturation; e. g. DSPC

possesses two fully saturated chains, longer than all the other measured ones, resulting in the highest measured stiffness. Overall, the obtained stiffness values for neat DOPC, POPC, DPPC and DSPC vesicles (Figure 1c, main text) are in good agreement with results from recent AFM-FS investigations on similar vesicles [11]. Another interesting aspect to highlight is that the stiffnesses measured for the hybrid lipid vesicles (POPC/DPPC and DPPC/DSPC) have intermediate values with respect to liposomes made of the two pure components.

AFM-based characterization of EVs size distribution, concentration and purity

AFM imaging was employed to obtain the size distribution of the EVs sample. A total of 166 EVs were imaged; from the topography of the AFM images, assuming the vesicle surface area conservation and by applying simple geometric consideration (see Ridolfi et al.[12] for further details) it is possible to obtain the values of the diameter that the vesicles would have had in solution, prior to their adsorption to the surface (we refer to this parameter as "Size"). Figure S4 displays the size distribution for the EVs sample used in this study. The measured EVs have a mean size of 74 nm with a standard deviation of 30 nm.

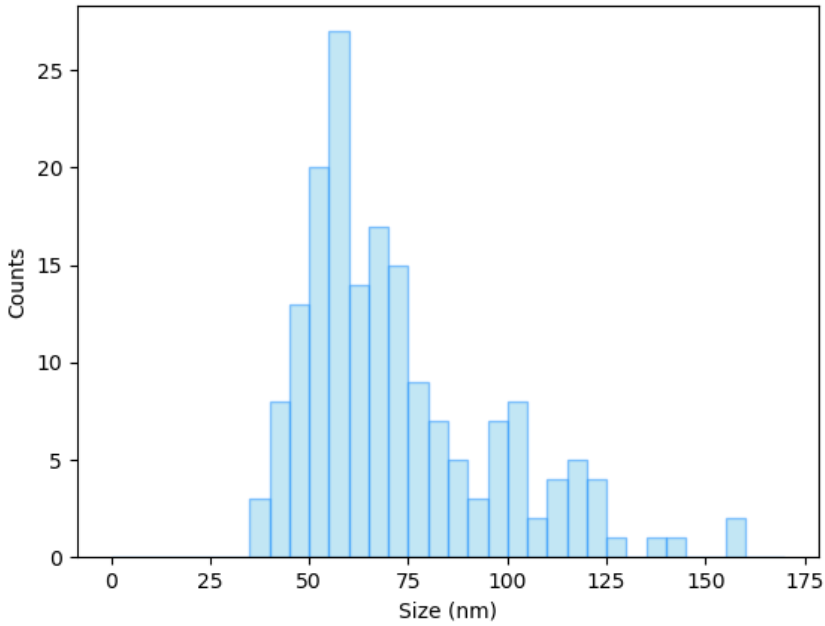

Figure S4: EVs size distribution obtained from the AFM imaging analysis. The size of the EVs (reported in the horizontal axis), indicates the diameter that the vesicles would have had in solution, prior to their adsorption.

Exploiting the AFM-based characterization method developed by Ridolfi et al.[7], it is also possible to detect the presence of contaminants that, from a physico-chemical point of view, do not behave like a lipid vesicle; the method is based on the calculation of the contact angle (CA) that each vesicle displays after adsorption on the surface. Both synthetic lipid vesicles and EVs are characterized by a narrow distribution of CA over the whole range of characteristic sizes. Figure S5 shows the CA values of each of the imaged EVs, plotted against their

size; as can be seen, the scatterplot displays only the fingerprint of the typical vesicle-like behavior, ruling out the presence of any contaminant on the surface.

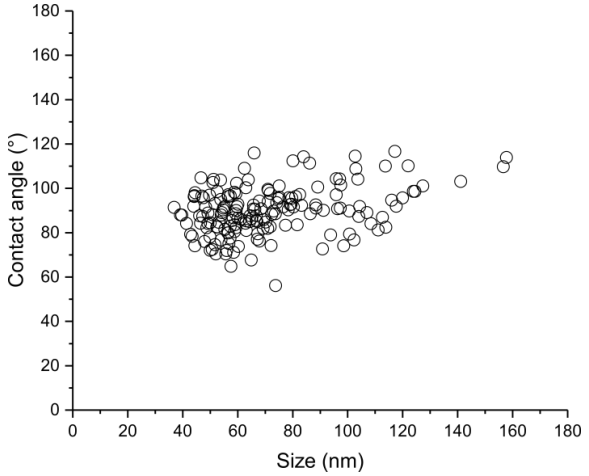

Figure S5: Scatterplot showing the contact angle of each EV, plotted against their respective size. According to this characterization, the EVs show the typical vesicle-like behavior, i.e. narrow CA distribution over the entire range of sizes (average CA value is 90° and the standard deviation is 11°); pointing to the absence of any spherical contaminant.

AFM imaging was also used to estimate the starting concentration of the EVs sample. To do this, we compared the number of DPPC liposomes (coming from a solution with a known concentration and having a size distribution similar to the EVs) adsorbed on the glass surface with the number of EVs adsorbed on the same glass surface. This represents only a qualitative procedure and it is based on different assumptions: i) the interactions of DPPC liposomes with the glass surface are similar to the EVs ones, ii) the recorded images are representative of both the vesicles samples, iii) the size distributions of the two samples are

similar to each other. The concentration of the DPPC starting solution is 0.02 mg/ml; analysing the AFM images, we recorded a total of 329 vesicles in 4 different images, giving an average of 82.25 vesicles per image. Measuring EVs from TRAMP cells, we sampled 5 images, obtaining a total number of 166 EVs; 33.20 EVs per image. From proportionality considerations, it is possible to estimate the concentration of the EVs, spotted on the glass coverslips, using the following expression:

DPPC concentration (mg/ml):DPPC liposomes per image=EVs concentration (mg/ml) :EVs per image

From the expression we obtained a concentration of 0.008 mg/ml for the EVs sample. Since the EVs starting solution have been diluted six times before being spotted on the glass surface, the starting concentration is~0.048 mg/ml.

Supplementary Characterization of liposomes/AuNPs hybrids

Small-Angle X-Ray Scattering

SAXS measurements on liposomes/AuNPs hybrids were recorded at ID02 beamline, ESRF (Grenoble, France), using a sample-to-detector distance of 10 m. The analysis of SAXS curves was carried out using Igor Pro[4]. SAXS measurements on liposomes/AuNPs aqueous dispersion were carried out in

sealed glass capillaries of 1 mm diameter.

The SAXS profiles of DOPC liposomes/AuNPs and POPC liposomes/AuNPs in Figure 2b were fitted according to a linear fit in the 0.0695-0.1142 nm^{-1}q-range, to obtain the slope values reported in the main text (-1.5404 ± 0.00297 for DOPC and -1.4987 ± 0.00612 for POPC). The fitting yielded a chisquare of 0.000239052 and 0.00106975, for DOPC/AuNPs and POPC/AuNPs respectively.

The SAXS results of inset of Figure 2b were collected at ID02 beamline, ESRF (Grenoble, France), using a sample-to-detector distance of 1 m.

The scattering intensity (I(q)) is defined by the following equation:

$$I(q) = KN_pV_p^2(\Delta\rho)^2P(q)S(q) + B$$

With k instrumental constant, N_p scattering nanoparticles' number per unit volume, V_p nanoparticle's volume, $\Delta\rho$ contrast of the experiment, B background intensity, P(q) e S(q) form and structure factors, respectively.

In order to obtain the structure factor of the liposome/AuNPs complex, we divided the scattering intensity of the liposomes/AuNPs hybrid by the scattering intensity of the neat AuNPs dispersion (at a suitable dilution of 1:10):

$$\frac{I(q)_{Hyb}}{I(q)_{NP}} \sim \frac{S(q)_{Hyb}P(q)_{Hyb}}{S(q)_{NP}P(q)_{NP}}$$

For a diluted AuNPs dispersion the structure factor can be considered equal to 1. In addition, in the high-q region (0.1-1.6 nm^{-1}), the form factor of

liposomes/AuNP hybrids can be approximated to the one of neat AuNPs, leading to the following:

$$\frac{I(q)_{Hyb}}{I(q)_{NP}} = S(q)_{Hyb}$$

The mean interparticle distance between the AuNPs within the aggregates (d) can be obtained from the S(q) vs q (nm^{-1}) plot (see inset of Figure 2b of the main text), by the following equation:

$$d = \frac{2\pi}{qmax}$$

With q_{max} q value corresponding to the maximum of the correlation peaks reported in the inset of figure 2b (main text).

UV-Vis Spectroscopy

The S.I. mean values for each liposomes/AuNPs mixtures are reported in Table S5, together with the relative standard deviation obtained from five repeated measurements on different samples (see "Preparation of liposomes/AuNPs hybrids" of SI).

	S.I. mean value	Standard deviation
DOPC	1.456	0.002
POPC	1.438	0.001
POPC/DPPC	1.377	0.005
DPPC	1.16	0.01
DPPC/DSPC	1.127	0.003

DSPC	1.026	0.006

Table S5 S.I. mean value and standard deviation for each liposomes/AuNPs hybrid.

The fitting parameters describing the sigmoidal best fit (eqn. 1 of the main text) for the S.I. values of liposomes plotted versus the AFM-determined stiffness, reported in Figure 3b of the main text, are the following:

a	**b**	**c**	**d**	**Chi square**
1.4831 ± 0.0485	-0.51151 ± 0.131	0.026043 ± 0.00266	0.0063004 ± 0.00265	0.0015

Table S6 Fitting parameters obtained by fitting the S.I. vs stiffness values of Figure 3c (main text) through the sigmoidal best fit (refer eqn 1 of main text for description of parameters).

The extent of AuNPs aggregation was also evaluated using different optical indexes, both taken from literature and defined in our lab.

In particular, as an alternative to the bending index defined in the main text, which is based on the determination of the area under the absorbance curve associated to AuNP aggregation, we defined another optical parameter (S.I. (2)). This alternative bending index allows evaluating AuNPs aggregation extent by calculating the intensity difference between the free AuNPs primary plasmon band (at 521 nm) and the aggregated AuNPs secondary plasmon peak, whose maximum is located at about 625 nm (see Figure S6). This result is then divided by the wavelength interval ($\Delta\lambda$) between the two peaks and normalized for the S.I. of neat AuNPs.

$$S.I.(2) = \frac{I_{625} - I_{521}}{\Delta\lambda}$$

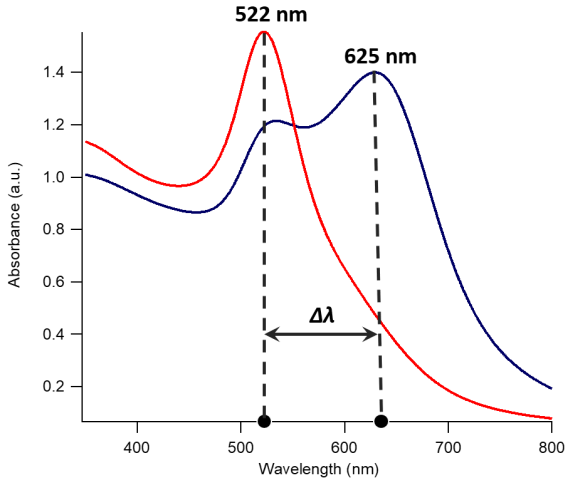

Figure S6 Visual description of the S.I. (2) evaluation.

We also selected another optical index from literature ($A.I._{CONAN}$) [13,14], which is commonly used to describe the aggregation of AuNPs on natural and synthetic vesicles and defined as follows:

$$A.I._{CONAN} = \frac{I_{521}}{I_{650} + I_{800}}$$

with I_{521} , I_{650} and I_{800} UV-Vis absorbances at 521, 650 and 800 nm respectively.

Both the S.I. (2) and the $A.I._{CONAN}$ show a sigmoidal behaviour as a function of membrane stiffness, as reported in Figure S7 and Table S7.

	S.I. (2)	A.I. CONAN
DOPC	-0.1965 ± 0.0004	0.785 ± 0.014
POPC	- 0.14 ± 0.03	0.83 ± 0.17
POPC/DPPC	0.12 ± 0.03	1.02 ± 0.05
DPPC	0.71 ± 0.06	1.99 ± 0.24
DPPC/DSPC	0.76 ± 0.01	2.36 ± 0.05
DSPC	1.04 ± 0.02	3.28 ± 0.24

Table S7 S.I. (2) and A.I. CONAN mean values and standard deviations for each liposomes/AuNPs hybrid.

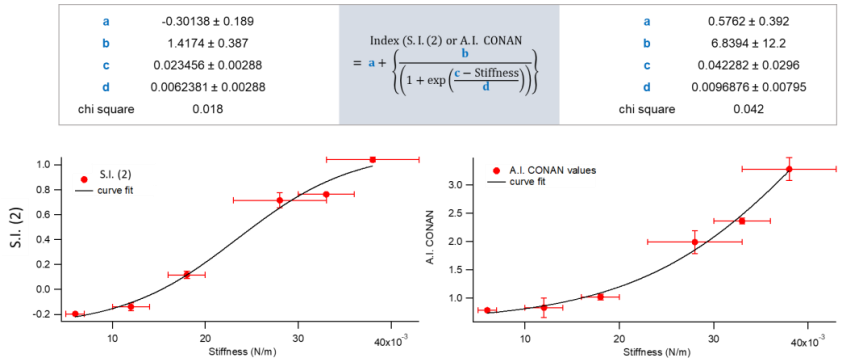

Figure S7 S.I. (2) and A.I. CONAN mean values and as a function of membrane stiffness. The sigmoidal fit curve is shown in black, together with the corresponding equation and fitting parameters (top inset).

Bibliography

1 J. Turkevich, P. C. Stevenson and J. Hillier, *Discuss. Faraday Soc.*, 1951, **11**, 55–75.

2 G. Frens, *Nat. Phys. Sci.*, 1973, **241**, 20–22.

3 C. Montis, L. Caselli, F. Valle, A. Zendrini, F. Carlà, R. Schweins, M. Maccarini, P. Bergese and D. Berti, *J. Colloid Interface Sci.*, 2020, **573**, 204–214.

4 S. R. Kline, *J. Appl. Crystallogr.*, 2006, **39**, 895–900.

5 M. Kotlarchyk and S.-H. Chen, *J. Chem. Phys.*, 1983, **79**, 2461.

6 T. Narayanan, M. Sztucki, P. Van Vaerenbergh, J. Gorini, L. Claustre, F. Sever and J. Morse, *J. Appl. Crystallogr.*, 2018, **51**, 1511–1524.

7 A. Ridolfi, M. Brucale, C. Montis, L. Caselli, L. Paolini, A. Borup, A. T. Boysen, F. Loria, M. J. C. Van Herwijnen, M. Kleinjan, P. Nejsum, N. Zarovni, M. H. M. Wauben, D. Berti, P. Bergese and F. Valle, *Anal. Chem.*, 2020, **92**, 10274–10282.

8 D. Nečas and P. Klapetek, *Cent. Eur. J. Phys.*, 2012, **10**, 181–188.

9 W. Haiss, N. T. K. Thanh, J. Aveyard and D. G. Fernig, *Anal. Chem.*, 2007, **79**, 4215–4221.

10 X. Liu, M. Atwater, J. Wang and Q. Huo, *Colloids Surfaces B Biointerfaces*, 2007, **58**, 3–7.

11 D. Vorselen, F. C. Mackintosh, W. H. Roos and G. J. L. Wuite, *ACS Nano*, 2017, **11**, 2628–2636.

12 A. Ridolfi, M. Brucale, C. Montis, L. Caselli, L. Paolini, A. Borup, A. T. Boysen, F. Loria, M. J. C. van Herwijnen, M. Kleinjan, P. Nejsum, N. Zarovni, M. H. M. Wauben, D. Berti, P. Bergese and F. Valle, *Anal. Chem.*, 2020, **92**, 10274–10282.

13 S. Busatto, A. Giacomini, C. Montis, R. Ronca and P. Bergese, *Anal. Chem.*, 2018, **90**, 7855–7861.

14 R. Carney, A. Zendrini, L. Paolini, S. Busatto and A. Radeghieri, *Front. Bioeng. Biotechnol.*, 2020, **7**, 1–10.

Manuscript n°4

Journal of Microscopy

Journal of Microscopy, Vol. 00, Issue 0 2020, pp. 1–10 doi: 10.1111/jmi.12910
Received 31 March 2020; accepted 14 May 2020

Gold nanoparticles interacting with synthetic lipid rafts: an AFM investigation

ANDREA RIDOLFI*,†,‡*, LUCREZIA CASELLI‡*, COSTANZA MONTIS*,‡, GAETANO MANGIAPIA§, DEBORA BERTI*,‡, MARCO BRUCALE*,† & FRANCESCO VALLE*,†

*Consorzio Interuniversitario per lo Sviluppo dei Sistemi a Grande Interfase (CSGI), Florence, Italy
†Consiglio Nazionale delle Ricerche, Istituto per lo Studio dei Materiali Nanostrutturati (CNR-ISMN), Bologna, Italy
‡Dipartimento di Chimica 'Ugo Schiff', Università degli Studi di Firenze, Florence, Italy
§GEMS am Heinz Maier-Leibnitz Zentrum (MLZ), Helmholtz-Zentrum Geesthacht GmbH, Garching, Germany

Key words. Atomic force microscopy, gold nanoparticles, lipid rafts, supported lipid bilayers.

Summary

Inorganic nanoparticles (NPs) represent promising examples of engineered nanomaterials, providing interesting biomedical solutions in several fields, like therapeutics and diagnostics. Despite the extensive number of investigations motivated by their remarkable potential for nanomedicinal applications, the interactions of NPs with biological interfaces are still poorly understood. The effect of NPs on living organisms is mediated by biological barriers, such as the cell plasma membrane, whose lateral heterogeneity is thought to play a prominent role in NPs adsorption and uptake pathways. In particular, biological membranes feature the presence of rafts, that is segregated lipid micro and/or nanodomains in the so-called liquid ordered phase (L_o), immiscible with the surrounding liquid disordered phase (L_d). Rafts are involved in various biological functions and act as sites for the selective adsorption of materials on the membrane. Indeed, the thickness mismatch present along their boundaries generates energetically favourable conditions for the adsorption of NPs. Despite its clear implications in NPs internalisation processes and cytotoxicity, a direct proof of the selective adsorption of NPs along the rafts' boundaries is still missing to date. Here we use multicomponent supported lipid bilayers (SLBs) as reliable synthetic models, reproducing the nanometric lateral heterogeneity of cell membranes. After being characterised by atomic force microscopy (AFM) and neutron reflectivity (NR), multidomain SLBs are challenged by prototypical inorganic nanoparticles, that is citrated gold nanoparticles (AuNPs), under simplified and highly controlled conditions. By exploiting AFM, we demonstrate that AuNPs preferentially target lipid phase boundaries as adsorption sites. The herein reported study consolidates and extends the fundamental knowledge on NPs–membrane interactions, which constitute a key aspect to consider when designing NPs-related biomedical applications.

Introduction

Despite the impressive technological advancement in the design of 'smart' inorganic nanoparticles (NPs), their impact on biological systems and related toxicity are still poorly understood (Nel *et al.*, 2009; Henriksen-Lacey *et al.*, 2017), limiting their effective clinical translation. The interaction of engineered nanomaterials, either intentionally or inadvertently released into the environment, with living organisms is mediated by biological barriers, such as cell plasma membranes, which primarily determine NPs biological fate and cytotoxicity (Beddoes *et al.*, 2015). Therefore, the interaction of NPs with biological interfaces is a key research topic, aiming at the safe use of nanotechnology and maximisation of its potential in therapeutics and diagnostics (Mendozza *et al.*, 2019; Zendrini *et al.*, 2020).

In this framework, lipid-based synthetic model membranes are useful platforms to mimic biological interfaces under simplified conditions, allowing for the identification of key determinants regulating nano-bio interactions (Gkeka *et al.*, 2013; Simonelli *et al.*, 2015; Su *et al.*, 2018). Supported lipid bilayers (SLBs) are often used as 2D biomembrane models (Richter *et al.*, 2006; Hardy *et al.*, 2013), enabling to precisely tune their physicochemical properties and avoiding the complications related to the 3D nature of biological membranes. They also represent versatile and promising platforms for the development of biosensors (Nikoleli *et al.*, 2018) and technological assays for biological applications (Worsfold *et al.*, 2006).

In addition, multicomponent SLBs models allow studying the lateral compositional heterogeneity that characterises

* Authors A. Ridolfi and L. Caselli contributed equally to this work.

Correspondence to: A. Ridolfi, Consorzio Interuniversitario per lo Sviluppo dei Sistemi a Grande Interfase (CSGI), via della Lastruccia 3, 50019, Florence, Italy. Tel: +39-051-6398519; e-mail: andrea.ridolfi@ismn.cnr.it

most biological membranes. The existence of discrete lipid domains in natural membranes was questioned for a long time before its direct experimental assessment (Munro, 2003). Recently however, advanced experimental techniques have provided convincing evidence that the self-organisation of lipids and proteins can induce subcompartmentalisation in cell membranes (Lingwood & Simons, 2010), which is thought to have a profound impact on their biological function (Sezgin *et al.*, 2017). A specific case of lateral organisation is represented by lipid rafts, defined as micro and/or nanodomains, enriched in lipids such as cholesterol, sphingomyelin, saturated glycerophospholipids and glycosphingolipids: these lipids segregate in the so-called liquid-ordered phase (L_o), which is immiscible with the surrounding liquid-crystalline (disordered, L_d) phase (Koynova & Tenchov, 2013). This phase heterogeneity induces a thickness mismatch between neighbouring domains and the consequent, ergonically unfavourable, exposure of hydrocarbon regions to water, which results in an energetic cost, due to interfacial energy (Heberle *et al.*, 2013). Rafts are thought to participate in the formation and targeting of nano-sized biogenic lipid vesicles (e.g. extracellular vesicles, EVs) (Busatto *et al.*, 2020). They are also actively involved in multiple membrane processes, for example, they act as structural platforms for organising protein machinery (Lingwood & Simons, 2010), they can preferentially associate with specific membrane proteins (Simons & Ikonen, 1997) and represent centres for the assembly of signalling molecules. From a mechanical point of view, the presence of phase boundaries and, hence, bilayers thickness mismatches, generates deformations and increases membrane permeability (Kuzmin *et al.*, 2005; Rawicz *et al.*, 2008; Sheikh & Jarvis, 2011). All these structural perturbations promote the selective adsorption of materials on the membrane; indeed, as pointed out by Hamada *et al.* (2012), lateral heterogeneity, promoted by the presence of micro-sized lipid rafts, regulates the adsorption of nano/microparticles, with the larger ones preferring the L_d phase-domains and the smaller ones being localised in the L_o phase-domains of cell-sized lipid vesicles. These selective NPs adsorption pathways are also present in the case of nano-sized lipid segregated domains and can be studied exploiting liposomes with tuneable rafts size (Heberle *et al.*, 2013). However, investigating the interaction of NPs with nanometric lipid rafts remains a major challenge, mainly hindered by the small size of the segregated domains, which makes standard optical techniques not suitable for the task. Recent studies demonstrated that gold nanoparticles (AuNPs) adsorb more strongly to phase-separated multicomponent lipid bilayers; in particular, they are believed to preferentially target phase boundaries, due to the intrinsic negative curvature that characterises these regions (Melby *et al.*, 2016; Sheavly *et al.*, 2019).

To the best of our knowledge, this behaviour has only been investigated by computational studies (Sheavly *et al.*, 2019) and experiments involving quartz crystal microbalance (QCM) (Melby *et al.*, 2016), which provide important but indirect evidences. In summary, the preferential adsorption of AuNPs along the boundaries of nano-sized lipid domains has never been directly observed.

To fill this gap, we exploit Atomic Force Microscopy (AFM), to directly visualise the preferential adsorption of AuNPs on the phase boundaries of multicomponent SLBs, presenting both an L_d and an L_o phase-like domains and previously characterised by neutron reflectivity (NR). The L_d domains are mainly composed of 1,2-dioleoyl-sn-glycero-3-phosphocholine (DOPC) with two unsaturated hydrocarbon chains that hinder molecular packing, while the L_o domains are mainly composed of 1,2-dipalmitoyl-sn-glycero-3-phosphocholine (DSPC) lipids; cholesterol molecules occupy the free volume between the lipid acyl chains (Toppozini *et al.*, 2014; Sezgin *et al.*, 2017). The quantitative localisation and morphometry of AuNPs adsorbed on the SLB reveal important information regarding their interaction with the lipid matrix. The study corroborates the already theorised differential NPs-lipid interaction taking place at the phase boundaries of lipid rafts. The presented results could help the development of future NPs-based applications that involve their adsorption on membranes characterised by nanoscale phase segregations.

Materials and methods

Materials

Tetrachloroauric (III) acid (≥99.9%), trisodium citrate dihydrate (≥99.9%), methanol (99.8%), $CHCl_3$ (≥99.9%), NaCl (≥99.5%) and $CaCl_2$ (99.999%) were provided by Sigma-Aldrich (St. Louis, MO, USA). The same for 1,2-dioleoyl-sn-glycero-3-phosphocholine (DOPC) (≥98.0%), cholesterol (≥99.5%) and 1,2-distearoyl-sn-glycero-3-phosphocholine (DSPC) (≥98.0%). All chemicals were used as received. Milli-Q grade water was used in all preparations.

AuNP preparation

Anionic gold nanospheres of 16 nm in size were synthesised according to the Turkevich-Frens method (Turkevich *et al.*, 1951; Frens, 1973). Briefly, 20 mL of a 1 mM $HAuCl_4$ aqueous solution were brought to boiling temperature under constant and vigorous magnetic stirring. Two millilitres of 1% citric acid solution were then added and the solution was further boiled for 20 min, until it acquired a deep red colour. The nanoparticles solution dispersion was then slowly cooled down to room temperature.

Vesicle preparation and SLB formation for neutron reflectivity measurements

Vesicle preparation. The proper amount of a DOPC/DSPC/cholesterol mixture (39/39/22 mol%) was dissolved in

chloroform and a lipid film was obtained by evaporating the solvent under a stream of nitrogen and overnight vacuum drying. The film was then swollen and suspended in warm (50°C) 100 mM NaCl water solution by vigorous vortex mixing, in order to obtain a final 0.5 mg mL^{-1} lipid concentration. The resultant multilamellar vesicles (MLVs) were tip sonicated with a Digital Sonifier Model 450 (Branson, Hampton, NH, USA), provided with a Horn Tip (diameter 25.4 mm), in an intermittent-pulse mode (5 s), with a power of 400 W (amplitude 50%), for 15 min to obtain a homogeneous dispersion of unilamellar vesicles (ULVs).

Surface cleaning procedure. DOPC/DSPC/cholesterol single lipid bilayers were formed on 50 × 80 × 15 mm^3 Silicon mirrors (Andrea Holm GmbH, Tann, Germany; roughness ≤ 5 Å). Substrates were preliminary rinsed in either ultrapure water and ethanol, in order to remove organic residues. After that, they were bath sonicated treated for 30 min in ethanol with a Bandelin DL 102 3L bath sonicator (Bandelin Ultraschall seit 1955, Berlin, Germany), followed by other 30 min in ultrapure water (Millipore Simplicity UV). The surfaces were then cleaned with a Novascan PSD-UV8 UV/ozone plasma (Boone, IA, USA) for 30 min and rinsed in ultrapure water. Finally, they were dried with nitrogen gas and stored in ultrapure water, ready for the deposition.

Vesicle fusion and SLB formation. $CaCl_2$ was added to the vesicle dispersion, reaching a final concentration of 10 mM, just before the injection in the NR measuring cell. This was performed in order to promote their adhesion to the support and their subsequent disruption. Vesicles were left incubating for 30 min; then, the saline buffer was switched to D_2O to promote the vesicle disruption and SLB formation. The use of D_2O instead of ultrapure water ensures a better resolution of the lipid structures for the NR measurements.

Vesicle preparation and SLB formation for AFM measurements

Vesicle preparation. The proper amount of a DOPC/DSPC/cholesterol mixture (39/39/22 mol%) was dissolved in chloroform and a lipid film was obtained by evaporating the solvent under a stream of nitrogen and overnight vacuum drying. The film was then swollen and suspended in warm (50 °C) ultrapure water solution by vigorous vortex mixing, in order to obtain a final 0.5 mg mL^{-1} lipid concentration. The resultant multilamellar vesicles in water were subjected to 10 freeze-thaw cycles and extruded 10 times through two stacked polycarbonate membranes with 100 nm pore size at room temperature, to obtain unilamellar vesicles with narrow and reproducible size distribution. The filtration was performed with the Extruder (Lipex Biomembranes, Vancouver, Canada) through Nuclepore membranes.

Surface cleaning procedure. All reagents were purchased from Sigma-Aldrich Inc (www.sigmaaldrich.com, St. Louis, MO, USA). DOPC/DSPC/Chol supported lipid bilayers were formed on microscopy borosilicate glass coverslips (Menzel Gläser). Glass slides were first immersed in a 3:1 mixture of 96% H_2SO_4 and 50% aqueous H_2O_2 ('oxidising piranha') solution for 2 h in order to remove any organic residue present on their surface. Then, the slides were cleaned in a sonicator bath (Elmasonic Elma S30H, Distrelec, Lainate, MI, Italy) for 30 min in acetone, followed by 30 min in isopropanol and 30 min in ultrapure water (Millipore Simplicity UV). Glass slides were then cleaned with air plasma for 15 min (air plasma cleaner PELCO easiGlow, Ted Pella Inc., Redding, CA, USA) and incubated in ultrapure water for 10 min in order to maximise the number of reactive silanols present on the surface. Finally, they were dried with nitrogen gas and stick to a magnetic disk, ready for the lipid solution deposition.

Vesicle fusion and SLB formation. A 100 µL droplet of buffer solution was first spotted on the SiO_2 slide. The buffer solution consisted of $CaCl_2$ 200 mM diluted 1:10 in KCl 100 mM. A 10 µL droplet containing the lipid mixture was then added to the buffer droplet and left incubating at room temperature for 30 min in order to promote the vesicle adsorption on the surface. After that, the droplet was removed and replaced by a 100 µL droplet of ultrapure water which was then left incubating for other 15 min. AuNPs deposition on the SLB was obtained by adding 5 µL of a 7.8 nM AuNPs dispersion to the ultrapure water droplet and leaving it to incubate for 10 min. After the system equilibrated, the large droplet was gently removed and the slide was inserted in the AFM fluid cell for the measurements.

Neutron reflectivity measurements. NR measurements were conducted at the REFSANS Horizontal TOF reflectometer of the Helmholtz-Zentrum Geesthacht located at the Heinz Maier-Leibnitz Zentrum in Garching, Germany (Kampmann *et al.*, 2006; Moulin & Haese, 2015). Neutrons in the wavelength range 3.0–21.0 Å were used to carry out the measurements. Two incident angles, namely 0.60° and 3.00°, allowed collecting data in the range $0.007 \leq Q/Å^{-1} \leq 0.22$. The arrival times and positions of scattered neutrons were detected on a Denex 2D 500 × 700 mm^2 multiwire ^{3}He detector (pixel size 2.1 × 2.9 mm^2, efficiency 80% at 7 Å, gamma sensitivity $< 10^{-6}$) positioned at 4.5 m from the sample. The detector was installed in a liftable vacuum tube in order to reach exit angles up to 5.2° at the maximum elongation. In order to receive sufficient statistics, a counting time of about 4 h for the measurement was chosen. The software MOTOFIT (Nelson, 2006) was employed for the analysis of the NR curve. Details on data analysis are reported in the SI.

AFM measurements

AFM setup. All AFM experiments were performed at room temperature on a Bruker Multimode 8 (equipped with

Nanoscope V electronics, a sealed fluid cell and a type JV piezoelectric scanner) using Bruker SNL-A probes (triangular cantilever, nominal tip curvature radius 2–12 nm, nominal elastic constant 0.35 N m^{-1}) calibrated with the thermal noise method (Hutter & Bechhoefer, 1993). The AFM fluid cell was filled with a saline buffer solution, consisting of KCl 100 mM, which has the main effect of reducing the Debye length that characterises the electrical double layer (EDL) interaction region between AFM tip and SLB (Müller *et al.*, 1999). In this way, better image resolution can be achieved.

AFM imaging. Imaging was performed in PeakForce mode. In order to minimise deformations or rupture events induced by the scanning probe, the applied force setpoint was kept under 200 pN range. Feedback gain was set on values high enough to obtain optimal image quality but low enough to prevent the introduction of noise signals that would otherwise interfere with the resolution of the different lipid domains, having a height difference of ∼1 nm. The average height value of all bare substrate zones was taken as the baseline zero height reference. Image background subtraction was performed using Gwyddion 2.53.16 (Nečas & Klapetek, 2012). In order to map the edges of lipid rafts and AuNPs, height ranges were manually optimised to define two image masks, the first only containing all Lo domains, the second singling out all NPs. Once both types of objects were correctly selected by appropriately chosen masks, a Gwyddion built-in function was used to automatically detect edges, and the resulting images were exported. Finally, the exported images containing the edges of either Lo domains or NPs, originally present in the same AFM image, were superimposed to reveal all NPs–lipid domains edge overlaps. To estimate the degree of preferential adsorption of NPs along the rafts' edges, we calculated the ratio between the number of NPs adsorbed along the boundaries and the total amount of NPs present in the images.

Results and discussion

Formation of supported lipid bilayers containing lipid rafts

The formation of a continuous planar bilayer [DOPC/DSPC/cholesterol (39/39/22 mol%)], covering the vast majority of the supporting surface, was achieved through vesicle fusion and characterised by NR. Briefly, as described in the Materials and Methods section, liposomes in a saline buffer were mixed with a low amount of $CaCl_2$, injected within the measurement chamber and left adsorbing on the support (a clean Si crystal). The presence of Ca^{2+} ions in solution promotes the crowding of vesicles on the surface by reducing the repulsive interactions between liposomes with surface charge. As reported by Richter *et al.* (2006), when a critical vesicle coverage is reached, the stress on the vesicles becomes sufficient to induce their rupture; in our case the phenomenon was also favoured by the additional osmotic shock, coming from the replacement of the saline buffer with ultrapure water. The edges of the newly-formed SLB are energetically unfavourable and cause the rupture of other surface-bound vesicles. If the density of adsorbed vesicles is sufficiently high, these cascade phenomena can lead to the complete surface coverage.

Given its ability to probe large sample areas (tens of millimetres), neutron reflectivity (NR) was herein applied to probe the effective formation of a homogeneous SLB and its structure along the normal to the SLB plane. Figure 1(A) shows a representative NR profile measured for the SLB in D_2O (green circles), together with the fitting curve (red continuous line). The curve was analysed with MOTOFIT and, consistently with the literature (Montis *et al.*, 2016, 2020; Luchini *et al.*, 2019), it was possible to model the profile of the SLB as a stack of five layers (see scheme in Fig. 1B): the silicon oxide layer, a layer of solvent (D_2O), a layer for the polar headgroups in contact with the support (inner heads), a layer for the lipid chains (chains) and, finally, a layer for the polar headgroups in contact with the solvent (outer heads). Each layer is characterised by a defined contrast (the scattering length density, SLD), thickness (d), roughness (ρ) and hydration (solvent %). The curve fitting results are reported in Table 1. The overall thickness of the bilayer is ∼ 5 nm (given by the sum of the thickness values related to the inner and outer heads, plus the lipid chains). The negligible hydration (0.1%) of the lipid chains layer indicates that the surface was almost completely covered by a homogeneous lipid bilayer. The analysis of the experimental data allowed reconstructing the entire profile of the SLB along the normal to the surface (see Fig. 1B).

While NR provides information on the average structure with respect to the bilayer normal, AFM can be used to resolve in detail the in-plane rafts morphology (Milhiet *et al.*, 2001; Yuan *et al.*, 2002; Mingeot-Leclercq *et al.*, 2008; Cai *et al.*, 2012). The SLB was formed on functionalised borosilicate glass coverslips, by injecting the liposomes (this time suspended in ultrapure water) in the buffer solution where they experienced an osmotic imbalance across the membrane, decreasing their pressurisation (please refer to 'Materials and methods' section for the details). As a result, following the adhesion to the substrate, liposomes will deform adopting more oblate shapes (Ridolfi *et al.*, 2019), increasing the area occupied by each vesicle and favouring the previously described vesicle fusion mechanism. As shown in Figure 1(C), consistently with NR data the surface is almost completely covered by a lipid bilayer, which presents nanometric domains of different heights, with the brighter areas corresponding to thicker membrane regions and the darker ones to thinner SLB portions. Accordingly, the height distribution of Figure 1(D) confirms the presence of two distinct lipid phase-like domains, with height values of $h_d = 3.7$ nm and $h_o = 4.7$ nm, in good agreement with the results obtained by Heberle *et al.* (2013) on the same vesicle preparation. This thickness mismatch can be ascribed to the coexistence of two lipid phases of different composition, dictating variations in the membrane's height

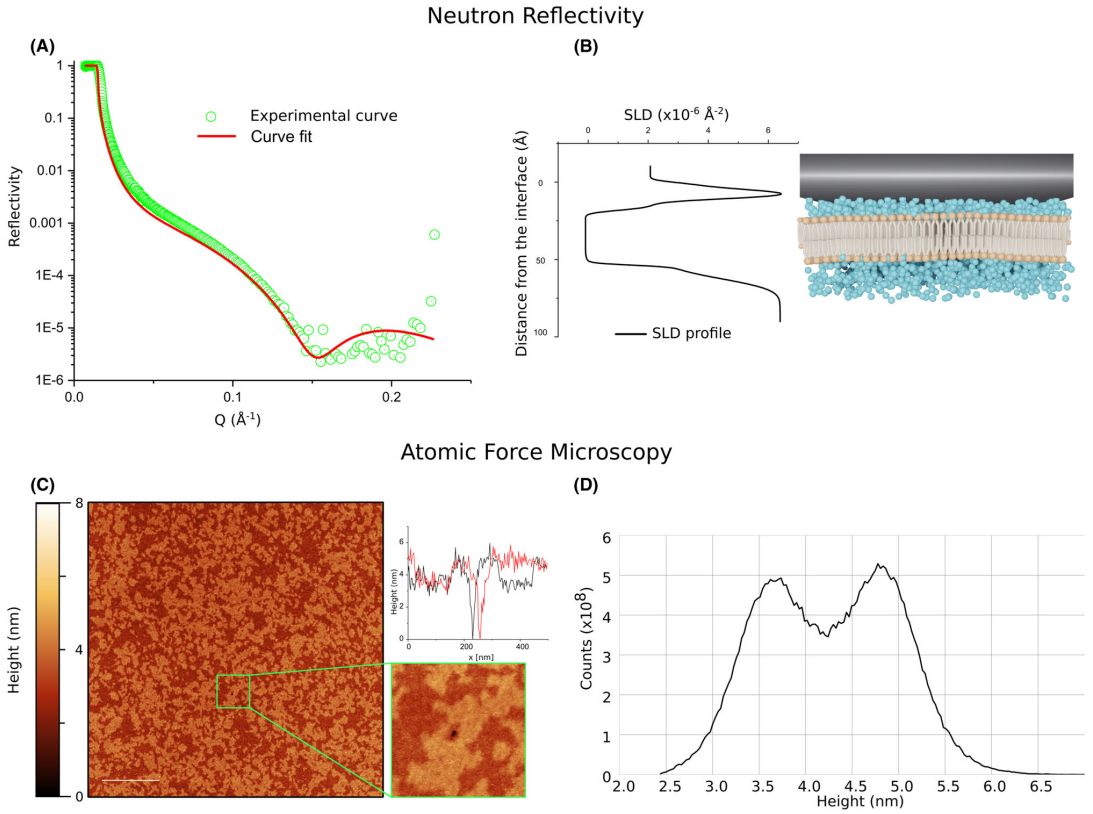

Fig. 1. Characterisation of the multicomponent SLB formed from DOPC/DSPC/cholesterol (39/39/22 mol%) liposomes by vesicle fusion. (A) Neutron Reflectivity profile (green circles) and best fit (continuous red line) corresponding to the SLB in D_2O; from the fitting analysis the average bilayer thickness is $\sim$ 5 nm. (B) Scattering length density (SLD) profile, describing variations of the SLD along the direction perpendicular to the bilayer. (C) Representative AFM topography of the SLB. The bilayer uniformly covers the surface, displaying both the L_o (brighter thicker regions) and L_d phases (darker thinner regions) as segregated domains. The reported scalebar is 1 μm. The 500 × 500 nm micrograph (bottom inset) displays the small hole in the bilayer that allowed flattening the image with respect to the SiO_2 surface. Two perpendicular height profiles were traced, horizontally and vertically, across the whole image (top inset); the profiles confirm the presence of the two distinct lipid phases covering the surface. (D) Height distribution obtained from the AFM image; the two distinct peaks, centred at $h_d = 3.7$ nm and $h_o = 4.7$ nm, describe the different heights that characterise the L_d and L_o phase, respectively.

(Lewis & Engelman, 1983; Petrache *et al.*, 2000; Bleecker *et al.*, 2016): in particular, membrane thickness was found to increase with length or degree of saturation of the lipid tails (Lewis & Engelman, 1983; Petrache *et al.*, 2000). Here the thicker domains can be associated with the L_o phase, which is enriched with cholesterol and DSPC, that is a fully saturated long chain lipid. On the contrary, thinner regions correspond to the L_d lipid phase mainly composed of DOPC, which is characterised by a shorter tail length and two chain unsaturated bonds. After having properly flattened the image, by the application of a mask (see Fig. S4), it is possible to determine the area fractions occupied by each of the two phases. Heberle *et al.* (2013) reported the area fraction corresponding to the L_d phase-like domains for liposomes of the very same composition to be 0.52 (at a temperature of 20°C); our calculations on SLBs at 28°C are in line with those findings, giving a L_d area fraction of 0.50. Results also suggest that the SLB formation did not significantly modify the amount of L_d and L_o lipids, originally present in the unfused vesicles and that the lipid phase behaviour is not affected by the presence of the solid support. The presented results strengthen the essential role of AFM in providing comprehensive morphological details on structure of rafted membranes. In the following paragraph, we extend the existing literature on AFM-based rafts characterisations (Milhiet *et al.*, 2001; Yuan *et al.*, 2002; Mingeot-Leclercq *et al.*, 2008; Cai *et al.*, 2012), by studying the structure of lipid rafts following their interaction with AuNPs.

Table 1. Curve fitting results of NR data obtained with MOTOFIT. The reported fitting parameters are referred to the three layers composing the bilayer [inner heads referred to the layer of polar headgroups in contact with the support, lipid chains referred to the hydrophobic region of the SLB, outer heads referred to the layer of polar headgroups in contact with the solvent (i.e. D_2O)]. For each layer four parameters are reported: d (Å), the thickness of the layer; ρ (Å), roughness of the layer; SLD (10^{-6} Å^{-2}), scattering length density of the layer (calculated from the layer composition); solvent % D_2O penetration in each layer.

Layer name	d (Å)	ρ (Å)	SLD (10^{-6} Å^{-2})	Solvent %
Inner heads	5 ± 2	2 ± 1	1.87	5 ± 1
Lipid chains	38 ± 3	1 ± 1	−0.18	0.1 ± 0.1
Outer heads	6 ± 2	2 ± 1	1.87	16 ± 4

Interaction of AuNPs with lipid rafts: localisation of AuNPs at the boundaries

In order to investigate the interaction of 16 nm citrated AuNPs (please refer to Materials and Methods for AuNP synthesis and to SI for AuNPs characterisation details) with the lipid rafts present in the SLB, 5 µL of the NPs dispersion were injected in the ultrapure water buffer. Different literature reports connect the presence of phase segregation within the lipid bilayer to the selective adsorption of NPs along the domains boundaries (Melby *et al.*, 2016; Sheavly *et al.*, 2019); however, a direct proof of this interaction is still missing to date. AFM represents one of the few techniques that could provide the sufficient resolution to simultaneously resolve the height difference between the two lipid domains ($\sim$ 1 nm) and the morphology of AuNPs. Despite the high resolution provided by AFM, the measurement remains challenging, as the spontaneous attachment of AuNPs to the probe (Fig. S5) can often lead to imaging artefacts. In order to overcome this problem, the AFM fluid cell was filled with the same saline buffer used for SLB formation and the force SetPoint was kept on very low values (lower than $\sim$ 200 pN). The use of the saline buffer as imaging solution should compensate the tip-sample electrical double-layer repulsion (Müller *et al.*, 1999) and limit the attachment of the NPs to the probe. In order to identify the portions of lipid bilayer characterised by the presence of AuNPs, images of 5×5 µm regions were initially acquired. Figure 2(A) shows a representative AFM topography of the SLB following the NPs injection. The bigger spherical objects represent vesicles that still have to fuse within the bilayer, while the smaller ones are the AuNPs, which seem to be homogeneously distributed above the SLB.

From a simple AFM topography, small lipid vesicles can be confused with AuNPs or AuNPs clusters; this could introduce statistical noise to the localisation and morphometrical analysis. We recently developed an AFM-based nanomechanical characterisation able to discriminate lipid vesicles from objects with the same morphology but different mechanical behaviour (Ridolfi *et al.*, 2019). This method evaluates the deformation that lipid vesicles undergo once adsorbed on a surface, by calculating their contact angle (α). Through the measurement of α and by assuming that the surface area of the vesicles is preserved upon adsorption, it is also possible to evaluate the diameter that characterises the unperturbed vesicles in solution (called Diameter in solution). As described in Figure 3, lipid vesicles are characterised by a narrow distribution of contact angles over a wide range of sizes (Diameter in solution), while AuNPs present a narrow size distribution and

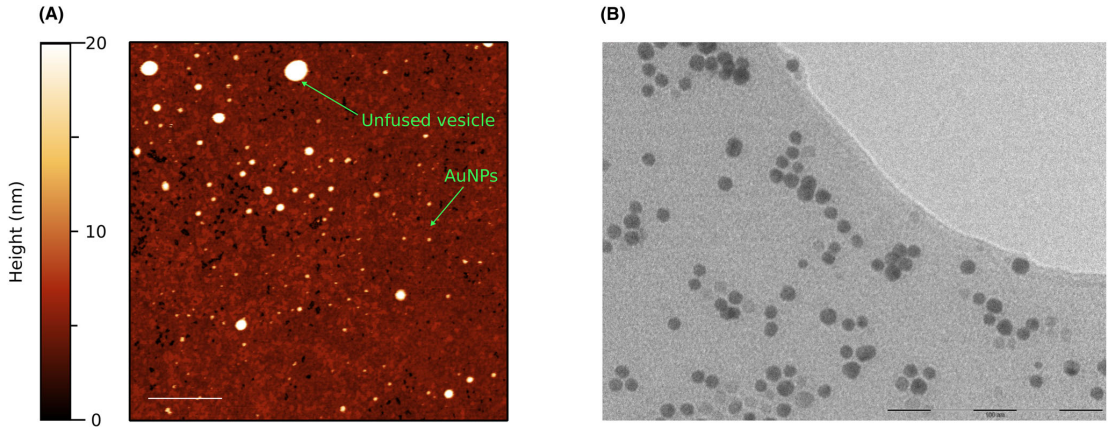

Fig. 2. (A) Representative AFM topography of the SLB following the interaction with AuNPs. Lipid rafts are still visible as differently shaded areas. The larger and heterogeneous spherical objects represent unfused vesicles while the smaller ones are the AuNPs that have been homogeneously adsorbed on the lipid bilayer. Scalebar is 1 µm. (B) Transmission electron microscopy (TEM) image of the AuNPs that were used in the experiments, scalebar is 100 nm (please refer to the SI for details regarding TEM characterisation).

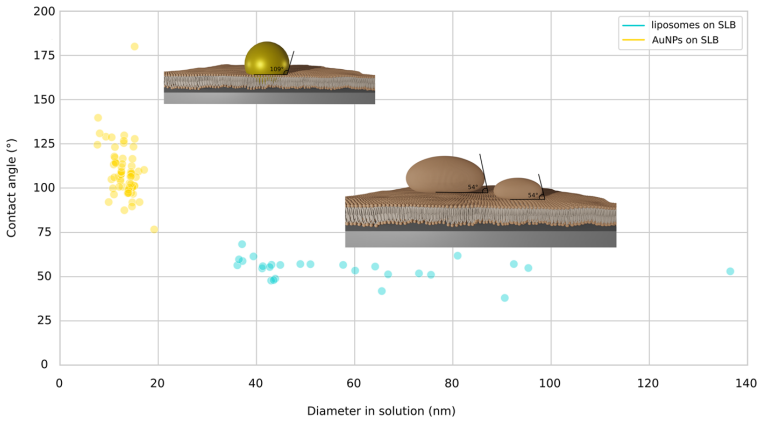

Fig. 3. Plot representing the distributions of contact angle vs solution diameter of either vesicles (blue circles) and AuNPs (yellow circles). Vesicles data have been obtained from the liposomes present in Figure 2(A) while the AuNPs data come from micrographs like the ones reported in Figure 4(A). Even though adsorbed on the SLB, liposomes show their nanomechanical fingerprint: a narrow contact angle distribution over a wide range of sizes. Their average contact angle is $\sim 54°$ hence describing highly deformed shapes, possibly due to the SLB formation procedure. AuNPs display narrow distributions for both their size and contact angle, with average values of 14 nm and 109°, respectively.

higher contact angle values. This enables the easy singling out of the AuNPs and their exclusive inclusion in the next analysis.

In order to precisely determine whether the NPs targeted specific locations on the lipid matrix, the size of the scanned region was further reduced. In Figure 4(A), representative images, with sizes of $\sim 600 \times 600$ nm, illustrating the SLB decorated by AuNPs have been reported. The micrographs of Figure 4(A) constitute the direct proof of the AuNPs selective adsorption along the segregated phase boundaries.

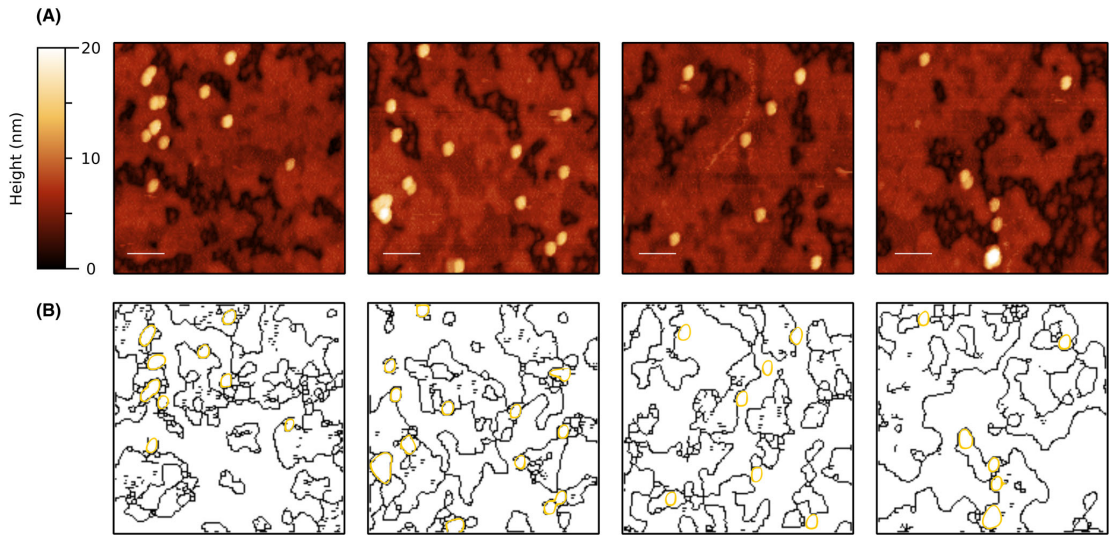

Fig. 4. (A) Representative AFM micrographs that clearly display the selective adsorption of AuNPs along the boundaries of the lipid rafts (brighter regions of the SLB that correspond to the Lo lipid phase). From the images it is also possible to distinguish between isolated and clustered NPs. All scalebars are 100 nm. (B) Contour images obtained from the micrographs. Black lines represent the rafts edges while gold circles define the contours of the AuNPs. The gold NPs edges are always in contact with at least one of the lines describing the lipid segregated phase boundaries.

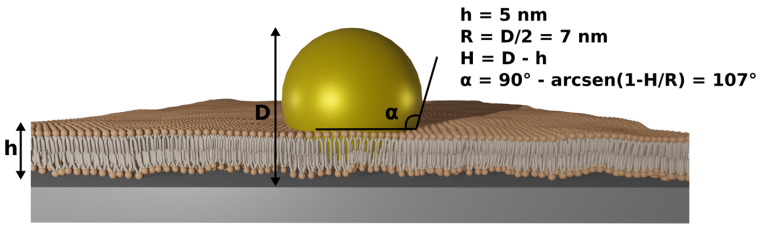

Fig. 5. Schematic representation of the configuration used to evaluate, from a conceptual point of view, the contact angle that would characterise an AuNP with a diameter of 14 nm, adsorbed on a rigid flat surface and surrounded by a ∼ 5 nm lipid bilayer.

In the free image processing software Gwyddion 2.53.16, the sequential application of different masks allowed mapping the edges of either the lipid rafts and NPs shown in Figure 4(A) and, hence, obtaining a clearer indication of their relative positions. In Figure 4(B) the contour images of NPs and rafts have been superimposed with different colours, to highlight that AuNPs preferentially targeted the boundaries of the two lipid phases; indeed, the lines describing their shapes are always in contact with the edges of the lipid rafts. To estimate the degree of preferential adsorption of NPs along the rafts' edges, we calculated the ratio between the number of NPs adsorbed along the boundaries and the total amount of NPs present on the SLB, finding that 91% of the NPs were located along the edges. These results prove the hypothesis that phase boundaries represent energetically favourable niches for lipid–NPs interactions. As previously discussed elsewhere (Sheavly *et al.*, 2019), NPs adsorption induces bilayer bending, which entails an energy penalty that increases the free energy associated with the overall process. This energy penalty is almost completely reduced along the phase boundaries, where the local negative curvature of the membrane, caused by the thickness mismatch between the two lipid phase-like domains minimises the free energy associated with the NPs adsorption (Sheavly *et al.*, 2019).

Inclusion of AuNPs within the lipid bilayer

AuNPs have a diameter of 16 nm (refer to SI for details), which is close to the average height measured with AFM imaging (14 ± 2 nm). This suggests that after adsorbing on the SLB, AuNPs probably penetrate the bilayer and reach the SiO_2 surface. This result further extends the characterisation of NPs–lipid interaction and corroborates our vision of rafts' boundaries as regions of increased permeability (Kuzmin *et al.*, 2005; Rawicz *et al.*, 2008; Sheikh & Jarvis, 2011), where the membrane can easily wrap around the adsorbed NPs. Recent findings (Montis *et al.*, 2020) confirm these results, suggesting that free-standing lipid bilayers can bend around the AuNPs surface, guided by citrate-lipid ligand exchange at the interface. All the above hypotheses are confirmed by the evaluation of the AuNPs contact angle with respect to the SLB. As suggested by Vinelli *et al.* (2008), the contact angle of a perfectly spherical, non-deformable (under the considered forces) object should be 180°, while we measured a substantially lower value. These apparent discrepancies can be rationalised by a careful morphological analysis, as detailed below.

The size of AuNPs is comparable with the tip radius; hence, the effect of tip convolution should be taken into account. This was performed by assuming the NPs as perfectly spherical and non-deformable objects with heights that coincide with their actual diameters. This is a reasonable assumption given that, during an AFM measurement, the error along the vertical direction is negligible compared to the ones in the scanning plane. As a consequence, all the measured radii were then corrected by ∼ 6 nm (corresponding to half the difference between the average NPs height and diameter measured by AFM). The NPs average contact angle, calculated with respect to the SLB and by using the corrected radii, gave a value of 109°, which is in very good agreement with the result that can be obtained from a simple geometrical model (Fig. 5), featuring a 14 nm spherical and undeformable NP immersed in a ∼5 nm lipid bilayer. For that case, α would be equal to 107°; this last result confirms that AuNPs penetrated the lipid bilayer and reached the underlying substrate.

Conclusion

The presence of lipid rafts within the cell membrane has been linked with multiple important biological functions, like the formation and targeting of lipid nanovesicles. The thickness mismatch that originates between the different immiscible segregated domains is thought to generate mechanical stresses that enhance the membrane permeability along these regions. We herein exploited atomic force microscopy to investigate the preferential adsorption of AuNPs along the phase boundaries of SLBs, generated from DOPC/DSPC/cholesterol (39/39/22 mol%) liposomes. Different works in the literature suggested a selective adsorption of AuNPs along the boundaries of lipid segregated domains, but a direct observation of this phenomenon is still missing to date. AFM allowed us to probe the existence of nanometric lipid rafts on the newly

formed SLB and to spot the presence of NPs along their edges, hence providing a direct proof of this preferential adsorption pathway. In addition, we provided useful details about the experimental procedures that could significantly improve the reliability of AFM imaging; indeed, one of the major challenges hindering this type of measurements is the frequent tip contamination, caused by the attachment of the NPs to the AFM probe. We showed that the use of a saline buffer as imaging solution within the AFM fluid cell leads to optimal image quality and strongly reduces tip contamination events. Then, through the application of an AFM-based morphometric nanomechanical characterisation, it was also possible to further investigate the reorganisation of the lipid bilayer, as a consequence of the AuNPs adsorption. We found out that the lipid matrix wrapped around the NPs, allowing them to penetrate within the hydrophobic region until reaching the rigid SiO_2 surface of the slides. The theoretical calculation of the morphological parameters describing this phenomenon is in perfect agreement with the experimental results and further corroborates our interpretation. Further studies will focus on extending this characterisation to membranes with varying compositions and employing NPs of different core and/or size.

Author contributions

The manuscript was written through contributions of all authors. All authors have given approval to the final version of the manuscript. The authors declare no competing financial interests.

Acknowledgements

This work was also supported by the Consorzio Sistemi a Grande Interfase (CSGI) through the evFOUNDRY project, Horizon 2020-Future and emerging technologies (H2020-FETOPEN), ID: 801367. We thank the SPM@ISMN research facility for support in the AFM experiments. Maier-Leibnitz Zentrum is acknowledged for provision of beam-time.

References

Beddoes, C.M., Case, C.P. & Briscoe, W.H. (2015) Understanding nanoparticle cellular entry: a physicochemical perspective. *Adv. Colloid Interface Sci.* **218**, 48–68.

Bleecker, J.V., Cox, P.A., Foster, R.N., Litz, J.P., Blosser, M.C., Castner, D.G. & Keller, S.L. (2016) Thickness mismatch of coexisting liquid phases in noncanonical lipid bilayers. *J. Phys. Chem. B* **120**, 2761–2770.

Busatto, S., Zendrini, A., Radeghieri, A., Paolini, L., Romano, M., Presta, M. & Bergese, P. (2020) The nanostructured secretome. *Biomater. Sci.* **8**, 39–63.

Cai, M., Zhao, W., Shang, X., Jiang, J., Ji, H., Tang, Z. & Wang, H. (2012) Direct evidence of lipid rafts by in situ atomic force microscopy. *Small* **8**, 1243–1250.

Frens, G. (1973) Controlled nucleation for the regulation of the particle size in monodisperse gold suspensions. *Nat. Phys. Sci.* **241**, 20–22.

Gkeka, P., Sarkisov, L. & Angelikopoulos, P. (2013) Homogeneous hydrophobic-hydrophilic surface patterns enhance permeation of nanoparticles through lipid membranes. *J. Phys. Chem. Lett.* **4**, 1907–1912.

Hamada, T., Morita, M., Miyakawa, M., Sugimoto, R., Hatanaka, A., Vestergaard, M.C. & Takagi, M. (2012) Size-dependent partitioning of nano/microparticles mediated by membrane lateral heterogeneity. *J. Am. Chem. Soc.* **134**, 13990–13996.

Hardy, G.J., Nayak, R. & Zauscher, S. (2013) Model cell membranes: techniques to form complex biomimetic supported lipid bilayers via vesicle fusion. *Curr. Opin. Colloid Interface Sci.* **18**, 448–458.

Heberle, F.A., Petruzielo, R.S., Pan, J., Drazba, P., Kučerka, N., Standaert, R.F., Feigenson, G.W. & Katsaras, J. (2013) Bilayer thickness mismatch controls domain size in model membranes. *J. Am. Chem. Soc.* **135**, 6853–6859.

Henriksen-Lacey, M., Carregal-Romero, S. & Liz-Marzán, L.M. (2017) Current challenges toward in vitro cellular validation of inorganic nanoparticles. *Bioconjug. Chem.* **28**, 212–221.

Hutter, J.L. & Bechhoefer, J. (1993) Calibration of atomic-force microscope tips. *Rev. Sci. Instrum.* **64**, 1868–1873.

Kampmann, R., Haese-Seiller, M., Kudryashov, V. *et al.* (2006) Horizontal ToF-neutron reflectometer REFSANS at FRM-II Munich/Germany: first tests and status. *Phys. B Condens. Matter.* **385–386**, 1161–1163.

Koynova, R. & Tenchov, B. (2013) Transitions between lamellar and nonlamellar phases in membrane lipids and their physiological roles. *OA Biochem.* **1**, 9.

Kuzmin, P.I., Akimov, S.A., Chizmadzhev, Y.A., Zimmerberg, J. & Cohen, F.S. (2005) Line tension and interaction energies of membrane rafts calculated from lipid splay and tilt. *Biophys. J.* **88**, 1120–1133.

Lewis, B.A. & Engelman, D.M. (1983) Lipid bilayer thickness varies linearly with acyl chain length in fluid phosphatidylcholine vesicles. *J. Mol. Biol.* **166**, 211–217.

Lingwood, D. & Simons, K. (2010) Lipid rafts as a membrane-organizing principle. *Science (80)* **327**, 46–50.

Luchini, A., Nzulumike, A.N.O., Lind, T.K., Nylander, T., Barker, R., Arleth, L., Mortensen, K. & Cárdenas, M. (2019) Towards biomimics of cell membranes: structural effect of phosphatidylinositol triphosphate (PIP 3) on a lipid bilayer. *Colloids Surf. B Biointerf.* **173**, 202–209.

Melby, E.S., Mensch, A.C., Lohse, S.E., Hu, D., Orr, G., Murphy, C.J., Hamers, R.J. & Pedersen, J.A. (2016) Formation of supported lipid bilayers containing phase-segregated domains and their interaction with gold nanoparticles. *Environ. Sci. Nano.* **3**, 45–55.

Mendozza, M., Caselli, L., Salvatore, A., Montis, C. & Berti, D. (2019) Nanoparticles and organized lipid assemblies: from interaction to design of hybrid soft devices. *Soft Matter.* **15**, 8951–8970.

Milhiet, P.E., Vié, V., Giocondi, M.C. & Le Grimellec, C. (2001) AFM characterization of model rafts in supported bilayers. *Single Mol.* **2**, 109–112.

Mingeot-Leclercq, M.P., Deleu, M., Brasseur, R. & Dufrêne, Y.F. (2008) Atomic force microscopy of supported lipid bilayers. *Nat. Prot.* **3**, 1654–1659.

Montis, C., Caselli, L., Valle, F. *et al.* (2020) Shedding light on membrane-templated clustering of gold nanoparticles. *J. Colloid Interf. Sci.* **573**, 204–214.

Montis, C., Gerelli, Y., Fragneto, G., Nylander, T., Baglioni, P. & Berti, D. (2016) Nucleolipid bilayers: a quartz crystal microbalance and neutron reflectometry study. *Colloids Surf. B Biointerf.* **137**, 203–213.

Montis, C., Salvatore, A., Valle, F., Paolini, L., Carlà, F., Bergese, P. & Berti, D. (2020) Biogenic supported lipid bilayers as a tool to investigate nano-bio interfaces. *J. Colloid Interf. Sci.* **570**, 340–349.

Moulin, J.-F. & Haese, M. (2015) REFSANS: reflectometer and evanescent wave small angle neutron spectrometer. *J. Large-Scale Res. Facil.* **1**, A9.

Müller, D.J., Fotiadis, D., Scheuring, S., Müller, S.A. & Engel, A. (1999) Electrostatically balanced subnanometer imaging of biological specimens by atomic force microscope. *Biophys. J.* **76**, 1101–1111.

Munro, S. (2003) Lipid rafts: elusive or illusive? *Cell* **115**, 377–388.

Nečas, D. & Klapetek, P. (2012) Gwyddion: an open-source software for SPM data analysis. *Cent. Eur. J. Phys.* **10**, 181–188.

Nel, A.E., Mädler, L., Velegol, D. *et al.* (2009) Understanding biophysicochemical interactions at the nano-bio interface. *Nat. Mater.* **8**, 543–557.

Nelson, A. (2006) Co-refinement of multiple-contrast neutron/X-ray reflectivity data using MOTOFIT. *J. Appl. Crystallogr.* **39**, 273–276.

Nikoleli, G.P., Nikolelis, D.P., Siontorou, C.G., Nikolelis, M.T. & Karapetis, S. (2018) The application of lipid membranes in biosensing. *Membranes (Basel)* **8**, 108.

Petrache, H.I., Dodd, S.W. & Brown, M.F. (2000) Area per lipid and acyl length distributions in fluid phosphatidylcholines determined by 2H NMR spectroscopy. *Biophys. J.* **79**, 3172–3192.

Rawicz, W., Smith, B.A., McIntosh, T.J., Simon, S.A. & Evans, E. (2008) Elasticity, strength, and water permeability of bilayers that contain raft microdomain-forming lipids. *Biophys. J.* **94**, 4725–4736.

Richter, R.P., Bérat, R. & Brisson, A.R. (2006) formation of solid-supported lipid bilayers: an integrated view. *Langmuir* **22**, 3497–3505.

Ridolfi, A., Brucale, M., Montis, C. *et al.* (2019) AFM-based high-throughput nanomechanical screening of single extracellular vesicles. *BioRxiv* 854539.

Sezgin, E., Levental, I., Mayor, S. & Eggeling, C. (2017) The mystery of membrane organization: composition, regulation and roles of lipid rafts. *Nat. Rev. Mol. Cell Biol.* **18**, 361–374.

Sheavly, J.K., Pedersen, J.A. & Van Lehn, R.C. (2019) Curvature-driven adsorption of cationic nanoparticles to phase boundaries in multicomponent lipid bilayers. *Nanoscale* **11**, 2767–2778.

Sheikh, K.H. & Jarvis, S.P. (2011) Crystalline hydration structure at the membrane-fluid interface of model lipid rafts indicates a highly reactive boundary region. *J. Am. Chem. Soc.* **133**, 18296–18303.

Simonelli, F., Bochicchio, D., Ferrando, R. & Rossi, G. (2015) Monolayer-protected anionic au nanoparticles walk into lipid membranes step by step. *J. Phys. Chem. Lett.* **6**, 3175–3179.

Simons, K. & Ikonen, E. (1997) Functional rafts in cell membranes. *Nature* **387**, 569–572.

Su, J., Esmaeilzadeh, H., Zhang, F., Yu, Q., Cernigliaro, G., Xu, J. & Sun, H. (2018) An ultrasensitive micropillar-based quartz crystal microbalance device for real-time measurement of protein immobilization and protein-protein interaction. *Biosens. Bioelectron.* **99**, 325–331.

Toppozini, L., Meinhardt, S., Armstrong, C.L., Yamani, Z., Kučerka, N., Schmid, F. & Rheinstädter, M.C. (2014) Structure of cholesterol in lipid rafts. *Phys. Rev. Lett.* **113**(22), 228101.

Turkevich, J., Stevenson, P.C. & Hillier, J. (1951) A study of the nucleation and growth processes in the synthesis of colloidal gold. *Discuss. Faraday Soc.* **11**, 55–75.

Vinelli, A., Primiceri, E., Brucale, M., Zuccheri, G., Rinaldi, R. & Samorì, B. (2008) Sample preparation for the quick sizing of metal nanoparticles by atomic force microscopy. *Microsc. Res. Tech.* **71**, 870–879.

Worsfold, O., Voelcker, N.H. & Nishiya, T. (2006) Biosensing using lipid bilayers suspended on porous silicon. *Langmuir* **22**, 7078–7083.

Yuan, C., Furlong, J., Burgos, P. & Johnston, L.J. (2002) The size of lipid rafts: an atomic force microscopy study of ganglioside GM1 domains in sphingomyelin/DOPC/cholesterol membranes. *Biophys. J.* **82**, 2526–2535.

Zendrini, A., Paolini, L., Busatto, S. *et al.* (2020) Augmented COlorimetric NANoplasmonic (CONAN) method for grading purity and determine concentration of EV microliter volume solutions. *Front. Bioeng. Biotechnol.* **7**, 452.

Supporting Information

Additional supporting information may be found online in the Supporting Information section at the end of the article.

Fig. S1. Experimental SAXS profile (markers) obtained for citrated AuNPs and curve fit (solid black line) according to the Schulz spheres model from the NIST package SANS Utilities.
Fig. S2. UV-Vis absorption spectra of citrated AuNP dispersion (after 1:5 dilution in water).
Fig. S3. AFM topography representing AuNPs either isolated or clustered, adsorbed on a bare mica substrate.
Fig. S4. AFM topography of the SLB obtained from DOPC/DSPC/Chol (39/39/22 %w/w) liposomes.
Fig. S5. AFM topography showing the effects of tip contamination on the imaging of AuNPs adsorbed on the lipid bilayer.
Table. S1. Chemical formula, molecular volumes and corresponding scattering length densities of species relevant to this study

Gold Nanoparticles interacting with Synthetic Lipid Rafts: an AFM investigation

Authors

Andrea Ridolfi* [†,1,2,3], Lucrezia Caselli [†,3], Costanza Montis[1,3], Gaetano Mangiapia[4], Debora Berti[1,3], Marco Brucale[1,2] and Francesco Valle[1,2].

Affiliations

[1] Consorzio Interuniversitario per lo Sviluppo dei Sistemi a Grande Interfase (CSGI), via della Lastruccia 3, 50019 Florence (Italy).

[2] Consiglio Nazionale delle Ricerche, Istituto per lo Studio dei Materiali Nanostrutturati (CNR-ISMN), via Gobetti 101, 40129 Bologna (Italy).

[3] Dipartimento di Chimica "Ugo Schiff", Università degli Studi di Firenze, via della Lastruccia 3, 50019 Florence (Italy).

[4] GEMS am Heinz Maier-Leibnitz Zentrum (MLZ). Helmholtz-Zentrum Geesthacht GmbH, Lichtenbergstr. 1, D-85747 Garching, Germany.

[†] A.R. and L.C. contributed equally to this work.

*Corresponding author. Email: andrea.ridolfi@ismn.cnr.it

SUPPLEMENTARY INFORMATION

AuNPs characterization

1. TRANSMISSION ELECTRON MICROSCOPY

Trasmission electron microscopy (TEM) images were acquired with a STEM CM12 Philips electron microscope equipped with an OLYMPUS Megaview G2 camera, at CeME (CNR Florence Research Area, Via Madonna del Piano, 10 - 50019 Sesto Fiorentino). Drops of citrated AuNP, diluted ten times, were placed on 200 mesh carbon-coated copper grids with a diameter of 3 mm and a thickness of 50 μm (Agar Scientific) and dried at room temperature. Then, samples were analyzed at an accelerating voltage of 100 keV.

2. SMALL ANGLE X-RAY SCATTERING (SAXS)

SAXS measurements were carried out on a S3-MICRO SAXS/WAXS instrument (HECUS GmbH, Graz, Austria) which consists of a GeniX microfocus X-ray sealed Cu Kα source (Xenocs, Grenoble, France) of 50 W power which provides a detector focused X-ray beam with λ = 0.1542 nm Cu Kα line. The instrument is equipped with two one-dimensional (1D) position sensitive detectors (HECUS 1D-PSD-50 M system), each detector is 50 mm long (spatial resolution 54 μm/channel, 1024 channels) and cover the SAXS q-range ($0.003 < q < 0.6\ ^{\circ}\text{Å}^{-1}$). The temperature was controlled by means of a Peltier TCCS-3 Hecus. The analysis of SAXS curves was carried out using Igor Pro[1]. SAXS measurements on AuNP aqueous dispersions, was carried out in sealed glass capillaries of 1.5 mm diameter. To analyze AuNPs profiles, we chose a model function with a spherical form factor and a Schulz size distribution[2], which calculates the scattering for a polydisperse population of spheres

with uniform scattering length density. The distribution of radii (Schulz distribution) is given by the following equation:

$$(R) = (z+1)^{z+1} x^z \frac{exp[-(z+1)x]}{R_{avg}\Gamma(z+1)}$$

where R_{avg} is the mean radius, x = R/R_{avg} and z is related to the polydispersity of the dispersion. The form factor is normalized by the average particle volume, using the 3rd moment of R:

$$\langle V \rangle = \frac{4\pi}{3}\langle R^{+3} \rangle = \frac{4\pi}{3}\langle R \rangle^3 \frac{(z+3)(z+2)}{(z+1)^2}$$

The scattering intensity is:

$$I(q) = \left(\frac{4\pi}{3}\right)^2 N_0 \Delta\rho^2 \int_0^\infty f(R) R^6 F^2(qR) dR$$

where N_0 is the total number of particles per unit volume, F(R) is the scattering amplitude for a sphere and $\Delta\rho$ is the difference in the scattering length density between the AuNP and the solvent.

The structural parameters of citrated gold nanoparticles were evaluated from the SAXS profile of Figure S1 according to the above model.

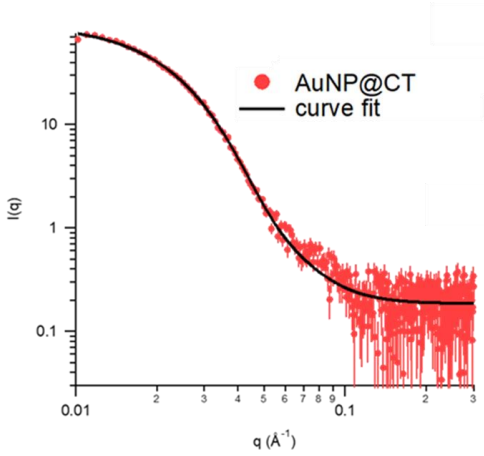

Figure S1 Experimental SAXS profile (markers) obtained for citrated AuNPs and curve fit (solid black line) according to the Schulz spheres model from the NIST package SANS Utilities. The size and polydispersity obtained from the fitting procedure are 13 nm and 0.3, respectively.

3. UV-VIS SPECTROSCOPY

UV-Vis spectra were measured with a JASCO UV-Vis spectrophotometer.

The size of citrate gold nanoparticles was further evaluated from UV-Vis Spectroscopy by the following equation[3]:

$$d = \exp\left(B_1 \frac{A_{spr}}{A_{450}} - B_2\right)$$

with d diameter of gold nanoparticles, A_{spr} absorbance at the surface plasmon resonance peak, A_{450} absorbance at the wavelength of 450 nm and B_1 and B_2 dimensionless parameters, taken as 3 and 2.2, respectively. The obtained diameter value is 16 nm.

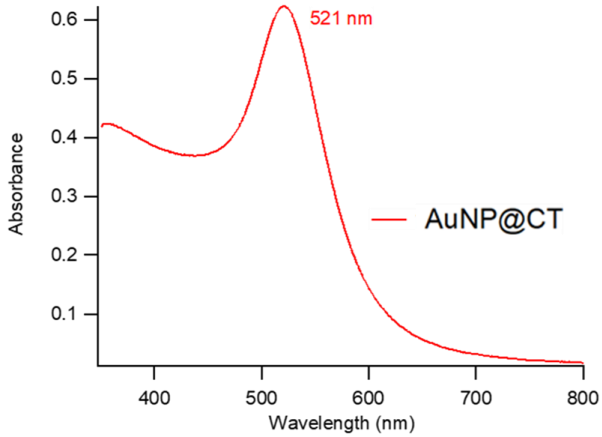

Figure S2 UV-Vis absorption spectra of citrated AuNP dispersion (after 1:5 dilution in water). The plasmon absorption peak is located at 521 nm.

The concentration of citrated gold nanoparticles was determined via UV-Vis spectrometry, using the Lambert-Beer law (E(λ) = ε(λ)lc) and considering the extinction values ε (λ) at the

LSPR maximum, i.e. λ = 521 nm. The extinction coefficient ε(λ) was determined by the following equation[4]:

$$ln\,(\varepsilon) = k ln(d) + a$$

with d core diameter of nanoparticles, and k and a dimensionless parameter (k = 3.32111 and a = 10.80505). The arithmetic mean of the size, obtained by both the optical and the scattering analyses, leads to an ε(λ) value of $4.8 \cdot 10^{8}$ $M^{-1}cm^{-1}$. Consequently, the final concentration of citrated AuNP is ~$7.8 \cdot 10^{-9}$ M.

4. ATOMIC FORCE MICROSCOPY

Preliminary AFM images of AuNPs adsorbed on bare mica substrates were performed in order to test the effect of using a saline buffer as imaging solution, to prevent the attachment of NPs to the AFM tip (please refer to the Materials and Methods section for details regarding the imaging setup and parameters).

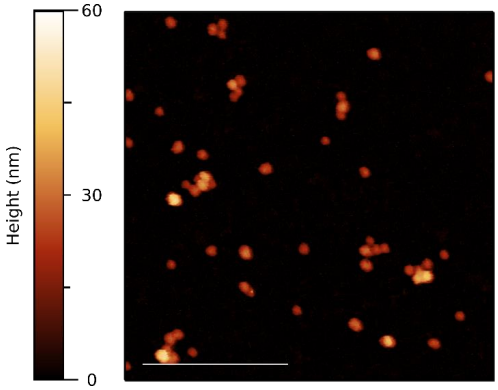

Figure S3 AFM topography representing AuNPs either isolated or clustered, adsorbed on a bare mica substrate. As reported in the Materials and Methods section, AFM imaging was performed using a saline buffer as imaging solution, in order to obtain better image quality and avoid tip contamination due to the attachment of the NPs to the probe. As can be seen from the image, isolated AuNPs get faithfully described by nearly perfect spherical shapes with an average contact angle close to 180°. Scalebar is 400 nm.

Neutron Reflectivity measurements

The software MOTOFIT was employed for the analysis of the NR curves. A five-layer model was employed to analyze the reflectivity profiles of neat SLBs, with scattering length density values calculated for each layer: a bulk subphase of Si (SLD = 2.07 * 10^{-6} $Å^{-2}$), a superficial layer of SiO_2 (SLD = 3.47 * 10^{-6} $Å^{-2}$); a second layer of D_2O (SLD = 6.393 * 10^{-6} $Å^{-2}$); a third layer composed of the polar headgroups of the SLB of the inner leaflet (SLD = 1.87 * 10^{-6} $Å^{-2}$); a fourth layer composed of the bilayer's lipid chains (SLD = -0.18 * 10^{-6} $Å^{-2}$); a fifth layer composed of the polar headgroups of the outer bilayer's leaflet (SLD = 1.87 * 10^{-6} $Å^{-2}$); a bulk superphase of solvent (D_2O, SLD = 6.393 * 10^{-6} $Å^{-2}$). The scattering length density values for the polar headgroups and lipid chains were estimated by taking into account the chemical compositions and the submolecular fragment volumes of phosphatidylcholines as determined by Armen et al. through molecular dynamic simulations[5] (see table S1).

Table S1. Chemical formula, molecular volumes and corresponding scattering length densities of species relevant to this study

Molecule	Chem. Formula	Volume ($Å^3$)	SLD(10^{-6} $Å^{-2}$)
PC headgroups	$C_{10}H_{18}NO_8P$	321.9	1.866
DSPC chains	$C_{34}H_{70}$	1004.6	-0.357
DOPC chains	$C_{34}H_{66}$	982.2	-0.212
cholesterol	$C_{27}H_{46}O$	630	0.210

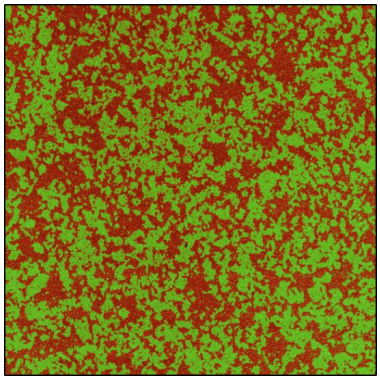

Figure S4 AFM topography of the SLB obtained from DOPC/DSPC/Chol (39/39/22 %w/w) liposomes. Using Gwyddion 2.53.16 it was possible to apply a mask to selectively cover the L_o phase (characterized by higher height values) and estimate the area fraction of each phase. The area fractions of the L_o and L_d phases are approximately 0.50, confirming the results obtained by Heberle et al.[6] on the very same vesicles preparation.

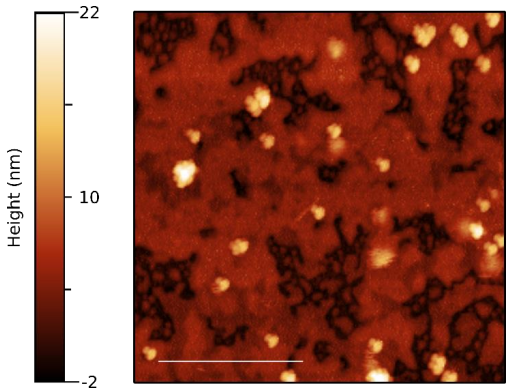

Figure S5 AFM topography showing the effects of tip contamination on the imaging of AuNPs adsorbed on the lipid bilayer. While the SLB gets correctly imaged, all the NPs appear in “clusters” characterized by similar shapes (same protrusions in all the directions). This is a clear indicator that the AFM probe has been contaminated by the attachment of one or multiple NPs which lead to the generation of imaging artifacts. Scalebar is 400 nm.

AUTHOR INFORMATION

Corresponding Author

* E-mail: andrea.ridolfi@ismn.cnr.it

Author Contributions

The manuscript was written through contributions of all authors. All authors have given approval to the final version of the manuscript.

Notes The authors declare no competing financial interests.

ACKNOWLEDGMENTS

This work was also supported by the Consorzio Sistemi a Grande Interfase (CSGI) through the evFOUNDRY project, Horizon 2020-Future and emerging technologies (H2020-FETOPEN), ID: 801367. We thank the SPM@ISMN research facility for support in the AFM experiments. Maier-Leibnitz Zentrum is acknowledged for provision of beam-time.

BIBLIOGRAPHY

1. Kline, S.R. (2006). Reduction and analysis of SANS and USANS data using IGOR Pro. J. Appl. Crystallogr. *39*, 895–900.

2. Kotlarchyk, M., and Chen, S.H. (1983). Analysis of small angle neutron scattering spectra from polydisperse interacting colloids. J. Chem. Phys. *79*, 2461–2469.

3. Haiss, W., Thanh, N.T.K., Aveyard, J., and Fernig, D.G. (2007). Determination of size and concentration of gold nanoparticles from UV-Vis spectra. Anal. Chem. *79*, 4215–4221.

4. Liu, X., Atwater, M., Wang, J., and Huo, Q. (2007). Extinction coefficient of gold nanoparticles with different sizes and different capping ligands. Colloids Surfaces B Biointerfaces *58*, 3–7.

5. Armen, R.S., Uitto, O.D., and Feller, S.E. (1998). Phospholipid component volumes:

Determination and application to bilayer structure calculations. Biophys. J. *75*, 734–744.

6. Heberle, F.A., Petruzielo, R.S., Pan, J., Drazba, P., Kučerka, N., Standaert, R.F., Feigenson, G.W., and Katsaras, J. (2013). Bilayer thickness mismatch controls domain size in model membranes. J. Am. Chem. Soc. *135*, 6853–6859.

Manuscript n°5

Colloids and Surfaces B: Biointerfaces 210 (2022) 112231

Contents lists available at ScienceDirect

Colloids and Surfaces B: Biointerfaces

journal homepage: www.elsevier.com/locate/colsurfb

Nanoscale structural and mechanical characterization of thin bicontinuous cubic phase lipid films

Andrea Ridolfi [a,b,c,*], Ben Humphreys [d,e,f], Lucrezia Caselli [a,c], Costanza Montis [a,c], Tommy Nylander [d,e,f], Debora Berti [a,c], Marco Brucale [a,b,*], Francesco Valle [a,b,*]

[a] Consorzio Interuniversitario per lo Sviluppo dei Sistemi a Grande Interfase, 50019 Firenze, Italy
[b] Consiglio Nazionale delle Ricerche, Istituto per lo Studio dei Materiali Nanostrutturati, 40129 Bologna, Italy
[c] Dipartimento di Chimica "Ugo Schiff", Università degli Studi di Firenze, 50019 Firenze, Italy
[d] Physical Chemistry, Department of Chemistry, Lund University, SE-221 00 Lund, Sweden
[e] Lund Institute of Advanced Neutron and X-ray Science - LINXS, SE- 223 70 Lund, Sweden
[f] NanoLund, Lund University, SE-221 00 Lund, Sweden

ARTICLE INFO

Keywords:
Cubic phase
Non-lamellar membranes
Atomic force microscopy
Mechanical properties

ABSTRACT

The mechanical response of lipid membranes to nanoscale deformations is of fundamental importance for understanding how these interfaces behave in multiple biological processes; in particular, the nanoscale mechanics of non-lamellar membranes represents a largely unexplored research field. Among these mesophases, inverse bicontinuous cubic phase Q_{II} membranes have been found to spontaneously occur in stressed or virally infected cells and to play a role in fundamental processes, such as cell fusion and food digestion. We herein report on the fabrication of thin (~150 nm) supported Q_{II} cubic phase lipid films ($SQ_{II}Fs$) and on their characterization via multiple techniques including Small Angle X-Ray Scattering (SAXS), Ellipsometry and Atomic Force Microscopy (AFM). Moreover, we present the first nanomechanical characterization of a cubic phase lipid membrane, through AFM-based Force Spectroscopy (AFM-FS). Our analysis reveals that the mechanical response of these architectures is strictly related to their topology and structure. The observed properties are strikingly similar to those of macroscopic 3D printed cubic structures when subjected to compression tests in material science; suggesting that this behaviour depends on the 3D organisation, rather than on the length-scale of the architecture. We also show for the first time that AFM-FS can be used for characterizing the structure of non-lamellar mesophases, obtaining lattice parameters in agreement with SAXS data. In contrast to classical rheological studies, which can only probe bulk cubic phase solutions, our AFM-FS analysis allows probing the response of cubic membranes to deformations occurring at length and force scales similar to those found in biological interactions.

1. Introduction

Lipid self-assembly encompasses a plethora of different mesophases, among which inverse bicontinuous cubic (Q_{II}) phases are some of the most intriguing [1–3]. These structures are characterized by a continuous lipid bilayer membrane that subdivides the three-dimensional space into two interwoven systems of water channels [4]. Curved membranes with structures similar to the lipid Q_{II} phases are believed to have an important role in Nature [5], which is not fully understood. These phases have been found to occur spontaneously in stressed or virally infected cells and are believed to be involved in numerous biological processes like cell fusion and food digestion [6]. Three types of lipid Q_{II} phase have been reported for lipid systems [3]: Q_{II}^{P}, Q_{II}^{D} and Q_{II}^{G}, respectively corresponding to the primitive (P), double diamond (D) and gyroid (G) infinite triply periodical minimal surfaces [7] (IPMS, see Fig. S1 for their representation). In these mesophases, lipid molecules self-assemble in a curved bilayer, where the middle plane is described by one of the three above-mentioned minimal surfaces.

Compared to planar membranes, the complex structure of cubic phases imparts them with considerably higher membrane surface-to-volume ratios as well as a defined geometry with connected aqueous cavities [8]. Thanks to the amphiphilic nature of their lipid components, these characteristics can be exploited for the encapsulation of hydrophobic, hydrophilic and bioactive molecules, proteins and nanoparticles

* Corresponding authors at: Consorzio Interuniversitario per lo Sviluppo dei Sistemi a Grande Interfase, 50019 Firenze, Italy

https://doi.org/10.1016/j.colsurfb.2021.112231
Received 21 July 2021; Received in revised form 3 November 2021; Accepted 15 November 2021
Available online 19 November 2021

[9,10]. A considerable amount of effort has therefore been put into the study of cubic phases as protein crystallization scaffolds [11–13] and, more recently, as nanoparticle-based drug delivery systems (i.e. cubosomes) [8,14–17]. On the other hand, the development of homogenous supported lipid Q_{II} phase films has received little attention despite their potential biomedical applications [18–21]. Analogously to how Supported Lipid Bilayers (SLBs) [22] are commonly used as surface-bound lamellar membrane models, Supported Q_{II} phase Films ($SQ_{II}Fs$) could be exploited as mimics of natural cubic membranes, allowing the study of their properties employing various surface techniques like Ellipsometry, Neutron/X-ray reflectivity and Atomic Force Microscopy (AFM). Results from such studies could help to shed light on biological interactions involving these intriguing and highly curved membranous interfaces. In this context, thin $SQ_{II}Fs$ approaching the typical length scales of naturally occurring cubic phase membranes [5] represent a versatile solution for advancing the current knowledge on the properties and functions of non-lamellar membranes.

To this purpose, we herein prepare thin (~150 nm) $SQ_{II}^{D}Fs$, starting from a glycerol-monooleate (GMO) solution. GMO is a natural food grade, biocompatible and biodegradable lipid, known to self-assemble into Q_{II} phases at standard temperature and pressures in excess water [23,24]. We then characterize the systems with multiple techniques including Small-Angle X-ray Scattering (SAXS), Ellipsometry and AFM. Exploiting the surface-supported nature of $SQ_{II}^{D}Fs$, we also probe the lipid architecture by means of AFM-based Force Spectroscopy (AFM-FS). This allowed us to perform the first mechanical characterization of a bicontinuous cubic membrane at the nanoscale, showing that the mechanical response of these structures to a localized deformation is strictly related to their topology and geometry. Interestingly, our analysis shows that the nanomechanical behaviour observed in $SQ_{II}Fs$ closely resembles the one of macroscopic IPMS-inspired structures studied in material science [25–28], which possess desirable combinations of high impact resistance and low density. In contrast to classical rheological studies which can only probe the mechanical properties of Q_{II} bulk phases [29–31], our AFM-FS analysis probes the response of these membranes to localized deformations, occurring at length and force scales approaching those found in biological and biomimetic interactions [32]. Moreover, the close relationship between the mechanical response and the topology of Q_{II}^{D} phase membranes allowed for the determination of their lattice parameter directly from the AFM force-distance curves, yielding results in good agreement with SAXS. According to our knowledge, this represents the first structural characterization of non-lamellar lipid membranes through AFM-FS and provides an alternative solution to scattering and electron microscopy-based techniques. Through characterizing the structure and the mechanics of cubic phase membranes at the nanoscale, by means of perturbations that resemble the ones found in biological systems, our results could help to better rationalize the role and function of these not fully understood, yet biologically relevant self-assemblies.

2. Experimental

2.1. Glycerol Monooleate solution

Glycerol monooleate (mono- and diglycerides ratio 44:1 by weight), denoted as RYLO™ MG19 Glycerol Monooleate (GMO), was produced and provided by Danisco Ingredients (now Dupont, Brabrand, Denmark) with the following fatty acid composition (Lot No. 2119/65–1): 89.3% oleic, 4.6% linoleic, 3.4% stearic and 2.7% palmitic acid. The product was then dissolved in chloroform reaching the desired concentrations for the different experiments.

2.2. Glycerol Monooleate bulk phases

In order to prepare the GMO bulk phase, the procedure employed by Mendozza et al. [33] was followed; briefly, 30 mg of GMO were solubilized in 1 ml of chloroform. The solvent was then removed with a gentle nitrogen flux, leaving a thin lipid film. The system was kept under vacuum overnight and sheltered from light. The dry film was fully hydrated with an excess of Milli-Q water and the sample was then centrifuged at least 5 times, changing the orientation of the vial (cap facing upward with another with cap facing downward) at each cycle. The lipid solution was then deposited on the thin Kapton film windows of the sandwich cells used for the SAXS measurements; the cells were subsequently filled with ultrapure water to ensure that the formed liquid crystalline is fully swollen in an excess of water.

2.3. Spin coating of Glycerol Monooleate films

GMO solutions were deposited on all substrates used in this study via spin coating. A single ≈ 10 μl drop was placed in the center of the substrate using a glass syringe. The substrate was then rotated at 2000 rpm for 35 s allowing the solvent to evaporate. Successful depositions resulted in iridescent films uniformly covering the whole substrate. After spin coating, lipid films were hydrated (i.e., put into the fluid cells that were used in the various experiments) in order to let the lipid film equilibrate and self-assemble into the desired cubic architecture. Regarding monoolein hydrolysis, a previous study [34] showed that the content of free oleic acid for the type of sample used in the present work was below 1 mol percent after equilibrating with 5wt% water at 40 °C for 8 weeks. It is therefore unlikely that under the present conditions, 25 °C and equilibration times of less than 1day, there would be significant hydrolysis of the GMO to free oleic acid even though the lipid liquid crystalline phases are in excess of water. Ellipsometry measurements could not be performed either on Kapton substrates or on Highly Ordered Pyrolytic Graphite; the first substrate is not detectable by the polarized light while the surface of the second one is too rough for obtaining a clear signal from the reflected beam. To solve the issue, we relied on polystyrene, which is known to have a surface energy similar to the Kapton substrates. In order to obtain a polystyrene layer that uniformly covers the entire Silicon surface, a 1% wt polystyrene solution in toluene was utilized. A 20 μl droplet was then added to the substrate while spinning it at 6000 rpm for 30 s. This procedure yielded a homogeneous polystyrene layer with thicknesses ranging from 15 to 20 nm. The thickness of the polystyrene layer was checked in every measurement by Ellipsometry, for our experiments the polystyrene layer average thickness was 16.1 ± 1.9 nm.

2.4. Small Angle X-ray Scattering

Small-Angle X-ray Scattering measurements were performed with a SAXS Lab Ganesha instrument (JJ-Xray, Denmark), equipped with a 30 W Cu X-ray micro-source (Xenocs, France) and a 2D 300 K Pilatus detector (Dectris, Switzerland). Measurements were performed with a pinhole collimated beam with the detector positioned asymmetrically at a distance of 480 mm from the sample, to yield azimuthally averaged intensities as a function of the scattering vector (q) over the range 0.016 – 0.75 $Å^{-1}$. The magnitude of the scattering vector is defined by $q = (4\pi\sin\theta)/\lambda$, where λ equals to 1.54 Å, Cu Kα wavelength, and θ is half of the scattering angle. Samples were loaded in sandwich cells with thin Kapton film windows and placed in a thermostat stage at 25 °C, controlled using a Julabo T Controller CF41 (Julabo Labortechnik GmbH, Germany). The d spacing was obtained from the positions of the Bragg peaks (q_{peak}) detected in the profiles of Fig. 2 by using the following equation:

$$d = 2\pi/q_{peak}$$

The lattice parameter of the cubic phase architecture, a, was calculated from the following equation:

$$a = d\left(h^2 + k^2 + l^2\right)^{1/2}$$

where h, k and *l* are the Miller indexes that describe the crystalline planes of the lattice.

2.5. Spectroscopic Ellipsometry

Ellipsometry measures the change in polarization of light upon reflection from a surface or interface. The parameters that are used to characterize this polarization change are the amplitude ratio, Ψ, and the phase shift, Δ. Light reflection is described by the Fresnel reflection coefficients for the component of the light polarized parallel (p-polarization), r_P, and perpendicular (s-polarization), r_S, to the plane of incidence. The ratio r_P/r_S is related to the measured Ψ and Δ by the following equation:

$$r_P/r_S = \tan(\Psi)e^{i\Delta}$$

When the film thickness increases to values on the same order of magnitude as the wavelength of the light, Δ and Ψ oscillate with the film thickness, making it challenging to be determined. To overcome this issue, spectroscopic ellipsometry offers the possibility to unambiguously determine the film thickness in the case of thicker films. Spectroscopic phase-modulated ellipsometer (SPME) (HORIBA Jobin Yvon, UVISEL) was therefore used for characterization of the interfacial films. The SPME configuration consisted of a light source, polarizer, sample, 50 kHz polarization modulator, and analyzer followed by a monochromator and detector or a multiwavelength detector. The light source was a xenon arc lamp with a spectral range from UV to near IR, i.e., a wavelength range of 190 – 2100 nm. In our experiments, the spectral range of 191 – 824 nm was selected, as this range was sufficient for the characterization of the film and gave a relatively fast acquisition time by using the multiwavelength mode (MWL). The angle of incidence was set to 70°. The beam diameter used in our experiments was 1.2 mm, yielding a spot size of 2.1 mm at the interface. The azimuth settings of modulator (M) and analyzer (A) were 0°and + 45°, respectively. The data acquisition in the MWL mode was performed every three minutes for several hours. Since prolonged exposure to UV light destabilized the film, wavelengths in the range of UV radiation were excluded from the beam by using an appropriate UV filter, when performing long (more than 10 h) acquisitions.

Data modelling was done using a four-layer model, i.e., silicon, SiO_2, polystyrene, and lipid film layer. The film layer was assumed to be composed of lipids and water, whose percentages (assumed to be constant along the height of the film) were left as free fitting parameters for obtaining the resulting film thickness. The DeltaPsi2 modeling package (HORIBA Jobin Yvon) was applied to determine the film thickness and the optical properties of the interfacial film. For the theoretical model, software default values of the optical constants for the silicon, the SiO_2 and the polystyrene layers were used. The optical constants for the lipid layer were previously determined by refractometry and Cauchy's equation was applied to account for the wavelength dependence of the refractive index [35]. To fit the data and hence obtain the values of film thickness, the Lorentz oscillator model (slightly modified for better describing the lipid film properties) was used in all the measurements; due to the use of polystyrene, the fitted wavelength range was then limited to 451 – 800 nm. To minimize the mean-squared error of the fitting, the Levenberg−Marquardt algorithm was employed.

2.6. Atomic Force Microscopy

A 10 mg/ml GMO solution in chloroform was spin coated on ZYB grade Highly Oriented Pyrolytic Graphite (Bruker, USA). The sample was then inserted into the AFM fluid cell (filled with ultrapure water) and left equilibrating for two hours before starting the experiments.

2.6.1. AFM setup

AFM experiments were performed at room temperature on a Bruker Multimode 8 (equipped with Nanoscope V electronics, a sealed fluid cell and a type JV piezoelectric scanner) using Bruker SNL-A probes (triangular cantilever, nominal tip curvature radius 2–12 nm, nominal elastic constant 0.35 Nm^{-1}) calibrated with the thermal noise method [36]. The AFM fluid cell was then filled with ultrapure water.

2.6.2. Imaging

Imaging was performed in PeakForce mode. When scanning larger areas, the applied force setpoint was kept in the 150–250 pN range and lateral probe velocity was not allowed to exceed 5 μm/s. This type of parameter optimization allowed for an accurate description of the film profile and estimation of its thickness. The average height value of all bare substrate zones was taken as the baseline zero height reference. Image background subtraction and thickness estimation were performed using Gwyddion 2.53 [37]. For revealing the presence of the cubic architecture, 100 × 100 nm^2 areas of the sample were scanned. In this case, parameters like force setpoint, gain and lateral probe velocity were optimized in order to achieve the best image quality and hence resolve the cubic lattice. Both image analysis and calculation of the autocorrelation function (ACF) were performed in Gwyddion 2.53 [37]. From the autocorrelation function image, it was then possible to obtain the profiles of the peaks and valleys defining the cubic architecture and hence to estimate the average lattice parameter of the whole structure (more details in the SI).

2.6.3. Force Spectroscopy

The mechanical response of the cubic phase lipid film was characterized by means of AFM-Force Spectroscopy. To this end, we recorded a series of force-distance curves at multiple XY positions (typically around 64–100 curves arranged in a square array) located on the surface of the lipid film. The acquired curves were then analyzed using a custom Python script automatically applying a Savitzky-Golay filter for noise smoothing, then discarding curves not presenting any indentation peak, finally locating each peak position within a curve. The procedure was iterated for all the recorded curves; a total of 211 curves were used for the analysis.

3. Results

In order to obtain $SQ_{II}^{D}Fs$ approaching the thicknesses of natural Q_{II} membranes, GMO was dissolved in chloroform at a concentration of 10 mg/ml and subsequently spin-coated on the different experimental substrates. As reported by Rittman et al. [19], this procedure yields an iridescent film that can be subsequently hydrated in order to allow the GMO molecules to self-assemble into the expected cubic architecture (Q_{II}^{D} phase for room temperature, atmospheric pressure and excess water); all these steps are graphically schematized in Fig. 1.

For SAXS, the GMO solution was directly spin-coated on the Kapton windows of the measuring cells; films were then hydrated and probed using X-rays (see Experimental section for more details). Fig. 2 shows the diffractogram of the GMO-based lipid film prepared from a 10 mg/ml GMO:chloroform solution, compared with the ones obtained from more concentrated GMO:chloroform solutions (100 and 1000 mg/ml). For comparison, the diffractogram of the fully hydrated bulk phase (see the Experimental section for sample preparation) is also included. Despite forming a conspicuous, homogeneous iridescent film, after being spin-coated on the substrate from a 10 mg/ml GMO:chloroform solution, no Bragg peaks are visible in the diffractogram.

This is most likely due to the relatively low intensity of the X-ray source in the lab SAXS setup employed for the measurements, which does not allow resolving the diffraction pattern from the limited number of cubic domains in the obtained thin lipid film. However, using more concentrated GMO:chloroform solutions (which yield thicker films by spin coating) resulted in progressively more defined Bragg peaks.

The position of the single peak from the sample prepared from 100 mg/ml GMO:chloroform solution is compatible with the

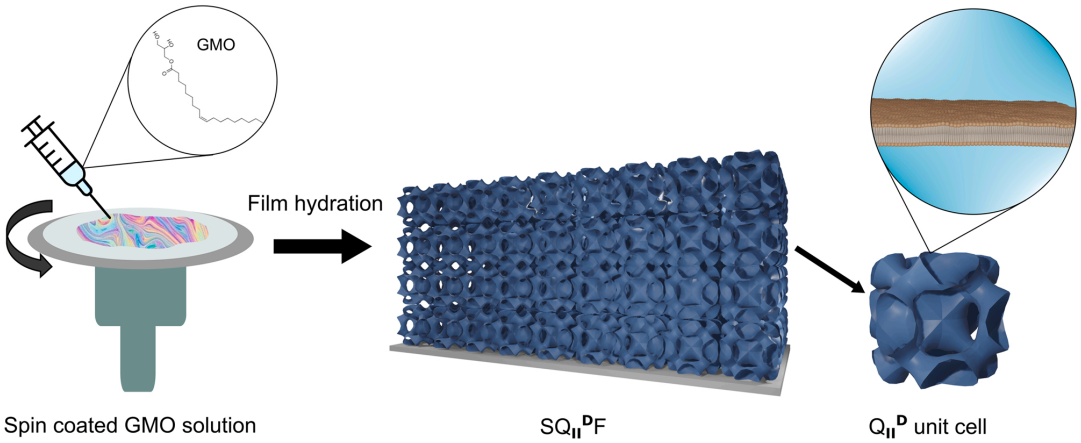

Fig. 1. : Fabrication of SQ$_{II}^{D}$Fs. The GMO/chloroform solution is deposited on top of a rigid substrate which is then put under rotation using a spin coater. This results in an iridescent film, visible to the naked eye, which can then be hydrated to allow GMO to self-assemble into the expected cubic architecture. At room temperature, atmospheric pressure and in excess of water, the resulting lipid film will be characterized by the repetition of multiple Q$_{II}^{D}$ (Pn-3 m space group symmetry) unit cells in the 3D space, hence generating the so called Q$_{II}^{D}$ phase. The surface of each unit cell presents a lipid bilayer that cover the whole IPMS.

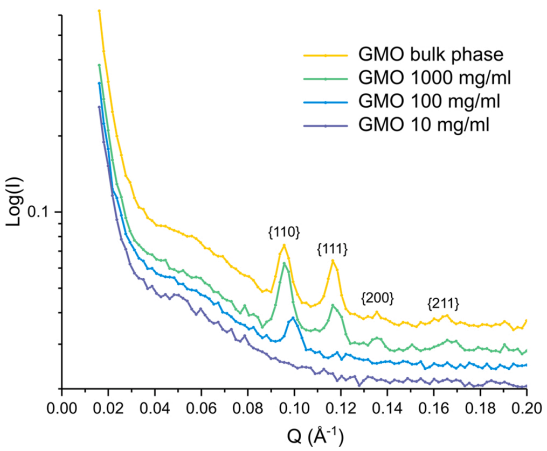

Fig. 2. : SAXS characterization of lipid Q$_{II}^{D}$ phase films at different GMO concentrations. While it is not possible to identify any Bragg peak in the more diluted sample (purple curve), they become more pronounced as the concentration of the sample is increased (until reaching the bulk phase). Peak positions are compatible with the formation of an ordered Q$_{II}^{D}$ phase, at all concentrations.

crystallographic plane identified by the {1 1 0} Miller indexes and corresponds to a lattice parameter of 90 Å while the lattice parameters determined for the film from a 1000 mg/ml GMO:chloroform solution and bulk phase are 92.6 ± 0.2 Å and 92.8 ± 0.3 Å, respectively (determined using the {1 1 0}, {1 1 1}, {2 0 0} and {2 1 1} Miller indexes, as described in Fig. 2). The analysis of the Bragg peaks position is consistent with the formation of an ordered Q$_{II}^{D}$ architecture that is mostly independent of the film thickness. All these results thus suggest that the same lipid arrangement should also be present in the sample obtained from the 10 mg/ml GMO:chloroform solution, despite it not being detectable by our lab SAXS setup. Due to this, the 10 mg/ml sample was further investigated to confirm the formation of SQ$_{II}^{D}$Fs.

Ellipsometry was used to confirm the formation of a thin SQ$_{II}^{D}$F from the 10 mg/ml GMO:chloroform solution; more precisely, to measure the thickness and the stability of the lipid film over time. Since Kapton cannot be probed by polarized visible light, the lipid solution was spin-coated on a silicon substrate coated with a thin polystyrene layer. As shown in Fig. 3, Ellipsometry reveals the formation of a continuous lipid film with a thickness of 110–150 nm. Results from Fig. 3 also reveal that the lipid film is destabilized by UV light, after an exposure of ~ 6 h, while the film remains stable for more than 15 h in visible light.

Polystyrene is partially miscible with the chloroform contained in the GMO solutions and this might have introduced some contamination of the lipid film. The effect of a 10 μl droplet of chloroform on the polystyrene substrate was checked by ellipsometry and revealed an average 10 nm decrease in the layer thickness; this effect was considered during the fitting procedure for estimating the thickness of the GMO films. Nevertheless, since GMO is not miscible with polystyrene, this contamination would only pertain to the lowest layer, not significantly

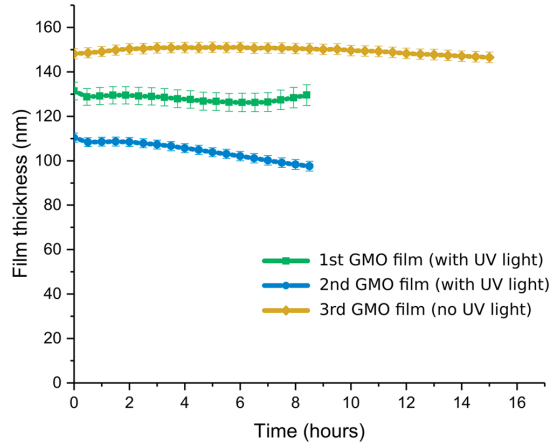

Fig. 3. : Results from the Ellipsometry analysis. Film thickness ranges from 110 to 150 nm. The 1st and 2nd acquisitions (green squares and blue circles) were performed using the entire wavelength spectrum (including UV light); as can be seen from the plot, after ~ 6 h, the film is destabilized by prolonged exposures to UV light. The measurement without UV light (gold diamonds) shows that the lipid film remains stable and preserves its original thickness even after 15 h.

influencing the lipid film. Unfortunately, these ellipsometry measurements are not possible on the Kapton substrates, but Kapton is known to have excellent resistance towards chloroform. Therefore, the effect of Kapton solubilization is negligible and is not expected to influence the SAXS patterns, which is related to the whole lipid layer. The local surface structure of these thin lipid films was then determined via AFM imaging in liquid. Image analysis reveals that the probed lipid film presented a cubic architecture, directly exposed to the water interface (Fig. 4a). According to Larsson [38], one of the two water channel networks must be capped at the surface of a bicontinuous cubic phase assembly, to ensure bilayer continuity. The pattern displayed in Fig. 4a and b therefore only represents the channel network open to the bulk water. This means that the observed features are separated by a distance equal to $a\sqrt{2}$, where a is the lattice parameter (for a more detailed representation and description refer to the work by Rittman et al. [19]). After performing routine image postprocessing procedures, the calculation of the 2D autocorrelation function (ACF) [37] (Fig. 4b) allows reducing the background noise and estimating a lattice parameter of 97.6 ± 0.3 Å (please refer to the SI for further details about the calculation). This is in good agreement with the SAXS analysis performed on thicker films and compatible with a Q_{II}^{D} phase.

Film morphology at larger length scales was then assessed by performing AFM imaging on 10 × 10 μm^2 regions (Fig. 4c). As estimated via AFM images, film thickness was ≈150 nm (Fig. 4d), in agreement with ellipsometry results. The results are also consistent with those proposed by Rittman et al. [19], who determined a lattice parameter of 100 ± 10 Å for similar spin-coated cubic phase lipid films.

After characterizing their structure, $SQ_{II}^{D}Fs$ were employed as cubic membrane models for investigating the mechanics of these non-lamellar lipid architectures. To this purpose, AFM-FS was used for probing the mechanical response of the Q_{II}^{D} lipid architecture to nanoscale deformations.

In a typical AFM-FS experiment, the AFM tip is used to indent the sample and study its mechanical response to deformations (Fig. 5). The forces experienced by the AFM tip while indenting the sample are recorded as a function of its penetration depth and plotted as force-distance curves (Fig. 6a). The results from the AFM-FS measurements demonstrate that the mechanical response of the Q_{II}^{D} cubic architecture is completely different from the typical Hertzian regime observed for SLBs [39]. As exemplified by the force-distance curve shown in Fig. 6a, after an initial, approximately linear regime, all the recorded force curves are characterized by a sequence of indentation peaks. Each peak corresponds to the sequential mechanical failure of successive cubic unit cells. Interestingly, the force required to penetrate each unit cell seems to be independent of the penetration depth, meaning that the

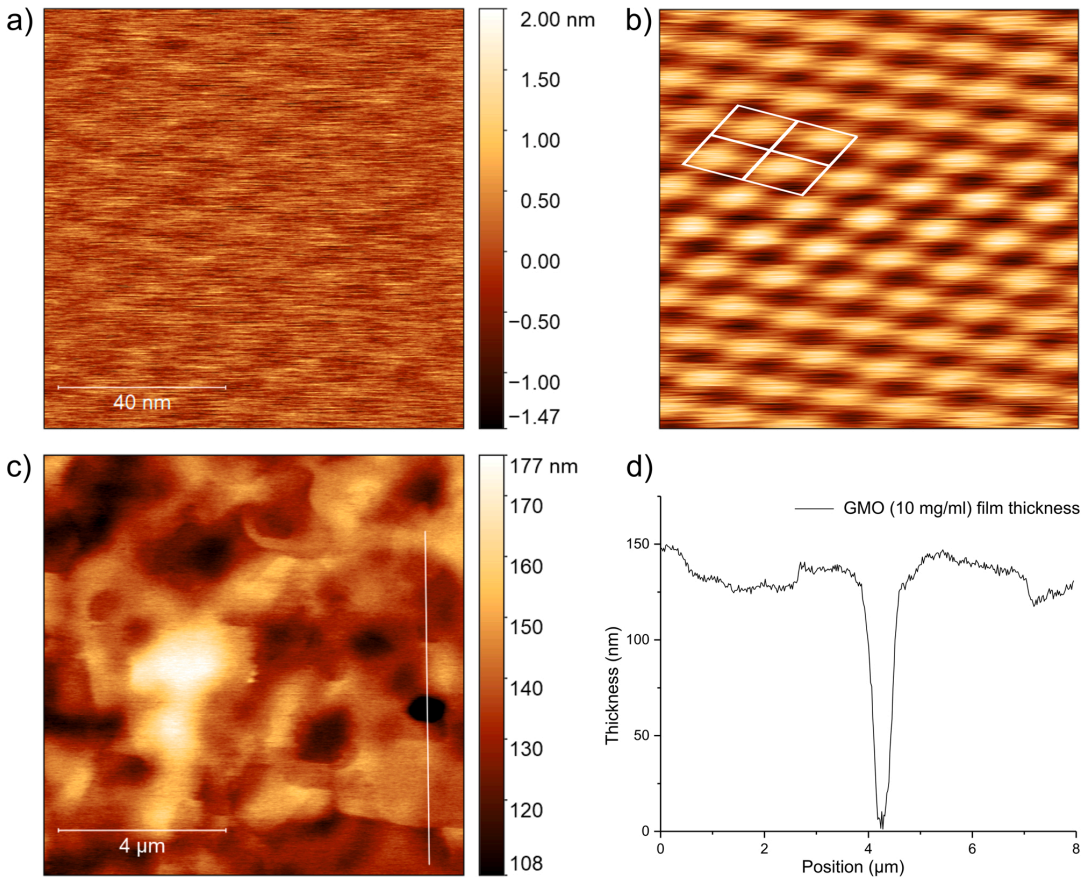

Fig. 4. : AFM imaging characterization of nanometric GMO-based lipid films: a) the topography of the film surface shows that the film possesses a cubic architecture, exposed to the water interface; b) applying a 2D ACF to the raw AFM image allows noise reduction and calculating the lattice parameter from the observed unit cell lattice pattern (white frame); c) 10 × 10 μm^2 topography of the lipid film, confirming the presence of an essentially continuous film; d) height profile along white line in panel c. Occasional $SQ_{II}^{D}F$ discontinuities allow estimating its thickness (≈150 nm).

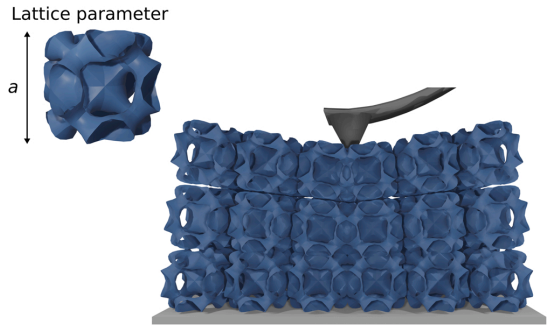

Fig. 5. : Representation of a typical AFM-FS experiment on a Q_{II}^{D} phase film; the AFM tip indents the sample causing a deflection of the cantilever. Recording the forces experienced during the indentation allows analyzing the mechanical response of the sample.

mechanical resistance of each cubic unit is relatively unaffected by the ones located in lower regions of the film, which still have to be indented.

While the mechanical properties of these nanoarchitectures are still not fully understood at the nanoscale, IPMS-inspired macroscopic structures are gaining increasing attention in engineering applications where their combination of light weight, high impact- and stress-resistance represents a promising solution for multiple structural challenges [25–28].

Even though these macroscopic structures and Q_{II} lipid membranes have vastly different length scales, they share the same topology. This suggests that some of the mechanical properties studied on macroscopic Q_{II} structures could remain valid for their nanoscale counterparts and could help the development of potential bioinspired nanomaterials.

Comparing our AFM-FS curves with the ones obtained from compression tests on macroscopic 3D printed IPMS-inspired architectures [25,26,28] reveals the same peculiar mechanical response emerging in both samples, despite their length scales differing by more than six orders of magnitude. This observation suggests that the mechanical behaviour of these structures is mostly conserved even at the nanoscale.

The indentation peaks located along the force-distance curves can also be used to obtain a complementary structural characterization of the Q_{II}^{D} mesophase. As can be seen in Fig. 5, the height of each cubic unit cell also represents the characteristic length scale of the whole architecture, i.e., its lattice parameter.

It is possible to obtain this structural parameter from AFM-FS curves, by calculating, for each force-distance curve, the ratio between the observed film thickness (as determined by the contact point, see Fig. 6a) and the number of peaks found in that specific curve (i.e., the number of unit cells that were penetrated before reaching the substrate). Eq. 1 summarizes the described procedure.

$$\frac{Film\quad thickness}{n^{\circ}\quad of\quad peaks\quad (unit\quad cells)} = Average\quad lattice\quad parameter \tag{1}$$

This allows us to obtain a direct estimation of the vertical separation between successive cells. Estimates from 211 curves were then pooled, yielding a monomodal distribution of values (Fig. 6b) which can be fitted with a Lorentzian function centered at~100 Å, in agreement with the lattice parameters from both the SAXS and the AFM imaging analyses (92.6 Å and 97.6 Å, respectively). According to our knowledge, this analysis provides the first example in the literature on the use of AFM-FS for characterizing the structure of non-lamellar lipid membranes. Despite lacking the accuracy of the more traditional scattering (involving both X-rays and/or neutrons) [18,40,41] and cryo-electron microscopy [6,42] techniques, AFM-FS represents an alternative way to obtain a structural analysis of these lipid mesophases surface layers.

4. Conclusions

In conclusion, this work reports on the fabrication of thin supported lipid films with nanometric thickness, presenting a Q_{II}^{D} architecture. After probing the structure and the stability of the systems by means of SAXS, Ellipsometry and AFM imaging, AFM-FS was used to obtain the first nanomechanical characterization of these membranes. Differentiating from classical rheological studies, which could only provide bulk characterizations, AFM-FS allowed us to probe the mechanics of these lipid architectures via forces occurring at the nanoscale level and generating localized deformations, that resemble the ones involved in biological membrane interactions [32]. The mechanical response of the probed lipid Q_{II}^{D} phase films also revealed interesting analogies with studies performed on similar macroscopic 3D printed structures, suggesting that the response of these architectures to an applied force is independent of their size and related to their topology. This finding could help the development of bioinspired nanomaterials but also promote the use of macroscale membrane models for understanding the complex mechanics of these non-lamellar lipid architectures. Finally, AFM-FS was employed for estimating the lattice parameter of the probed Q_{II}^{D} membranes; the analysis of the force-distance curves gave results in good agreement with both the previous SAXS and AFM imaging experiments. In this context, our AFM-FS analysis provides the first example of this technique being used for characterizing the structure of non-lamellar lipid mesophases, thus offering an alternative solution to the more commonly used scattering and cryo-electron microscopy-based techniques.

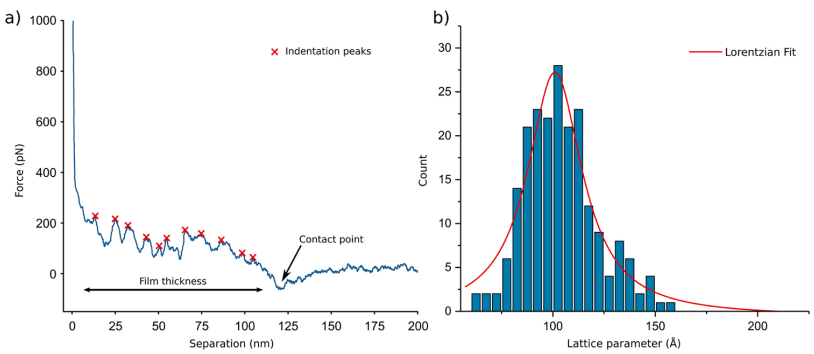

Fig. 6. : AFM-FS analysis of the lipid Q_{II}^{D} phase film: a) representative force-distance curve, describing the forces experienced by the AFM tip during the indentation of the cubic architecture; red crosses identify indentation peaks, corresponding to the mechanical failure of successive cubit unit cells; b) distribution of the lattice parameters obtained by dividing, in each force-distance curve, the value corresponding to the contact point by the number of peaks found in that specific curve; the distribution was fitted with a Lorentzian function and its centre was located at a lattice parameter value of 100 Å, in agreement with previous SAXS and AFM imaging analyses.

CRediT authorship contribution statement

Andrea Ridolfi: Conceptualization, Investigation, Writing – review & editing, **Ben Humphreys:** Investigation, Supervision, Writing – review & editing, **Lucrezia Caselli:** Conceptualization, Writing – review & editing, **Costanza Montis:** Conceptualization, Writing – review & editing, **Tommy Nylander:** Conceptualization, Supervision, Writing – review & editing, **Debora Berti:** Conceptualization, Supervision, Writing – review & editing, **Marco Brucale:** Conceptualization, Supervision, Writing – review & editing, **Francesco Valle:** Conceptualization, Supervision, Writing – review & editing.

Declaration of Competing Interest

The authors declare that they have no known competing financial interests or personal relationships that could have appeared to influence the work reported in this paper.

Acknowledgements

This research has received funding from the Horizon 2020 Framework Programme under the grants FETOPEN-801367 "evFOUNDRY" and FETPROACT-952183 "Biogenic Organotropic Wetsuits (BOW)". We thank the SPM@ISMN research facility for support in the AFM experiments.

Appendix A. Supporting information

Supplementary data associated with this article can be found in the online version at doi:10.1016/j.colsurfb.2021.112231.

References

[1] R. Mezzenga, J.M. Seddon, C.J. Drummond, B.J. Boyd, G.E. Schröder-Turk, L. Sagalowicz, Nature-inspired design and application of lipidic lyotropic liquid crystals, Adv. Mater. 31 (2019), https://doi.org/10.1002/adma.201900818.
[2] G.C. Shearman, O. Ces, R.H. Templer, J.M. Seddon, Inverse lyotropic phases of lipids and membrane curvature, J. Phys. Condens. Matter. 18 (2006), https://doi.org/10.1088/0953-8984/18/28/S01.
[3] K. Larsson, Cubic lipid-water phases: structures and biomembrane aspects, J. Phys. Chem. 93 (1989) 7304–7314, https://doi.org/10.1021/j100358a010.
[4] J. Zhai, S. Sarkar, C.E. Conn, C.J. Drummond, Molecular engineering of super-swollen inverse bicontinuous cubic and sponge lipid phases for biomedical applications, Mol. Syst. Des. Eng. (2020), https://doi.org/10.1039/d0me00076k.
[5] Z.A. Almsherqi, T. Landh, S.D. Kohlwein, Y. Deng, Chapter 6 cubic membranes. the missing dimension of cell membrane organization, Int. Rev. Cell Mol. Biol. (2009), https://doi.org/10.1016/S1937-6448(08)02006-6.
[6] D. Demurtas, P. Guichard, I. Martiel, R. Mezzenga, C. Hébert, L. Sagalowicz, Direct visualization of dispersed lipid bicontinuous cubic phases by cryo-electron tomography, Nat. Commun. 6 (2015), https://doi.org/10.1038/ncomms9915.
[7] S. Andersson, S. Lidin, S.T. Hyde, K. Larsson, Minimal surfaces and structures: from inorganic and metal crystals to cell membranes and biopolymers, Chem. Rev. 88 (1988), https://doi.org/10.1021/cr00083a011.
[8] H.M.G. Barriga, M.N. Holme, M.M. Stevens, Cubosomes: the next generation of smart lipid nanoparticles? Angew. Chem. Int. Ed. 58 (2019) 2958–2978, https://doi.org/10.1002/anie.201804067.
[9] T.G. Meikle, C.J. Drummond, F. Separovic, C.E. Conn, Membrane-mimetic inverse bicontinuous cubic phase systems for encapsulation of peptides and proteins (in:), Adv. Biomembr. Lipid Self-Assembly (2017) 63–94, https://doi.org/10.1016/bs.abl.2017.01.002.
[10] M. Mendozza, L. Caselli, A. Salvatore, C. Montis, D. Berti, Nanoparticles and organized lipid assemblies: from interaction to design of hybrid soft devices, Soft Matter 15 (2019) 8951–8970, https://doi.org/10.1039/c9sm01601e.
[11] V. Cherezov, H. Fersi, M. Caffrey, Crystallization screens: compatibility with the lipidic cubic phase for in meso crystallization of membrane proteins, Biophys. J. 81 (2001) 225–242, https://doi.org/10.1016/S0006-3495(01)75694-9.
[12] V. Cherezov, J. Clogston, Y. Misquitta, W. Abdel-Gawad, M. Caffrey, Membrane protein crystallization in meso: lipid type-tailoring of the cubic phase, Biophys. J. 83 (2002) 3393–3407, https://doi.org/10.1016/S0006-3495(02)75339-3.
[13] M. Caffrey, A comprehensive review of the lipid cubic phase or in meso method for crystallizing membrane and soluble proteins and complexes, Acta Crystallogr. Sect. FStructural Biol. Commun. 71 (2015) 3–18, https://doi.org/10.1107/S2053230×14026843.
[14] C. Montis, B. Castroflorio, M. Mendozza, A. Salvatore, D. Berti, P. Baglioni, Magnetocubosomes for the delivery and controlled release of therapeutics, J. Colloid Interface Sci. (2015), https://doi.org/10.1016/j.jcis.2014.11.056.
[15] M. Mendozza, C. Montis, L. Caselli, M. Wolf, P. Baglioni, D. Berti, On the thermotropic and magnetotropic phase behavior of lipid liquid crystals containing magnetic nanoparticles, Nanoscale (2018), https://doi.org/10.1039/c7nr08478a.
[16] M. Fornasier, S. Biffi, B. Bortot, P. Macor, A. Manhart, F.R. Wurm, S. Murgia, Cubosomes stabilized by a polyphosphoester-analog of pluronic F127 with reduced cytotoxicity, J. Colloid Interface Sci. (2020), https://doi.org/10.1016/j.jcis.2020.07.038.
[17] J. Gustafsson, H. Ljusberg-Wahren, M. Almgren, K. Larsson, Cubic lipid−water phase dispersed into submicron particles, Langmuir 12 (1996), https://doi.org/10.1021/la960318y.
[18] A.P. Dabkowska, M. Valldeperas, C. Hirst, C. Montis, G.K. Pálsson, M. Wang, S. Nöjd, L. Gentile, J. Barauskas, N.J. Steinke, G.E. Schroeder-Turk, S. George, M. W.A. Skoda, T. Nylander, Non-lamellar lipid assembly at interfaces: controlling layer structure by responsive nanogel particles, Interface Focus 7 (2017), https://doi.org/10.1098/rsfs.2016.0150.
[19] M. Rittman, M. Frischherz, F. Burgmann, P.G. Hartley, A. Squires, Direct visualisation of lipid bilayer cubic phases using Atomic Force Microscopy, Soft Matter 6 (2010) 4058–4061, https://doi.org/10.1039/c002968h.
[20] M. Rittman, H. Amenitsch, M. Rappolt, B. Sartori, B.M.D. O'Driscoll, A.M. Squires, Control and analysis of oriented thin films of lipid inverse bicontinuous cubic phases using grazing incidence small-angle X-ray scattering, Langmuir (2013), https://doi.org/10.1021/la401580y.
[21] A.M. Squires, J.E. Hallett, C.M. Beddoes, T.S. Plivelic, A.M. Seddon, Preparation of films of a highly aligned lipid cubic phase, Langmuir (2013), https://doi.org/10.1021/la304726m.
[22] E.T. Castellana, P.S. Cremer, Solid supported lipid bilayers: from biophysical studies to sensor design, Surf. Sci. Rep. 61 (2006) 429–444, https://doi.org/10.1016/j.surfrep.2006.06.001.
[23] C.V. Kulkarni, W. Wachter, G. Iglesias-Salto, S. Engelskirchen, S. Ahualli, Monoolein: a magic lipid? Phys. Chem. Chem. Phys. (2011) https://doi.org/10.1039/c0cp01539c.
[24] S.T. Hyde, S. Andersson, B. Ericsson, K. Larsson, A cubic structure consisting of a lipid bilayer forming an infinite periodic minimum surface of the gyroid type in the glycerolmonooleat-water system, Zeitschrift Fur Krist. - New Cryst. Struct. 168 (1984), https://doi.org/10.1524/zkri.1984.168.1-4.213.
[25] M.M. Sychov, L.A. Lebedev, S.V. Dyachenko, L.A. Nefedova, Mechanical properties of energy-absorbing structures with triply periodic minimal surface topology, Acta Astronaut. 150 (2018) 81–84, https://doi.org/10.1016/j.actaastro.2017.12.034.
[26] D.W. Abueidda, M. Bakir, R.K. Abu Al-Rub, J.S. Bergström, N.A. Sobh, I. Jasiuk, Mechanical properties of 3D printed polymeric cellular materials with triply periodic minimal surface architectures, Mater. Des. 122 (2017) 255–267, https://doi.org/10.1016/j.matdes.2017.03.018.
[27] L. Zhang, S. Feih, S. Daynes, S. Chang, M.Y. Wang, J. Wei, W.F. Lu, Energy absorption characteristics of metallic triply periodic minimal surface sheet structures under compressive loading, Addit. Manuf 23 (2018) 505–515, https://doi.org/10.1016/j.addma.2018.08.007.
[28] Z. Qin, G.S. Jung, M.J. Kang, M.J. Buehler, The mechanics and design of a lightweight three-dimensional graphene assembly, Sci. Adv. 3 (2017), https://doi.org/10.1126/sciadv.1601536.
[29] C. Rodríguez-Abreu, M. García-Roman, H. Kunieda, Rheology and dynamics of micellar cubic phases and related emulsions, Langmuir 20 (2004) 5235–5240, https://doi.org/10.1021/la0498962.
[30] R. Mezzenga, C. Meyer, C. Servais, A.I. Romoscanu, L. Sagalowicz, R.C. Hayward, Shear rheology of lyotropic liquid crystals: a case study, Langmuir 21 (2005) 3322–3333, https://doi.org/10.1021/la046964b.
[31] C. Speziale, R. Ghanbari, R. Mezzenga, Rheology of ultraswollen bicontinuous lipidic cubic phases, Langmuir 34 (2018) 5052–5059, https://doi.org/10.1021/acs.langmuir.8b00737.
[32] G. Bao, S. Suresh, Cell and molecular mechanics of biological materials, Nat. Mater. 2 (2003) 715–725, https://doi.org/10.1038/nmat1001.
[33] M. Mendozza, C. Montis, L. Caselli, M. Wolf, P. Baglioni, D. Berti, On the thermotropic and magnetotropic phase behavior of lipid liquid crystals containing magnetic nanoparticles, Nanoscale 10 (2018) 3480–3488, https://doi.org/10.1039/c7nr08478a.
[34] S. Murgia, F. Caboi, M. Monduzzi, H. Ljusberg-Wahren, T. Nylander, Acyl migration and hydrolysis in monoolein-based systems, in: T. Nylander, B. Lindman (Eds.), Progress in Colloid and Polymer Science, Springer Berlin Heidelberg, Berlin, Heidelberg, 2002, pp. 41–46, https://doi.org/10.1007/3-540-45291-5_6.
[35] A. Stamm, A. Svendsen, J. Skjold-Jørgensen, T. Vissing, I. Berts, T. Nylander, The triolein/aqueous interface and lipase activity studied by spectroscopic ellipsometry and coarse grained simulations, Chem. Phys. Lipids. 211 (2018) 37–43, https://doi.org/10.1016/j.chemphyslip.2017.10.011.
[36] J.L. Hutter, J. Bechhoefer, Calibration of atomic-force microscope tips, Rev. Sci. Instrum. 64 (1993) 1868–1873, https://doi.org/10.1063/1.1143970.
[37] D. Nečas, P. Klapetek, Gwyddion: an open-source software for SPM data analysis, Cent. Eur. J. Phys. 10 (2012) 181–188, https://doi.org/10.2478/s11534-011-0096-2.
[38] K. Larsson, Aqueous dispersions of cubic lipid–water phases, Curr. Opin. Colloid Interface Sci. 5 (2000) 64–69, https://doi.org/10.1016/S1359-0294(00)00040-6.
[39] S. Garcia-Manyes, F. Sanz, Nanomechanics of lipid bilayers by force spectroscopy with AFM: a perspective, Biochim. Biophys. Acta Biomembr. 1798 (2010) 741–749, https://doi.org/10.1016/j.bbamem.2009.12.019.

[40] P. Garstecki, R. HoŁyst, Scattering patterns of self-assembled cubic phases: 2. Analysis of the experimental spectra, Langmuir 18 (2002) 2529–2537, https://doi.org/10.1021/la011299h.
[41] B. Angelov, A. Angelova, V.M. Garamus, G. Lebas, S. Lesieur, M. Ollivon, S. S. Funari, R. Willumeit, P. Couvreur, Small-angle neutron and X-ray scattering from amphiphilic stimuli-responsive diamond-type bicontinuous cubic phase, J. Am. Chem. Soc. 129 (2007) 13474–13479, https://doi.org/10.1021/ja072725.
[42] S.B. Rizwan, Y.D. Dong, B.J. Boyd, T. Rades, S. Hook, Characterisation of bicontinuous cubic liquid crystalline systems of phytantriol and water using cryo field emission scanning electron microscopy (cryo FESEM), Micron. 38 (2007) 478–485, https://doi.org/10.1016/j.micron.2006.08.003.

Supplementary Information

Nanoscale structural and mechanical characterization of thin bicontinuous cubic phase lipid films

Andrea Ridolfi[a,b,c,], Ben Humphreys[d], Lucrezia Caselli[a,c], Costanza Montis[a,c], Tommy Nylander[d,e,f], Debora Berti[a,c], Marco Brucale[a,b,*] and Francesco Valle[a,b,*].*

[a] Consorzio Interuniversitario per lo Sviluppo dei Sistemi a Grande Interfase, 50019 Firenze, Italy.

[b] Consiglio Nazionale delle Ricerche, Istituto per lo Studio dei Materiali Nanostrutturati, 40129 Bologna, Italy.

[c] Dipartimento di Chimica "Ugo Schiff", Università degli Studi di Firenze, 50019 Firenze, Italy.

[d] Department of Physical Chemistry, Department of Chemistry, Lund University, SE-221 00 Lund, Sweden.

[e] Lund Institute of Advanced Neutron and X-ray Science - LINXS, SE- 223 70 Lund, Sweden.

[f] NanoLund, Lund University, SE-221 00 Lund, Sweden.

* corresponding authors

Figure S1

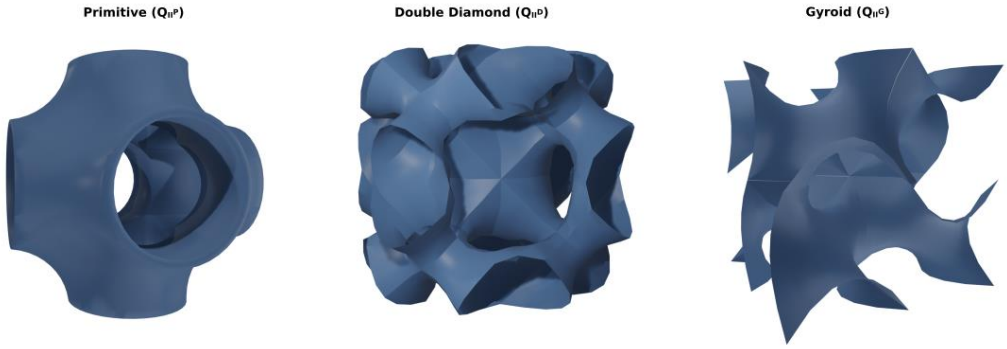

The three types of Q_{II} unit cells observed for lipid liquid crystalline mesophases, corresponding to Infinite Triply Periodical Minimal Surfaces (IPMS). The IPMS describe the midplane of the curved lipid bilayer that form the bicontinuous structure.

Figure S2

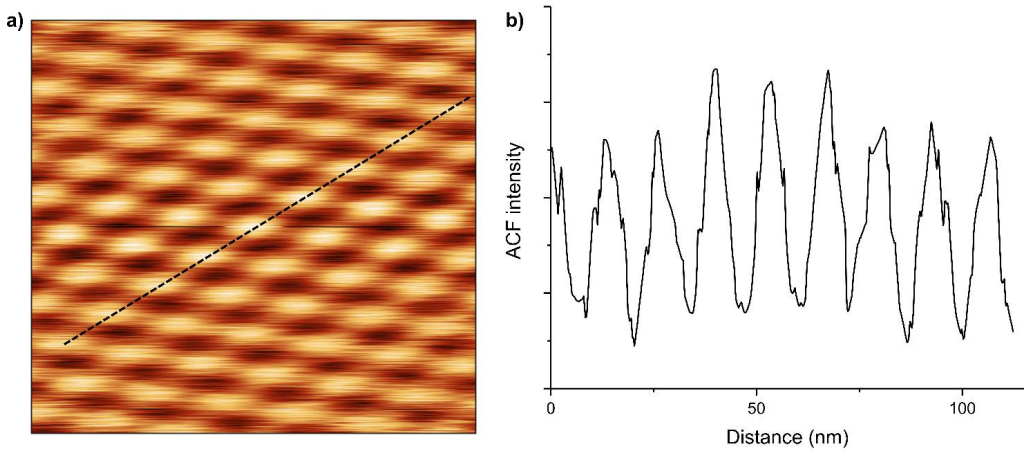

Calculation of the lattice parameter from the AFM image

From the autocorrelation function (ACF) image (Figure 4 b and Figure S2 a) it is possible, exploiting the free image analysis software Gwyddion 2.53 [1], to select a specific section of the image (Figure S2 a dotted black line) and to obtain the profiles that describe the peaks and valleys defining the observed pattern; this allows estimating their spacing via the average peak to peak distance (Figure S2 b). As explained in the manuscript, in order for the bilayer to remain continuous, one of the network of channels is capped by the bilayer [2]; this translates into a spacing between the features equal to $a\sqrt{2}$ with a being the lattice parameter (for a more detailed representation and description refer to the work by Rittman et al. [3]). For this reason, the average peak to peak distance obtained from the profile of Figure S2 b has to be divided by $\sqrt{2}$ to yield the lattice parameter of the cubic architecture. In order to obtain the lattice parameter reported in the manuscript, the average peak to peak distance from multiple sections (selected along both the “diagonal directions”) were evaluated.

[1] D. Nečas, P. Klapetek, Gwyddion: An open-source software for SPM data analysis, Cent. Eur. J. Phys. 10 (2012) 181–188. https://doi.org/10.2478/s11534-011-0096-2.

[2] K. Larsson, Aqueous dispersions of cubic lipid–water phases, Curr. Opin. Colloid Interface Sci. 5 (2000) 64–69. https://doi.org/https://doi.org/10.1016/S1359-0294(00)00040-6.

[3] M. Rittman, M. Frischherz, F. Burgmann, P.G. Hartley, A. Squires, Direct visualisation of lipid bilayer cubic phases using Atomic Force Microscopy, Soft Matter. 6 (2010) 4058–4061. https://doi.org/10.1039/c002968h.

Manuscript n°6

Volume 24
Number 5
7 February 2022
Pages 2669–3500

PCCP

Physical Chemistry Chemical Physics

rsc.li/pccp

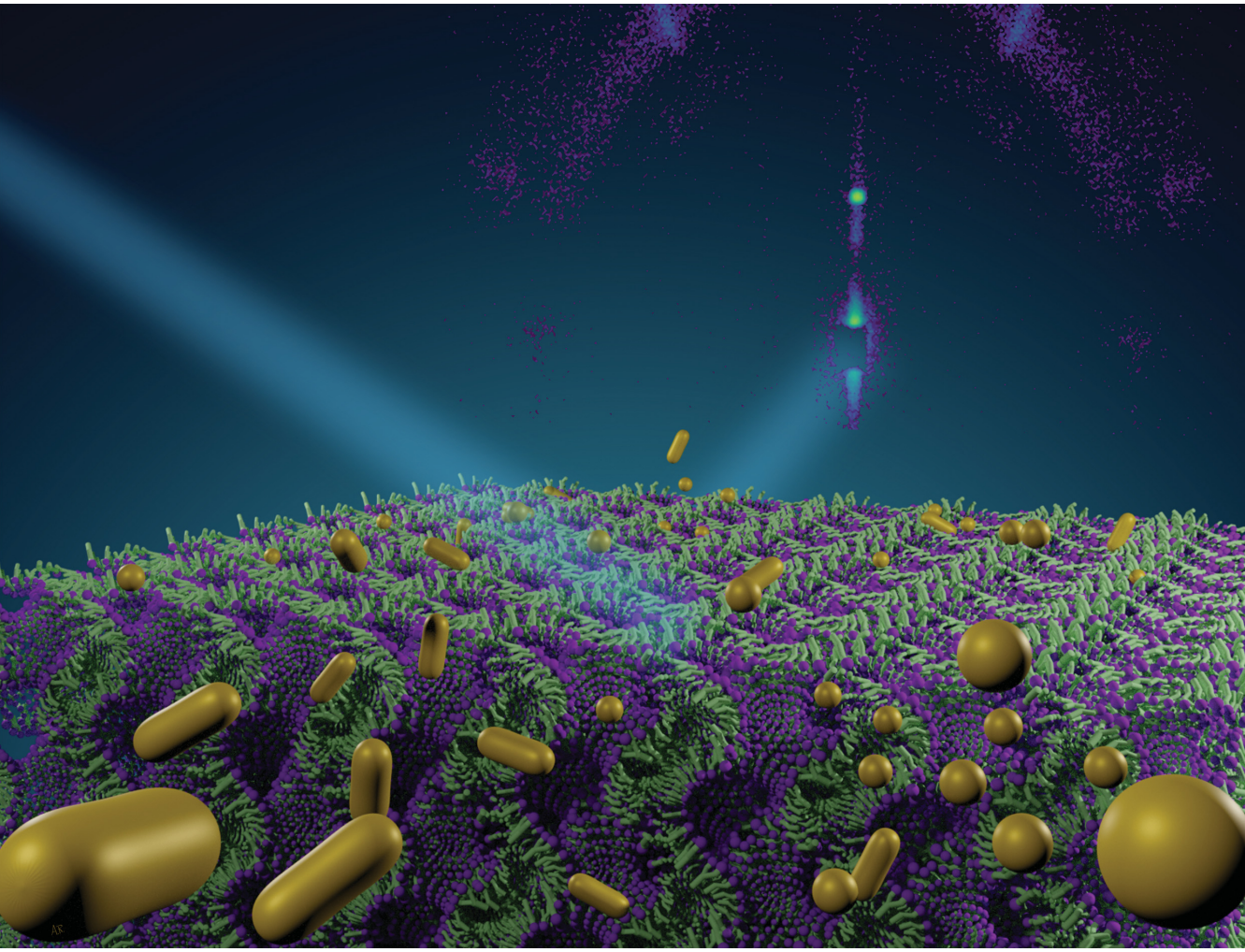

ISSN 1463-9076

ROYAL SOCIETY OF CHEMISTRY

PAPER

Tommy Nylander, Costanza Montis *et al.*
Interaction of nanoparticles with lipid films: the role of symmetry and shape anisotropy

PCCP

ROYAL SOCIETY OF CHEMISTRY

PAPER

View Article Online
View Journal | View Issue

Cite this: *Phys. Chem. Chem. Phys.*, 2022, **24**, 2762

Interaction of nanoparticles with lipid films: the role of symmetry and shape anisotropy†

Lucrezia Caselli,[a] Andrea Ridolfi,[ab] Gaetano Mangiapia,[c] Pierfrancesco Maltoni,[‡a] Jean-François Moulin,[c] Debora Berti,[a] Nina-Juliane Steinke,[§d] Emil Gustafsson,[e] Tommy Nylander[*fg] and Costanza Montis[*a]

The bioactivity, biological fate and cytotoxicity of nanomaterials when they come into contact with living organisms are determined by their interaction with biomacromolecules and biological barriers. In this context, the role of symmetry/shape anisotropy of both the nanomaterials and biological interfaces in their mutual interaction, is a relatively unaddressed issue. Here, we study the interaction of gold nanoparticles (NPs) of different shapes (nanospheres and nanorods) with biomimetic membranes of different morphology, *i.e.* flat membranes (2D symmetry, representative of the most common plasma membrane geometry), and cubic membranes (3D symmetry, representative of non-lamellar membranes, found in Nature under certain biological conditions). For this purpose we used an ensemble of complementary structural techniques, including Neutron Reflectometry, Grazing Incidence Small-Angle Neutron Scattering, on a nanometer lengthscale and Confocal Laser Scanning Microscopy on a micrometer length scale. We found that the structural stability of the membrane towards NPs is dependent on the topological characteristic of the lipid assembly and of the NPs, where a higher symmetry gave higher stability. In addition, Confocal Laser Scanning Microscopy analyses highlighted that NPs interact with cubic and lamellar phases according to two distinct mechanisms, related to the different structures of the lipid assemblies. This study for the first time systematically addresses the role of NPs shape in the interaction with lipid assemblies with different symmetry. The results will contribute to improve the fundamental knowledge on lipid interfaces and will provide new insights on the biological function of phase transitions as a response strategy to the exposure of NPs.

Received 14th July 2021,
Accepted 7th October 2021

DOI: 10.1039/d1cp03201a

rsc.li/pccp

Introduction

Living organisms are increasingly exposed to nanomaterials, either intentionally administered or unintentionally released in the environment. The interaction of nanosystems with

Costanza Montis

Costanza Montis is Assistant Professor of Physical Chemistry at the Department of Chemistry, University of Florence, and member of the Italian Consortium for Colloid and Surface Science (CSGI). She received her PhD in Chemical Sciences from the University of Florence in 2013. Her main research activity focuses on the understanding of complex phenomena occurring at interfaces, from a physicochemical perspective. Her scientific interests are in physical chemistry of soft matter and include the biophysical understanding of nano-bio interfaces; the design of lipid-nanoparticles hybrid materials for biomedical applications; the engineering/characterisation of biogenic extracellular vesicles; the study of nanostructured materials for applications in restoration of works of art.

[a] *Department of Chemistry, University of Florence and CSGI, Florence, Italy. E-mail: costanza.montis@unifi.it*
[b] *ISMN-CNR and CSGI, Bologna, Italy*
[c] *German Engineering Materials Science Centre (GEMS) at Heinz Maier-Leibnitz Zentrum (MLZ), Helmholtz-Zentrum Hereon, Lichtenbergstr. 1, 85748 Garching bei München, Germany*
[d] *ISIS, Rutherford Appleton Laboratory Didcot, Oxfordshire, UK*
[e] *Department of Chemistry, Uppsala University, Uppsala, Sweden*
[f] *Department of Chemistry, Physical Chemistry, Lund University, Lund, Sweden. E-mail: tommy.nylander@fkem1.lu.se*
[g] *NanoLund, Lund University, Lund (Sweden, Lund Institute of Advanced Neutron and X-Ray Science - LINXS), Lund, Sweden*

† Electronic supplementary information (ESI) available: Supplementary Materials and Methods and data analysis. See DOI: 10.1039/d1cp03201a

‡ Current affiliation: Department of Materials Science and Engineering, Uppsala University, Uppsala, Sweden.
§ Current affiliation: Institut Laue-Langevin, Grenoble, France.

biological matter proceeds through an intricate balance of forces,[1–3] occurring at the nano-bio interface, where nanomaterials, *e.g.* nanoparticles, meet biological fluids and barriers (such as biological membranes). Disentangling these contributions is key to understand the fate of the nanoparticles in living systems, in particular their toxic effects and, concerning nanomaterials designed for nanomedicine, their efficacy in reaching their biological target.[4–10] In this context, where multiple factors and forces are simultaneously at play, the concept of symmetry, which can be related both to the shape of NPs and to the nanoscale structure of the target biological membrane, is particularly interesting.

The role of NPs shape asymmetry is currently the focus of extensive research. Both experimental and computational studies highlight that the anisotropy of NPs is a determining factor in their internalization pathways in cells.[4,11–15] In particular, NPs shape modifies the area available for NPs adsorption on lipid surfaces,[16] therefore modulating the strength of NP-membrane adhesion forces. Additionally, topological effects are significant in the surface functionalization of NPs (*e.g.*, ligand surface density), affecting their chemical identity.[17] Finally, a high surface curvature, either uniformly distributed on the surface of NPs (*e.g.*, small NPs with sizes of a few nm) or localized at the sharp edges of asymmetric NPs (*e.g.*, nanorods), is associated to higher energetic costs in terms of wrapping and internalization by membranes.[3,12,14,15] Anisotropic NPs, unlike spheres, can reorient in proximity to the lipid interface to minimize this energy penalty and maximize the adhesion strength to the membrane.[18]

On the other side, biological membranes are commonly characterized by a planar geometry with a bidimensional structure, *i.e.*, an infinite plan constituted by a lipid bilayer. However, such arrangement can undergo striking temporary or permanent topological modifications in selected conditions, for instance in cell trafficking phenomena or in pathological conditions, often related to a significant symmetry alteration. In particular, curved membrane configurations characterized by a 3D symmetry, as cubic bicontinuous arrangements, are known to occur in cells under pathological conditions (*e.g.*, drug detoxification, starving, infection, oxidative stress, and cancer disease) or during certain phases of cell life (*e.g.* membrane fusion).[19–21] Up to now, the investigations related to these so-called ''cubic membranes'' have been limited to a descriptive level, while their biological function remains practically unexplored.[20,21] This is mainly due to the transient nature of non-lamellar biological membranes, which makes their investigation in natural systems very challenging.[21] In this framework, lipid models of synthetic nature, mimicking cubic membranes structure, can be used to simplify the investigation. Our recent findings[22–24] show that it is possible to obtain solid-supported lipid model surface layers of cubic symmetry, with controlled physicochemical and structural features, enabling the study of NPs-cubic membranes interaction in highly simplified and controlled conditions.

Here we investigate how gold nanoparticles (AuNPs) of different symmetry (namely gold nanospheres (AuNSs) and gold nanorods (AuNRs)) but similar size and surface coating, interact with target lipid films of different internal structure (namely a lamellar phase, of 2D symmetry, and a cubic phase, of 3D symmetry). By combining neutron scattering techniques (Neutron Reflectivity and Grazing-Incidence Small-Angle Neutron Scattering (GISANS)) with Confocal Laser Scanning Microscopy (CSLM), we unravel NPs-lipid films interaction as a function of time, from few minutes to many hours, and at different lengthscales (from nanometers to micrometers).

Our results show that the shape and symmetry of both the NPs and the lipid mesophase are key factors in driving the mechanism and strength of NP–lipid film interaction. Overall, these findings improve our understanding of the nano-bio interface. In addition, this contribution provides potential insights into the role of cubic membranes in biological systems.

Results and discussion

Characterization of gold nanoparticles and lipid films of different symmetry

Cationic gold nanospheres (AuNSs) and nanorods (AuNRs) in water were prepared according to well-known synthetic routes.[25–28] The concentration of particles was determined by ICP-AES, as described in the ESI.† Fig. 1, Panel (a) shows the Small Angle X-ray Scattering (SAXS) profiles and Transmission Electron Microscopy (TEM) images of both AuNSs and AuNRs. SAXS of AuNSs were analysed with a spherical form factor with Schulz polydispersity. AuNSs were found to be polydisperse spheres (PD 0.4) with a metal core of 3.4 nm, in perfect agreement with TEM (d = 3.4 ± 0.6 nm). SAXS data of AuNRs were analysed applying a model with cylindrical form factor with a polydisperse cross section. The fitting parameters are consistent with 7.4 (length width^{-1}) aspect ratio nanorods (length 19.2 nm, diameter 2.6 nm (PD 0.2)), in line with TEM analysis (length 18 ± 5 nm, diameter 4 ± 1 nm). The cationic capping agents of AuNSs and AuNRs (mearcaptoundecyl-*N*,*N*,*N*-trimethyl ammonium bromide (TMA) and cetyltrimethyl ammonium bromide (CTAB), respectively) determine for both spheres and rods an overall positive zeta potential (+26 ± 1 mV for AuNSs, +45 ± 2 mV for AuNRs). In summary, both AuNSs and AuNRs are characterized by a net positive charge, which has been shown to result in a strong attractive interaction with zwitterionic phospholipid membranes, characterized by a slightly negative zeta potential.[1,29] In addition, spherical NPs are characterized by a diameter similar to the rods cross section diameter; therefore, the main difference between AuNSs and AuNRs is the strong asymmetry of AuNRs, with two curved surfaces (the poles), separated by a cylindrical body.

Lipid films on glass coverslips of different liquid crystalline structure were prepared by spin-coating *n*-hexane solutions of 1-monoolein (GMO) to produce a cubic phase film and of GMO/DOPC (1,2-dioleoyl-*sn*-glycero-3-phosphocholine) (50/50 mol%) to obtain a lamellar phase film. For CLSM experiments, a fluorescent hydrophobic dye (Nile Red, 0.1 mol% with respect

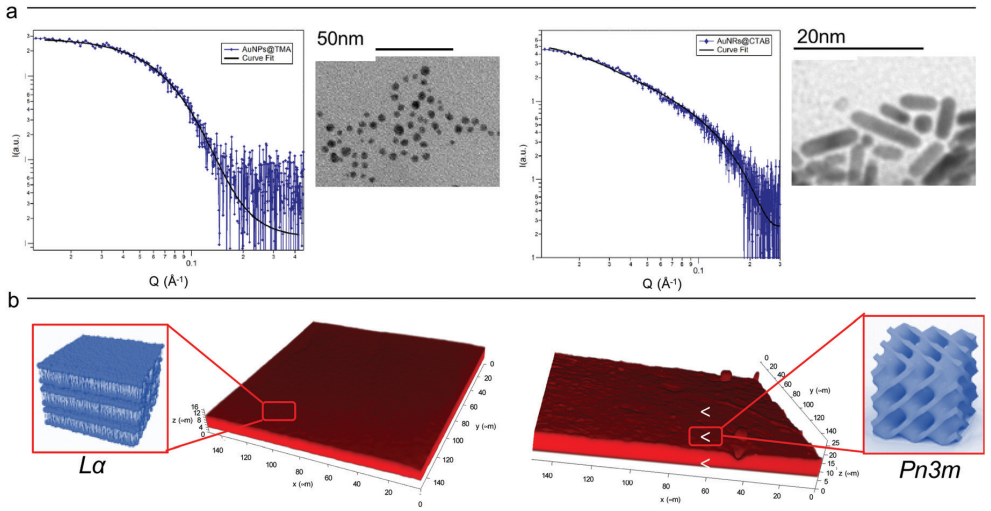

Fig. 1 (Panel a) Physicochemical properties of NPs. Left: SAXS profile of AuNSs in water (at a concentration of 1.1×10^{15} particles mL^{-1}) and the corresponding fit with a Schulz polydisperse spheres model (see ESI,† for details). The inset shows a typical TEM image of AuNSs; Right: SAXS profile of AuNRs in water (at a concentration of 2.4×10^{14} particles mL^{-1}) and curve fitting according to a Cylinder poly radius model. The inset reports a TEM image of AuNRs; (Panel b) physicochemical properties of lipid films. Three-dimensional reconstruction of a confocal fluorescence *z*-stack of images of the lamellar (left side) and the cubic (right side) films (tilted surface area of 150 × 150 μm). The insets depict the lamellar Lα (left side) and cubic *Pn3m* (right side) structures.

to the total lipid amount) was added. The lipid films were then dried in vacuum to completely remove the solvent and subsequently hydrated with an excess of water. Fig. 1, Panel (b), displays the 3D reconstructions of fully hydrated GMO and GMO/DOPC films. The morphology of the films at the micron-scale appears very similar, *i.e.*, a homogeneous thickness (of 10 ± 2 μm for both films), with low roughness. Due to the different compositions, it is expected that the lipid films are characterized by a different structural arrangement at a nanometric length scale: a *Pn3m* cubic phase for GMO films and a Lα lamellar phase for GMO/DOPC films (see the schemes in Fig. 1b). This was confirmed by neutron reflectometry as described in the following section.

Nanoparticles-lipid films interaction at a nanometric lengthscale

GMO and GMO/DOPC films were formed on ultra-polished silicon blocks and fully hydrated with excess D_2O, they were then equilibrated for 12 h before characterisation with Neutron Reflectivity. Subsequently, AuNSs in D_2O were pumped in the measurement cell at a concentration of 3×10^{14} particles mL^{-1} (corresponding to 0.12 mg mL^{-1} gold concentration). It is worth noticing that, being lamellar and cubic films prepared with the same total amount of lipid, the same AuNSs concentration was employed to challenge lamellar and cubic films. Then, after 8 h incubation, the reflectivity curve for the lipid films in the presence of AuNSs was recorded.

The reflectivity profiles of GMO/DOPC (Fig. 2a) and GMO (Fig. 2b) films without NPs are consistent with the formation of highly ordered mesophases, with multiple Bragg reflections. Also the detector images (inset in Fig. 2) show considerable off-specular scattering that reflects the structure of the lipid films. In particular, the reflectivity profile of the GMO-DOPC film features two prominent Bragg peaks located at 0.099 and 0.192 $Å^{-1}$, corresponding to the first two reflexes of the lamellar Lα phase. As sketched in Fig. 2a (left inset), the lamellar structure of the micrometric film consists of a stack of flat lipid bilayers separated by water layers. The unit cell spacing was calculated using the *Q*-position of the maximum intensity first-order reflexes[30] (see ESI,† for details), yielding a value of 64 ± 1 Å. This value is consistent with previous results obtained for a bulk GMO/DOPC Lα-phase.[31] Considering a thickness of about 34–37 Å for the GMO/DOPC bilayer (based on 37 Å and 34 Å for DOPC and GMO bilayers,[32,33] respectively), the water interlayers will have a thickness of 26–29 Å. The reflectivity profile of the GMO lipid film (Fig. 2b) presents at least two clearly distinguishable Bragg peaks, indicating also in this case a highly ordered internal structure. The position of these two peaks are at *Q*-values 0.091 and 0.111 $Å^{-1}$. These *Q* values can be associated to an inverse cubic phase with crystallographic space group *Pn3m*, corresponding to Miller indices (110) and (111). As depicted in the right inset, this structure has a bicontinuous nature, featuring a single lipid bilayer with negative curvature at the interface between lipid polar headgroups and water, which divides the inner space into two sets of interwoven aqueous channels. The lattice spacing *d*, calculated as described in the ESI,† is 95 ± 0.5 Å, corresponding to a water channel diameter of 44 Å,[34] similar to the diameter of the NPs.

When AuNSs are added to the GMO/DOPC film, the reflectivity still shows Bragg reflection peaks typical of the lamellar

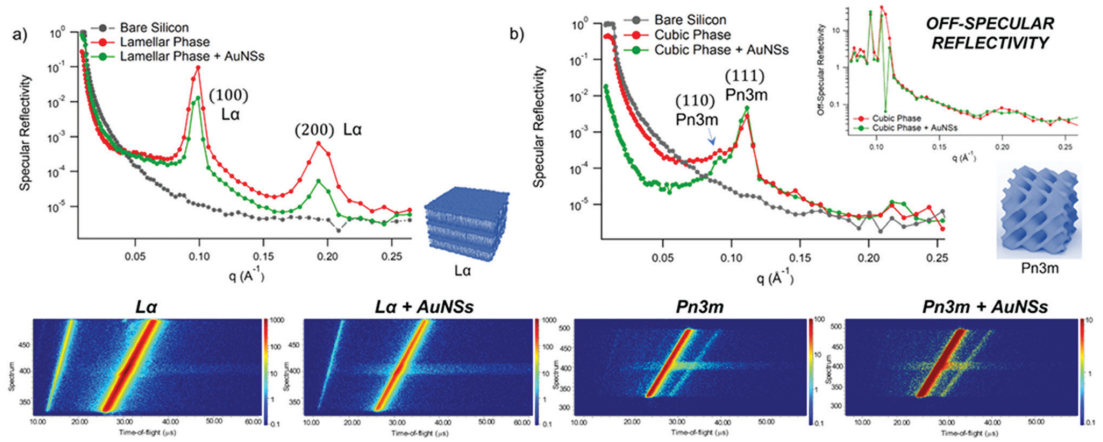

Fig. 2 (Panel a) Structural characterization of GMO/DOPC films interacting with AuNSs. Top: Specular reflectivity profiles of the GMO/DOPC film in the absence and in the presence of AuNSs, together with the reflectivity of the bare silicon. The inset sketches the inner Lα structure of the film; Bottom: Images of the reflectivity detectors acquired for the Lα phase in the absence and in the presence of AuNSs; (Panel b) structural characterization of GMO films interacting with AuNSs. Specular reflectivity of the GMO film in the absence and in the presence of AuNSs, together with the reflectivity of the bare silicon. The top inset represents the Off-specular reflectivity of GMO films in the absence and in the presence of AuNSs, while the bottom inset sketches the inner cubic *Pn3m* structure of the lipid film; Bottom: Images of the reflectivity detectors acquired for the *Pn3m* phase in the absence and in the presence of AuNSs. Measurements acquired at OFFSPEC,[55] ISIS Neutron and Muon Source (United Kingdom). The reflectivity profiles of lamellar and cubic films in the presence of AuNSs were acquired after 8 h of incubation, with 5 h acquisition time, leading to a lipid films/AuNSs total interaction time of 13 h.

arrangement. Although the positions are unchanged compared to before adding the particles, the presence of AuNSs produces a significant reduction in the peaks intensity. This suggests that a partial disruption of the bilayer arrangement occurs (a possible effect of lipid removal caused by the liquid flow through the sample cell had been previously ruled out with a control experiment, see ESI,† Fig. S4). However, the same AuNSs seem to have negligible impact on the nanostructure of the cubic lipid film: while a modification of the curve at low Q might suggest a variation of the overall film thickness and roughness, the presence of AuNSs does not significantly modify neither the position nor the intensity of the Bragg peaks, compared to the neat GMO film. This suggests that the nanostructure in the cubic film is stable and does not change even after 13 h of interaction (8 h of incubation + 5 h of measurement) with the AuNSs.

We further investigated the structure of AuNSs/cubic phase films by means of GISANS. The aim was to reveal possible effects of AuNSs on cubic phases, occurring over a longer time (8 h of incubation + 24 h of measurement, for a total AuNSs-membrane interaction time of 32 h). This technique allows also investigating the in-plane lipid arrangement and reveal how it changes upon AuNSs injection.[35] Lamellar films only have structural order with respect to the normal of the layers, while cubic phases are also characterized by high lateral ordering, whose possible modifications can be easily detected by GISANS. We performed GISANS on a neat GMO cubic film in D_2O, previously equilibrated for 12 h (Fig. 3a). Then, we added AuNSs at the same concentration as used for the Neutron Reflectivity measurements and left to incubate for 8 h.

The Q_z/Q_y GISANS pattern of GMO film in the absence of AuNSs shows isolated spots, which represent the (110) and (111) Bragg reflections of the *Pn3m* structure. By performing horizontal line cuts (*i.e.* at constant Q_z) from the 2D GISANS plot, we determined the position of these highest intensity points (see Fig. S1 of ESI,† for details). The obtained Q values correspond to a *Pn3m* cubic space group, with an obtained lattice parameter of 102 Å, in good agreement with the Neutron Reflectivity analysis. The presence of a spot-like pattern suggests a oriented cubic structure at the interface,[36] rather than a typical powder pattern that is mostly the case for the corresponding bulk GMO. The addition of AuNSs (Fig. 3b) smears out the spot-like pattern, which is now barely distinguishable from the Debye–Scherrer ring. This suggests a significant increase of the structural disorder within the mesophase, which can be either due to a partial disruption of the cubic symmetry or to a loss of spatial orientation, as well as loss of material from the surface. Interestingly, we also observed a significant shrinkage of the cubic phase lattice parameter in the presence of AuNSs (*i.e.*, 2 nm) (see Fig. S2 of ESI†), implying a dehydration of the structure induced by AuNSs. In summary, GISANS data reveal a non-negligible impact of AuNSs on the cubic structure, when observed on longer time scales, thus complementing Neutron Reflectivity data. To conclude, for (relatively) short interaction times (Neutron Reflectivity data), the structural order of the lamellar mesophase decreases, while, in the same timeframe, the cubic phase mesostructure appears preserved. However, for longer incubation times (GISANS), AuNSs also affect the structural order of the cubic film. Therefore, the cubic mesophase appears significantly more stable than the lamellar one, when subjected to AuNSs exposure.

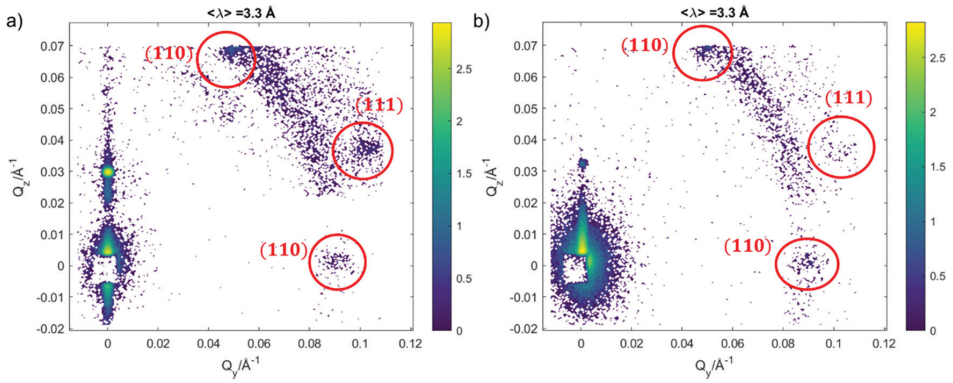

Fig. 3 (a) GISANS pattern of GMO cubic *Pn3m* films, in the absence of NPs; (b) GISANS pattern of the GMO cubic *Pn3m* phase in the presence of AuNSs. Measurements acquired at REFSANS, Heinz Maier-Leibnitz Zentrum, Garching, Germany. In both the patterns, intensities are reported in a logarithmic scale. The reflectivity profiles of the cubic film in the presence of AuNSs was acquired after 8 h of incubation, with 24 h acquisition time, leading to a lipid film/AuNSs total interaction time of 32 h.

Fig. 4 shows Neutron Reflectivity data obtained for the same lipid films (lamellar in Fig. 4a and cubic in Fig. 4b) exposed to AuNRs at an Au concentration of 0.12 mg mL^{-1}, measured under the same experimental conditions as AuNSs. In contrast to AuNSs, AuNRs completely destroy both the lamellar and cubic arrangements, as evident from the absence of Bragg reflexes in the corresponding reflectivity profiles as well as in the reduced off-specular scattering in the inserted detector images. Indeed, for both the lamellar and the cubic film the Neutron Reflectivity profile of the remaining layer indicates a thickness consistent with a pure GMO or GMO/DOPC bilayer (curve fitting results are in the ESI,† Fig. S2). AuNRs and AuNSs have similar size, *i.e.* similar cross section of the AuNRs and AuNSs diameter, and bear a net cationic surface charge. Therefore, the enhanced effect of AuNRs with lipid films suggests a strong role played by NPs shape asymmetry in the interaction with model lipid films.

Clearly, the drastic effect of AuNRs is not dependent on whether the film has a lamellar or a cubic phase structure, in the time frame of our experimental observations. To gain further insight on this fast disruption process, we performed Neutron Reflectivity kinetics studies, allowing for monitoring the structural alteration produced by AuNRs on shorter time scales.[37] We measured the reflectivity of lipid films in H_2O, just

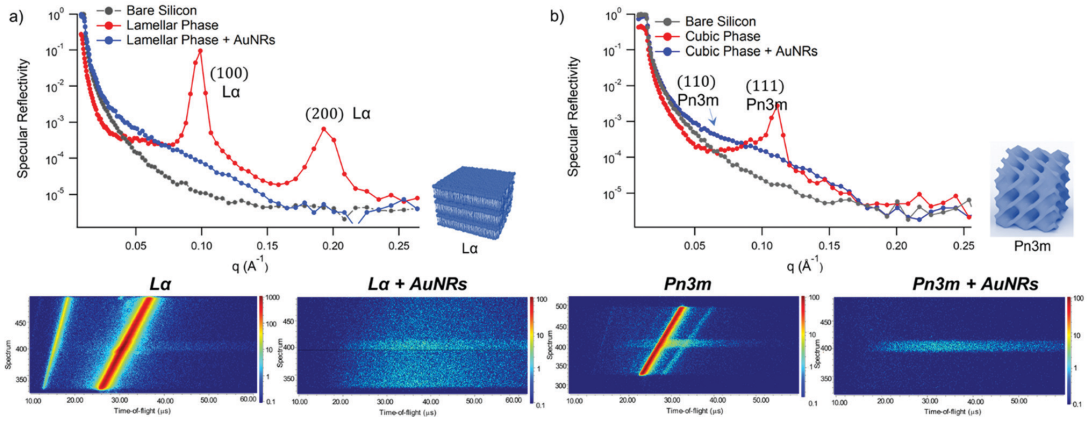

Fig. 4 (Panel a) Structural characterization of GMO/DOPC films interacting with AuNRs. Top: Specular reflectivity profiles of the GMO/DOPC film in the absence (red curve) and in the presence of AuNRs, together with the reflectivity of the bare silicon. The inset sketches the inner Lα structure of the film; Bottom: Detector images acquired for the Lα phase in the absence and in the presence of AuNRs; (Panel b) structural characterization of GMO films interacting with AuNRs. Specular reflectivity of the GMO film in the absence and in the presence of AuNRs, together with the reflectivity of the bare silicon. The inset sketches the inner cubic *Pn3m* structure of the lipid film; Bottom: Detector images acquired for the *Pn3m* phase in the absence and in the presence of AuNRs. Measurements acquired at OFFSPEC, ISIS Neutron and Muon Source (United Kingdom). The reflectivity profiles of lamellar and cubic films in the presence of AuNRs were after 8 h of incubation, with 5 h acquisition time, leading to a lipid films/AuNRs total interaction time of 13 h.

before and after the injection of AuNRs into the measuring cell, following the change in the reflectivity at time intervals of 2.5 min, covering a time period of 5 h. Representative data are shown in Fig. 5 as the (Q_z,Q_x) images from the reflectivity measurements for the lamellar (Panel a) and cubic film (Panel b), before and after AuNRs addition. The (Q_z,Q_x) maps of both lamellar and cubic films in the absence of NPs show pronounced off-specular patterns, featuring well defined "Bragg sheets" (see the red line in the left (Q_z,Q_x) plot of Panel b, as an example). The high intensity of the off-specular Bragg sheets allowed us to monitor the impact of AuNRs on the structure of lipid films over time. Panels a and b highlight a strong effect of AuNRs on both lamellar and cubic arrangements. The main effect is the smearing out of the characteristic Bragg sheets with time that ultimately leads to the complete loss of the off-specular signal. This indicates a total disruption of the films internal structure. Interestingly, lamellar films completely lose their structural organization significantly faster than cubic ones, with Braggs sheets completely vanishing within 12 min. In contrast, the cubic phase off-specular signal is still detectable after more than 2 h of incubation with AuNRs. Thus, cubic phases show larger structural stability when exposed to rods than lamellar ones. This is consistent with the previous reported effect of spherical particles.

In summary, Neutron Reflectivity and GISANS data allowed characterizing NPs-lipid films interactions at a nanoscale level, revealing that: (i) AuNRs are more effective than AuNSs in inducing structural modifications in the lipid films (ii) cubic phases are more stable than lamellar phases. In this respect, the first point is consistent with other studies reported in literature. Indeed, several computational and experimental studies highlighted that AuNRs exhibit a stronger interaction with lipid membranes and that this a consequence of the anisotropic shape of NPs.[38,39] In addition, our results demonstrate that this behaviour of AuNRs does not depend the structure of the lipid assembly, *i.e.*, it applies both to planar membranes and to bilayers which are highly curved. On the other hand, the higher stability of cubic phases towards the interaction with NPs might be counterintuitive. In fact, cubic phase-nanoparticle dispersions (cubosomes) are known to be particularly prone to attach to target membranes, where lipid exchange can occur.[40] For the case with AuNP, the adhesion of NPs to an already curved membrane might be more favourable if the curvature of the particle matches that of the lipid aqueous interface. We further investigated this aspect on the micron-scale by studying the same systems with Confocal Laser Scanning Microscopy (CLSM). This allowed us to follow the morphological modification induced by NPs on lipid films.

Nanoparticles-lipid films interaction at a micrometer length scale

We performed the CLSM study over the same time frame of Neutron kinetics measurements. For this purpose, fluorescently

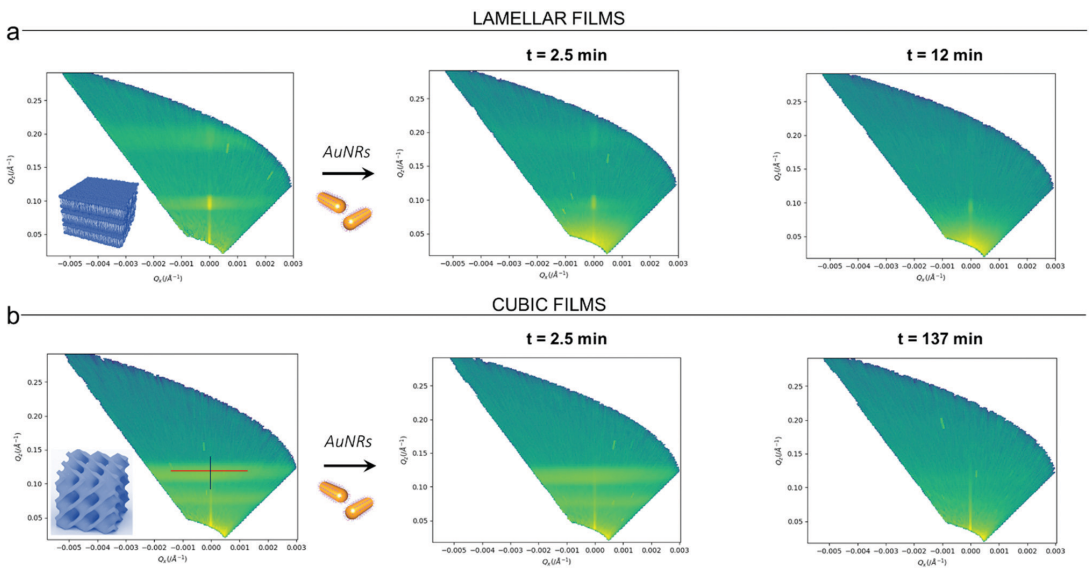

Fig. 5 (Panel a) Structural characterization of GMO/DOPC films interacting with AuNRs at short time-frames: (Q_z,Q_x) representations of the off-specular scattering of a lamellar film in the absence of AuNRs and at different times from the injection of AuNRs (acquisition in H_2O). (Panel b) Structural characterization of GMO films interacting with AuNRs at short time-frames: (Q_z,Q_x) representations enhancing the off-specular scattering of a cubic film in the absence of AuNRs and at different times from the injection of AuNRs (acquisition in H_2O). The integrated intensity along the specular reflectivity line (see blue line in the left (Q_z,Q_x) plot of Panel b) gives the specular reflectivity profile of lamellar and cubic films. Measurements of lamellar and cubic films in the presence of AuNRs were every 2.5 min with an acquisition of 5 min over 5 h, starting soon after the injection of AuNRs into the measurement chamber (incubation time $\sim$0 s). Here, representative (Q_z,Q_x) representations acquired after 2.5 and 12 min (Panel a) or 2.5 and 137 min (Panel b) of lipid films/AuNRs incubation times are reported.

labelled lamellar and cubic phases (Fig. 1, Panel b) were imaged right after (less than 1 s) and at different times after the injection of NPs. Fig. 6 gathers representative lateral-view CLSM images of a lamellar film exposed to AuNSs (Fig. 6a) and AuNRs (Fig. 6b). The action of spherical AuNSs (added at the same concentration employed in Neutron Reflectivity experiments) produces an initial swelling of the film (20 min), which increases the distance between the different lamellae composing the structure (Fig. 6a). This process leads to the progressive peeling-off of the lamellar film (60 min), with a gradual detachment of the outer surface layers. Once removed from the original matrix, these lipid layers start to bend and fold, ultimately rolling up in closed onion-like vesicular structures (180 min), which partially attach to the lipid film surface. After 180 min of incubation, only a thin layer of the original lamellar film is preserved onto the glass surface, partially covered by micron-sized multilamellar vesicles. The addition of asymmetrically shaped AuNRs (Fig. 6b) has a similar impact on the film morphology, which seems to progress in a similar way as with the AuNSs. However, the overall process is faster, consisting of an initial massive swelling of the lamellar membrane, which is observed after just 1 min from AuNRs addition. Moreover, the peeling-off of the film starts already after 5 min and, differently from the case of AuNSs, leads to the complete disruption of the lamellar film within 10 min, with only polydisperse vesicular structures remaining adsorbed onto the glass surface.

A completely different behaviour is observed when cubic phase lipid films are exposed to the same AuNPs. Spherical NPs added at the same concentration (Fig. 7a) seem to "excavate" the cubic membrane, producing an initial thinning of the film over selected areas (see the highlighted area in Fig. 7a, 30 min). The progressive excavation leads to the formation of cavities, whose depth increases with time, eventually reaching the glass surface. After 180 min of incubation, the lipid film, although mostly intact, presents micron-sized holes, which are clearly highlighted from the 3D reconstruction of the film, reported in Fig. 7a. As previously observed for the case of lamellar membranes, the addition of AuNRs produces faster and more profound morphological modifications (Fig. 7b): AuNRs initially increase the films roughness (20 min), with the formation of "hills and hollows" across the micrometric membrane. Similarly to what was previously observed for spherical AuNSs, the lipid film is progressively excavated, showing micron-sized cavities, whose depth increases with time. However, in this case the erosion process is faster and progresses within a few minutes. Complete retraction of the cubic film occurs in localized areas on the glass substrate, giving rise to large spheres of lipid matrix (50 min). After 50 min, the lipid film is completely dewetted, leaving only isolated lipid spheres onto the glass substrate. Then, these lipid spheres are decomposed/removed due to the presence of the AuNRs (51 min).

The micrometric spheres disruption process, occurring within few seconds, can be analysed in detail, by following the temporal evolution of a horizontal section of the droplet. For this purpose, top-view images of a lipid droplet at different

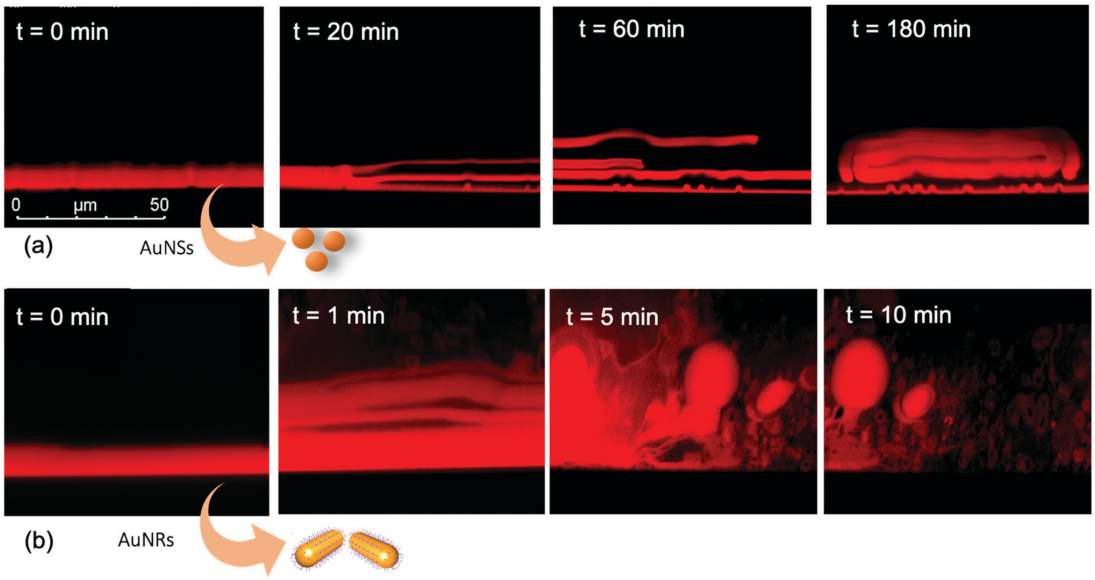

Fig. 6 (a) CLSM images (lateral view) of AuNSs interacting with a GMO/DOPC lamellar film. From left to right: lamellar film right after (t = 0 s), after 20 min, 60 min, and 180 min from the addition of AuNSs. (b) CLSM images (lateral view) of AuNRs interacting with a GMO/DOPC lamellar film. From left to right: lamellar film right after (t = 0 min), after 1 min, 5 min, and 10 min from the addition of AuNRs. Here, t = 0 corresponds to a lipid films/AuNPs incubation time ~0 s, as the time needed for each image recording is less than 1 s.

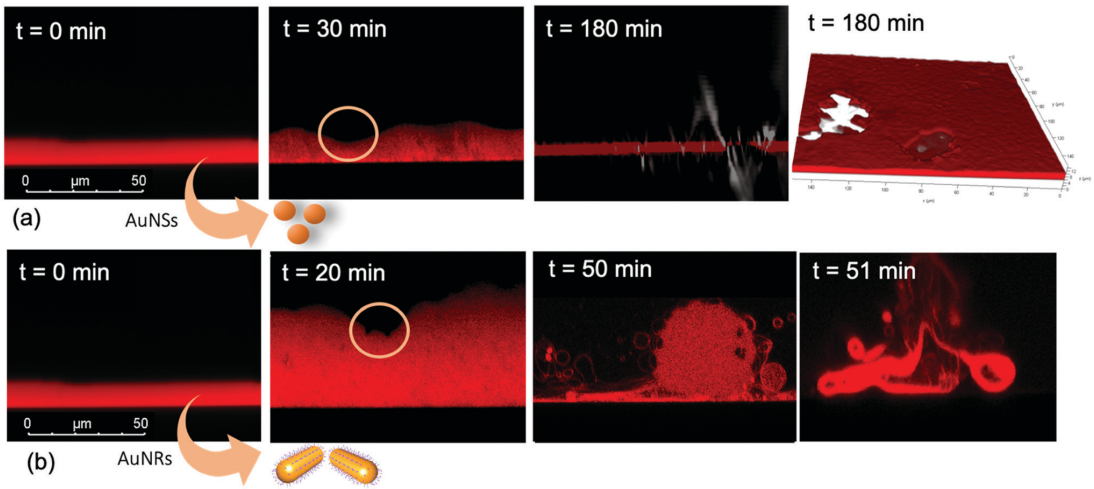

Fig. 7 (a) CLSM images (lateral view) of AuNSs interacting with a GMO cubic film. From left to right: lamellar film right after (t = 0 min) and after 30 min and 180 min from the addition of AuNSs. A 3D reconstruction of the film after 180 min interaction is also shown, highlighting the presence of micron sized holes in the film. (b) CLSM images (lateral view) of AuNRs interacting with a GMO cubic film. From left to right: cubic film right after (t = 0 min) and after 20 min, 50 min, and 51 min from the addition of AuNRs. Here, t = 0 corresponds to a lipid films/AuNPs incubation time ~0 s, as the time needed for each image recording is less than 1 s.

times from formation (from 0 to 10 s) have been acquired in fluorescence and transmission mode. This allowed us to simultaneously capture the fluorescence of the Nile Red labelled lipid matrix, and the gold nanoparticles. Representative images acquired within 10 s from the droplet formation are reported in Fig. 8a. At the beginning of the process, AuNRs, which can be visualized as black spots in the image, are located as micron-sized clusters at the edges of the spherical lipid droplet. Then, they start to excavate and unroll the lipid droplet starting from the edges of the sphere. This led to the complete collapse of the sphere within 10 s (see also the ESI,† video). In addition, it is possible to further analyse the mechanism of interaction of AuNRs with the lipid films by monitoring their excavation of the film in detail (Fig. 8b). Briefly, the AuNRs concentrate at the edges of the film as clusters, which progressively interact with the lipid interface and erode it. Interestingly, these clusters (which are highlighted with a zoom in Fig. 8b), appear to be elongated, which suggests that they are formed by end-to-end interactions of the AuNRs. On the contrary, for AuNSs only small clusters of round shape appear on the lipid film (see ESI,† Fig. S3). It is worth pointing out that, while cationic AuNSs and AuNRs form a stable dispersion in water, their lipid membrane-induced clustering is a clear hallmark of the strong interaction occurring at the nano-bio interface, as shown in several studies, both on synthetic and on biogenic lipid membrane.[29,41,42] This is likely due to the attractive interaction of the nanoparticles with the lipid membrane driven by *e.g.* electrostatic, hydrophobic and van der Waals interactions. This leads to the accumulation of the particles at the interface that promotes aggregation. In addition, for the cationic nanoparticles, the interaction with a membrane with an apparent negative net-charge leads to a reduction of nanoparticle charge that further promotes aggregation. Overall, the results gathered lead to two main conclusions: (i) in agreement with the Neutron Reflectivity analysis, the impact of AuNRs on both lamellar and cubic model films is stronger and leads to faster structural and morphological modifications with respect to AuNSs; (ii) NPs interact with lamellar and cubic phases according to two different and well-defined mechanisms, *i.e.* the peeling-off of the lamellar assembly and the excavation-dewetting of the cubic phase assembly.

The role of symmetry in NPs-lipid films interactions

The experimental results obtained with the different combined experimental techniques give a clear picture of the role that structure and morphology play to control NPs interactions with model membrane at different length scales. The mechanism is strongly affected by the structure of both the lipid film, *e.g.* the phase behaviour, and morphology, *i.e.* shape asymmetry of the NPs, as briefly summarized in Fig. 9.

The effect of NPs shape asymmetry. Both Neutron Reflectivity and CLSM results point out a major role of NPs asymmetric shape in the interaction with model membranes. Neutron Reflectivity results show that AuNRs have a profound impact on the structure of both lamellar and cubic films, where a complete loss of structural order occurs in less than 15 min and after 2 h for Lα and *Pn3m* phases, respectively. On the contrary, the combination of Neutron Reflectivity and GISANS analyses shows a significantly less effect of the AuNSs on the lipid films. Indeed, we only detected a partial disruption of lamellar and cubic structures after 13 h and 32 h of incubation, respectively. The slightly higher zeta potential of AuNRs as

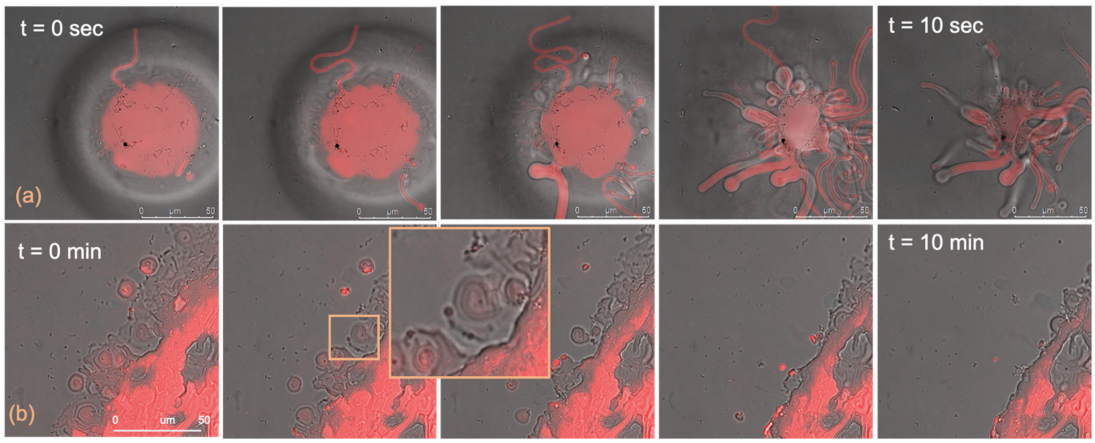

Fig. 8 CLSM images of AuNRs interacting with a GMO cubic film (overlay of fluorescence and transmission images): (a) disruption mechanism of a cubic film dewetted droplet by AuNRs, through the sequential extraction of lipid tubules from the bulk. (b) Mechanism of film excavation by AuNRs. Here, t = 0 corresponds to a lipid films/AuNRs incubation time ~0 s, as the time needed for each image recording is less than 1 s.

compared to AuNSs could be considered as relevant in driving their stronger interaction with lipid interfaces; however, CLSM findings clarify that NPs shape is the main factor at play: when challenging lipid films, AuNRs form elongated clusters, which seem to be particularly effective in eroding the lipid films (Fig. 8b). In addition, tubules extraction phenomena are highlighted for AuNRs disrupting dewetted lipid films droplets (Fig. 8a), which are a typical feature of AuNRs interacting with other lipid interfaces.[29]

Our results are consistent with other studies, according to which the impact of NPs surface functionalization, composition and size on lipid membranes are recognized as the key determinants in NPs cytotoxicity.[1,5,29,42–46] However, much less is known on the effect of the NP shape on both model and natural biomembranes, and some of the reported observations are contradictory. Asymmetric NPs have a higher surface area/volume ratio, which is theoretically predicted to maximize the surface available to interact and attach to membranes. The main driving forces here are van der Waals and possible electrostatic attractive forces,[1,16] as well as hydrophobic interactions, depending on the NPs properties. This has often been connected to a high affinity to bilayered biomimetic systems[29] and natural membranes,[47] which in turn has been linked to an enhanced cellular uptake.[48,49] On the other hand, the higher surface curvature at the edges of non-spherical NPs is predicted to increase the energy barrier required for the wrapping of the NPs by membranes, that can drive the internalization by cells.[3] Recent experimental findings report lower cellular uptake of asymmetric NPs compared to spherical ones.[14,15] In addition, to the best of our knowledge, the impact of NPs shape on their interaction with nonlamellar lipid films, mimicking curved bilayers, has not been studied before.

Here, employing spherical and rod-like AuNPs of comparable diameter and surface charge, we can separately study the effect of NPs shape on their interaction with membranes. We found that, when NPs size is similar to the lipid bilayer thickness, shape is of major importance, with asymmetric geometries producing more destructive effects on the lipid film structure and integrity. In particular, CLSM results suggest that, thanks to their asymmetric nature, AuNRs are able to maximize their interfacial interaction with lipid films, by forming end-to-end elongated clusters, while AuNSs seem to form more spherical clusters. Our results suggest that formation of the NPs elongated clusters facilitate the extraction of lipid tubules from the film. Eventually this was found leading to the complete erosion and disruption of the layer (see Fig. 9 scheme). Importantly, this behaviour was observed for both lamellar and non-lamellar films, highlighting a universal effect of NPs asymmetry on membranes of different structures.

The effect of membrane phase structure. Besides NPs shape, we found that membrane phase structure is another key factor that controls NPs interactions. Neutron Reflectivity and CLSM analyses highlighted that, for a given NP type, membrane geometry determines both the strength, pathway and results of interaction with NPs. Specifically, our Neutron Reflectivity results show that, independently from their shape, NPs induce a faster disruption of the nanostructure of lamellar films compared to cubic ones. This results into faster morphological modifications at the micron-scale as observed using CSLM. By combining the Neutron Reflectivity and CSLM data, we defined two different mechanisms that describe the interaction of NPs with lamellar and cubic phases and are responsible for their different stability towards nanomaterials (see Fig. 9).

The faster structural modification of Lα films induced by both AuNSs and AuNRs (Neutron Reflectivity and GISANS analyses) is associated with an initial swelling, followed by a progressive exfoliation of the multilamellar arrangement (CSLM analysis), that proceeds from the outer lamellar layers. We can hypothesize that, after their injection, NPs start to penetrate the outer part of the lamellar arrangement, *i.e.* the part directly exposed to water. This penetration would primarily

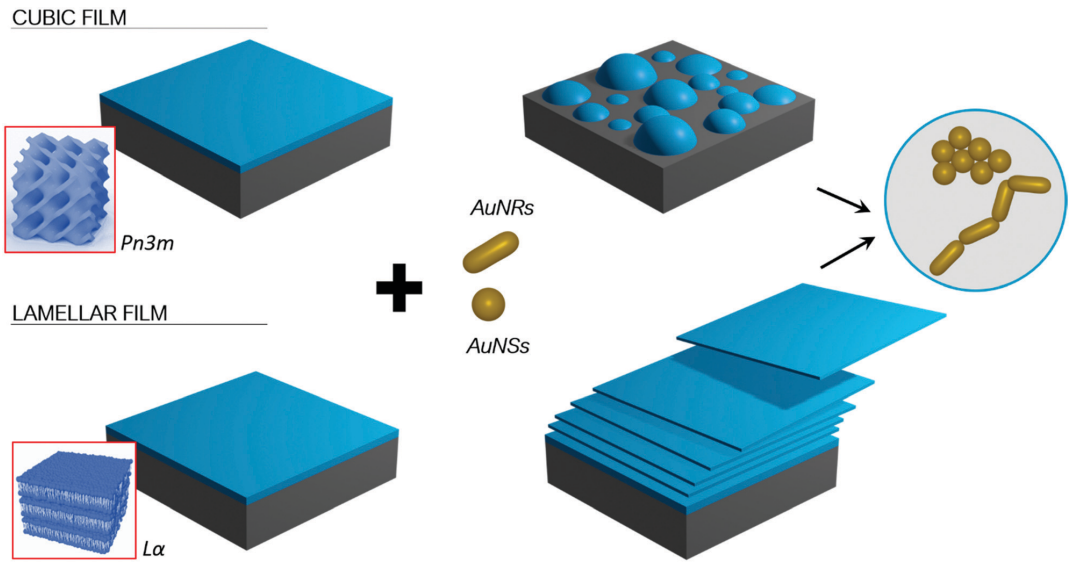

Fig. 9 Schematic illustration of the results of the interaction between AuNPs and cubic and lamellar phase lipid films. AuNPs induce the excavation and then dewetting of the cubic films (on the top), while provoking a progressive exfoliation of the lamellar arrangement (on the bottom). The disruption of both cubic and lamellar films is faster with AuNRs than with AuNSs, related to the different clustering processes of AuNPs interacting with lipid membranes, *i.e.* symmetrical clustering of AuNSs *versus* edge-to-tail asymmetric aggregation of AuNRs.

occur thanks to electrostatic and dipolar interactions between the cationic coating of NPs and the polar headgroup of lipids composing the membrane. This interaction would enable the insertion of NPs, together with their hydration shell, within the hydrophilic domains of the phase, *i.e.* the water layers separating the different lamellae. Then, the mismatch between the thickness of the water layers (around 2–3 nm) and NPs hydrodynamic size of about 4–5 nm (see Dynamic Light Scattering results in the ESI†) would be responsible for the initial swelling of the lamellar film. This is likely due to the insertion of NPs of larger size than the lamellar spacing and observed through CSLM. The increasing inter-lamellar distance would reduce the interactions between different lamellae, producing the detachment of the outer lamellar layers, which are the first ones to be in contact with NPs. Indeed, lipid bilayers of equal composition are held together only by weak van der Waals forces, in equilibrium with repulsive electrostatic and entropic contributions.[50] Thus, inter-bilayer interactions are easily overcome by attractive single bilayer-NPs forces mainly of electrostatic nature. The thinning of the film favors the penetration of NPs deeper into the film, *i.e.* coming closer to the solid support and promoting progressive peeling-off the lipid film. The loss of the lamellar periodicity as the layers are being detached can be connected with the progressive smearing out of the Lα-structural features, observed through Neutron Reflectivity (Fig. 2, 4 and 5).

On the other hand, a different interaction mechanism can be expected for the case of cubic phase films, accounting for their higher structural stability. Neutron Reflectivity and GISANS data highlight a progressive disordering and disruption of the cubic *Pn3m* nanostructure induced by NPs, which starts from the shrinkage of its lattice parameter (see GISANS analysis). This nanoscale phenomenon coincides with a progressive excavation of the film observed at the micron-scale (CSLM analysis), leading to de-wetting. Interestingly, this phenomenon proceeds from NPs clusters, which, acting like micron-sized "diggers", progressively erode and unroll the lipid matrix. We can hypothesize that, in this case, NPs are not able to fully penetrate the internal aqueous region of the film. Indeed, cubic phases represent a 3D highly interconnected network, where a continuous lipid bilayer folds in the space originating bicontinuous lipid and aqueous domains,[20] where the aqueous nanochannels has a diameter of around 4.4 nm. This liquid crystalline 3D architecture with intertwined systems of water channels of similar size as NPs would impede their full insertion; indeed, in the Lα phase, different lamellae can progressively detach the one from the other, with minimal energy required at each detachment step. On the contrary, the swelling of the cubic arrangement induced by the insertion of NPs would result in a modification of the whole cubic arrangement, due to its highly interconnected (*i.e.* bicontinuous) nature, which would involve an higher energy cost. Instead, the attractive NPs-lipid headgroups forces would result in the absorption of NPs, residing onto the film surface as clusters (see Fig. 8 and Fig. S3 of ESI†). As highlighted by Neutron Reflectivity analysis, their presence induces an immediate shrinking of the phase, leading to local release of water and dehydration of the phase. We can speculate that this phenomenon drives the progressive collapse of the cubic arrangement. Such process would then

proceed from the different points where NPs accumulate across the membrane. Ultimately this leads to isolated lipid droplets onto the solid substrate.

The enhanced stability of cubic phases compared to lamellar ones might have important biological implications. As already discussed, curved membranes assembled with cubic symmetry are known to form in cells under certain conditions (*e.g.*, viral infection, oxidative stress, starving, membrane fusion and formation of extracellular vesicles). However, cubic membrane-related investigations have been limited to a descriptive level, while the biological function of these arrangements remains unexplored.[20]

Engineered NPs often have a similar size range as biologically relevant entities (*i.e.*, DNA, surface proteins, biogenic extracellular vesicles, and viruses), often resulting in similar interaction pathways with cells.[1] Thus, we might connect the higher resilience exhibited by cubic membranes towards NPs with a similar behaviour towards natural nano-objects, such as viral pathogens. Within this perspective, our results seem to suggest a possible ''protective role'' of the cubic architecture, occurring in critical cell conditions to minimize the membrane response towards harmful external perturbations.

To summarize, we found that NPs-lipid membrane interactions depend both on the nanostructure of the membrane and the shape of NPs. These two variables represent two sides of the same coin, as a single parameter, *i.e.* symmetry, can describe their variations. In these terms, we can state that NPs with asymmetric shape promote a stronger interaction with the lipid matrix. On the other hand, when referring to the structure and morphology of the lipid membrane, we observed that flat 2D membranes experience more substantial disruptive effects than curved ones with 3D symmetry when exposed to NPs. Importantly, we also pointed out that a variation in NPs symmetry only affects the strength of interaction with lipid films, but not the interaction pathway; on the contrary, membranes with different morphologies lead to completely different interaction mechanisms. This is the basis for the observed differences in the structural resilience of these systems.

Experimental

Materials

Tetrachloroauric(III) acid ($\geq$99.9%), (11-mercaptoundecyl)-*N*,*N*,*N*-trimethylammonium bromide ($\geq$90%), cetyl trimethyl ammonium bromide (99%), octanethiol (98.5%), ascorbic acid (98%), $AgNO_3$ (99%), HCl, toluene (99.8%), MeOH (99.8%), EtOH (99.8%), $CHCl_3$ (99%), tetraoctylammonium bromide (98%), $NaBH_4$ (98%), *n*-hexane (99%), 1,2-dioleoyl-*sn*-glycero-3-phosphocholine (DOPC) and Nile Red ($\geq$98%) were provided by Sigma-Aldrich (St. Louis, MO). A glycerol monooleate sample (mono- and diglycerides ratio 44 : 1 by weight), denoted as RYLO™ MG19 Glycerol Monooleate (GMO), was produced and provided by Danisco Ingredients (now Dupont, Brabrand, Denmark) with the following fatty acid composition (Lot No. 2119/65-1): 89.3% oleic, 4.6% linoleic, 3.4% stearic and 2.7% palmitic acid. All chemicals were used as received. Milli-Q grade water was used in all preparations.

Synthesis of gold nanospheres (AuNSs)

Gold nanospheres functionalized with the cationic derivative *N*,*N*,*N*-trimethyl(11-mercaptoundecyl)ammonium bromide (TMA) were synthesized as described by McIntosh *et al.*[27,28] First, octanethiol-capped spherical gold nanoparticles (NSs) were prepared following the two-phase method developed by Brust *et al.*:[25,26] an aqueous solution of $HAuCl_4$ (15 mL, 30 mM) was mixed with a solution of tetraoctylammonium bromide (TOAB) in toluene (40 mL, 50 mM). The two-phase mixture was vigorously stirred until all the $HAuCl_4$ was transferred from the aqueous solution into the organic phase; TOAB acts as the phase-transfer reagent. Octanethiol (7.81 μL) was then added to the organic phase. A freshly prepared aqueous solution of sodium borohydride (12.5 mL, 0.4 M) was slowly added with vigorous stirring. On addition of the reducing agent, the organic phase changed colour from orange to deep brown within a few seconds. After further stirring for 3 h, the organic phase was separated, evaporated to 5 mL in a rotary evaporator and mixed with 200 mL ethanol to remove excess thiol. The mixture was kept for 4 h at −18 °C until a dark brown precipitate was formed, and the supernatant was removed with a pipette; the precipitate was washed with 200 mL of ethanol and put again in the freezer. After 4 h, the ethanol supernatant was removed with a pipette and completely evaporated in a rotary evaporator, obtaining octanethiol-capped gold nanoparticles. NSs capped with TMA were prepared by stirring 100 mg of octanethiol-capped NSs and 150 mg of *N*,*N*,*N*-trimethyl(11-mercaptoundecyl)ammonium bromide in 20 mL of degassed tetrahydrofuran under argon for two days at room temperature. The black precipitate of the gold nanoparticles was purified by repeated suspension, centrifugation, and decantation with dichloromethane. NSs capped with TMA were then dissolved in pure water without the need for pH adjustment. Such NPs have been found to be face-centered cubic (fcc) polyhedral.[51,52]

Synthesis of gold nanorods (AuNRs)

Gold NRs were synthesized according to a newly developed seedless growth protocol by El-Seyed.[53] Briefly, $HAuCl_4$ (5.0 mL; 1.0 mM) was added to 5.0 mL of Cetyl trimethyl ammonium bromide (CTAB, 0.2 M) at 27 °C, under magnetic stirring. Then, $AgNO_3$ (250 μL; 4.0 mM) was added. Subsequently, HCl (8.0 μL, 37%) was added to obtain a pH of 1–1.15. Then, we added 70 μL ascorbic acid (78.8 mM) under magnetic stirring and waited until the solution was clear. Immediately afterward, Ice-cold $NaBH_4$ (15 μL; 0.01 M) was added and allowed to react overnight. The final dispersion of AuNRs capped with CTAB was characterized by a dark pink colour. The excess of CITAB was removed from the dispersion by 10 cycles of centrifugation, each followed by precipitation of CITAB crystals and removal of the supernatant containing AuNRs. This AuNRs have been found to be single crystals of face-centered cubic (fcc) structure, with one of the main cubic axes oriented along the length of the rod.[54]

Preparation of lamellar and cubic lipid films

We obtained lamellar and cubic phase lipid films from GMO/DOPC 50/50% mol/mol and pure GMO, respectively. The lipid solutions in *n*-hexane (30/70 lipid/hexane % w/w) were spin-coated onto a solid substrate for 10 s at 700 r.p.m and then for 60 s at 2000 r.p.m. Most of the solvent evaporates during this procedure. The lipid-coated substrate was then immediately immersed in excess Milli Q water, leading to lamellar or cubic lipid films by hydration. For the case of lipid films prepared for CLSM analysis, lipid formulations were labelled with the hydrophobic dye Nile Red (0.1 mol% with respect to the total lipid amount), enabling the visualization of lipid layers; 100 μL of the lipid solution in n-hexane were deposited onto a hydrophilic round glass substrate (diameter of 15 mm) prior to spin-coating. Lipid films formed onto the glass substrate were then sealed into a single-well sample holder and hydrated with 2 mL of water before imaging. For the case of Neutron Reflectivity analysis, samples were formed by depositing 1 mL of *n*-hexane lipid solution on $50 \times 80 \times 15$ mm^3 ultra-polished Silicon n-doped single crystal (100) oriented (Siltronix, Archamps-France for the experiments performed at ISIS and Andrea Holm GmbH, Tann, Germany; roughness ≤ 5 Å for the experiments performed at MLZ) to cover almost the whole surface. After spin-coating and hydration, the substrate was sealed into a flow-cell type sample holder. To remove any excess contamination and the remaining *n*-hexane, an excess of water (at least 25 times the sample cell volume, *i.e.* 1.8 mL) was flushed through the sample cell. Silicon substrates were preliminary rinsed in either ultrapure water and ethanol, in order to remove organic residues. After that, they were bath sonicated for 30 min in ethanol with a Bandelin DL 102 3 L bath sonicator, followed by other 30 min in ultrapure water (Millipore Simplicity UV). The surfaces were then cleaned with a Novascan PSD-UV8 UV/ozone plasma for 30 min and rinsed in ultrapure water. Finally, they were dried with nitrogen gas and stored in ultrapure water, ready for deposition.

Neutron reflectivity

Static Neutron Reflectivity measurements (Section Synthesis of gold nanospheres (AuNSs)) were carried out at the OFFSPEC reflectometer[55] (Isis Neutron and Muon Source, Rutherford Appleton Laboratory, UK).

Neutrons in the wavelength range 1.0–14.5 Å were used to perform the measurements. Two incident angles, 0.50 deg and 2.00 deg allowed collecting data in the range $0.008 \leq Q/\text{Å}^{-1} \leq 0.3$. The arrival times and positions of scattered neutrons were detected on a ^{3}He 1×300 mm linear scintillator area detector (1.2 mm pixel size) positioned at 3.5 m from the sample. The linear detector also recorded the off-specular reflectivity in the vertical direction, which yields information about the in-plane structure at the interface. The detector consists of 768 wavelength shifting fibres with 0.5 mm pitch, resulting in an observable Q_x range of -6.5×10^{-4} to 6.5×10^{-4} Å^{-1}. The observable Q-range corresponds to real space distances, d, of approximately 1–40 mm (real and reciprocal space are related *via* $d = 2\pi/Q$). The set-up allows for a $\Delta Q_z/Q_z$ resolution of 2–5%. In order to achieve a good signal-to-noise ratio, a counting time of about 5 h for the measurement was used.

Neutron Reflectivity kinetic measurements were performed at the REFSANS Horizontal TOF reflectometer operated by the Helmholtz-Zentrum Hereon at the Heinz Maier-Leibnitz Zentrum (MLZ) in Garching, Germany.[56] Neutrons in the wavelength range 3.0–21.0 Å were used to perform the measurements. A vertically collimated beam having a width of 40 mm was used to maximise the intensity. An incident angle of 3.0 deg allowed collecting data in the range $0.032 \leq Q/\text{Å}^{-1} \leq 0.22$ with a resolution of $\Delta Q_z/Q_z = 8\%$. In this way we cover the region in which the evolution of Bragg peaks as well as that of the off-specular scattering may be followed as a function of time. The arrival times and positions of scattered neutrons were detected on a Denex 2D 500×700 mm^2 multiwire ^{3}He detector (pixel size 2.1×2.9 mm^2, efficiency 80% at 7 Å, gamma sensitivity $<10^{-6}$) positioned at 4.5 m from the sample. The detector was installed in a liftable vacuum tube forming an angle of 5.2 deg with respect to the horizon. Reflectivities were acquired at time intervals of 5 min, over a time of 5 h. Raw data were reduced and converted to Q-space images, obtaining Q_x/Q_z maps.[57]

In all the evaluations, the vertical component Q_z was corrected for the ballistic effect due to the gravitational field.

Grazing incidence small angle neutron scattering (GISANS)

GISANS measurements were performed at the REFSANS, using most of the same settings adopted for carrying out Neutron Reflectivity measurements. The only differences concern the wavelength band composing the incident beam (ranging from 2.7 to 18.1 Å with a wavelength resolution $\Delta\lambda/\lambda = 5\%$), which corresponds to different penetration depths within the sample. A radial collimator was used to focus the beam on the detector, placed at 10.2 m from the sample. Acquired data were divided in wavelength slices having a width of 10% with respect to the mean value. For a given wavelength slice, the two-dimensional intensity data sets describe different (Q_y, Q_z) ranges. As for the Neutron Reflectivity investigations, z represents the direction which is normal to the liquid/nanoparticle interface; x indicates the beam direction oriented towards the scattering beam, whereas y is the remaining axis defining a levogyrous cartesian system. Also for the GISANS analysis, the Q_z component was corrected for the ballistic effect.

GISANS was employed to investigate films' properties along the directions perpendicular and parallel to the substrate interface. The in-plane film structure can be studied from the scattering patterns on the (Q_y,Q_z) plane. If α_i and α_f are the angles of incidence and reflection of the neutron beam, respectively, then the three spatial components of the scattering vector (which is defined as the difference between the wave vector of the scattered beam $\overrightarrow{k_f}$ and that of the incident beam $\overrightarrow{k_i}$ are:

$$\begin{bmatrix} Q_x \\ Q_y \\ Q_z \end{bmatrix} = \frac{2\pi}{\lambda} \begin{bmatrix} \cos\alpha_f \cos 2\theta_f - \cos\alpha_i \\ \cos\alpha_f \sin 2\theta_f \\ \sin\alpha_i + \sin\alpha_f \end{bmatrix}$$

where λ is the neutron wavelength, while $2\theta_f$ indicates the scattering angle in the *xy* plane, which is relevant to determine lateral correlation lengths. The angle of incidence (0.5 deg) was chosen to get slices above and below the wavelength-dependent critical angle for total reflection (α_c).

Confocal laser scanning microscopy

A Leica CLSM TCS SP8 confocal microscope, operating in inverted mode, with a 63 × 1.3 numerical aperture water immersion objective, was used to image the lipid-based surface structures in excess water. The fluorescence of Nile Red lipophilic dye was excited at 561 nm and the fluorescence was acquired in the 571–650 nm emission range, with a PMT. Images were taken with a resolution of 512 × 512 pixels using a 400 Hz bidirectional scan with each scanning line averaged four times. Leica software was used to create three-dimensional reconstructions of the *z*-stacks.

Conclusions

In this contribution we explored the impact of symmetry and shape anisotropy on nano-bio interactions, focusing both on the geometry of nanoparticles and on the symmetry of the target membrane. By combining structural techniques with nanoscale resolution with Confocal Microscopy imaging, we connected structural and morphological modifications of lipid films induced by NPs, occurring at different length scales. Overall, our results show that breaking the 3D symmetry at the nano-bio interface (passing from a 3D sphere to a 1D rod in the NPs and from a 3D cubic phase to a 2D lamellar phase in the lipid film) results in an enhanced interaction. In addition, our findings provide new hints on the role of cubic membranes in Nature. Indeed, the biological function of cubic membranes occurring in stressed or starving cells,[58] or in cells exposed to infectious agents is, to date, debated: cubic membranes might result from aberrant membrane protein and/or lipid interactions in infected or pathological states, or might be a specific cellular response to these pathologies.[19] For instance, it has been hypothesized that viruses dysregulate cholesterol homeostasis of the host, to promote the formation of a cubic membrane as a protective environment to facilitate virus assembly and proliferation.[59] However, other studies hypothesize that the transformation from lamellar to cubic membranes is an adaptive strategy of cells under unhealthy conditions, as a method of defence.[60] Our results on cubic films, highlighting a striking higher resilience of cubic films as compared to lamellar ones towards NPs, support this latter hypothesis, suggesting a protective function of cubic membranes, which is inherently related to their 3D symmetry. Indeed, in this perspective, cubic membranes would represent biological barriers with enhanced structural resilience, occurring in cells as a "last defence" under extreme conditions, as in infected, stressed, or starved cells.

Conflicts of interest

There are no conflicts to declare.

Acknowledgements

This work has been supported by the European Community through the evFOUNDRY project (H2020-FETopen, ID: 801367) and the BOW project (H2020-EIC-FETPROACT-2019, ID: 952183). The authors also acknowledge CSGI for the economic support. Dr Mirko Severi is acknowledged for ICP-AES measurements; Heinz Maier-Leibnitz Zentrum (MLZ) (Garching bei München, Germany) and ISIS, Rutherford Appleton Laboratory Didcot, Oxfordshire (UK) are acknowledged for provision of beam-time.

References

1 M. Mendozza, L. Caselli, D. Berti and A. Salvatore, Nanoparticles and organized lipid assemblies: from interaction to design of hybrid soft devices inorganic stimuli responsive, *Soft Matter*, 2019, **15**, 8951–8970.
2 R. Michel and M. Gradzielski, Experimental Aspects of Colloidal Interactions in Mixed systems of liposome and inorganic nanoparticle and their applications, *Int. J. Mol. Sci.*, 2012, **13**, 11610–11642.
3 S. Dasgupta, T. Auth and G. Gompper, Nano- and microparticles at fluid and biological interfaces, *J. Phys.: Condens. Matter*, 2017, **29**, aa7933.
4 C. M. Beddoes, C. P. Case and W. H. Briscoe, Understanding nanoparticle cellular entry: a physicochemical perspective, *Adv. Colloid Interface Sci.*, 2015, **218**, 48–68.
5 A. M. Farnoud and S. Nazemidashtarjandi, Emerging investigator series: interactions of engineered nanomaterials with the cell plasma membrane; what have we learned from membrane models?, *Environ. Sci.: Nano*, 2019, **6**, 13–40.
6 M. Henriksen-Lacey, S. Carregal-Romero and L. M. Liz-Marzán, Current challenges toward *in vitro* cellular validation of inorganic nanoparticles, *Bioconjugate Chem.*, 2017, **28**, 212–221.
7 E. Blanco, H. Shen and M. Ferrari, Principles of nanoparticle design for overcoming biological barriers to drug delivery, *Nat. Biotechnol.*, 2015, **33**, 941–951.
8 P. Falagan-Lotsch, E. M. Grzincic and C. J. Murphy, One low-dose exposure of gold nanoparticles induces long-term changes in human cells, *Proc. Natl. Acad. Sci. U. S. A.*, 2016, **113**, 13318–13323.
9 C. J. Murphy, A. M. Vartanian, F. M. Geiger, R. J. Hamers, J. Pedersen, Q. Cui, C. L. Haynes, E. E. Carlson, R. Hernandez, R. D. Klaper, G. Orr and Z. Rosenzweig, Biological responses to engineered nanomaterials: needs for the next decade, *ACS Cent. Sci.*, 2015, **1**, 117–123.
10 L. Caselli, A. Ridolfi, J. Cardellini, L. Sharpnack, L. Paolini, M. Brucale, F. Valle, C. Montis, P. Bergese and D. Berti, A plasmon-based nanoruler to probe the mechanical properties of synthetic and biogenic nanosized lipid vesicles, *Nanoscale Horiz.*, 2021, **6**, 543–550.
11 K. L. Chen and G. D. Bothun, Nanoparticles Meet Cell Membranes: Probing Nonspecific Interactions using Model Membranes, *Environ. Sci. Technol.*, 2014, **48**, 873–880.

12 A. H. Bahrami, Orientational changes and impaired internalization of ellipsoidal nanoparticles by vesicle membranes, *Soft Matter*, 2013, **9**, 8642.
13 S. Dasgupta, T. Auth and G. Gompper, Wrapping of ellipsoidal nano-particles by fluid membranes, *Soft Matter*, 2013, **9**, 5473–5482.
14 S. Dasgupta, T. Auth and G. Gompper, Shape and orientation matter for the cellular uptake of nonspherical particles, *Nano Lett.*, 2014, **14**, 687–693.
15 R. Vácha, F. J. Martinez-Veracoechea and D. Frenkel, Receptor-mediated endocytosis of nanoparticles of various shapes, *Nano Lett.*, 2011, **11**, 5391–5395.
16 Q. Mu, G. Jiang, L. Chen, H. Zhou, D. Fourches, A. Tropsha and B. Yan, Chemical Basis of Interactions Between Engineered Nanoparticles and Biological Systems, *Chem. Rev.*, 2014, **114**, 7740–7781.
17 E. Gonzalez Solveyra and I. Szleifer, What is the role of curvature on the properties of nanomaterials for biomedical applications?, *Wiley Interdiscip. Rev.: Nanomed. Nanobiotechnol.*, 2016, **8**, 334–354.
18 S. Nangia and R. Sureshkumar, Effects of nanoparticle charge and shape anisotropy on translocation through cell membranes, *Langmuir*, 2012, **28**, 17666–17671.
19 Z. A. Almsherqi, S. D. Kohlwein and Y. Deng, Cubic membranes: a legend beyond the Flatland * of cell membrane organization, *J. Cell Biol.*, 2006, **173**, 839–844.
20 Z. A. Almsherqi, T. Landh and S. D. Kohlwein, *Cubic Membranes: The Missing Dimension of Cell Membrane Organization*, Elsevier Inc., 1st edn, 2009, vol. 274.
21 Y. Deng and M. Mieczkowski, Three-dimensional periodic cubic membrane structure in the mitochondria of amoebae Chaos carolinensis, *Protoplasma*, 1998, 16–25.
22 D. P. Chang, J. Barauskas, A. P. Dabkowska, M. Wadsäter, F. Tiberg and T. Nylander, Non-lamellar lipid liquid crystalline structures at interfaces, *Adv. Colloid Interface Sci.*, 2015, **222**, 135–147.
23 A. P. Dabkowska, M. Valldeperas, C. Hirst, C. Montis, G. K. Pálsson, M. Wang, S. Nöjd, L. Gentile, J. Barauskas, N. J. Steinke, G. E. Schroeder-Turk, S. George, M. W. A. Skoda and T. Nylander, Non-Lamellar lipid assembly at interfaces: controlling layer structure by responsive nanogel particles, *Interface Focus*, 2017, **7**, 20160150.
24 A. Ridolfi, B. Humphreys, L. Caselli, C. Montis, T. Nylander, D. Berti, M. Brucale and F. Valle, Exploring the structure and mechanics of thin supported inverse bicontinuous cubic phase lipid films, *bioRxiv*, 2021, DOI: 10.1101/2021.03.29.437497.
25 S. Tatur and A. Badia, Influence of hydrophobic alkylated gold nanoparticles on the phase behavior of monolayers of DPPC and clinical lung surfactant, *Langmuir*, 2012, **28**, 628–639.
26 M. Brust, M. Walker, D. Bethell, D. J. Schiffrin and R. Whyman, Synthesis of Thiol-derivatised Gold Nanoparticles in a Two-phase Liquid-Liquid System, *J. Chem. Soc., Chem. Commun.*, 1994, 801–802.
27 C. M. McIntosh, E. A. Esposito, A. K. Boal, J. M. Simard, C. T. Martin and V. M. Rotello, Inhibition of DNA transcription using cationic mixed monolayer protected gold clusters, *J. Am. Chem. Soc.*, 2001, **123**, 7626–7629.
28 S. Tatur, M. Maccarini, R. Barker, A. Nelson and G. Fragneto, Effect of functionalized gold nanoparticles on floating lipid bilayers, *Langmuir*, 2013, **29**, 6606–6614.
29 C. Montis, V. Generini, G. Boccalini, P. Bergese, D. Bani and D. Berti, Model lipid bilayers mimic non-specific interactions of gold nanoparticles with macrophage plasma membranes, *J. Colloid Interface Sci.*, 2018, **516**, 284–294.
30 D. E. Sands, *Introduction to Cristallography*, W.A. Benjamin, Inc., New York, NY, 1969.
31 V. Cherezov, J. Clogston, Y. Misquitta, W. Abdel-Gawad and M. Caffrey, Membrane protein crystallization in meso: lipid type-tailoring of the cubic phase, *Biophys. J.*, 2002, **83**, 3393–3407.
32 G. Popescu, J. Barauskas, T. Nylander and F. Tiberg, Liquid crystalline phases and their dispersions in aqueous mixtures of glycerol monooleate and glyceryl monooleyl ether, *Langmuir*, 2007, **23**, 496–503.
33 N. Kučerka, S. Tristram-Nagle and J. F. Nagle, Structure of fully hydrated fluid phase lipid bilayers with monounsaturated chains, *J. Membr. Biol.*, 2006, **208**, 193–202.
34 R. Negrini and R. Mezzenga, Diffusion, molecular separation, and drug delivery from lipid mesophases with tunable water channels, *Langmuir*, 2012, **28**, 16455–16462.
35 P. Müller-Buschbaum, Grazing incidence small-angle neutron scattering: challenges and possibilities, *Polym. J.*, 2013, **45**, 34–42.
36 S. J. Richardson, P. A. Staniec, G. E. Newby, N. J. Terrill, J. M. Elliott, A. M. Squires and W. T. Góźdź, Predicting the orientation of lipid cubic phase films, *Langmuir*, 2014, **30**, 13510–13515.
37 R. Kampmann, M. Haese-Seiller, V. Kudryashov, B. Nickel, C. Daniel, W. Fenzl, A. Schreyer, E. Sackmann and J. Rädler, Horizontal ToF-neutron reflectometer REFSANS at FRM-II Munich/Germany: first tests and status, *Phys. B: Condens. Matter*, 2006, **385–386**, 1161–1163.
38 K. Yang and Y. Q. Ma, Computer simulation of the translocation of nanoparticles with different shapes across a lipid bilayer, *Nat. Nanotechnol.*, 2010, **5**, 579–583.
39 W. K. Fong, T. L. Hanley, B. Thierry, N. Kirby, L. J. Waddington and B. J. Boyd, Controlling the nanostructure of gold nanorod-lyotropic liquid-crystalline hybrid materials using near-infrared laser irradiation, *Langmuir*, 2012, **28**, 14450–14460.
40 P. Vandoolaeghe, A. R. Rennie, R. A. Campbell, R. K. Thomas, F. Höök, G. Fragneto, F. Tiberg and T. Nylander, Adsorption of cubic liquid crystalline nanoparticles on model membranes, *Soft Matter*, 2008, **4**, 2267–2277.
41 C. Montis, A. Salvatore, F. Valle, L. Paolini, F. Carlà, P. Bergese and D. Berti, Biogenic supported lipid bilayers as a tool to investigate nano-bio interfaces, *J. Colloid Interface Sci.*, 2020, **570**, 340–349.
42 T. Pfeiffer, A. De Nicola, C. Montis, F. Carlà, N. F. A. Van Der Vegt, D. Berti and G. Milano, Nanoparticles at Biomimetic

Interfaces: Combined Experimental and Simulation Study on Charged Gold Nanoparticles/Lipid Bilayer Interfaces, *J. Phys. Chem. Lett.*, 2019, **10**, 129–137.

43 P. Vedantam, G. Huang and T. R. J. Tzeng, Engineered nanoparticles interacting with cells: size matters, *J. Nanobiotechnology*, 2013, **4**, 13–20.

44 C. Montis, L. Caselli, F. Valle, A. Zendrini, F. Carlà, R. Schweins, M. Maccarini, P. Bergese and D. Berti, Shedding light on membrane-templated clustering of gold nanoparticles, *J. Colloid Interface Sci.*, 2020, **573**, 204–214.

45 B. Pelaz, G. Charron, C. Pfeiffer, Y. Zhao, J. M. De La Fuente, X. J. Liang, W. J. Parak and P. Del Pino, Interfacing engineered nanoparticles with biological systems: anticipating adverse nano-bio interactions, *Small*, 2013, **9**, 1573–1584.

46 A. Ridolfi, L. Caselli, C. Montis, G. Mangiapia, D. Berti, M. Brucale and F. Valle, Gold nanoparticles interacting with synthetic lipid rafts: an AFM investigation, *J. Microsc.*, 2020, **280**, 194–203.

47 S. Salatin, S. Maleki and A. Y. Khosroushahi, Effect of the surface modification, size, and shape on cellular uptake of nanoparticles, *Cell Biol. Int.*, 2015, **39**, 881–890.

48 S. E. A. Gratton, P. A. Ropp, P. D. Pohlhaus, J. C. Luft, V. J. Madden, M. E. Napier and J. M. Desimone, The effect of particle design on cellular internalization pathways, *Proc. Natl. Acad. Sci. U. S. A.*, 2008, **105**, 11613–11618.

49 R. Agarwal, V. Singh, P. Jurney, L. Shi, S. V. Sreenivasan and K. Roy, Mammalian cells preferentially internalize hydrogel nanodiscs over nanorods and use shape-speci fi c uptake mechanisms, *Proc. Natl. Acad. Sci. U. S. A.*, 2013, **110**, 1–6.

50 J. N. Israelachvili, *Intermolecular and Surface Forces*, 3rd edn, Elsevier, 2011.

51 T. Mori and T. Hegmann, Determining the composition of gold nanoparticles: a compilation of shapes, sizes, and calculations using geometric considerations, *J. Nanoparticle Res.*, 2016, **18**, 1–36.

52 S. I. Stoeva, B. L. V. Prasad, S. Uma, K. J. Stoimenov, P. K. Zaikovski, V. Sorensen and C. M. Klabunde, Face-Centered Cubic and Hexagonal Closed-Packed Nanocrystal Superlattices of Gold Nanoparticles Prepared by Different Methods, *J. Phys. Chem. B*, 2003, **107**, 7441–7448.

53 M. R. K. Ali, B. Snyder and M. A. El-Sayed, Synthesis and optical properties of small Au nanorods using a seedless growth technique, *Langmuir*, 2012, **28**, 9807–9815.

54 T.-S. Deng, J. E. S. van der Hoeven, A. O. Yalcin, H. W. Zandbergen, M. A. van Huis and A. van Blaaderen, Oxidative Etching and Metal Overgrowth of Gold Nanorods within Mesoporous Silica Shells, *Chem. Mater.*, 2015, **27**, 7196–7203.

55 R. M. Dalgliesh, S. Langridge, J. Plomp, V. O. De Haan and A. A. Van Well, Offspec, the ISIS spin-echo reflectometer, *Phys. B: Condens. Matter*, 2011, **406**, 2346–2349.

56 J.-F. Moulin and M. Haese, *REFSANS: reflectometer and evanescent wave small angle neutron spectrometer. Journal of large-scale research facilities*, J. large-scale Res. Facil. JLSRF.

57 A. Hafner, P. Gutfreund, B. P. Toperverg, A. O. F. Jones, J. P. de Silva, A. Wildes, H. E. Fischer, M. Geoghegan and M. Sferrazza, Combined specular and off-specular reflectometry: elucidating the complex structure of soft buried interfaces, *J. Appl. Crystallogr.*, 2021, **54**, 924–948.

58 R. Mezzenga, J. M. Seddon, C. J. Drummond, B. J. Boyd, G. E. Schröder-Turk and L. Sagalowicz, Nature-Inspired Design and Application of Lipidic Lyotropic Liquid Crystals, *Adv. Mater.*, 2019, **31**, 1–19.

59 Y. Deng, Z. A. Almsherqi, M. M. L. Ng and S. D. Kohlwein, Do viruses subvert cholesterol homeostasis to induce host cubic membranes?, *Trends Cell Biol.*, 2010, **20**, 371–379.

60 Q. Xiao and E. Al, Why Do Membranes of Some Unhealthy Cells Adopt a Cubic, *ACS Cent. Sci.*, 2016, **2**, 943–953.

Electronic Supplementary Material (ESI) for Physical Chemistry Chemical Physics.

Supplementary Information for:

Interaction of nanoparticles with lipid films: the role of symmetry and shape anisotropy

Lucrezia Caselli[a], Andrea Ridolfi[b], Gaetano Mangiapia[c], Pierfrancesco Maltoni[a], Jean-Francois Moulin[c], Nina-Juliane Steinke[d], Debora Berti, Emil Gustafsson[e], Tommy Nylander [f]* and Costanza Montis [a]*

[a] *Department of Chemistry, University of Florence and CSGI, Florence (Italy);* [b]*ISMN-CNR and CSGI, Bologna (Italy);* [c] *Heinz Maier-Leibnitz Zentrum (MLZ), Garching bei München (Germany);* [d]*ISIS, Rutherford Appleton Laboratory Didcot, Oxfordshire (UK);* [e]*Department of Chemistry, Uppsala University, Uppsala (Sweden);* [f]*Department of Chemistry, Lund University, Lund (Sweden).*

Small Angle X-ray Scattering

SAXS measurements were carried out on a S3-MICRO SAXS/WAXS instrument (HECUS GmbH, Graz, Austria) which consists of a GeniX microfocus X-ray sealed Cu Kα source (Xenocs, Grenoble, France) of 50 W power which provides a detector focused X-ray beam with λ = 0.1542 nm Cu Kα line. The instrument is equipped with two one-dimensional (1D) position sensitive detectors (HECUS 1D-PSD-50 M system), each detector is 50 mm long (spatial resolution 54 μm/channel, 1024 channels) and cover the SAXS Q-range (0.003< Q <0.6˚Å −1). The temperature (25°C) was controlled by means of a Peltier TCCS-3 Hecus. The analysis of SAXS curves was carried out using Igor Pro (Kline, 2006). SAXS measurements on AuNPs aqueous dispersions, were carried out in sealed glass capillaries of 1.5 mm diameter. The concentration of AuNSs in water was $1.1 \cdot 10^{15}$ particles/mL.

To analyze AuNSs scattering profile we chose a model function with a spherical form factor and a Schulz size distribution (Kotlarchyk and Chen, 1983) from the NIST package SANS Utilities. This model calculates the scattering for a polydisperse population of spheres with uniform scattering length density. The distribution of radii is a Schulz distribution given by the following equation:

$$f(R) = (z+1)^{z+1} x^z \frac{exp[-(z+1)x]}{R_{avg}\Gamma(z+1)}$$

where R_{avg} is the mean radius, $x = R/R_{avg}$, z is a parameter related to the polydispersity and $\Gamma(x)$ indicates the Gamma function. The form factor is normalized by the average particle volume, using the 3rd moment of R:

$$\langle V \rangle = \frac{4\pi}{3}\langle R^3 \rangle = \frac{4\pi}{3}\langle R \rangle^3 \frac{(z+3)(z+2)}{(z+1)^2}$$

The scattering intensity is:

$$I(Q) = \left(\frac{4\pi}{3}\right)^2 N_0(\Delta\rho)^2 \int_0^\infty f(R)R^6F^2(QR)dR$$

where N_0 is the total number of particles per unit volume, $F(QR)$ is the scattering amplitude for a sphere and $\Delta\rho$ is the difference in scattering length density between the particle and the solvent.

The SAXS profile of AuNRs (at a concentration of $2.4 \cdot 10^{14}$ particles/mL) was fitted by the Cylinder poly radius model from the NIST package SANS Utilities; this model calculates the form factor for a polydisperse right circular cylinder with uniform scattering length density and a Schulz polydispersity of the cylinder length is considered. The function calculated is the orientationally averaged cylinder form factor which is then averaged over a Schulz distribution of the cylinder length $2H$. The size averaged form factor is thus:

$$P(Q) = \int_0^\infty \int_0^{\pi/2} f(2H)F^2(Q\alpha)\sin\alpha \, d\alpha \, d(2H)$$

where f($2H$) is the normalized Schulz distribution of the length $2H$. The limits of the integration are adjusted automatically to cover the full range of length. The scattering amplitude, F, is:

$$F(Q\alpha) = 2V_{cyl}(\rho_{cyl}-\rho_{solv})j_0(QH\cos\alpha)\frac{j_1(QR\sin\alpha)}{(QR\sin\alpha)}$$

Where $j_1(QR\sin\alpha)$ is the first order Bessel function, $V_{cyl} = 2\pi HR^2$, $j_0(QH\cos\alpha) = \frac{\sin(\mathrm{QH}\cos\alpha)}{\mathrm{QH}\cos\alpha}$, with α defined as the angle between the cylinder axis and the scattering vector (Q) and ρ_{cyl} and ρ_{solv} the scattering length density of the nanorod and the solvent respectively. The integral over α averages the form factor over all possible orientations of the cylinder with respect to Q.

Transmission Electron Microscopy (TEM)

Transmission electron microscopy (TEM) images were acquired with a STEM CM12 Philips electron microscope, at CeME (CNR Florence Research Area, Via Madonna del Piano, 10 - 50019 Sesto Fiorentino). The sample was placed on a 200 mesh carbon-coated copper grid.

Dynamic Light Scattering (DLS)

DLS measurements were performed using a Malvern Panalytical Zetasizer Nano ZS90 instrument which does DLS measurements at a fixed scattering angle of 90°. A 4 mW laser of 633 nm wavelength is used as light source, the lag times of

the correlator start from 25 ns as shortest and go up to 8000 s, using a maximum number of 4000 channels. After checking monomodality with a CONTIN fit, the ACFs were analyzed through the cumulant fitting stopped to the second order, allowing an estimate of the hydrodynamic diameter and the polydispersity of AuNSs and AuNRs, which were found equal to: 25.6 ± 0.2 and 37.6 ± 0.1 nm (hydrodynamic diameter) with a 0.3 and 0.21 (PDI), respectively.

Z-Potential

Zeta potential measurements were performed using a Zeta Potential Analyzer (Zeta Plus, Brookhaven Instruments Corporation, Holtsville, NY). Zeta potentials were obtained from the electrophoretic mobility u, according to Helmholtz-Smoluchowski equation: $\zeta = (\eta/\varepsilon) \times u$ with η being the viscosity of the medium, ε the dielectric permittivity of the dispersing medium. The Zeta Potential values are reported as averages from ten measurements.

Inductively Coupled Plasma Atomic Emission Spectroscopy (ICP-AES)

This analysis was kindly done by Dr. Mirco Severi, in order to define the concentration of NPs dispersions, with an ICP-AES Varian 720-ES. For the analysis, 200 μL of NPs dispersion were placed in a vial, then the solvent was evaporated under slight nitrogen flow. The sample, consisting of a dry film of nanoparticles, was diluted to 5 mL with 0.1% super pure nitric acid, obtained by

distillation under boiling, then, to the sample, 1 ppm of Ge was added, as internal standard; the sample thus treated was analysed.

The operating conditions for the ICP-AES analysis have been optimized to obtain the maximum signal intensity and are as follows:

Instrument: Varian 720-ES

Power R.F: 1.20 KW

Flow rate of Argon Plasma: 16.5 L min^{-1}

Auxiliary Argon flow rate: 1.50 L min^{-1}

Argon nebulizer flow rate: 0.75 L min^{-1}

Replicated reading time: 5 seconds

Instrument stabilization time: 30 seconds

Sample introduction settings:

Sample uptake: 30 seconds

Flow rate: 1 mL min^{-1}

Rinse time: 70 seconds

Fast Pump (sample delay / rinse): active

Smart rinse: active

Replicates: 3

From the ICP-AES data, it results that the quantity of gold in 200 μL of AuNSs and AuNRs dispersions is equal to 259 μg and 278 μg; as a result, the concentrations of Au in AuNSs and AuNRs is 1.3 mg/mL and 1.4 mg/mL,

respectively. The AuNSs and AuNRs concentration per ml was subsequently evaluated considering the size of AuNPs determined through SAXS and is equal to $3.2 \cdot 10^{15}$ and $7.4 \cdot 10^{14}$ particles/mL for AuNSs and AuNRs, respectively.

Evaluation of the spacing parameter of cubic and lamellar films through NR

The unit cell spacing (d) of cubic and lamellar films was evaluated from NR data (i.e., with hkl Miller indices, hkl, (100) and (200)), using the Q-position of the Bragg reflection peaks of cubic and lamellar phases. In particular, the lamella phase features two prominent Bragg peaks located at 0.099 and 0.192 $Å^{-1}$, corresponding to the first two reflexes of the lamellar, L_α, phase (i.e., with Miller indices, *hkl*, (100) and (200)). The unit cell spacing was calculated using the q-position of the maximum Bragg reflection peaks $d = 2\pi h/Q_h$, yielding a value of 6.4±0.1 nm as the mean between the two peak positions. The reflectivity profile of the GMO lipid film presents two clearly distinguishable Bragg peaks at q values 0.093 and 0.115 $Å^{-1}$, corresponding to Miller indices (110) and (111) of the Pn3m inverse cubic phase. The lattice spacing d, can be calculated from $d = 2\pi(h^2 + k^2 + l^2)^{1/2}/Q_{100}$ (Sands, 1969), yielding a value of 9.51±0.05 nm as the mean between the two peak positions.

Evaluation of the spacing parameter of cubic films through GISANS

In order to obtain the lattice parameter of the Pn3m cubic architecture (in the presence and in the absence of AuNSs), we used the GISANS images shown in the main text (Figure 3). We performed horizontal line cuts from the 2D GISANS data, along selected Qz values, obtaining the Intensity *vs* Qy plots, reported in Figure S2. The Qy values corresponding to the intensity's maxima were then used to determine the Q value of a spot on the Q_y/Q_z GISANS plot, according to following equation:

$$\boldsymbol{Q^2 = Q_y^2 + Q_z^2}$$

The lattice parameter (d) is then evaluated from the following equation: $d = 2\pi(h^2 + k^2 + l^2)^{1/2}/Q_{hkl}$ (with h, k and l miller indices identifying a Bragg reflection peak). Q_{hkl} is taken as the mean between the Q-values obtained for the different intensity's spots of each horizontal line cut.

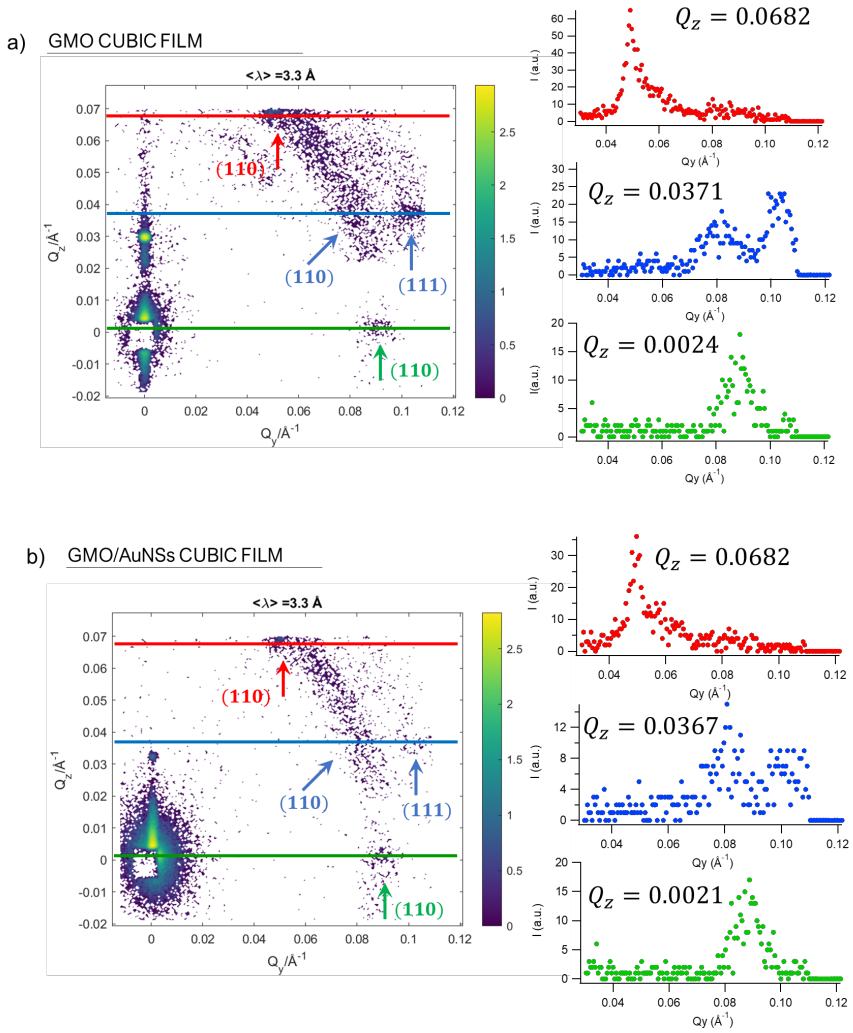

Figure S1: a) Left part: GISANS 2D plot of the GMO/water film; the horizontal lines represent the directions along which the line cuts are performed. Right part: horizontal Intensity vs Qy line cuts obtained from the 2D GISANS plot along different Qz.

Analysis of NR profiles of cubic and lamellar films interacting with AuNRs

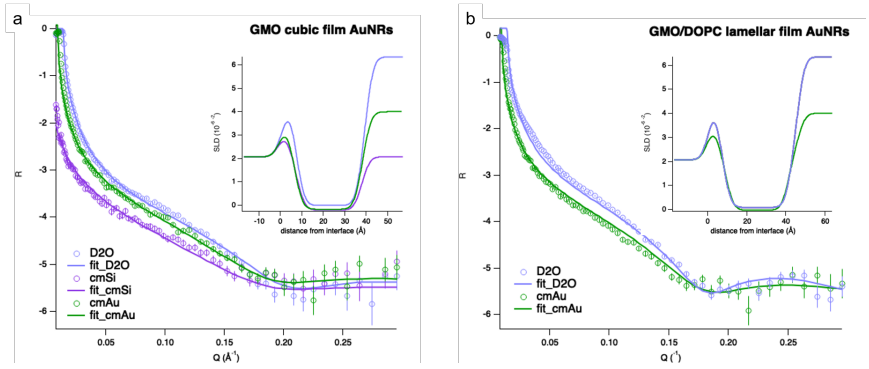

Figure S2: Neutron Reflectometry profiles of (a) GMO cubic films and (b) GMO/DOPC lamellar films upon interaction with AuNRs. Three contrasts were measured for GMO/AuNRs system: D_2O (SLD 6.34e-6 $Å^{-2}$), cmAu (SLD 4.6e-6 $Å^{-2}$, where Au is contrast-matched), cmSi (SLD 2.07e-6 $Å^{-2}$, where Si is contrast-matched), while two contrasts were measured for GMO/AuNRs system (D_2O, cmAu). It was possible to analyze both GMO (a) and GMO/DOPC (b) systems according to a five-layers model, accounting for the formation of a lipid bilayer. For GMO the bilayer thickness is 34 +/- 3 nm, while for GMO/DOPC the bilayer thickness is 40 +/- 4 nm, consistent with the parameters expected from the literature ((Chang *et al.*, 2016)). The bilayer thickness was obtained by analyzing the data with motofit (Nelson, 2006), considering scattering length density values of: 2.07e-6 $Å^{-2}$ (silicon layer), 3.41e-6 $Å^{-2}$ (Silicon oxide layer), 2.17e-6 $Å^{-2}$ (GMO polar headgroup layer), -2.12e-7 $Å^{-2}$ (GMO and DOPC lipid chain layer), 2e-6 $Å^{-2}$ (mixed GMO/DOPC polar headgroup layer). In both cases, the layer appear homogeneous, with high coverage of the substrate (inferred from the low hydration degree of the systems <10%)

CLSM images of AuNSs clusters on lipid films

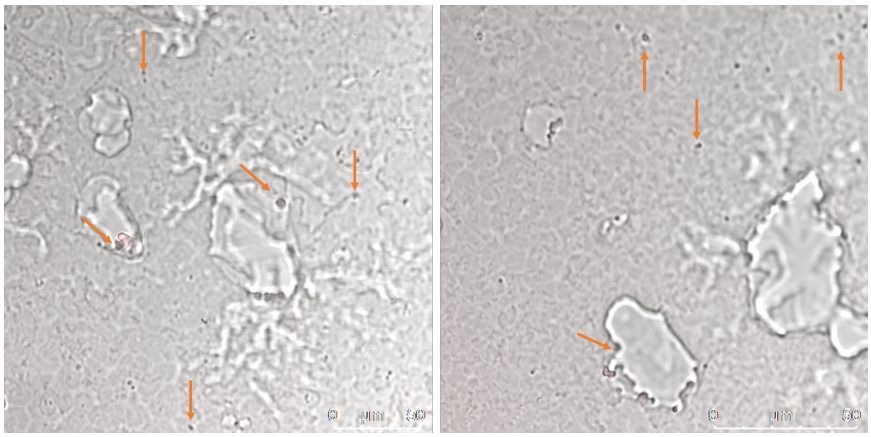

Figure S3: Representative transmission CLSM images of GMO cubic films incubated with AuNSs. The orange arrows in the figure highlight the presence of multiple round-shaped black spots attributable to the presence of AuNSs clusters.

Stability of lipid films upon water flow

A possible effect of lipid removal caused by the liquid flow through the sample cell had been investigated by means of Neutron Reflectivity (OFFSPEC, ISIS Neutron and Muon Source (United Kingdom)). In particular, the Reflectivity of a GMO lipid film in D_2O, adsorbed onto silicon, has been acquired before (black profile in Figure S.4) and after rinse with D_2O (green profile in Figure S.4), flushed into cell at the same flow rate used for the injection of AuNPs, i.e. 0.1 ml/min. The difference in the intensity of black and green profiles is due to the different acquisition time, i.e. 5 hours vs 30 minutes, respectively. However, in spite of the shorter acquisition time, the green profile shows a well distinct pattern of Bragg reflexes, which is similar to the one highlighted in the black profile and identifies a cubic Pn3m arrangement. This demonstrates that the lipid films are structurally stable and fully preserved upon liquid flow through the sample cell.

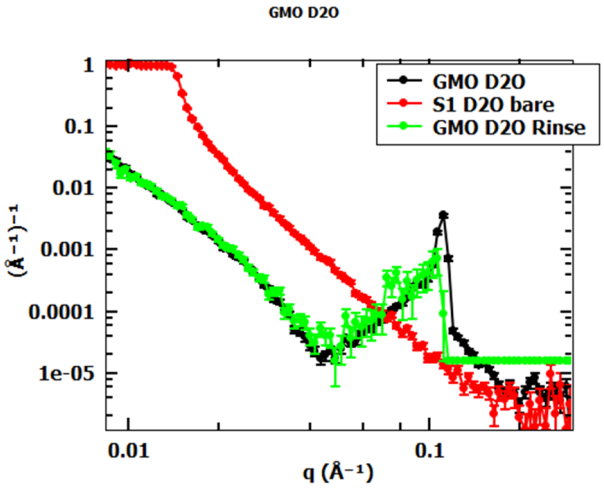

Figure S4: Specular reflectivity profiles of a GMO film acquired in D_2O before and after rinse with D_2O, together with the reflectivity of the bare silicon in D_2O.

Bibliography

Chang, P. D. *et al.* (2016) 'Interfacial properties of POPC/GDO liquid crystalline nanoparticles deposited on anionic and cationic silica surfaces', *Physical Chemistry Chemical Physics*, 18(38), pp. 26630–26642.

Kline, S. R. (2006) 'Reduction and analysis of SANS and USANS data using IGOR Pro', *Journal of Applied Crystallography*, 39(6), pp. 895–900. doi: 10.1107/S0021889806035059.

Kotlarchyk, M. and Chen, S.-H. (1983) 'Analysis of small angle neutron scattering spectra from polydisperse interacting colloids', *The Journal of Chemical Physics*, 79(5), p. 2461. doi: 10.1063/1.446055.

Nelson, A. (2006) 'Co-refinement of multiple-contrast neutron/X-ray reflectivity data using MOTOFIT', *Journal of Applied Crystallography*. International Union of Crystallography, 39(2), pp. 273–276. doi:

10.1107/S0021889806005073.

Sands, D. E. (1969) *Introduction to Cristallography*. W.A. Benjamin, Inc., New York, NY.